

**Effects of anisotropy of the interfacial energies on  
pattern formation within solidification of ternary  
eutectics: A phase-field study**

For obtaining the academic degree  
**Doctor of Engineering (Dr.-Ing.)**  
at the Faculty of Mechanical Engineering  
Karlsruhe Institute of Technology (KIT)

approved  
**Dissertation**  
of

**M.Sc. Kaveh Dargahi Noubary**

Date of examination: 23. September 2022  
Examiner: Prof. Dr. rer. nat. Britta Nestler  
Co-examiner: Prof. Dr. Hans Jürgen Seifert



This document is licensed under a Creative Commons  
Attribution-ShareAlike 4.0 International License (CC BY-SA 4.0):  
<https://creativecommons.org/licenses/by-sa/4.0/deed.en>

**Effects of anisotropy of the interfacial energies on  
pattern formation within solidification of ternary  
eutectics: A phase-field study**

Zur Erlangung des akademischen Grades eines  
**Doktors der Ingenieurwissenschaften (Dr.-Ing.)**  
von der KIT-Fakultät für Maschinenbau des  
Karlsruher Instituts für Technologie (KIT)

angenommene  
**Dissertation**

von

**M.Sc. Kaveh Dargahi Noubary**

Tag der mündlichen Prüfung:	23. September 2022
Hauptreferentin:	Prof. Dr. rer. nat. Britta Nestler
Korreferent:	Prof. Dr. Hans Jürgen Seifert



# Abstract

A grand-potential-based phase-field model is used to simulate the solidification processes of ternary eutectics and to study the effects of the anisotropic interfacial energies on the evolved microstructures. In the course of the endeavor, thermodynamic properties of the investigated material systems, such as the equilibrium concentrations and the Gibbs energy values in the existing phases, are derived from the CALPHAD databases. The directional solidification *DS* processes have been simulated in NiAl-10Mo and Bi-In-Sn systems, based on the reported parameters of the experimental works in the literature. The achieved results are validated by the Jackson-Hunt analysis and by comparisons to the experimental data. The final microstructure in the NiAl-10Mo system contains Mo-rich fibers embedded in a NiAl-rich matrix. It is observed that in the evolved fibers, the cross sections have squared shapes when the anisotropy in the solid-solid interfaces is active. The simulations in the Bi-In-Sn ternary eutectic system result in evolutions of lamellae with  $\alpha\beta\alpha\delta$  stacking sequences, when the interfaces are modeled isotropically. In the latter system, the experimentally reported  $[\alpha\beta]_a[\alpha\delta]_b$  superstructures are observed in the final products, when the anisotropy is activated in the  $\alpha\beta$  and/or  $\alpha\delta$  interfaces. For a more precise study of the ongoing mechanisms, the rotating directional solidification *RDS* process has been simulated and in the resultant circular trajectories, the roles of the anisotropy are analyzed systematically. It is observed that in accordance with the experimental results, the anisotropy in the  $\alpha\beta$  phase boundaries plays a more pronounced role in the pattern formation, compared to the  $\alpha\delta$  boundaries. With respect to the imprinted temperature gradients, the tilted growths of the solidified phases are observed in the simulations in which the tilt angles increase when there is an increase in the anisotropy strength. This analysis is performed by measuring the variations in the radii of the circular trajectories. Finally, the tilting phenomenon has been studied in the directional solidification of an idealized ternary system, in order to reduce the complexities related to the material properties. A formulation is derived to predict the tilt angle as a function of the system and process parameters like the interfacial energies, the diffusion coefficients, the temperature gradients and the solidification velocities.

# Kurzfassung

Mit einem auf dem großkanonischen Potential basierten Phasenfeldmodell werden die Erstarrungsprozesse von ternären Eutektika simuliert und die Auswirkungen der anisotropen Grenzflächenenergien auf die entstehenden Mikrostrukturen untersucht. Dabei werden thermodynamische Eigenschaften der untersuchten Materialsysteme, wie die Gleichgewichtskonzentrationen und die Gibbs-Energiewerte in den vorhandenen Phasen, aus den CALPHAD-Datenbanken abgeleitet. Die gerichteten Erstarrungsprozesse wurden in den Systemen NiAl-10Mo und Bi-In-Sn basierend auf den in der Literatur berichteten Parametern der experimentellen Arbeiten simuliert. Die erzielten Ergebnisse werden durch die Jackson-Hunt-Analyse und durch Vergleiche mit den experimentellen Daten validiert. Das endgültige Mikrogefüge im NiAl-10Mo-System enthält eine NiAl-reiche Matrix, die in Mo-reiche Fasern eingebettet ist. Es kann beobachtet werden, dass die Querschnitte in den entstandenen Fasern quadratische Formen haben, wenn die Anisotropie in den Festkörper/Festkörper-Grenzflächen aktiv ist. Die Simulationen im ternären eutektischen Bi-In-Sn-System führen zur Entwicklung von Lamellen mit  $\alpha\beta\alpha\delta$ -Stapelfolgen, wenn die Grenzflächen isotrop modelliert werden. Im letztgenannten System werden die experimentell berichteten  $[\alpha\beta]_a[\alpha\delta]_b$ -Überstrukturen in den Endprodukten beobachtet, wenn die Anisotropie an den  $\alpha\beta$ - und/oder  $\alpha\delta$ -Grenzflächen aktiviert wird. Für eine genauere Untersuchung der ablaufenden Mechanismen wurde der rotierende, gerichtete Erstarrungsprozess simuliert und die Rolle der Anisotropie in den daraus resultierenden kreisförmigen Verläufen systematisch analysiert. In Übereinstimmung mit den experimentellen Ergebnissen wird festgestellt, dass die Anisotropie in den  $\alpha\beta$ -Phasengrenzen eine stärkere Rolle bei der Musterbildung spielt als in den  $\alpha\delta$ -Grenzen. In Bezug auf die aufgeprägten Temperaturgradienten wird in den Simulationen ein gekipptes Wachstum bei den erstarrten Phasen beobachtet, wobei die Kippwinkel bei einer Zunahme der Anisotropiestärke zunehmen. Diese Analyse wird durch eine Messung der Variationen der Radien der kreisförmigen Verläufe durchgeführt. Schließlich wurde das Phänomen der Kippung bei der gerichteten Erstarrung eines idealisierten ternären Systems untersucht, um die Komplexität im Zusammenhang mit den Materialeigenschaften zu verringern. Es wird eine Formulierung abgeleitet, damit es möglich ist, den Kippwinkel als Funktion der System- und Prozessparameter wie der Grenzflächenenergien, der Diffusionskoeffizienten, der Temperaturgradienten und der Erstarrungsgeschwindigkeiten vorherzusagen.

# Contents

<b>1</b>	<b>Introduction and motivation</b>	<b>2</b>
<b>2</b>	<b>Phase-field method</b>	<b>6</b>
2.1	Phase-field model . . . . .	6
2.2	Anisotropy formulation . . . . .	10
2.3	Implementations and tools . . . . .	10
2.3.1	The solvers . . . . .	10
2.3.2	Discretization technique . . . . .	11
2.3.3	Boundary conditions ( <i>BC</i> ) . . . . .	12
2.3.4	Moving window technique . . . . .	12
2.3.5	Nucleation mechanism . . . . .	13
<b>3</b>	<b>Simulations setup</b>	<b>14</b>
3.1	Directional Solidification ( <i>DS</i> ) . . . . .	14
3.2	Rotating Directional Solidification ( <i>RDS</i> ) . . . . .	16
<b>4</b>	<b>Literature review on material properties</b>	<b>22</b>
4.1	Ni-Al-Mo ternary system . . . . .	22
4.2	Bi-In-Sn ternary system . . . . .	24
<b>5</b>	<b>Gibbs energies modeling in ternary systems</b>	<b>30</b>
5.1	General method for Gibbs energies modeling . . . . .	30
5.2	NiAl-10Mo ternary system . . . . .	36
5.3	Bi-In-Sn ternary system . . . . .	40

---

5.4	Summary and conclusions . . . . .	41
<b>6</b>	<b>Phase-field simulations</b>	<b>44</b>
6.1	<i>DS</i> simulation studies of NiAl-10Mo system . . . . .	44
6.1.1	Jackson-Hunt analysis in 2D . . . . .	45
6.1.2	Free growth of the solidified phases in 2D . . . . .	49
6.1.3	3D simulation . . . . .	51
6.1.4	Summary and conclusions . . . . .	52
6.2	<i>DS</i> simulation studies of Bi-In-Sn system . . . . .	52
6.2.1	Jackson-Hunt analysis in 2D . . . . .	53
6.2.2	Free growth of the solidified phases in 2D . . . . .	55
6.2.3	Summary and conclusions . . . . .	70
6.3	<i>RDS</i> simulation studies of Bi-In-Sn system . . . . .	70
6.3.1	Isotropic interfacial energies . . . . .	72
6.3.2	Anisotropic interfacial energies . . . . .	75
6.3.3	Summary and conclusions . . . . .	88
6.4	Tilted growth in <i>DS</i> study of an idealized system . . . . .	89
6.4.1	The system . . . . .	90
6.4.2	Tilt angle measurement technique . . . . .	92
6.4.3	Effects of the process and system parameters on tilt angle . . . . .	94
6.4.3.1	Interfacial energies ratio ( $R$ ) . . . . .	96
6.4.3.2	Diffusion coefficients ( $D$ ) . . . . .	97
6.4.3.3	Temperature gradient ( $G^{DS}$ ) . . . . .	97
6.4.3.4	Solidification velocity ( $v$ ) . . . . .	98
6.4.3.5	Overview of the affecting parameters . . . . .	98
6.4.4	Approximation of the tilt angle . . . . .	100
6.4.5	Summary and conclusions . . . . .	101
<b>7</b>	<b>Summary and outlook</b>	<b>104</b>

---

<b>Acknowledgements</b>	<b>108</b>
<b>Appendix A Appendices to chapter 5</b>	<b>110</b>
A.1 NiAl-10Mo system . . . . .	110
A.2 Bi-In-Sn system . . . . .	113
<b>Appendix B Appendices to chapter 6</b>	<b>114</b>
B.1 NiAl-10Mo system . . . . .	114
B.2 Bi-In-Sn system . . . . .	115
B.3 Idealized system . . . . .	116
<b>List of Symbols</b>	<b>118</b>
<b>List of Abbreviations and Acronyms</b>	<b>122</b>
<b>List of Figures</b>	<b>124</b>
<b>List of Tables</b>	<b>132</b>
<b>Bibliography</b>	<b>134</b>



# Chapter 1

## Introduction and motivation

The efficiency and versatility of the phase-field method as a powerful numeric technique in the simulation studies of the microstructure evolutions have been proved in various studies [1–3]. The simulations of dendritic [4–6], eutectic [7–11] and peritectic [12, 13] growths, as well as the spinodal decompositions [14, 15], can be mentioned as examples of the performed studies in the literature. Due to the considerable influence of the microstructure on the material properties [16–19], the mentioned studies have given new intuitions about the macroscopic behaviors in the investigated material systems. As an example, the occurred instabilities at the microscopic level are proved to have significant roles in the macroscopic behaviors [20, 21]. In the diffusion-controlled eutectic reactions in the directionally solidified systems, different instabilities have been reported as the following: bifurcations in the solidified lamellae [22, 23], growth of the eutectic colonies [24–26], oscillations in the solidified phases boundaries [22, 27] and the tilting of the formed phases with respect to the imprinted temperature gradients [28–30]. It is mentioned that the anisotropy in the interfacial energies is a key parameter in the formation of stable/unstable microstructural patterns [31–34]. As one example of the stably evolved patterns, the fibrous microstructures in the directional solidification of the NiAl-10Mo ternary eutectic system can be mentioned. The experimental evidence in this system shows the formation of Mo-rich fibers embedded in the NiAl-rich matrices. The formed fibers have cubic cross-sectional shapes due to the interfacial energy anisotropies [35]. The effects of the process parameters like the solidification velocities on the resultant patterns are investigated in this reference.

Despite the previous system, the eutectic reaction in the Bi-In-Sn ternary system is another example in which the anisotropic behavior leads to instabilities in the evolved solid phases. If the  $\alpha$ ,  $\beta$  and  $\delta$  solid phases are formed in grains with isotropic interfacial energies,  $\alpha\beta\alpha\delta$ -type arrangements are observed. Otherwise, superstructures in the general form of  $[\alpha\beta]_a[\alpha\delta]_b$  are reported in the experimental works of [22, 36–38], where

$a$  and  $b$  are higher-than-one natural numbers. Although these investigations reveal lots of facts about the ongoing mechanisms in the considered material systems, there are still open questions about the roles of the interfacial energy anisotropies on the evolved patterns. Since in the experimental studies it is difficult to distinguish between the effects of different material parameters, simulation studies can give new insights by producing the possibility of such investigations in less complicated and more efficient ways. Therefore, in this work, the solidification processes in the indicated ternary alloys are simulated. A grand-potential-based [39, 40] phase-field model is used for this purpose. In general, the processes are initially simulated assuming isotropic solid-solid interfaces to simplify reaching the stable solid phase growths. Afterwards, the anisotropies are activated and their influences on microstructure evolutions are studied. The main approach in the conducted studies is a systematic variation of the anisotropy strength.

In ensuing chapters, initially, the phase-field model is introduced and its related tools are explained. Then, the simulation setups for both directional and rotating directional solidification processes are discussed which are benefited in the forthcoming studies. Next, the literature reviews are performed focusing on both **NiAl-10Mo** and **Bi-In-Sn** ternary systems in order to summarize the beneficial experimental, simulative and thermodynamic data. The latterly indicated thermodynamic data are obtained from the CALPHAD databases [41] including the equilibrium concentrations of the elements in the involved phases and the information of the Gibbs free energies as the most required thermodynamic data for the simulations. Afterwards, the directional solidification simulations are conducted in the **NiAl-10Mo** system in two and three dimensions leading to the expected cubic form of the evolved fibers in 3D. For the case of the **Bi-In-Sn** system, simulations are completed in 2D and the anticipated results related to the anisotropic behaviors in the interfacial energies are achieved in the formed microstructures. These results are mainly the formation of previously mentioned  $[\alpha\beta]_a[\alpha\delta]_b$ -type superstructures. In the rotating directional solidification studies, the tilted growths of the solidified phases with respect to the imprinted temperature gradients are resulted. All results are validated based on the theoretical and/or experimental evidence in the literature. Although, the tilting in the last indicated case is the result of the anisotropic behavior in the interfacial energies, but due to its complex nature, a further study is performed to detect its additional affecting parameters. In the course of this endeavor, an idealized ternary system is chosen in which the Gibbs energies are modeled in the forms of second-order-polynomial cones. These cones have the same physical properties for all involving phases to reduce the complexity of the system. The energy paraboloid of the liquid phase is located in the center of the ternary diagram and the other congruent paraboloids representing the solid phases are placed at equal distances from the center. The directional solidification simulations are performed with the systematic variations in the system and the process

parameters. The report of the observed patterns and derivation of a function to estimate the tilt angles is the final performed study in this work.



# Chapter 2

## Phase-field method

### 2.1 Phase-field model

From one point of view, the phase-field models implemented in the literature for simulation studies of solidification processes can be classified into two categories: free-energy-functional-based models [42] and grand-potential-functional-based models [39, 40]. In these models investigating the multi-phase, multi-component alloys with  $N$  various phases and  $K$  components, the evolved phase fields can be saved in the vector  $\boldsymbol{\phi}(\mathbf{x}, t) = (\phi_1(\mathbf{x}, t), \phi_2(\mathbf{x}, t), \dots, \phi_N(\mathbf{x}, t))$ . Similarly, the vector  $\mathbf{c}(\mathbf{x}, t)$  includes the concentration fields in form of  $(c_1(\mathbf{x}, t), c_2(\mathbf{x}, t), \dots, c_K(\mathbf{x}, t))$  in a simulation domain  $\Omega \in \mathbb{R}^d, d \in \{1, 2, 3\}$ . Fulfillment of the constraints  $\sum_{\hat{\alpha}=1}^N \phi_{\hat{\alpha}} = 1$  and  $\sum_{i=1}^K c_i = 1$  are required in the representation of the mentioned fields. The Greek letters  $\alpha, \beta, \delta, \dots$  are used as the phase names, except the letter  $\gamma$  which denotes the interfacial energies in the following. In order to reach a physical formulation compatible with the occurring effects within the phase transformation processes, an entropy functional  $S(e, \mathbf{c}, \boldsymbol{\phi})$  can be defined in form of:

$$S(e, \mathbf{c}, \boldsymbol{\phi}) = \int_{\Omega} \left[ s(e, \mathbf{c}, \boldsymbol{\phi}) - (\varepsilon \tilde{a}(\boldsymbol{\phi}, \nabla \boldsymbol{\phi}) + \frac{1}{\varepsilon} \tilde{w}(\boldsymbol{\phi})) \right] d\Omega. \quad (2.1)$$

In this formulation which is used to obtain a free-energy-based phase-field model, physical effects such as latent heat release, heat and mass transfers and the Gibbs-Thomson relation can be taken into account. The parameter  $e$  denotes the internal energy of the system and the parameter  $s$  denotes the bulk entropy density.  $\varepsilon$  is a term related to the length of the diffused evolving phase-field interfaces.  $\tilde{a}(\boldsymbol{\phi}, \nabla \boldsymbol{\phi})$  and  $\tilde{w}(\boldsymbol{\phi})$  are the parameters that formulate the surface entropy densities considering the thermodynamics of the interfaces [42]. The free energy densities of the pure phases  $f_{\alpha}(T, \mathbf{c})$  are interpolated

to form the total free energy  $f(T, \mathbf{c}, \boldsymbol{\phi})$  of the system and the internal energy density is expressed as  $e = f + sT$ , where  $T$  stands for the temperature. The chemical potentials of the involved phases are defined as  $\mu_i = \partial f / \partial c_i$ ; therefore,  $\partial s / \partial c_i$  is equal to  $-\mu_i / T$ . A general class of phase diagrams can be incorporated into the phase-field model due to the presence of the free energies  $f_\alpha$  in the discussed formulations. Hence, an ideal solution formulation for the bulk free energy density and later a more generalized Redlich-Kister-Muggianu expression is introduced in [42]. The governing equations with respect to time  $t$ , i.e.  $\partial e / \partial t$  and  $\partial c_i / \partial t$  are solved based on these expressions and the conservation laws for  $e$  and  $c_i$  ( $i = 1, 2, \dots, K$ ). The non-conserved phase-field variables  $\phi_\alpha$ ,  $\alpha = 1, 2, 3, \dots, N$  are formulated by variational differentiation of  $S(e, \mathbf{c}, \boldsymbol{\phi})$  to ensure the increase of the total entropy in the indicated reference.

If we focus on the interface formulation, two different approaches are presented in the literature: In the first approach, the material in the diffuse interface is considered to be in an intermediate state between the bulk phases. The introduced models in the works of Wheeler et al. [43], Caginalp et al. [44] and Warren et al. [45] can be mentioned as examples of such interface definitions in the literature. In contrast, the interface can be considered as a mixture of two phases in which the bulk properties of both are preserved [46, 47]. Plapp showed in his work from 2011 that by exploiting a grand-potential functional instead of the free energy functional as the start point of the phase-field modeling, both approaches can be captured by the standard variational procedure [40]. Later, Choudhury et al. [39] noticed some limitations for the formerly derived phase-field models based on the free energy functionals which increased the motivation to use the grand-potential-based phase-field models. As a summary of these limitations, it has been shown that the role of grand-chemical-potential excess to the interfacial energy contribution in the modeled systems cannot be neglected in some cases, and has a significant effect on the evolved patterns. Therefore, the benefited phase-field model in the simulation studies of current work is such a model, in which a grand-potential functional  $\Psi$  as the following is considered [10]:

$$\Psi(\boldsymbol{\phi}, \boldsymbol{\mu}, T) = \int_{\Omega} \left[ (\varepsilon a(\boldsymbol{\phi}, \nabla \boldsymbol{\phi}) + \frac{1}{\varepsilon} w(\boldsymbol{\phi})) + \psi(\boldsymbol{\phi}, \boldsymbol{\mu}, T) \right] d\Omega. \quad (2.2)$$

$\psi(\boldsymbol{\phi}, \boldsymbol{\mu}, T)$  is related to the driving force of the reaction which can be calculated based on the existing experimental or thermodynamic data of the free energies. The individual grand potentials are interpolated from this parameter as [39]:

$$\psi(\boldsymbol{\phi}, \boldsymbol{\mu}, T) = \sum_{\hat{\alpha}=1}^N \psi_{\hat{\alpha}}(\boldsymbol{\mu}, T) h_{\hat{\alpha}}(\boldsymbol{\phi}). \quad (2.3)$$

The hat symbols  $\hat{\square}$  are introduced to distinguish the phases from their indices in this formulation.  $h_{\hat{\alpha}}$  is the interpolation function and in the interface, the isotropic gradient energy density is defined as:

$$a(\boldsymbol{\phi}, \nabla \boldsymbol{\phi}) = \sum_{\hat{\alpha} < \hat{\beta}}^{N,N} \gamma_{\hat{\alpha}\hat{\beta}} \left| \mathbf{q}_{\hat{\alpha}\hat{\beta}} \right|^2, \quad (2.4)$$

in which  $\gamma_{\hat{\alpha}\hat{\beta}}$  represents the interfacial energy density and  $\mathbf{q}_{\hat{\alpha}\hat{\beta}} = \phi_{\hat{\alpha}} \nabla \phi_{\hat{\beta}} - \phi_{\hat{\beta}} \nabla \phi_{\hat{\alpha}}$  is the generalized gradient vector. The potential energy density is represented by the equation:

$$w(\boldsymbol{\phi}) = \frac{16}{\pi^2} \sum_{\hat{\alpha} < \hat{\beta}}^{N,N} \gamma_{\hat{\alpha}\hat{\beta}} \phi_{\hat{\alpha}} \phi_{\hat{\beta}} + \sum_{\hat{\alpha} < \hat{\beta} < \hat{\delta}}^{N,N,N} \gamma_{\hat{\alpha}\hat{\beta}\hat{\delta}} \phi_{\hat{\alpha}} \phi_{\hat{\beta}} \phi_{\hat{\delta}}, \quad (2.5)$$

where  $\gamma_{\hat{\alpha}\hat{\beta}\hat{\delta}}$  is a higher-order parameter and is introduced to emerge in the binary interfaces preventing the formation of a third phase [10]. It also affects the triple points to form amended contact angles between the contacting phases [42]. In the next step, minimization of eq. (2.2) is performed to obtain the following Allen-Cahn-type evolution equations of the phase- and concentration- fields:

$$\begin{aligned} \tau \varepsilon \frac{\partial \phi_{\hat{\alpha}}}{\partial t} = & - \varepsilon \underbrace{\left( \frac{\partial a(\boldsymbol{\phi}, \nabla \boldsymbol{\phi})}{\partial \phi_{\hat{\alpha}}} - \nabla \cdot \frac{\partial a(\boldsymbol{\phi}, \nabla \boldsymbol{\phi})}{\partial \nabla \phi_{\hat{\alpha}}} \right)}_{:=rhs_{1,\hat{\alpha}}} - \frac{1}{\varepsilon} \frac{\partial w(\boldsymbol{\phi})}{\partial \phi_{\hat{\alpha}}} \\ & - \underbrace{\frac{\partial \psi(\boldsymbol{\phi}, \boldsymbol{\mu}, T)}{\partial \phi_{\hat{\alpha}}}}_{:=rhs_{2,\hat{\alpha}}} - \frac{1}{N} \underbrace{\sum_{\hat{\beta}=1}^N (rhs_{1,\hat{\beta}} + rhs_{2,\hat{\beta}})}_{\Lambda}, \end{aligned} \quad (2.6)$$

$$\begin{aligned} \frac{\partial \boldsymbol{\mu}}{\partial t} = & \left[ \sum_{\hat{\alpha}=1}^N h_{\hat{\alpha}}(\boldsymbol{\phi}) \left( \frac{\partial \mathbf{c}_{\hat{\alpha}}(\boldsymbol{\mu}, T)}{\partial \boldsymbol{\mu}} \right) \right]^{-1} \left( \nabla \cdot \left( \mathbf{M}(\boldsymbol{\phi}, \boldsymbol{\mu}, T) \nabla \boldsymbol{\mu} - \mathbf{J}_{at}(\boldsymbol{\phi}, \boldsymbol{\mu}, T) \right) \right. \\ & \left. - \sum_{\hat{\alpha}=1}^N \mathbf{c}_{\hat{\alpha}}(\boldsymbol{\mu}, T) \frac{\partial h_{\hat{\alpha}}(\boldsymbol{\phi})}{\partial t} - \sum_{\hat{\alpha}=1}^N h_{\hat{\alpha}}(\boldsymbol{\phi}) \left( \frac{\partial \mathbf{c}_{\hat{\alpha}}(\boldsymbol{\mu}, T)}{\partial T} \right) \frac{\partial T}{\partial t} \right). \end{aligned} \quad (2.7)$$

In these equations which are solved concurrently,  $\nabla \cdot (\dots)$  is the divergence operator of the term which exists in the brackets and  $\tau$  is the kinetic coefficient as defined in [39]. The Lagrange multiplier  $\Lambda$  is defined to ensure the satisfaction of constraint  $\sum_{\hat{\alpha}=1}^N \phi_{\hat{\alpha}} = 1$ . In eq. (2.7), vector  $\boldsymbol{\mu}$  has  $K - 1$  amounts of the constituent chemical potentials.

Considering the previously indicated constraint  $\sum_{i=1}^K c_i = 1$ , the concentration vector  $\mathbf{c}_{\hat{\alpha}}$  is composed of  $K - 1$  independent amounts in the same dimension as the chemical potential vector. The mobility function  $\mathbf{M}$  includes the diffusion coefficient matrix  $\mathbf{D}$  to characterize the diffusion-controlled processes and is defined as [39]:

$$\mathbf{M}(\phi, \boldsymbol{\mu}, T) = \sum_{\hat{\alpha}=1}^N \mathbf{D}_{\hat{\alpha}} \frac{\partial \mathbf{c}_{\hat{\alpha}}(\boldsymbol{\mu}, T)}{\partial \boldsymbol{\mu}} h_{\hat{\alpha}}(\phi). \quad (2.8)$$

Due to the appeared larger interface widths in the phase-field model compared to the physical values [40], the anti-trapping current  $\mathbf{J}_{at}$  [48, 49] is exploited to suppress the influences of these artificially enlarged interfaces. The thermodynamic databases are coupled with this model to obtain the chemical potentials as derivatives of the free energies with respect to the concentrations. Hence, the term  $g_{\alpha}$  representing the Gibbs energies in these databases can be replaced by the term  $f_{\alpha}$  in the above formulations, and by employing the inverse function, the concentration vectors can be calculated as the functions of  $\boldsymbol{\mu}$ :

$$\mathbf{c}_{\alpha}(\boldsymbol{\mu}, T) = \left[ \frac{\partial g_{\alpha}(\mathbf{c}, T)}{\partial c_{\alpha}} \right]^{-1}. \quad (2.9)$$

The individual grand potentials  $\psi_{\alpha}(\boldsymbol{\mu}, T)$  are defined in the next step as:

$$\psi_{\alpha}(\boldsymbol{\mu}, T) = g_{\alpha}(\mathbf{c}_{\alpha}(\boldsymbol{\mu}, T), T) - \boldsymbol{\mu} \cdot \mathbf{c}_{\alpha}(\boldsymbol{\mu}, T), \quad (2.10)$$

which are benefited in the calculation of  $\psi(\phi, \boldsymbol{\mu}, T)$  based on eq. (2.3). Therefore, the grand potentials are solely expressed in terms of the Gibbs free energies and their derivatives [9]. By considering the volume and pressure of the system constant, the thermodynamical consistency is guaranteed and the Gibbs energies become responsible for the determination of the driving forces instead of the free energies. This procedure will be discussed in more detail in chapter 5. In the thermodynamic CALPHAD databases, the formulation of the Gibbs energies is expressed as:

$$g = g^0 + {}^{id}g_{mix} + {}^{xs}g_{mix}. \quad (2.11)$$

In this formulation, the terms  $g^0$  and  ${}^{id}g_{mix}$  denote the Gibbs energies due to the mechanical and the ideal mixings of the involved phases, respectively.  ${}^{xs}g_{mix}$  is the excess energies [9] which is a nontrivial term and not applicable for the concentration estimations. Therefore, the first two terms are considered in the energy calculations.

## 2.2 Anisotropy formulation

In simulation studies of the systems with noticeable anisotropies in the interfacial energies, a cubic positive anisotropy formulation is applied as given in [42]. This is simply done by adding  $a_c(\mathbf{q}_{\hat{\alpha}\hat{\beta}})$  as a new term to eq. (2.4), expressing a more generalized gradient energy density function:

$$a(\phi, \nabla\phi) = \sum_{\hat{\alpha}<\hat{\beta}}^{N,N} \gamma_{\hat{\alpha}\hat{\beta}} \left( a_c(\mathbf{q}_{\hat{\alpha}\hat{\beta}}) \right)^2 \left| \mathbf{q}_{\hat{\alpha}\hat{\beta}} \right|^2. \quad (2.12)$$

$a_c(\mathbf{q}_{\hat{\alpha}\hat{\beta}})$  is defined as:

$$a_c(\mathbf{q}_{\hat{\alpha}\hat{\beta}}) = 1 - \zeta_{\hat{\alpha}\hat{\beta}} \left( 3 - 4 \frac{\left| \mathbf{q}_{\hat{\alpha}\hat{\beta}} \right|_4^4}{\left| \mathbf{q}_{\hat{\alpha}\hat{\beta}} \right|^4} \right), \quad (2.13)$$

in which  $\zeta_{\hat{\alpha}\hat{\beta}}$  is the anisotropy strength. Obviously, in the case of taking zero value, the isotropic formulation of eq. (2.4) is returned.  $|\mathbf{q}|_4^4 = \sum_{i=1}^d (\mathbf{q}_i^4)$  and  $|\mathbf{q}|^4 = \left[ \sum_{i=1}^d (\mathbf{q}_i^2) \right]^2$  are the additional utilized parameters in this formulation.

## 2.3 Implementations and tools

### 2.3.1 The solvers

The introduced model in section 2.1 is implemented in multi-physics phase-field-frameworks PACE3D [50, 51] and WALBERLA [52, 53]. PACE3D is the main benefited framework in the current study which stands for "Parallel Algorithms for Crystal Evolution in 3D". This solver includes a large number of implemented models and by employing massively parallel calculations, makes the possibility of large-scale simulations on the high-performance computing HPC systems. The employed various optimization techniques have made the possibility of simulating different tailored structures and studying the internal interactions in different processes. Proper scalings of the solver have been observed in Hazel Hen [54], ForHLR I and ForHLR II [55] supercomputers with up to 96100 employed cores [50]. For example, PACE3D has been utilized in a number of published simulation studies, such as [56–58], and many others.

WALBERLA stands for "Widely Applicable Lattice-Boltzmann from ERLAnge" and is a massively parallel software forming an efficient and scalable framework. The parallel algorithms are implemented on the block-structured grids which make the scaling possibilities on different HPC clusters [59, 60]. The modularity and flexibility of this framework have made the practical possibility to implement the intended phase-field model [61]. A large number of simulation studies have so far been conducted using this software package. The works of [62, 63] can exemplarily be mentioned among the published works.

### 2.3.2 Discretization technique

The governing equations 2.6 and 2.7 are discretized in space employing the finite difference method and in time using an explicit Euler scheme [50, 61]. The simulation domain  $\Omega \in \mathbb{R}^d$ ,  $d \in \{1, 2, 3\}$  is divided into a block structure in order to make the parallelization. Figure 2.1, schematically illustrates these procedures.

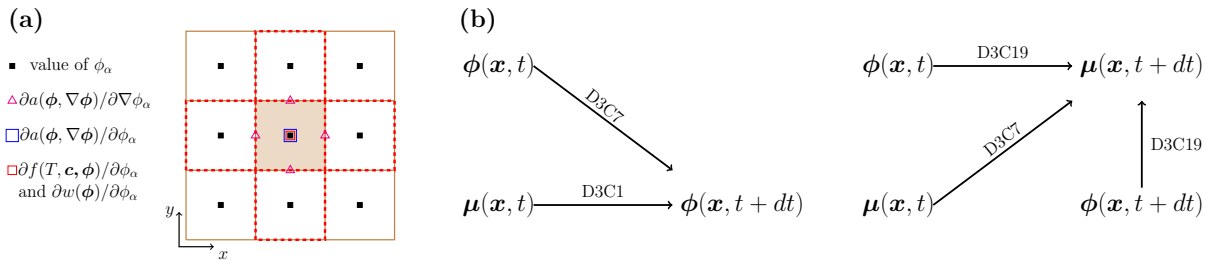


Figure 2.1: Schematic illustrations of (a): the spatial positions to calculate parameters of eq. (2.6) [50] and (b): the algorithm to calculate temporal evolutions of eqs. (2.6) and (2.7) with the time step of  $dt$  [64].

In fig. 2.1(a), the updates of the phase fields, as well as their fluxes, are shown in a two-dimensional scheme. The central cell which is highlighted in brown is the intended cell of the calculations, while its neighboring cells are marked with the red dashed lines. The values of each parameter in these cells are required to gain the desired amounts in the central cell. Based on this figure, in order to solve eq. (2.6) numerically, the phase fields have to be determined at the cell centers, whereas the fluxes are computed in the cell edges [50, 65]. In fig. 2.1(b), the algorithm to calculate the phase-fields (eq. (2.6)) and the chemical potentials (eq. (2.7)) at time  $t + dt$  is shown. This calculation is indeed based on the available data at time  $t$  and  $dt$  denotes the considered time step in the simulation studies. As it can be noticed, to gain the phase evolutions, only the data of  $\phi$  and  $\mu$  at time  $t$  are required, whereas the chemical potential calculation needs an additional  $\phi$  data at time  $t + dt$ . Hence, the  $\phi$  calculations have to be done prior to the chemical potentials [64]. In the depicted "Dn Cm" notation,  $n$  indicates the dimensions

and  $m$  stands for the total number of accesses to the cells. For example,  $D3C7$  denotes a calculation that is performed using data of a central cell plus 6 neighboring cells in three dimensions.

### 2.3.3 Boundary conditions ( $BC$ )

In the boundary cells of the simulation domain, for which the necessary neighboring cells of the calculations do not exist, the boundary conditions play vital roles in the determination of the field values. If we consider the field  $\mathbf{U}(\mathbf{x}, t)$ ,  $\mathbf{U} \in \{\phi, \mu\}$ , the utilized boundary conditions and their definitions are listed in Table 2.1.

Table 2.1: The utilized boundary conditions  $B.S.$  in the simulation studies and their definitions.

Boundary condition name	Definition
Dirichlet	$\mathbf{U}(\mathbf{x}, t) _{\mathbf{x} \text{ in boundary cells}} = \text{constant}$
Isolate or Neumann	$\frac{\partial \mathbf{U}(\mathbf{x}, t)}{\partial \mathbf{x}} _{\mathbf{x} \text{ in boundary cells}} = 0$
Periodic	connects two adjacent domain boundaries

These  $BC$  formulations have been utilized in literature, for example in the works of [9, 10, 61, 66, 67].

### 2.3.4 Moving window technique

In solidification problems, one approach to reduce the necessary computational power is to shift the solidified phases out of the simulation domain, focusing computation on areas of highest interest and importance, such as the solid-liquid interfaces [1]. This technique is known as the *moving window technique*, which was introduced by Vondrous et al. [68] in 2014. In this procedure, the further evolutions of the solidified phases beyond a certain point are neglected as they are lower than the liquid phase evolution in orders of magnitude [64]. The schematic illustrations of the moving window are shown in Fig. 5 of [68] and Fig. 2 of [64]. In both of the mentioned figures, the evolution equations are only solved in the specified boxes, leading to a significant increase in the calculation efficiencies [68].

### 2.3.5 Nucleation mechanism

In the performed simulation studies, whenever nucleation of a third phase ( $\delta$  for example) in the  $\alpha$ -liquid interfaces has to be modeled, the following nucleation mechanism is implemented in the utilized phase-field model:

$$\xi_\delta = \begin{cases} n_{\text{dist}} \cdot \mathbf{A} & \forall \phi_\alpha \phi_l > 0, \quad dt \bmod i = 0 \\ 0, & \text{else.} \end{cases} \quad (2.14)$$

$\xi_\delta$  is a noise term which is added to eq. (2.6) based on the works of Schoof et al. [69] and Kellner et al. [70]. The extension of the originally introduced approach in [69] is performed in [70], leading to the outstanding results in the simulation of the eutectic colony formations as the investigated process. The simulations of eutectic and off-eutectic compositions in the directionally solidified AlCu-5Ag system are other examples of its successful applications [11]. This mechanism works by considering a nucleation criterion in the noise term. Fulfillment of the criterion is tested after a number  $i$  of the time steps  $dt$  within the simulation. This number is predefined by the user and named as the *interval*.  $\mathbf{A}$  is the amplitude and  $n_{\text{dist}}$  is the function to uniformly distribute the noise. At each nucleation step, the concentrations in the solid-liquid interfaces are calculated and the deviations from the equilibrium concentrations are noticed. If this deviation is higher than a predefined limit  $c_{\text{limit}}$ , the  $\delta$  phase nucleation occurs due to the implementation of the noise function. In the nucleated domain cells, the satisfaction of the constraints  $\sum_\alpha \phi_\alpha = 1$  and  $c_{\text{new}} = c_{\text{old}}$  are fulfilled to ensure consistency in the phase evolutions.

# Chapter 3

## Simulations setup

### 3.1 Directional Solidification (*DS*)

The directional solidification processes have to be simulated in this work, to study the effects of the anisotropically modeled interfacial energies on the formed patterns. Thus, the used simulation setup for such a procedure is the first discussed task in this chapter. In order to simulate the *DS* processes, a Bridgman-type setting is benefited which is introduced for the first time by Percy Williams Bridgman in the 1920s [71]. In this setting, a cylindrical crucible is lowered vertically into a tubular furnace along its axis, with a constant velocity [71, 72]. Subsequently, the imposed temperature gradient produces the solidification front which is necessary for the formation of the bulks of the single-crystal materials. Since then, different variations of this technique have been implemented, but the main principles of the procedure have remained untouched [72]. As examples of the single crystal growths by this technique in the literature, the evolutions of  $\text{LaBr}_3\text{:Ce}$  [73],  $\text{LaCl}_3\text{:Ce}$  [73], Al-7wt%Si [74],  $\text{Li}_2\text{B}_4\text{O}_7$  [75], CdTe [76] and CdZnTe [76] systems can be mentioned. In addition, various microstructures like the dendrites [28, 77, 78], eutectics [79, 80] and peritectics [81–83] are obtained by this technique in different material systems. It is widely used either for the high-temperature casting of Ni-based superalloys [84, 85] which is the main simulation topic of the current work.

In order to have an overview of the role of the imposed temperature profile in the *DS* processes, the experimental setup is schematically illustrated in fig. 3.1. This illustration includes two configurations for (a): the bulk, and (b): the thin samples, respectively. In fig. 3.1(a), the vertical movement of the crucible with the constant velocity  $v$ , makes the progress in the solidification process. The temperature gradient  $G^{DS}$  in this setting is provided by the surrounded heater and cooling coils in the  $y$  direction. The annular baffles are placed to separate the furnace heaters and the heat sink. Maximum and

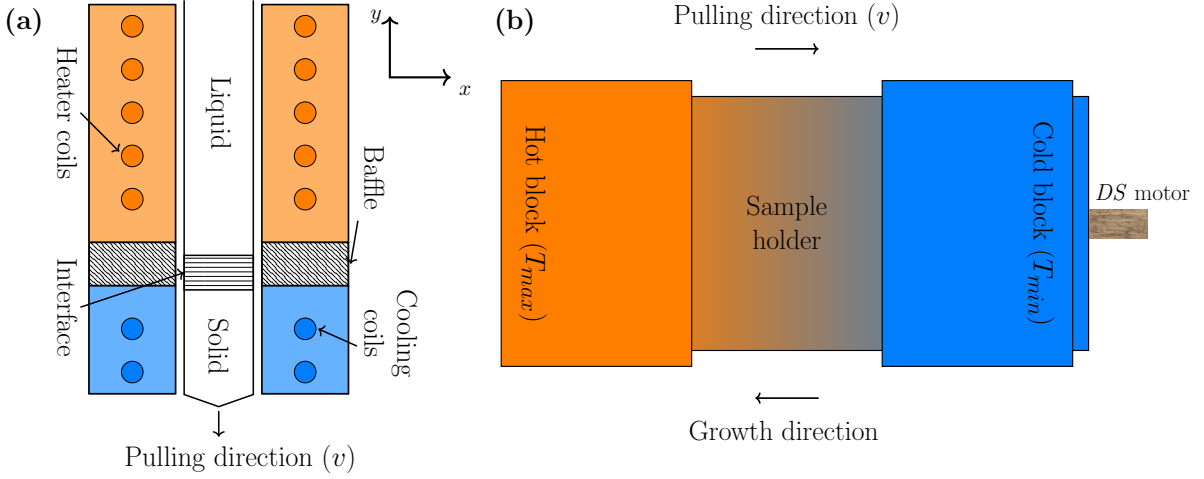


Figure 3.1: Schematic illustrations of the experimental setups in directional solidification for (a): bulk samples [72] and (b): thin samples [86].

minimum temperatures of the system are controlled by the coil temperatures [72]. The next setup in fig. 3.1(b), which is used for the thin samples, is composed of the hot and the cold blocks as well as a sample holder with the provided moving possibility by a *DS* motor [72]. If a pulling direction from left to right is assumed, the solidification front moves in the opposite direction, resulting in the growth from the right to the left. Hence,  $x$  is the direction of  $G^{DS}$  in this configuration and the isothermal gradient lines are assumed to exist along  $y$ . For both configurations, the time- and the space-dependent temperature profile can be formulated as:

$$T(x, t) = T_0 + G^{DS}(pos - vt), \quad (3.1)$$

in which *pos* stands for the position ( $y$  in the setting of fig. 3.1(a) and  $x$  in the setting of fig. 3.1(b)),  $t$  stands for the time and  $T_0$  is a base temperature defined by the user. In fig. 3.2(a) the schematic illustration of this formulation is shown. Front temperature  $T_f$  is adjusted in the interface which is below the melting temperature  $T_M$  by a slight amount. As it can be noticed, there is a linear dependency between the system temperature and the distance increases. Additionally, an overall temperature reduction in the simulation domain occurs as time passes. Due to the mentioned linear dependency between the temperature and the space,  $\nabla^2 T$  becomes equal to zero, which guarantees the satisfaction of the heat equation in the steady-state. As utilizations of this formulation, the simulative works of Hötzer et al. [67] and Kellner et al. [9, 70] can be mentioned. Next, the simulation setups for which this temperature profile is used in the two- and three-dimensions, are schematically illustrated in fig. 3.2(b) and 3.2(c). In both types,

the constituent solid phases which are filled initially are labeled by the Greek letters  $\alpha, \beta, \delta, \dots, \eta$ . The fillings start from  $x = 0$  until a user-defined altitude. The phases can have different arrangements like the lamellar, the rod, or the Voronoi tessellations [9, 87] which results in the free evolutions of the solidified phases. The rest of the domain is filled with the liquid phase as illustrated in yellow in the figures. The boundary condition formulations are as previously presented in section 2.3.3. The bottom of the simulation domains ( $x = 0$ ) is exposed to the Neumann boundary conditions. Whereas the opposite sides ( $x = x_{max}$ ) are exposed to the Dirichlet boundary conditions to resemble the infinite liquid fluxes in the simulation domains. Other boundaries are modeled with the periodic B.Cs resembling the repeat of the simulated microstructures in these directions.

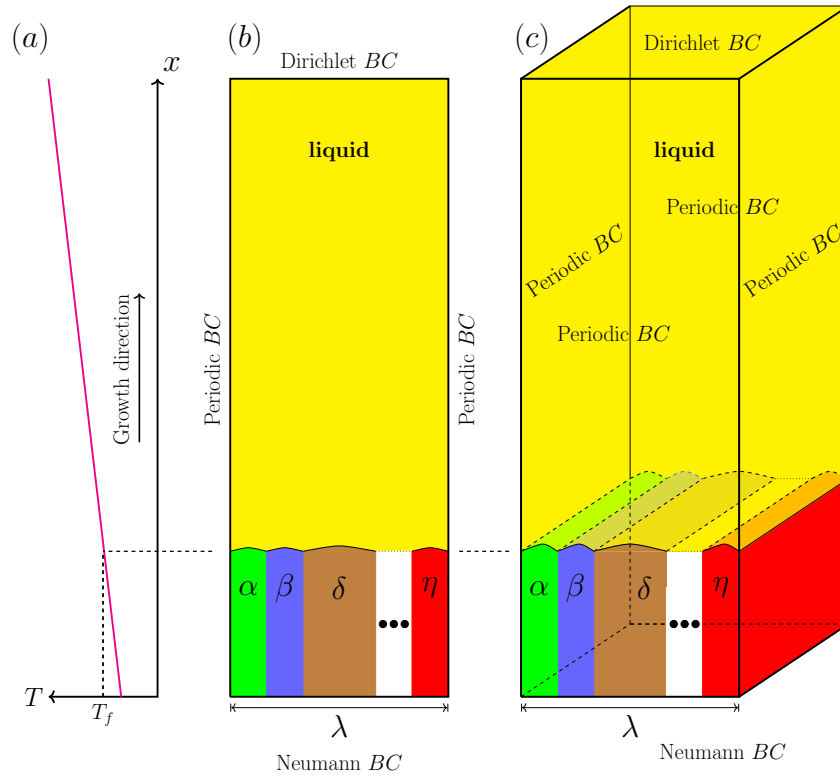


Figure 3.2: Schematic illustrations of (a): the temperature formulation in eq. (3.1), (b) and (c): the utilized setups in the DS studies of two- and three-dimensional simulations.

This setup is used in the simulation studies of the different material systems in sections 6.1, 6.2 and 6.4.

## 3.2 Rotating Directional Solidification (*RDS*)

In fig. 3.3(a), the experimental setup of the rotating directional solidification *RDS* procedure as the next used setup in the simulation studies of current work is depicted. This

experimental setup is initially introduced by Oswald et al. [88] as a precursor study of this kind on 1993. Akamatsu et al. [89] made the additional investigations in the later years. The true motivation for this setup and its beneficial utilization in the understanding of the ongoing mechanisms in the solidification processes will be discussed later in section 4.2. In this section, its related temperature equation is derived considering the heat conservation law and the physical rotation of the disk as illustrated in the schematic illustration of fig. 3.3(a). Such disk rotation can be modeled by the rotation of the formulated temperature profile within the performed simulations in PACE3D software (see section 2.3.1). The rotation of the temperature profile instead of the simulation domain rotation, leads to a reduction of the computational effort in the simulation studies.

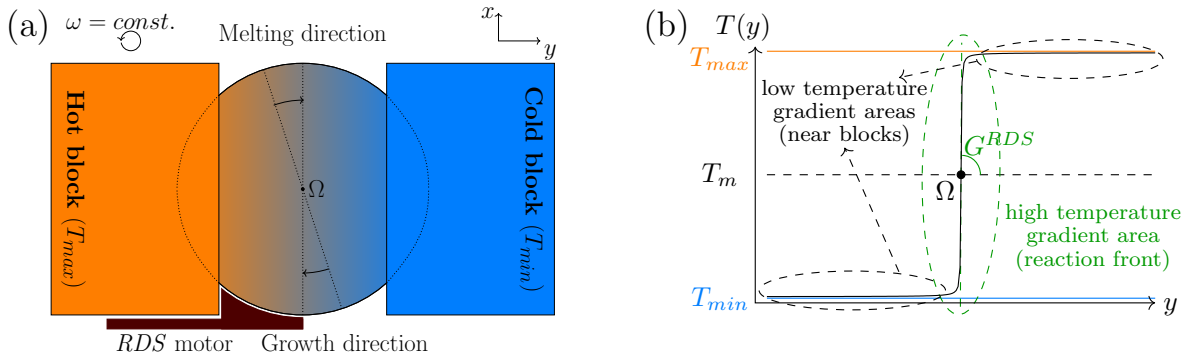


Figure 3.3: Schematic illustrations of (a): RDS setup based on the experimental work of Moshagheghi et al. [90]. (b): The temperature profile in RDS simulations (eq. (3.4)) at time = 0.  $T_{max}$  and  $T_{min}$  represent the temperatures of the hot and cold blocks or the considered maximum and minimum temperatures in the simulations, respectively. The solidification/melting fronts are located in the "high-temperature gradient area" [91].

In order to formulate the temperature, the satisfaction of the heat equation in the steady-state ( $\nabla^2 T = 0$ ) should be considered as discussed previously for the *DS* setting in section 3.1. In addition, for a correct representation of the ongoing physical effects in the *RDS* processes, the following constraints should be considered:

- (i) In the derived temperature function, the effects of the cold and hot isothermal blocks have to be represented. In the domains in between the minimum and maximum temperatures caused by these blocks, the function should cause the temperature variation by some means to reflect the disk rotation effects either. As in the hot and cold blocks a uniform heat distribution is assumed, a low-temperature gradient in near-block segments of the rotating disk should be represented in the sought formulation. In the other segments indicating the vicinity of the disk center, an acute temperature change is crucial for the correct formation of the solidification

and the melting fronts. Therefore, a linear function representing a constant temperature gradient in the whole domain (like eq. (3.1) for the *DS* case), can not be recommended. Utilizing a linear function can result in an enormous temperature rise by the distance increase from the rotation center, leading to the destabilization of the modeled material system. This especially specially comes into account in the large domain simulations.

- (ii) Precise calculation of the phase-field evolution equations (eqs. (2.6) and (2.7) in section 2.1) should be ensured demanding continuous differentiability of the derived temperature function with respect to the space and time.

Based on the mentioned constraints, the usage of three different linear functions composing a piecewise function cannot be considered. Although such a piecewise function can represent the temperature gradient variation in the simulation domain, the non-continuity of its derivatives can cause problems in the correct calculation of the phase-field equations in the connection points. Instead, the  $\tan^{-1}$  function can be regarded as an option which has the ability to fulfill the declared constraints. Such function is schematically depicted in fig. 3.3(b) in which the cold and the hot blocks' temperatures are represented by the lower and the upper asymptotes, respectively. The mentioned asymptotes can represent any desired minimum and maximum temperatures in the system rather than the blocks'. In order to establish well-defined melting and solidification fronts, a sharper temperature change in the middle disk area exists compared to the outer sides. The initial temperature setting at time  $t = 0$  is considered without the rotational effect as the starting point of the formulation in the following. By applying the depicted coordinate system in fig. 3.3(a), the temperature  $T$  as a function of  $y$  is constructed as:

$$T(y) = T_m + A_0 \cdot \tan^{-1} \left( \frac{G^{RDS} \cdot y}{A_0} \right), \quad (3.2)$$

in which, the temperature at disk center  $\Omega$  ( $x = 0, y = 0$ ) is denoted by  $T_m$  and  $G^{RDS}$  is its gradient. The discussed asymptotic values are controlled by the constant coefficient  $A_0$ . As expected,  $\frac{dT}{dy}$  is equal to  $G^{RDS}$  at  $y = 0$ . The next step is to employ the rotational matrix to model the disk-rotation effect. In course of this endeavor, a rotation angle of  $\theta$  equal to the  $\omega t$  is considered, where  $\omega$  stands for the angular velocity. The  $x' - y'$  is attained as the new coordinate system:

$$\begin{bmatrix} x' \\ y' \end{bmatrix} = \begin{bmatrix} \cos(\omega t) & -\sin(\omega t) \\ \sin(\omega t) & \cos(\omega t) \end{bmatrix} \begin{bmatrix} x \\ y \end{bmatrix} = \begin{bmatrix} x \cdot \cos(\omega t) - y \cdot \sin(\omega t) \\ x \cdot \sin(\omega t) + y \cdot \cos(\omega t) \end{bmatrix}. \quad (3.3)$$

The final time- and space-dependent rotating temperature profile, is completed by the combination of eqs. (3.2) and (3.3) as:

$$T(x, y, t) = T_m + A_0 \cdot \tan^{-1} \left[ \frac{G^{RDS}}{A_0} (x \cdot \sin(\omega t) + y \cdot \cos(\omega t)) \right]. \quad (3.4)$$

It is worth mentioning here that, in the utilization of eq. (3.4), the values of  $T_m$ ,  $A_0$  and  $G^{RDS}$  should be selected in a way to result in  $\nabla^2 T \simeq 0$  in the different points of the simulation domain. As it will be discussed later in section 3.2, this condition is satisfied well in the phase-field studies of the  $RDS$  process in the investigated system of the current work.

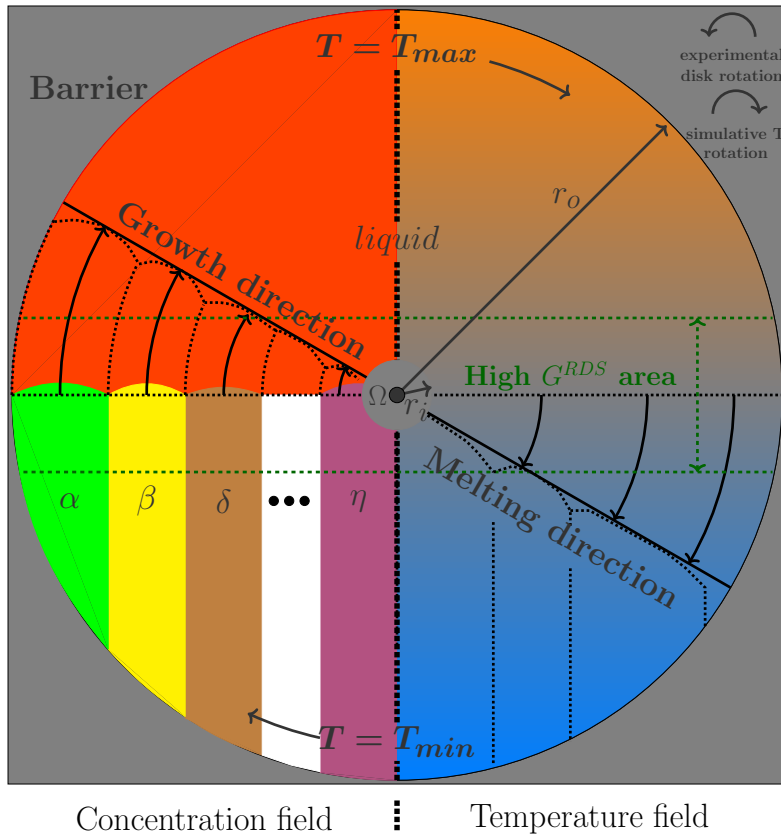


Figure 3.4: Schematic illustration of the  $RDS$  setup based on [91]. The simultaneous effects of the temperature and concentration fields on the whole domain are shown by the semicircle depictions for the sake of simplicity.

Figure 3.4, schematically illustrates the simulative setup in the  $RDS$  studies. The left half of this figure shows the concentration field at the initial simulation step, i.e.  $t = 0$ , whereas the right half shows the initial temperature field, respectively. Both fields influence the entire domain throughout the simulation process. The half-domain

illustration is only for the sake of brevity. The gray barrier section shown is to confine the initial rectangular domain and form the desired circular simulation area. This is done due to the fact that, the multi-physics phase-field-framework PACE3D typically deals with the rectangular domains, and therefore, the barrier areas are formulated and utilized in a similar manner to the works of [92–94]. In such areas, neither the temperature formulation (eq. (3.4)) nor the field evolution equations (eqs. (2.6) and (2.7)) are solved. Despite the works of [92–94], in which the simulated barriers have flat surface geometries, in this work, the considered curved-shape barriers cause limitations in calculations of the gradient normals to the boundaries as a linear problem. Hence, numeric instabilities can take place in the barrier boundary sections due to the direct contact with the evolving phase fields. As a solution, a layer of one solid phase with the thickness of one cell can be placed between the barrier region and the simulation domain containing the evolving phases, permanently. Therefore, the contact of the barrier with a converged and stable phase field is guaranteed by this technique.

The melting and solidification conditions coincide in the middle of the simulation domain, which results in zero growth velocity at the rotation center  $\Omega$ . This area is modeled with another barrier in order to prevent the growth of unwanted phases. The same color labeling of fig. 3.3 is used in order to illustrate the temperature field on the right-hand side of fig. 3.4. The green dashed lines specify the area with the higher temperature gradient which contains both the solidification and melting fronts. In the bottom half of the domain which has the lower temperature  $T_{min}$ , the solid phases are filled in the desired initial pattern. The lower half of the domain is filled with the liquid phase which is exposed to the high temperature with the maximum value of  $T_{max}$ . The formulated temperature profile is rotated in this configuration in the opposite direction of the disk rotation in the experimental works in order to resemble the same effects.

In section 3.2, the introduced setup is used in simulation studies of rotating directional solidification in the ternary eutectic Bi-In-Sn system.



# Chapter 4

## Literature review on material properties

### 4.1 Ni-Al-Mo ternary system

Due to their favorable material properties like the high melting points [95], low densities and high thermal conductivities [96], NiAl-based alloys have come into focus for industrial applications in recent years. The aerospace industry [97] and gas turbine manufacturing [98] can specifically be mentioned for these applications in which the high-temperature resistances of these alloys are required. Meanwhile, the reported weaknesses in the strength and toughness of such alloys have opened new discussions in the enhancement techniques. As part of this effort, adding a reinforcing element like Cr, Mo, W or V to the initial binary alloy has worked as a beneficial technique in the performed studies. The resultant ternary systems show improved compressive creep resistances and strain rate properties with the retained advantages of the primary NiAl binary alloy in the investigated systems [99–102]. Additional studies have been conducted for further mechanical properties enhancements in the literature. As an example, Misra et al. [103] have shown the reinforcement possibility of the NiAl-based alloys with the formation of a softer fcc phase. In their investigated Ni-30Fe-23Al and NiAl-31Cr-3Mo alloys, the local plasticity in the lately formed fcc phases results in global plasticity in the alloys. In Ni-Al-Mo ternary system, experimental investigations have been conducted to amend the corrosion resistance by Galetz et al. [104] and Latreche et al. [105], as well as the oxidation resistance by Li et al. [106]. Sheng et al. have revealed valuable information on the effects of the fine microstructure on the mechanical properties in quaternary NiAl-Cr(Mo)/Nb alloys in their works from 2008 [107] and 2009 [108]. In [107], the prepared alloys by the injection-casting having finer microstructures are compared with the conventionally cast alloys.

The investigation shows a 100% increase in compressive ductility and a 50% increase in the yield strength at room temperature. Based on their later study [108], by doping **Hf** and **Ho** to the system using the suction-cast technique, **HfAlNi<sub>2</sub>** and **HoNi<sub>2</sub>Al<sub>3</sub>** phases are formed in the system. These formations which happen along the **NiAl** and **Cr(Mo)** interfaces, make the microstructure finer leading to better microhardness and compressive properties in the alloy. The directional solidification technique which is previously discussed in section 3.1, can be a promising method to gain the enhanced mechanical properties in the **Ni-Al-Mo** ternary alloy. The nontrivial eutectic reaction in this system is described by an isopleth section and is noted as **NiAl-10Mo** in the following. The regular formation of **NiAl**- and **Mo**-rich phases as the matrix and fibers are reported leading to considerable improvements in the mechanical properties [109–111]. The *DS* experiments performed by Zhang et al. [35], include different solidification velocities  $v$  with the constant temperature gradient of  $G^{DS} = 33.4 \text{ K mm}^{-1}$ .  $v$  is varied between  $2 \text{ }\mu\text{m s}^{-1}$  and  $300 \text{ }\mu\text{m s}^{-1}$ , and the evolved patterns are reported. In the resultant microstructures, for the slow growth rates ( $2 \text{ }\mu\text{m s}^{-1} \leq v \leq 35 \text{ }\mu\text{m s}^{-1}$ ) the formed interfaces have planar morphologies, whereas in  $40 \text{ }\mu\text{m s}^{-1} \leq v \leq 300 \text{ }\mu\text{m s}^{-1}$  the formation of cellular interfaces is observed. In their study, the line-intersect method is used to measure the fiber spacings  $\lambda$ . For each experiment, about 300 spacings and 100 fiber sizes are measured and the resultant values show good correlations with the expected Jackson-Hunt-type behavior,  $v\lambda^2 = c$  [112]. The constant  $c$  has the value of  $34.81 \text{ }\mu\text{m}^3/\text{s}$  in their report [35]. Additionally, it is observed that the growth rates lower than  $35 \text{ }\mu\text{m s}^{-1}$  have more well-aligned and regular eutectic structures. The average volume fractions of the fibers  $v_f$  lie in the range of **14.6-15.0%** depending on the growth rate. It is also mentioned that the fiber arrangements in the transverse sections are almost **hexagonal** with not circular cross-sectional areas but **rectangular**. The conclusion from the later observation of the fiber shape is the highly **anisotropic** behavior of the matrix-fiber interfacial energies [35].

In order to simulate this *DS* process, moreover to the discussed experimental data, the thermodynamic properties of the system have to be determined. The implemented database by Peng et al. [113] is used for this purpose. This database is constructed for the quaternary **Ni-Al-Cr-Mo** system and includes the ternary **NiAl-10Mo** subsystem as well. A combination of observations from solidification experiments and computational thermodynamics is the main approach in the implementation of such databases. The CALPHAD method [41] is used to model the liquidus surface of the system. In fig. 4.1 (bottom left) the ternary diagram of the system is depicted, including the isopleth cut of the **NiAl-10Mo** eutectic reaction as well as the liquidus projections. The matrix, the fiber and the liquid phases are shown in dark blue, red and light blue colors, respectively. This color style will remain unchanged in the forthcoming simulative micrographs in section 6.1 for the sake of simplicity. In the utilized database, the element concentrations at the eutectic point

are equal to the listed values in the top-left table of the figure. The illustrated phase diagram in fig. 4.1 includes the discussed eutectic reaction, which results in a fibrous microstructure as the solidification product. This reaction occurs at the temperature of 1875.47 K with  $\simeq 0.1$  mol-% of Mo concentration [113]. Liquid-matrix and liquid-fiber areas exist in the phase diagram as expected, in the hypo- and hyper-eutectic regions, respectively. In the matrix phase, the concentration of Mo is near-zero which can cause difficulties in the simulation studies. This point will be discussed later in the modeling procedure of the system, prior to the simulations.

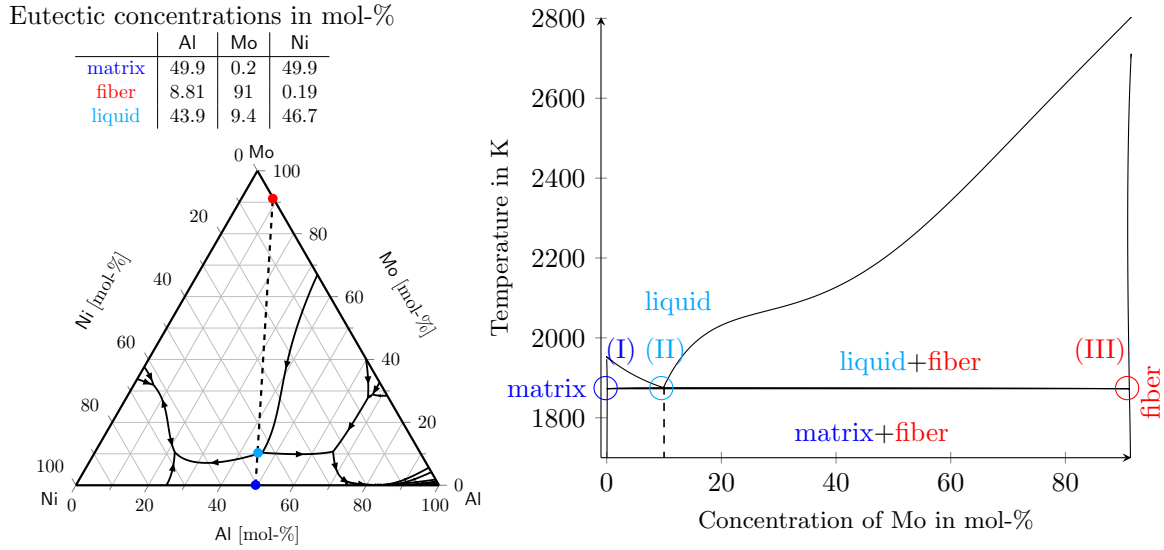


Figure 4.1: Bottom left: The ternary diagram of the Ni-Al-Mo system including the liquidus projections. Dashed line: The isopleth matrix-fiber connecting cut of NiAl-10Mo ternary eutectic. Top left: The eutectic concentrations of the elements in the constituent phases at  $T = 1875.47$  K. Right: Two-dimensional phase diagram in the isopleth cut of the ternary diagram. All data are based on the CALPHAD database of [113].

Based on the discussed experimental and thermodynamic data which are the simulation prerequisites, the modeling and latterly the simulations of this system are performed in sections 5.2 and 6.1.

## 4.2 Bi-In-Sn ternary system

Bi-In-Sn ternary eutectic is the next investigated material system in the current work. The favorable properties of this system like its relatively low melting point ( $T_M \simeq 332$  K [114]), have made it desirable and practical in the experimental studies of the solidification processes by both *DS* (see section 3.1) and *RDS* (see section 3.2) techniques [22, 36–38, 90].

This fact is due to the possibility of accurate in situ observations of the ongoing mechanisms in the solidification experiments. The works of [22, 36–38] can exemplarily be mentioned in which the obtained microstructures are proclaimed in a variation of the applied process conditions like the solidification velocities. The three-phase lamellar pattern with  $\alpha\beta\alpha\delta$  repeat unit is reported to be the dominant growth pattern in the stably formed grains of the solidified products. In this representation,  $\alpha$  stands for the  $\mathbf{BiIn}_2$ ,  $\beta$  stands for the  $\beta\text{-In}$  and  $\delta$  stands for the  $\gamma\text{-Sn}$  crystalline phases, respectively. The observed solid-liquid interfaces are reported to be non-faceted [86] and the stability of the mentioned pattern is declared to be a result of the mirror symmetries in the middle of the  $\beta$  and  $\delta$  phases. This results in solute redistribution at the solidification fronts [22, 36, 115]. Rex et al. [38] in their experimental and numerical work, investigated the transient states referring to the initial stages of the formation of the constituent solid phases in the undercooled melt. They observed the  $\mathbf{BiIn}_2$  phase or  $\mathbf{BiIn}_2$  together with the  $\gamma\text{-Sn}$  phase, solidify initially and after passing a pulling distance, the third solid phase appears. The solid-liquid interface temperature initially decreases in this process as long as the two-phase configuration exists. By the appearance of the third solid phase, the temperature rises spontaneously causing an irregular layer of the fine microstructure which leads to the final stable arrangement of  $\alpha\beta\alpha\delta$  multi-layers. Sample composition and the solidification factors are recognized to be the key parameters in the number and sequence of the transient states. The adjustment between numerical simulations which are performed based on the phase-field method, and the experiments have led to convenient results in the assessment of the thermophysical parameters in the system like the nucleation undercooling and the diffusion coefficients of the existing elements in the liquid phase [38]. Witusiewicz et al. [36], by studying the effects of the solidification velocities on the pattern formation in their  $DS$  experiments, have observed well compatibility of the evolved lamellar spacing values in the 2D samples with the Jackson-Hunt relationship [112]. They have also indicated that, for the velocity of  $0.5 \mu\text{m s}^{-1}$ , with a constant temperature gradient of  $8 \text{ K mm}^{-1}$ , the most perfectly aligned regular microstructure results with the average lamellar spacing value of  $23.4 \mu\text{m}$ . In bulk sample investigations, they have noticed good agreements between their findings and the formerly reported results by Ruggiero et al. [37]. Bottin-Rousseau et al. [22], by choosing a restricted velocity range have shown the agreement of the Jackson-Hunt relationship constant ( $c = v\lambda^2$ ) as computed in their work, with the results of [36].

Another advantage of  $\mathbf{Bi-In-Sn}$  ternary eutectic which makes it favorable for the experimental, as well as the simulation studies, is the reported **2D patterns** in the stable growth regions of the bulk or quasi-2D samples [86]. This point can decrease the cost of the investigations by reducing the 3D samples into the two-dimensions. On one hand, the mentioned reduction leads to the considerable savings in the required computational

power of the simulation studies, but on the other hand it can be questioned that, how to deal with the 3D nature of the occurring phenomena in the solidification processes like the **lamellae branchings** [116–118] in the simulations? The answer lies in the introduced simulative nucleation mechanism in section 2.3.5 as it can reproduce, similar physical effects in two dimensions. Hence, in the performed 2D simulations of this material system, the expected physical effects of the experiments can be thoroughly resulted which will be discussed later in section 6.2.2.

The next point is the role of **anisotropy** in the interfacial energies  $\gamma$  on the pattern formation. In [89, 90], the grains with negligible anisotropies are labeled as the **floating grains**, whereas the grains with significant anisotropic interfaces are labeled as the **locked grains**. The evolved patterns of the locked grains can deviate from  $\alpha\beta\alpha\delta$ , leading to the formation of  $\alpha\beta\delta$  or  $[\alpha\beta]_a[\alpha\delta]_b$  superstructure in which  $a$  and  $b$  are the integers higher than the unity [22]. In some cases, these patterns stay stable and do not vanish until the end of the experiments. The possibility of the formation of the  $\alpha\beta\delta$  pattern in the ternary eutectics is shown either by Choudhury et al., using the phase-field method [115]. But for the latter case, there are still open questions. Determination of the precise nature of the instability process by both experimental and numerical techniques demands more investigations. In the course of this endeavor, the *RDS* technique is a beneficial method in addition to the *DS* method, for studying the material properties in this system. Mo-hagheghi et al. in their *RDS* study investigating the thin samples [90], have observed the same  $\alpha\beta\alpha\delta$  stacking sequences as found in the *DS* experiments. The trajectories of the solidified phases were circular as expected, due to the results of the rotating samples. In spite of a broad variation range in the influencing parameters like the solidification velocities and the thicknesses of the samples, this pattern is reported to be stable in this reference. Additionally, the **tilted** growth of the solidified phases with respect to the applied temperature gradient direction has been reported in the locked grains [90]. Based on the observations of Akamatsu et al. [89], the patterns are reproducible features of the eutectic grains to which they belong. This indicates the dependency of the evolved microstructures on the characteristics of the interface boundary **Wulff plots**. Considering "symmetric-pattern approximation" [119], which is the symmetry in the solid-liquid interfaces, the evolved trajectories in the *RDS* experiments should be circular in the floating grains. In contrast, the locked grains lead to the cusp singularities in the Wulff plots and the growths with the faceted lamellar patterns [89]. In these lamellae, the  $\alpha\beta$  interface anisotropy is reported to have a more dominant influence on the development of the inclined trajectories compared to the  $\alpha\delta$  interface anisotropy [90].

In the works of [22, 86] additional instabilities to the lamellae branchings like the **lamellae eliminations** are also reported in the solidified phases depending on the experimental conditions. These instabilities mainly occur as responses of the system to

variations in the solidification velocities and in most cases are recovered at further steps of the experiments. Lamellae branching generally happens when the velocity exceeds certain criteria, whereas lamellae elimination occurs when it is decreased below the lower velocity limit of the system. In both cases, the system shows a tendency to return to the stable  $\alpha\beta\alpha\delta$  pattern by mechanisms like **phase invasion** (see Fig. 13 of [86]), **phase exchange** (Fig. 14 of [86]) and **continuous elimination of all phases** (Fig. 7 of [86]). It is worth mentioning that, although these mechanisms have 3D natures in the transitional areas, but finally the resultant patterns show the 2D natures. The conclusions of the performed literature review can be summarized as:

- (i) Anisotropic behavior of the interfacial energies in the Bi-In-Sn ternary eutectic system is a key factor in pattern formation. Therefore, in addition to the *DS* simulations, the *RDS* simulations can lead to beneficial insights in the characterization of the ongoing mechanisms in these processes.
- (ii) The growth velocity is another important factor in the pattern formation and the occurred instabilities within the solidification processes.

In both of the indicated points, there are still open questions demanding further simulative investigations. In current work, the anisotropic behavior is focused on for a more detailed study. The thermodynamic information of the system is obtained from [114] which is implemented by Witusiewicz et al. based on the CALPHAD method [41]. The commercial tool Thermo-Calc [120], is benefited to utilize the database and obtain the desired data including the phase equilibria and the values of the Gibbs energies in the constituent phases. In order to get an overview, the ternary diagram is shown in fig. 4.2 in which the liquidus projections are illustrated with the black solid lines. The figure also includes the concentration of the elements in the eutectic reaction in different phases. Yellow, blue, magenta and red circles specify positions of the solid  $\alpha, \beta, \delta$  and the liquid phases in the eutectic reaction, respectively. This coloring code will remain unchanged in the performed phase-field simulations of section 6.2 for the sake of simplicity.

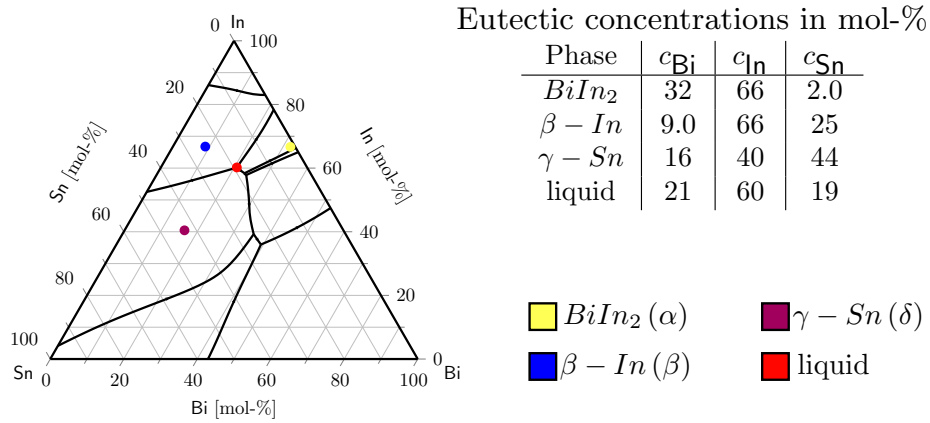


Figure 4.2: Ternary diagram of the *Bi-In-Sn* system [114] including the liquidus projections and the concentrations of the elements in the eutectic reaction.

Based on the discussed experimental and thermodynamic data, the Gibbs energies of the involved phases in the eutectic solidification process are modeled in section 5.3 and the phase-field simulations are performed in sections 6.2 and 6.3 consequently.



# Chapter 5

## Gibbs energies modeling in ternary systems

### 5.1 General method for Gibbs energies modeling

In order to perform the phase-field simulations of physical material systems, the thermodynamic data of the investigated systems have to be incorporated into the considered models. The required data to calculate the driving forces of the reactions are mostly obtained from the CALPHAD databases [41] in the current work. In these databases, the pressure, the temperature and the concentrations are stored as variables to define the Gibbs energy functions in the individual phases. Considering the existing Allen-Cahn or Cahn-Hilliard phase-field models, various methods have been established for thermodynamic data incorporation [7, 121–130]. Steinbach et al. [126], have used a method to directly access the database at different steps of the running simulations in their study from 2007. As the computational effort in such a direct coupling method can be relatively high, the thermodynamic information calculations are accomplished at certain time intervals. The required data in the quasi-equilibrium stages which are not obtained in the investigated intervals are extrapolated subsequently. Next to the direct coupling method, another approach is employed by Qin and Wallach [127] in which the desired thermodynamic information is precomputed before the simulations by virtue of the MT-DATA [131] and is saved in the data files. On one hand, this precalculation can reduce the required computational effort, but on the other hand in case of additional data need within the simulations, the interpolations are required for the approximations which can lead to accuracy losses. As another data coupling approach, the direct incorporation of the Gibbs energy functions from the CALPHAD databases in the utilized phase-field models is performed by Böttger et al. [128] and Zhu et al. [129]. In this approach, no external

libraries are required as the exact determination of the thermodynamic information is possible. The iterative methods are often required to solve these Gibbs energy functions as they are usually saved in the CALPHAD databases with computationally intensive formulations. Thus, further methods have been implemented in the literature to simplify the original energy functions and compute the necessary thermodynamic information within the simulations. As a common method, parabolic functions are used to approximate the Gibbs energies. Like any other approximation method, the result accuracy is one of the main questions in the utilization of this technique. It can be declared that the accuracy depends on the considered concentration and temperature ranges, drastically. The capability of the parabolic functions may be reduced by an increase in the mentioned ranges. This can be more pronounced if the functions are utilized in the wider concentration and temperature ranges than their originally approximated ranges. In other words, defining a broad temperature-composition space to attain and utilize such functions can be challenging. Welland et al. [122] have used the parabolically approximated functions in their phase-field simulations and have compared them with an approximated minimiser approach. In the vicinity of the equilibrium conditions, both approximation methods have shown satisfying accordances with the original CALPHAD data. Meanwhile, by growing deviations from the equilibrium states, the approximated minimiser functions show better accordances with the original data rather than the parabolic functions. However, for most of the phase-field simulation studies in the physical processes, such as the investigated solidification studies in current work, a limited temperature-composition range is usually adequate to reproduce the desired thermodynamic data.

Considering the parabolically approximated functions, the advantages of their utilization can be summed up as their lightweight computations (see Appendix 1 of [132]), their appropriate representation of the thermodynamics and the possibility of their implementation in both free-energy-based [42, 126] and grand-potential-based [39, 40] phase-field models. Therefore, different binary [7, 8, 122, 133, 134] and ternary [7, 9, 10, 87, 135, 136] systems have been modeled by these functions in the literature. For the utilized grand-potential-based model in the current work (see section 2.1), the necessary modeling parameters like the concentrations, the grand potentials and the chemical potentials, can be obtained from the approximated functions. As an example, based on eq. (2.10) in section 2.1, in the calculation of the grand potentials the concentrations should be derived as the functions of the chemical potentials. In other words,  $\boldsymbol{\mu}^{-1}(\mathbf{c})$  should be determined in this formulation. This can be achieved simply (and computationally cheaply) by a representation of the Gibbs functions in the forms of the second-order polynomials.

The utilized toolchain for modeling the Gibbs energies in this work is introduced by Noubary et al. [132], which is implemented for the binary and the ternary material systems. In this semi-automated toolchain, a detailed definition of the investigated material

systems, as well as the occurred phase transformations, are essential as inputs to the simulations. For this purpose, the utilized temperature and concentration ranges should be defined. The concentration range is selected to be near-equilibrium in order to guarantee the function's validity in the case of minor deviations from the equilibrium conditions in the simulations. The Least-squares method is benefited to derive the functions in this framework. Additional thermodynamic information is considered in the function approximation procedure to minimize the susceptibility of the model to external influences. This consideration becomes highly important in cases of the more complex material systems in which the primary formulations can not represent the expected thermodynamic information quite well. The flowchart of the general procedure is schematically depicted in fig. 5.1. The framework is structured for utilization before the onset of the simulations. Therefore, no direct connection to the CALPHAD databases is needed within the simulation runs. The present components in the system and the reaction type should be defined to the toolchain besides the exploited database. Based on the number of the defined elements, the binary or ternary reaction is realized in the system. By specifying the desired temperature range and concentration of the elements in the melt (mostly eutectic concentrations), the phase transformations are defined. In order to assure the existence of consistent driving forces and the correct solidification reactions in the simulations, the investigated temperatures should be selected below the melting temperature of the involved phases. It is worth mentioning here that, the accuracy of the resultant Gibbs energy functions can be influenced by the amounts of the selected temperatures. Hence, for a precise approximation, multiple runs of the toolchain with different defined ranges of the temperatures may be required for all involved phases. The following steps summarize the general procedure of temperature-dependent Gibbs energies approximation. It also includes an optional step for the modification of the results if necessary.

- STEP 1 Considering the investigated temperatures and concentrations in the melt, the equilibrium between the constituent phases is computed and the corresponding concentrations  $c_{\alpha}^{eq}$  are calculated. This calculation can be done by a software that can handle the CALPHAD databases. For the modeled systems of the current work, the Thermo-Calc software package [120] is utilized. But the other software packages like OpenCalphad [137], Pandat [138], Pycalphad [139] and the FactSage [140] can be used either.
- STEP 2 The Gibbs energies of the involved phases are obtained separately from the database in the considered temperatures. In the course of this endeavor, a predefined concentration range is necessary around the equilibrium concentrations. This range is designated by the user and separate files are created in the toolchain to save the results.

STEP 3 Numerical least squares method is employed to approximate the Gibbs energy functions based on the saved files in the previous step at each temperature for the existing phases independently.

STEP 4 Temperature-dependent Gibbs energy functions are obtained by the interpolation of the single-temperature results in each involved phase.

STEP 5 As the equality of the chemical potentials is one of the essential criteria for the thermodynamic equilibrium in the system, the chemical potentials are calculated from the approximated functions and their values are compared at the utilized temperatures.

*modi* (Optional) The fitted Gibbs energy functions are modified if the calculated chemical potentials deviate from each other considerably at STEP 5. This modification is performed by parameter variations based on additional thermodynamic criteria which are not considered in the previous steps.

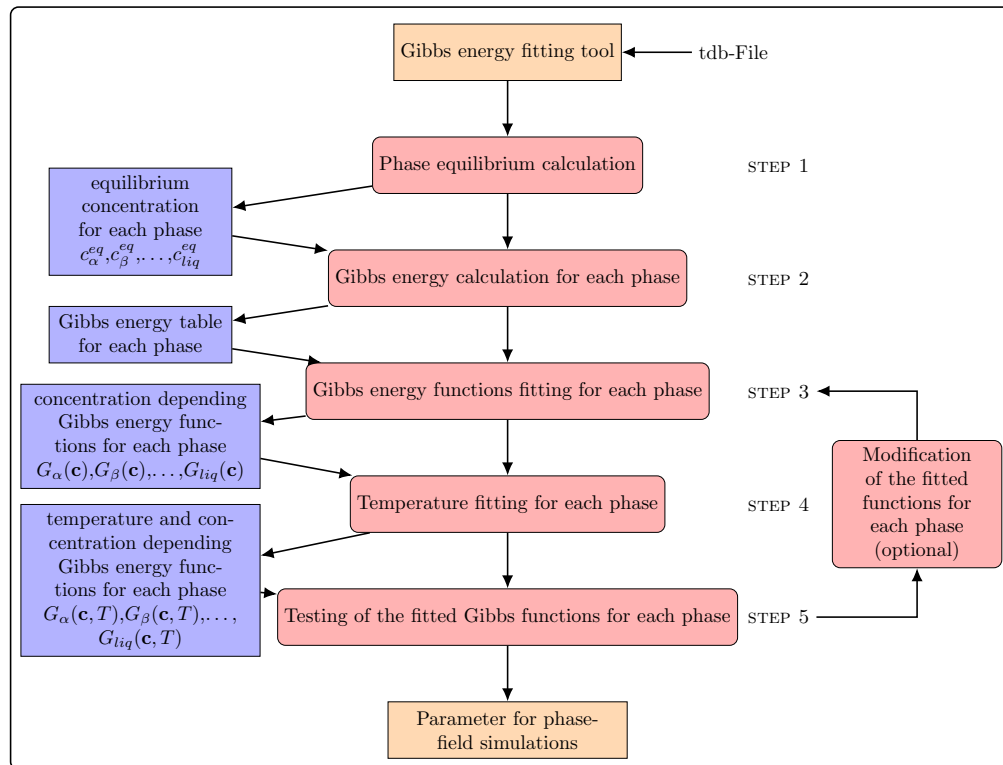


Figure 5.1: Flowchart of the Gibbs energies approximation algorithm, used in the current work based on [132].

The PACE3D solver (introduced in section 2.3.1), includes C-based tools to generate macrofiles based on this toolchain. Further verification of the results from the CALPHAD

databases is possible in the solver as well. The used numerical least-squares method in STEP 3 can cause some deviations from the exact equilibrium conditions. Meanwhile, the investigated concentration range adjustment, as well as the modification of the number of the calculation points in STEP 2, can enhance the accuracy of the calculations. Hence, by this accuracy enhancement, good correlations between the original and the derived thermodynamic data in the vicinity of the equilibrium concentrations can be achieved. For the investigated binary **B** and ternary **T** systems, the various approximation functions in STEP 3 can be chosen apart from the discussed parabolic functions. A list of possible functions is presented in Table 5.1. As it can be observed, the listed functions lead to unique solutions for the required derivations.

Table 5.1: The utilized approaches to obtain the approximated Gibbs energy functions in STEP 3 of the toolchain based on [132].

Label	Approach type	Equation
$B_i$	Ideal solution	$f(x, T) = a_0 x + a_1 + RT(x \ln(x) + (1 - x) \ln(1 - x))$
$B_l$	Logarithmic	$f(x) = a_0 \ln(x)$
$B_p$	Parabolic	$f(x) = a_0 x^2 + a_1 x + a_2$
$T_i$	Ideal solution	$f(x_0, x_1, T) = a_0 x_0 + a_1 x_1 + a_2 + RT(x_0 \ln(x_0) + x_1 \ln(x_1) + (1 - x_0 - x_1) \ln(1 - x_0 - x_1))$
$T_p$	Parabolic	$f(x_0, x_1) = a_0 x_0^2 + a_1 x_1^2 + a_2 x_0 x_1 + a_3 x_0 + a_4 x_1 + a_5$

STEP 5, is the accuracy checkpoint of the approximated Gibbs energy functions in representing the thermodynamic equilibrium and the degree of conformity between the functions and the CALPHAD databases. This checking is performed in the desired work domain, i.e. the investigated element concentrations and the temperatures. Accordingly, a visual comparison of the obtained energy data with the original CALPHAD information can be done as shown later in fig. 5.3 of section 5.2. In the expected equilibrium points, the average and maximum deviations between the functions as well as the chemical potentials can be calculated and compared in order to check the correct establishment of the equilibrium conditions quantitatively. The rebuilding of a phase diagram based on the approximated functions and a comparison with the original CALPHAD data is another approach to check the accuracy of the results in the nonvariant reactions. This is performed for example in fig. 5.4 of section 5.2. Any failure in satisfactorily reproducing the original data by the approximated functions indicates the modification necessity by considering additional thermodynamic criteria. These criteria can be summarized as:

- (i) The equal chemical potentials in the constituent phases of the system, at the equilibrium concentrations.

- (ii) The common tangent existence between the solid phases in the expected equilibrium concentrations at the desired temperature.

Assuming a total number of  $N$  phases in the system, in which the liquid is the last phase, and by consideration of the chemical potential of phase  $i$  as  $\mu_i = \frac{\partial g_i}{\partial x}$  in the binary as well as  $\mu_{ij} = \frac{\partial g_i}{\partial x_j}$ ,  $j = 1, 2$  for the ternary systems, the following equations ensure the equality of the chemical potentials:

$$\begin{aligned} \mu_1 = \mu_2 = \cdots = \mu_N & \quad \text{binary systems} \\ \mu_{10} = \mu_{20} = \cdots = \mu_{N0}, \mu_{11} = \mu_{21} = \cdots = \mu_{N1} & \quad \text{ternary systems.} \end{aligned} \quad (5.1)$$

The existence of a common tangent is guaranteed by:

$$\begin{aligned} g_i|_{x_i^{eq}} + \mu_i|_{x_i^{eq}} \cdot (x_{i+1}^{eq} - x_i^{eq}) &= g_{i+1}|_{x_{i+1}^{eq}} & \text{binary systems} \\ g_i|_{x_{i0}^{eq}, x_{i1}^{eq}} + \mu_{i0}|_{x_{i0}^{eq}, x_{i1}^{eq}} \cdot (x_{(i+1)0}^{eq} - x_{i0}^{eq}) + & \text{ternary systems} \\ \mu_{i1}|_{x_{i0}^{eq}, x_{i1}^{eq}} \cdot (x_{(i+1)1}^{eq} - x_{i1}^{eq}) &= g_{i+1}|_{x_{(i+1)0}^{eq}, x_{(i+1)1}^{eq}} & i = 1, 2, \dots, N - 2. \end{aligned} \quad (5.2)$$

The newly generated Gibbs energy formulations after these modifications are validated by repeating steps 4 and 5. In this stage, good accordances between the newly formulated Gibbs energy functions and the original CALPHAD data are expected as the later constraints are applied. It is worth mentioning here that, the performed modification should not be regarded as the CALPHAD data adjustment. The final purpose of the approximation is to obtain a simplified and computationally efficient (see Appendix 1 of [132]) representation of the CALPHAD data suitable for simulation studies. The later modification is to enhance the applicability and the correlation of the modeled Gibbs energy functions with the anticipated physical properties of the material systems. It is also worth mentioning that, the discussed approach is not unconditionally appropriate for all material systems. The toolchain in the approximation of the Gibbs energy functions is restricted to binary and ternary material systems without the stoichiometric phases. However, in cases of the systems without stoichiometric phases having well-defined equilibrium conditions, satisfying results are expected.

In the following sections, the toolchain is utilized in Gibbs energy approximations of NiAl-10Mo and Bi-In-Sn ternary eutectic systems. Additionally, the resultant functions are validated in STEP 5 of the toolchain by comparison with the original CALPHAD data. The phase-field simulations of the solidification processes are performed subsequently in the indicated systems.

## 5.2 NiAl-10Mo ternary system

The CALPHAD database of Peng et al. [113] is the basis of the Gibbs energy function approximations for the NiAl-10Mo system in this section. Following the approximation steps in the previous section, in STEP 1 the components Mo, Al and Ni are defined to the toolchain. The eutectic compositions are set to these elements, i.e. 10.3 mol-% Mo, 44.8 mol-% Al and 44.8 mol-% Ni. The eutectic temperature is defined as 1875.47 K based on the database. The system pressure is fixed to the atmospheric pressure and a total number of one mole of the components is defined in the system. Several points below the melting point are considered in the calculation of the equilibriums. In Table 5.2, equilibrium concentrations have been shown for the exemplary temperature of 1871 K in this step.

Table 5.2: The equilibrium concentrations of the involved solid phases in the eutectic reaction of NiAl-10Mo system at the exemplary temperature of 1871 K [113]. The concentrations of the non-variant reaction at the eutectic temperature are reported as the liquid concentrations.

Phase	$c_{\text{Mo}}$ in mol-%	$c_{\text{Ni}}$ in mol-%	$c_{\text{Al}}$ in mol-%
fiber (Mo-rich)	91.2	0.16	8.64
matrix (NiAl-rich)	0.092	50.464	49.444
liquid	9.4	46.7	43.9

For the calculation of the Gibbs energies in STEP 2, a regular mesh around the equilibrium concentrations is used. This mesh contains a user-specified number of points with the step widths of  $\Delta x = 0.1 \text{ mol} - \% \text{Mo}$ ,  $\Delta y = 0.1 \text{ mol} - \% \text{Al}$  surrounding the equilibrium concentrations. The mesh is delimited by a circle whose radius is set to  $0.5 \text{ mol} - \%$ . Depending on the position of the equilibrium points, only points in the simplex are chosen. The positions of these equilibria and their surrounding points in the liquidus projection of the Ni-Al-Mo system are depicted in fig. 5.2.

In order to approximate data points in STEP 3, ternary parabolic curves ( $T_p$  in Table 5.1) are used in the individual temperatures. By combining the approximated functions in these temperatures, the new temperature-dependent Gibbs energy formulations are derived in STEP 4. The resulting parameters as well as the Gibbs energies and the chemical potential values are listed in Table A.1 of Appendix A. The exemplary temperature of 1871 K is selected for visual comparison with the CALPHAD data and the obtained results are illustrated in fig. 5.3(a). Iso-concentration lines ( $c_{\text{Mo}} = \text{const.}$ ), are illustrated in this figure and the values of the Mo concentrations are indicated beside each line. The single squares denote the values based on the CALPHAD data which have close matches with the fitted functions in the vicinity of the equilibrium points in the

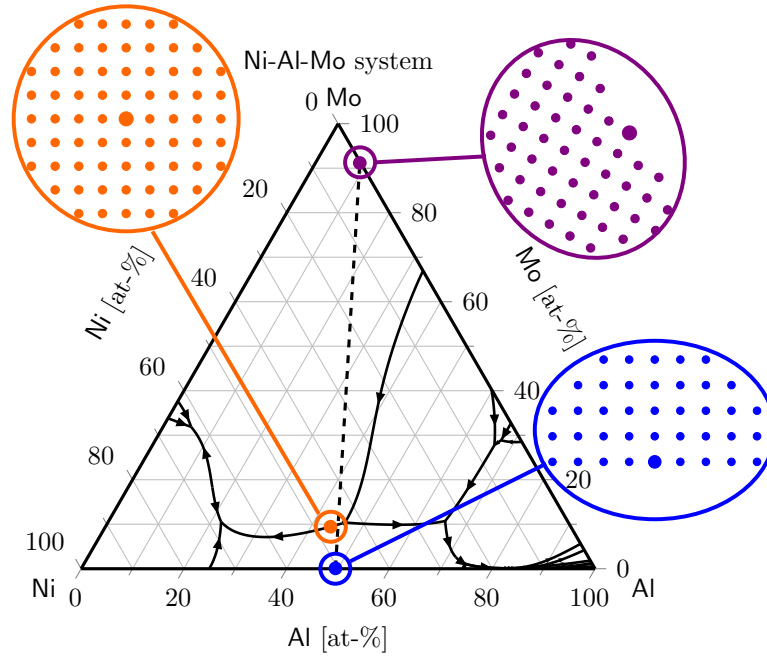


Figure 5.2: The liquidus projections of the ternary system Ni-Al-Mo based on [113]. In the magnified regions, the calculation points with a spacing of  $\Delta x = 0.1 \text{ mol} - \% \text{Mo}$ ,  $\Delta y = 0.1 \text{ mol} - \% \text{Al}$  around the equilibrium (bold point) for each phase are shown in the temperature  $T = 1871 \text{ K}$ . The dashed line indicates the later used isopleth section for the NiAl-10Mo ternary eutectic.

involved phases. Similar good accordances for the other aforementioned temperatures are observed which proves the accuracy of the fitted Gibbs energies in reproducing the Gibbs energies. In Table A.1, the obtained functions are referred as  $g_{app}$  and a maximum deviation of 0.01% between the approximated Gibbs energies and the original data  $g_{cal}$  is found in the fiber phase.

For an additional check of the fitted functions, chemical potentials are calculated for the considered phases at the mentioned temperature. These chemical potentials differ between the phases and hence they do not reproduce the accurate equilibrium from STEP 1. The difference for  $\mu_0$  is up to 18%, whereas it leads to a slightly lower value of 13% for  $\mu_1$ . To analyze these differences, the phase diagram around the equilibrium concentrations is reconstructed by using the common tangent rule and a comparison between the results and the originally derived phase diagram from the CALPHAD database is done in fig. 5.4. The illustrated CALPHAD data in this figure is the dashed line cut of the ternary diagram in fig. 5.2, or the phase diagram of fig. 4.1 in section 4.1. The segments I, II and III are the areas in the vicinities of the fiber, liquid and the matrix phase equilibriums. It is observed that the phase boundary of the NiAl-rich matrix is located at an unphysical negative Mo concentration of  $\simeq -0.04 \text{ mol} - \%$ . In order to circumvent this problem, as well as the deviations of the chemical potentials, the optional modification

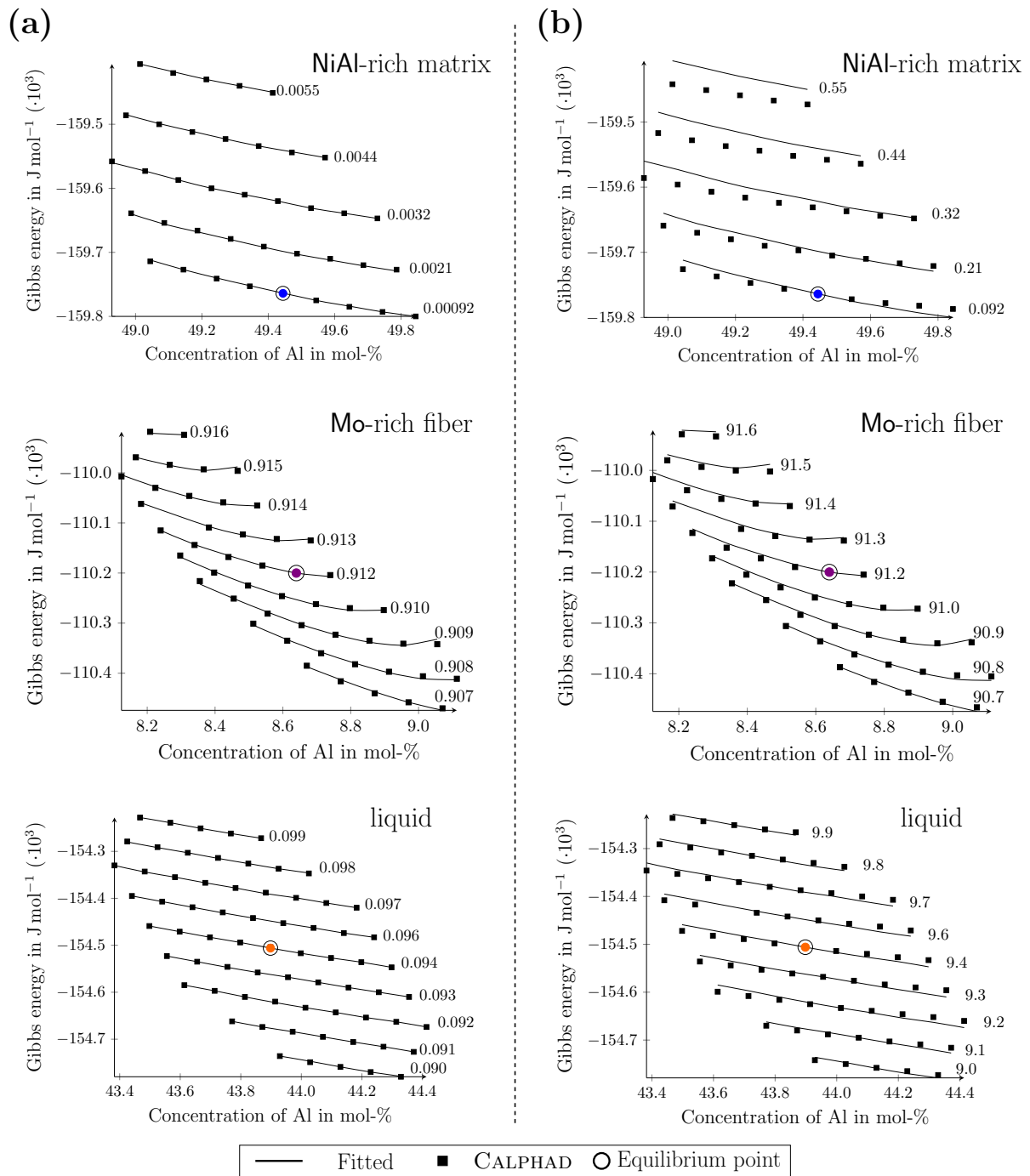


Figure 5.3: Comparisons between the generated Gibbs energy curves (solid lines) with the CALPHAD database in the NiAl-10Mo system [113] for matrix, fiber and liquid phases. The temperature is 1871 K and the concentrations of Mo are shown next to each curve. (a): The initial approximation results before modification (Table A.1), (b): The modified Gibbs energy functions (Table A.2) based on [132].

step, *modi* in section 5.1, is performed to adjust the fitting coefficients ( $a_0, \dots, a_5$ ) in the involved phases. As declared previously, in this procedure the coefficients are modified using eqs. (5.1) and (5.2) to reach similar chemical potentials with the minimum deviation of the Gibbs energies from the original CALPHAD data for all phases.

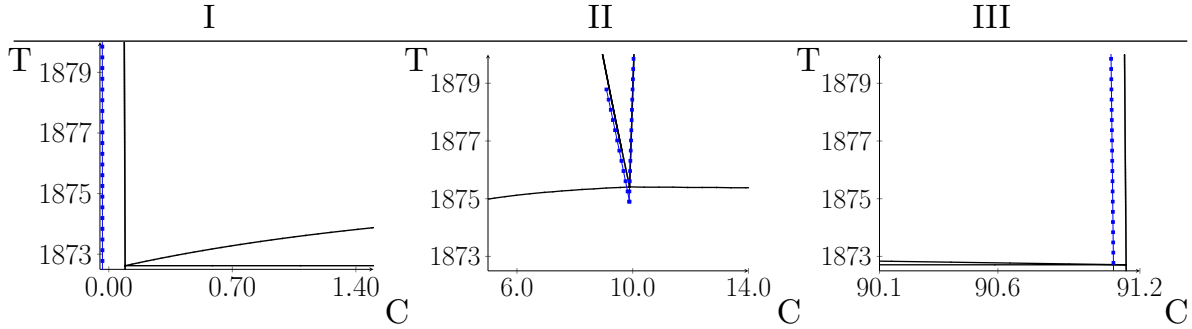


Figure 5.4: Rebuilding of the CALPHAD phase diagram in the NiAl-10Mo system (the blue lines) as illustrated in fig. 4.1 (the black lines). This is performed by the initially approximated Gibbs energy formulations in Table A.1.  $T$  is the temperature in Kelvin and  $C$  is the concentration of Mo in mol-%. The segments I, II and III are the areas in the vicinity of the fiber, liquid and matrix phases, respectively.

Further, the existence of a common tangent plane is ensured for all solid phases to settle the equilibrium conditions. The obtained result of the modification procedure is compiled in Table A.2 of Appendix A and is named as the modified Gibbs energy functions  $g_{mod}$ . Based on this table for the previously used exemplary temperature of 1871 K, a maximum deviation of 0.02% in the reproduction of the Gibbs energies is resulted in the matrix phase between the CALPHAD data and the approximated functions. Meanwhile, equality in the chemical potentials is almost achieved at the equilibrium concentrations between the different phases (*max* deviation=0.18%). By this fact, the suitability of the approximated functions in the representation of thermodynamics can be indicated.

In a similar manner to the initially obtained Gibbs energy formulations, for the modified functions the approximated Gibbs energies are compared with the CALPHAD data in the vicinity of the equilibrium concentrations in fig. 5.3(b). As it can be noticed, good correlations are achieved for the fiber and the liquid phases. The Gibbs energy of the matrix phase shows larger deviations with a maximum value of 0.02%, due to the made modification in the system. However, in the vicinity of the equilibrium points, the fitted functions match well with the CALPHAD database. A similar comparison like fig. 5.4 is performed in fig. 5.5 between the CALPHAD data and the rebuilt phase diagrams by means of the modified Gibbs energy functions, which shows the solved problem of the negative Mo concentration in the matrix phase.

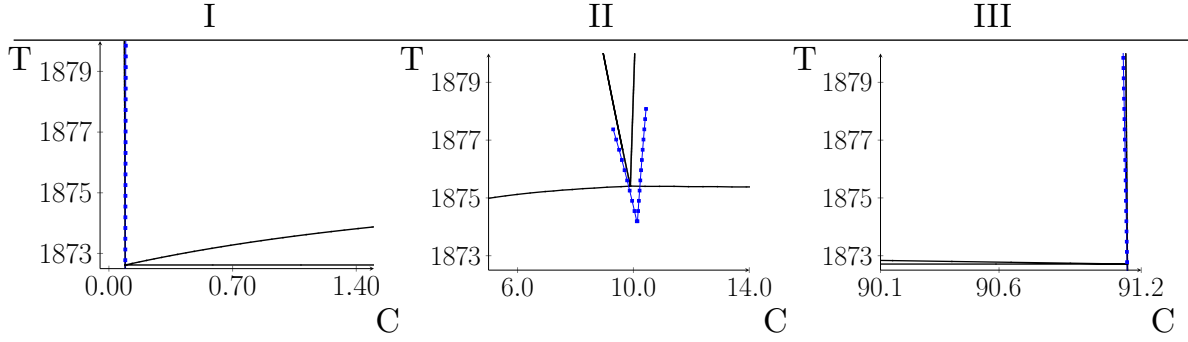


Figure 5.5: Rebuilding of the CALPHAD phase diagram in the NiAl-10Mo system (the blue lines) as illustrated in fig. 4.1 (the black lines). This is performed by the modified Gibbs energy formulations in Table A.2 (blue lines).  $T$  is the temperature in Kelvin and  $C$  is the concentration of Mo in mol-%. The segments I, II and III are the the areas in vicinity of the fiber, liquid and matrix phases, respectively.

In section 6.1, the phase-field simulations of the eutectic solidification in the NiAl-10Mo system are performed utilizing the achieved Gibbs energy formulations.

### 5.3 Bi-In-Sn ternary system

In a similar procedure to the previous section, the Gibbs energies are modeled for the Bi-In-Sn ternary system, utilizing the explained general procedure in section 5.1. The benefited database is established by Witusiewicz et al. [114] based on the CALPHAD method and is introduced previously in section 4.2. In the first step of the Gibbs energy functions approximation procedure, a temperature series below the eutectic point is selected and the equilibrium concentrations in the involved phases ( $\alpha$ ,  $\beta$ ,  $\delta$  and liquid) are calculated at the individual temperatures. The Thermo-Calc [120] commercial tool is used for this purpose. In this case, the resultant equilibrium concentrations in  $T = 331$  K, as an exemplary temperature, are reported in Table 5.3. A good correlation between these concentration values and the experimentally reported compositions [36, 86] belonging to the near eutectic states, exists. As it can be observed, the concentration deviations for the undercooling of 1 K in the involved phases, are mainly pronounced for the  $\delta$  phase with a maximum of  $\simeq 7\%$  in  $c_{\text{Bi}}$ . This is a sign of the solubility shift in this phase. The next step is the calculation of the Gibbs energies in the vicinity of the equilibrium concentrations for the individual temperatures separately. The step width of  $\Delta c_{\text{Bi}} = \Delta c_{\text{In}} = 0.1$  mol-% with a radius of 0.5 mol-% is selected for this purpose. The second-order polynomials ( $T_p$  in Table 5.1) in form of  $g(c_{\text{Bi}}, c_{\text{In}}) = a_0 c_{\text{Bi}}^2 + a_1 c_{\text{In}}^2 + a_2 c_{\text{Bi}} c_{\text{In}} + a_3 c_{\text{Bi}} + a_4 c_{\text{In}} + a_5$  are employed to obtain the Gibbs formulations in the next step. The constant coefficients  $a_0, \dots, a_5$  are

calculated with the additional criteria of eqs. (5.1) and (5.2) for sake of the accurate representations of the thermodynamics. The results are saved separately at each temperature, respectively. As the final step, the constants  $a_i$ ,  $i = 0, 1, \dots, 5$  are interpolated linearly to achieve the  $a_i(T)$ ,  $i = 0, 1, \dots, 5$  coefficients, forming the temperature-dependent Gibbs energy formulations for each phase. The resultant parameters for the  $\alpha, \beta, \delta$  and the liquid phases are summarized in Table A.3 of Appendix A. In addition, in the temperature of 331 K, the approximated values for the Gibbs energies  $g_{app}$  can be compared with the CALPHAD data. The approximated chemical potentials in the equilibrium points which are defined as  $\mu_{app,i}^{eq} = \partial g_{app} / \partial c_i$ ,  $i = \text{Bi, In}$ , are calculated either to be compared in different phases. As the comparison result, the chemical potential deviations are less than 2%. For the Gibbs energy values, these deviations yield below 0.1% indicating a good representation of the thermodynamics by the approximated functions.

*Table 5.3: The equilibrium concentrations of the involved phases in the eutectic reaction at the exemplary temperature of 331 K based on [114]. The concentrations of the non-variant reaction at the eutectic temperature are reported as the liquid concentrations.*

Phase	$c_{\text{In}}$ in mol-%	$c_{\text{Bi}}$ in mol-%	$c_{\text{Sn}}$ in mol-%
$\alpha (\text{BiIn}_2)$	66.67	32.01	1.32
$\beta (\beta - \text{In})$	66.96	8.02	25.02
$\delta (\gamma - \text{Sn})$	39.21	14.84	45.95
<i>liquid</i>	60.36	20.37	19.27

In fig. 5.6, the established equilibrium concentrations for different phases are compared with the CALPHAD data in a larger temperature range below the melting point. As it can be seen, the approximated functions represent the equilibrium conditions quite well including the occurred solubility shifts. This fact is more pronounced in the  $\delta$  phase, in which  $\simeq 25\%$  change in the concentration of In and  $\simeq 100\%$  change in the concentration of Bi exists in the considered temperature range of 10 K.

The achieved correlations, ensure the validity of the approximated functions in the ensuing simulative investigations of section 6.2 which are conducted in a much narrow temperature range compared to fig. 5.6.

## 5.4 Summary and conclusions

In this chapter, a general method is introduced to approximate the Gibbs energy functions from the CALPHAD databases for the binary and ternary material systems. These functions are generated in the forms of the second-order polynomials which are suitable

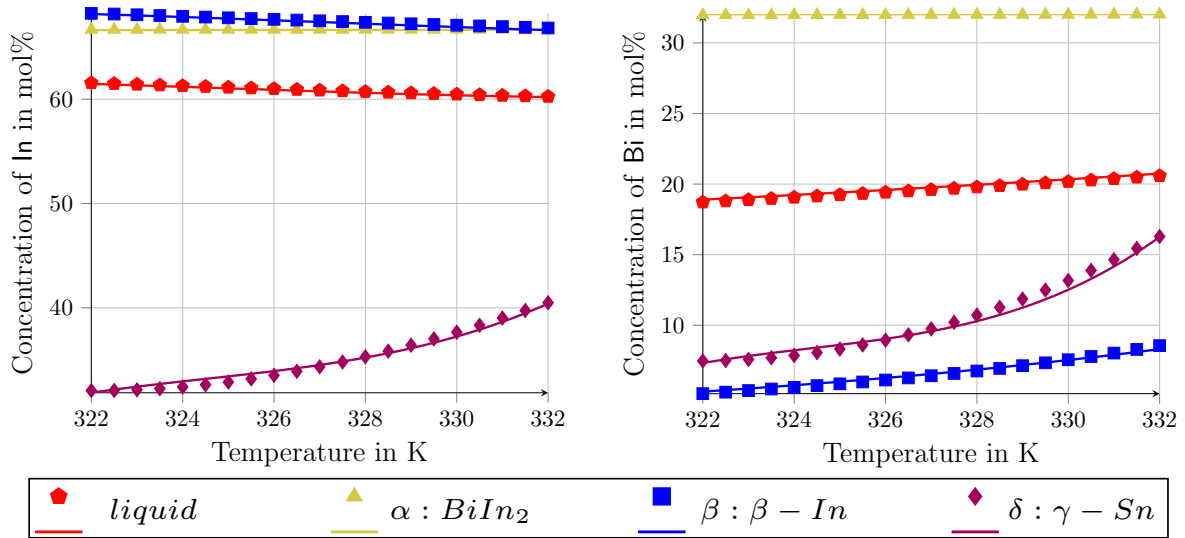


Figure 5.6: The comparisons between the equilibrium concentrations in the involved phases of the eutectic reaction in the Bi-In-Sn system, based on the CALPHAD data (solid points) [114] and the approximated functions in this work (solid lines) [91].

to be used in the grand-potential-based phase-field models. In the constructed toolchain, the databases in the forms of \*.tdb-files are defined as the inputs and are used to gain the equilibrium concentrations in the involved phases of the investigated reactions. The values of the Gibbs energies in the equilibria and near-equilibrium concentrations are calculated in the individual user-specified temperatures, separately. As the final goal of the toolchain is to obtain the temperature- and concentration-dependent energy functions, the individual temperature results are combined by employing linear interpolation. To validate the resultant formulations, the equilibrium concentrations are re-calculated based on them and the achieved values are compared with the original CALPHAD data. This can be performed in form of rebuilding the different segments in the phase diagrams which are in the considered temperature-concentration ranges of the investigated material systems. Afterwards, in cases of deviations from the expected equilibrium conditions, additional thermodynamic criteria are considered to modify the initially obtained Gibbs energy formulations.

As the physical systems, the eutectic reactions in the NiAl-10Mo and Bi-In-Sn ternaries are investigated and the accomplished functions are saved to be used in the performed phase-field studies in the upcoming sections. These functions are tested in the representation of the thermodynamics and their accuracies are validated.



# Chapter 6

## Phase-field simulations

### 6.1 *DS* simulation studies of NiAl-10Mo system

In this section, the simulation studies of directional solidification in the NiAl-10Mo eutectic system are performed based on the obtained Gibbs energy formulations in section 5.2. Multi-physics multi-phase PACE3D framework (see section 2.3.1) has been used in the simulation studies. The work of Zhang et al. [35] is benefited to get the relevant experimental data and to validate the obtained simulation results. The forthcoming studies consist of three parts: Initially, two-dimensional small domain simulations (the domain of one fiber spacing  $\lambda$ ) with a regularly-defined arrangement of the matrix and the fiber phases in the solid states next to each other beneath the liquid phase, are performed. This setup is schematically illustrated in fig. 3.2(b) of section 3.1, including the Mo-rich phase as the fiber and the NiAl-rich phase as the matrix. This arrangement is realized as the simplest arrangement to attain the stability of the solid-phases growth and to validate the obtained results in a less complex setting. The mentioned validation is achieved by means of the Jackson-Hunt analysis [112] and by comparing the evolved microstructures with the reported experimental data in the literature (summarized in section 4.1). Next, a two-dimensional simulation with the Voronoi tessellation of the initial solid seeds growing into the liquid phase is performed. By means of this simulation, the tendency of the randomly distributed fibers in the initial filling for the free evolution is shown. This simulation is conducted in a similar manner to the works of [9, 67, 87]. Finally, a three-dimensional simulation is completed with the introduced 3D setup in fig. 3.2(c), in which the effect of the anisotropy of the interfacial energies in the evolving fiber shapes, is checked. Simulations of the NiAl-10Mo system are performed in the solidification velocities of  $15 \mu\text{m s}^{-1}$ ,  $25 \mu\text{m s}^{-1}$  and  $30 \mu\text{m s}^{-1}$  in 2D, and  $30 \mu\text{m s}^{-1}$  in 3D, respectively. These velocities are the investigated values in the experimental work of Zhang et al. [35]. The volume fraction

of the fibers is set to the value of  $v_f = 0.15$  based on the mentioned reference. Considering the rectangular or the cuboid simulation domains, different boundary conditions are applied in the domain bounds as illustrated in fig. 3.2(b,c) and explained in section 2.3.3. The cubic positive anisotropy formulation (described in section 2.2) is activated with the anisotropy strength of 0.07 ( $\zeta_{\hat{\alpha}\hat{\beta}}$  in eq. (2.13)) in the upcoming simulations. The moving window technique is benefited (see section 2.3.4) to reduce the necessary computational power for the studies. The utilized material and process parameters are listed in Table B.2 of Appendix B.

### 6.1.1 Jackson-Hunt analysis in 2D

In the experimental work of [35], for the solidification velocity  $v = 30 \mu\text{m s}^{-1}$ , the average measured fiber spacing is reported to be  $\lambda = 1.106 \mu\text{m}$ . These velocity and  $\lambda$  values are set as the process parameters in the first series of the investigated simulation studies in this section. In order to establish the necessary driving force for the reaction, an undercooling of  $\Delta T = 5 \text{ K}$  is considered. The obtained microstructure is illustrated in fig. 6.1 which shows the concentration fields. In the top segment of this figure, the growth of the fiber and the matrix phases (red and dark blue) in the liquid phase (light blue) is shown. As it can be noticed, after the initial oscillations in the solidified phase boundaries such a stable growth is achieved. The mentioned oscillations occur due to the establishment of the curved interfaces in the initial time steps of the simulation just after  $t = 0$ . In fig. 6.1 (bottom), the measured **Mo** concentrations in the middle of the evolving phases are plotted with respect to the growth distance. These plotted values are in good correlations with the original CALPHAD data as shown previously in fig. 4.1 of section 4.1. The deviation area in the  $0 \leq \text{growth distance} \leq 0.9 \mu\text{m}$ , belongs to the mentioned initial steps of the simulation in which the steady-state condition is not reached yet. Similarly, in the  $5.5 \mu\text{m} \leq \text{growth distance} \leq 6 \mu\text{m}$  which belongs to the near-solid-liquid interface regions, concentration deviations come to exist due to the phase area variations in these regions. In the other investigated solidification velocities, i.e.  $v = 15 \mu\text{m s}^{-1}$  and  $v = 25 \mu\text{m s}^{-1}$ , similar stable growths like fig. 6.1 are reached, respectively.

In order to study the liaison between the adjusting undercooling  $\Delta T$  and the evolved fiber spacing values in different growth velocities, the Jackson-Hunt analysis is performed in the following. This analysis is popular for its favorable achievements in the interpretation of the growth dynamics in the solidification processes [110, 141]. The theory is initially introduced by K. A. Jackson and J. D. Hunt in their study in 1966 [112]. They described the liaison between the undercooling, the fiber/lamellar spacing and the solidification velocity in the binary eutectic reactions as:

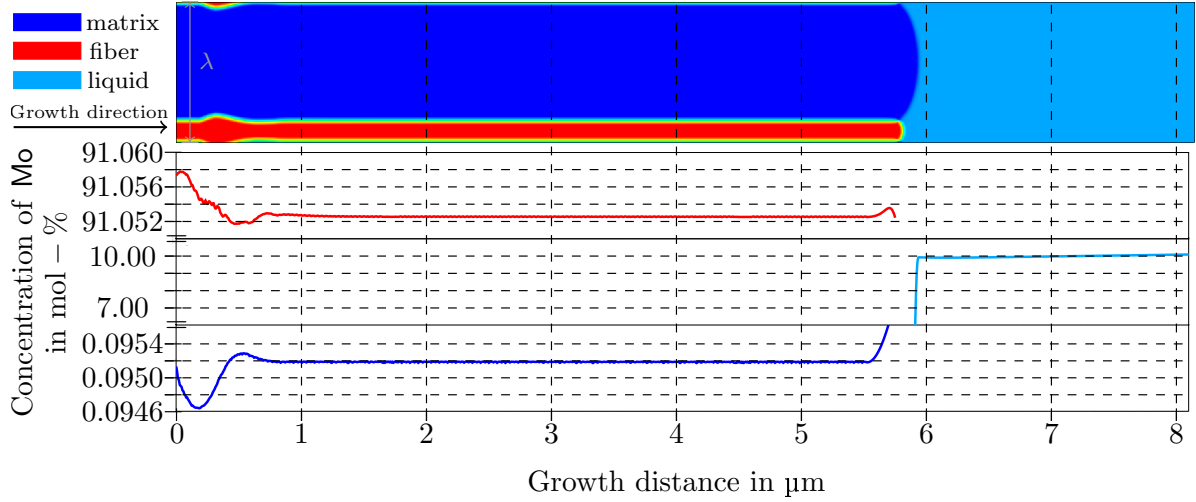


Figure 6.1: 2D simulation result of the eutectic solidification in the NiAl-10Mo ternary system with the growth velocity  $v = 30 \mu\text{m s}^{-1}$ . Top: the illustration of the Mo-rich fiber embedded in the NiAl-rich matrix, below the liquid phase in a single lamella based on [132]. Bottom: the plots of the concentration fields in the middle of the individual phases.

$$\Delta T = K_1 v \lambda + \frac{K_2}{\lambda}, \quad (6.1)$$

in which  $K_1$  and  $K_2$  are constants based on the material parameters and the phase fractions of the solidified phases. As a result of eq. (6.1), the undercooling decreases by the increase of  $\lambda$ , until reaching a global minimum. Further increase of the lamellar spacing, leads to the increase of the undercooling. By solving  $\partial \Delta T / \partial \lambda = 0$ , the Jackson-Hunt spacing  $\lambda_{JH}$  is gained as:

$$\lambda_{JH} = \sqrt{\frac{K_2}{K_1 v}}. \quad (6.2)$$

McCartney et al. [142] in their study from 1980, extended this theory to the solidification of the ternary eutectics with the growth of two solid phases. In 1999, Himemiya and Umeda [143] generalized the theory further to the ternary eutectics with three solid phases  $\alpha, \beta$ , and  $\delta$  arranged in  $\alpha\beta\delta$  or  $\alpha\beta\alpha\delta$  stacking sequences. In their study, the regular lamellar, the hexagonal rod and the semi-regular brick-type microstructures are investigated. It is concluded that the lamellar model is useful in the easy prediction of the undercooling-spacing relations, regardless of the real morphology of the solidified system. In 2011, Choudhury et al. [115] extended the Jackson-Hunt relation for the arbitrary periodic lamellar microstructures in the ternary eutectics with three distinct solidifying

phases. In the latter study, a system with  $\alpha, \beta$  and  $\delta$  solid phases is considered and the general expressions of the concentration fields  $c$  ahead of the individual solid phases in the solidification front are derived. This is done by utilizing the Fourier series expansion for the concentrations and the solutions of the stationary diffusion equation in form of  $v\partial c + D\nabla^2 c = 0$ . The average front temperatures for the involved phases are obtained by the Gibbs-Thomson equation along the front cells resulting in the calculation of the undercoolings in forms of  $\Delta T_\alpha, \Delta T_\beta$  and  $\Delta T_\delta$  [115]. In order to obtain the constants of the Jackson-Hunt relation ( $K_1$  and  $K_2$  in eqs. (6.1) and (6.2)), the front undercoolings can be assumed to be equal;  $\Delta T_\alpha = \Delta T_\beta = \Delta T_\delta$ . This assumption can correlate well with the reality in the simulation studies of the NiAl-10Mo system in current work, as the utilized temperature profile (eq. (3.1)) is not varying in directions perpendicular to the growth direction and its gradient is quite low in the solidification direction. Therefore, a Jackson-Hunt analysis is conducted in the following and the acquired results are compared with the expected analytic solution and the existing experimental data. A similar procedure is followed by Kellner et al. [9] in their simulation studies of the NiAl-34Cr system. Hence, in the investigated solidification velocities ( $15 \mu\text{m s}^{-1}$ ,  $25 \mu\text{m s}^{-1}$  and  $30 \mu\text{m s}^{-1}$ ), the spacing values are varied in the predefined ranges around the experimentally reported average fiber spacing values  $\lambda_{ave}^{exp}$  [35] and the adjusted undercoolings are measured. The mentioned variations are in the approximate ranges of  $\lambda \in [0.6 \cdot \lambda_{ave}^{exp}, 1.5 \cdot \lambda_{ave}^{exp}]$  for each single growth velocity. Figure 6.2(a) shows the obtained undercooling-spacing plots. The solid curves in this sub-figure, are based on the simulation results which are labeled in each solidification velocity by different colorings. The general shapes of these curves are in good agreement with the expected Jackson-Hunt-type curve shapes including the global minimums  $\lambda_{JH}^{sim}$ . Additionally,  $\lambda_{min}^{exp}$  and  $\lambda_{max}^{exp}$  are the experimentally measured minimum and maximum values of the formed fiber spacings based on Table 1 of [35]. In all of the resultant curves, the values of  $\lambda_{JH}^{sim}$  are located in the  $[\lambda_{min}^{exp}, \lambda_{max}^{exp}]$  intervals and generally in the vicinity of the  $\lambda_{ave}^{exp}$ . A deviation of 13% occurs as the maximum deviation belonging to the smallest velocity, but the result is still in the desired experimental range. This indicates a good correlation with the simulations and the experiments in the representation of the fiber spacings.

In fig. 6.2(b), the obtained values of  $\lambda_{JH}^{sim}$ , are plotted against the investigated solidification velocities to make a comparison with the anticipated analytic solution based on [115], as well as the experimentally reported average values for the fiber spacings in [35]. Good correlations between the analytic solution and the simulation results are achieved with a maximum deviation of 3.3% in the solidification velocity  $v = 25 \mu\text{m s}^{-1}$ . Further comparisons with the experimental results show larger deviations in the depicted data points with a maximum of 12.5% in  $v = 15 \mu\text{m s}^{-1}$ . In Table 6.1, a comparison between the evolved phase fractions in the simulation results and the experimental studies

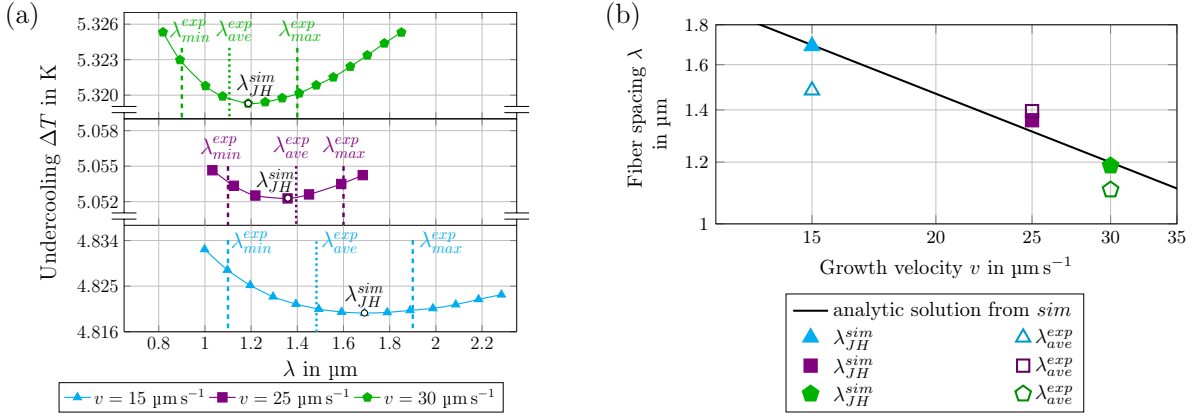


Figure 6.2: The Jackson-Hunt analysis results of the simulation studies in the NiAl-10Mo system based on [132]. (a): comparison of the obtained minimums in the simulations with the minimum, the maximum and the average experimental values of [35]. (b): comparison of the simulation results with the analytic solution proposed in [115] and the average values of the fiber spacings in [35]. *exp*: experimental, *sim*: simulation, *max*: maximum, *min*: minimum, *ave*: average.

of [35] is performed as the closing analysis of this section. The simulative phase fractions are measured in the results with the minimum values of the undercooling or in the other words, the simulations with  $\lambda_{JH}^{sim}$  as their fiber spacings. Good accordance is observed in the compared amounts with a maximum deviation of 6.0% belonging to the growth velocity of  $30 \mu\text{m s}^{-1}$ .

Table 6.1: Comparison of the evolved phase fractions in the simulation studies with the experimental results of [35] based on [132].

solidification velocity in $\mu\text{m s}^{-1}$	phase fraction of Mo-rich fiber		
	experimental	simulation	dev.
15	14.7 %	14.74 %	0.3 %
25	14.8 %	14.7 %	0.7 %
30	14.9 %	14.0 %	6.0 %

As deductions of this section, it can be declared that the simulation results have good correlations with the theoretical and the experimental spacing-undercooling and volume-fraction relations. The available analytic/experimental data indicate the applicability of the performed simulations in representing the anticipated physical properties in the NiAl-10Mo system. The validated simulations are regarded as the prerequisite to performing a two-dimensional simulation in the larger domain or a three-dimensional simulation in the upcoming sections.

### 6.1.2 Free growth of the solidified phases in 2D

In order to study the free evolution of the fibers, a 2D simulation is performed with a Voronoi tessellation of randomly distributed Mo-rich nuclei in the NiAl-rich matrix. This simulation aims to check the tendency of the system for evolving into the expected fibrous microstructure, without the initial filling of the solid phase bulks. Another aspect to analyze in this case is the achieved fiber spacings. The use of Voronoi tessellations in simulation studies of the *DS* processes has also been followed for the Ni-Al-Cr and Al-Ag-Cu systems [9, 67, 87] or in the studies of the eutectic colonies formation [70] in the literature. In the course of this endeavor, the solidification velocity is set to a value of  $30 \mu\text{m s}^{-1}$ , which is the fastest growth rate investigated in the previous section. This velocity set is due to the favored saving of the running time and computational power in the higher velocities. Like the simulations in section 6.1.1, the setup and boundary conditions used in this simulation are the same as the schematic illustration in fig. 3.2(b). A domain of  $11.06 \mu\text{m}$  is considered in the following which is ten times larger than  $\lambda_{ave}^{exp}$ . A total number of 144 CPUs are utilized on the IAM-MMS HPC cluster for this simulation which has taken an approximate computational time of two months. Figure 6.3 shows the evolved morphologies at the different growth distances  $x_{growth}$  as well as the corresponding solid-liquid SL interface profiles. In this configuration, the sizes of the initial nuclei are selected small enough in order not to affect the growing fiber sizes (see fig. 6.3, bottom right). At the  $x_{growth} = 8.8 \mu\text{m}$ , 8 evolving fibers exist and the SL interface is more or less flat. By reaching a growth distance of  $18.5 \mu\text{m}$ , one rod is eliminated and the interface profile takes a convex shape causing changes in the resultant fiber spacings in the further growths of  $18.5 \mu\text{m} \leq x_{growth} \leq 26.64 \mu\text{m}$ . In the growth distance of  $61.55 \mu\text{m}$ , the SL interface flattens more. The additional oscillations in the spacing values and the interface shape are observed after reaching the  $x_{growth} = 73.6 \mu\text{m}$ . Consequently, the SL interface becomes almost flat and remains stable in further distance increases, by reaching  $x_{growth} = 80.88 \mu\text{m}$ . The growth distance of  $167.9 \mu\text{m}$  is an illustrated example of such distances.

It can be concluded that the solid-liquid interface evolves from an initially curved shape to an almost planar solidification front as expected for the directional solidification of the ternary eutectics. The experimentally observed fiber spacings in this solidification velocity range from  $0.9 \mu\text{m}$  to  $1.4 \mu\text{m}$  in the experimental work which corresponds 12 and 7 fibers in the  $11.06 \mu\text{m}$  domain. Hence, it is found that the simulation results are consistent with the experiments.

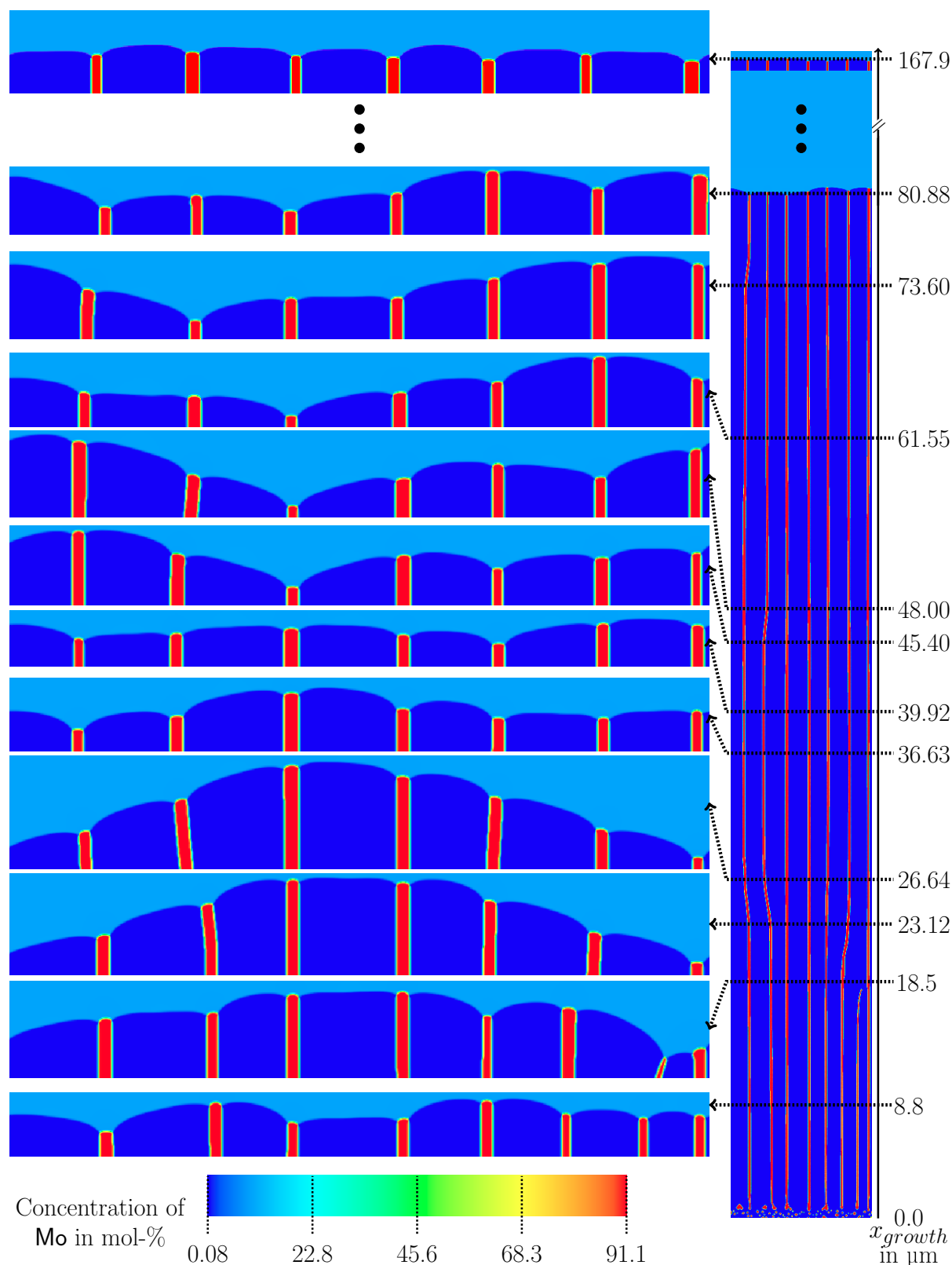


Figure 6.3: 2D simulation of the fibrous microstructure in eutectic solidification of the NiAl-10Mo system with Voronoi tessellation of the initial nuclei. The solidification velocity is  $30 \mu\text{m s}^{-1}$ . The solid-liquid interface profiles as well as the evolving microstructures in different growth distances are illustrated on the left. The concentration of Mo in the involved phases is depicted in this figure.

### 6.1.3 3D simulation

A hexagonal arrangement of the fibers in the matrix phase is expected in the 3D simulations based on the reported experimental evidence in the literature (see section 4.1). The setup is similar to the schematic illustration of fig. 3.2(c), in which the lateral four sides of the simulation domain are modeled with the periodic boundary conditions (see section 2.3.3). The simulation is performed with a predefined set of one fiber in the middle and a quarter of fiber in the corners of the domain. By mirroring the domain, a steady-state hexagonal arrangement can be established in the phase-field simulation. Figure 6.4 shows the evolved microstructure. The fiber spacing is equal to  $1.106 \mu\text{m}$ , which is the average of the experimentally measured values for the solidification velocity of  $30 \mu\text{m s}^{-1}$ . This simulation is initially started with the circular-shaped fibers and the resultant square shape is established due to the anisotropy of the interfacial energies between the matrix and fibers. A total number of 54 CPUs are used in the bwUniCluster at KIT, taking an approximate running time of one month.

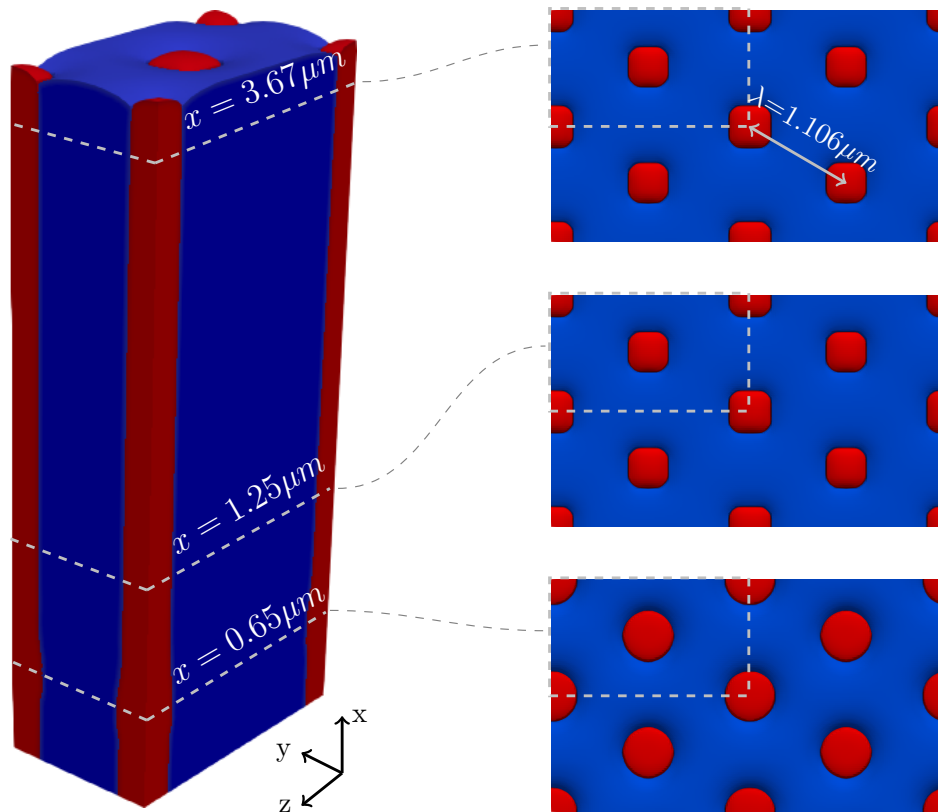


Figure 6.4: Evolution of the fibers in the eutectic solidification of the NiAl-10Mo system from the initial circular filling to the final square shape. The shape change is due to the anisotropy of the interfacial energies.

The expected role of the anisotropic interfaces on the formed pattern can be noticed in this simulation.

### 6.1.4 Summary and conclusions

In this section, phase-field simulations of the directional solidification in the NiAl-10Mo ternary eutectic system are performed. The necessary thermodynamic data for the simulations are obtained from the CALPHAD database. The simulation results are validated by means of the Jackson-Hunt analysis and by comparison with the applicable experimental results in the literature. A two-dimensional simulation with Voronoi tessellation of the initial solid phases is performed and the free evolution of the solid phases in the liquid phase is yielded. The most important role of the anisotropic interfaces in this system is noticed in the fiber formations in the three-dimensional simulation. The initially filled circular fibers evolved into square shapes due to this effect. Such a fiber shape has previously been observed in the experimental works in literature and the simulation result has shown a good correlation. This is the most important anisotropy-related phenomenon that is observed in the simulation study of this system.

## 6.2 *DS* simulation studies of Bi-In-Sn system

The performed literature review in section 4.2, including the experimentally observed patterns in the directional and rotating directional solidification processes of the Bi-In-Sn system, as well as its CALPHAD-based thermodynamic model, serve as the necessary foreknowledge in the ensuing simulation efforts. The approximated Gibbs free energy formulations in section 5.3 are employed to determine the system properties like the established phase equilibria, the values of the chemical potentials and the driving forces in the ongoing solidification processes. The *DS* simulations are performed prior to the *RDS* sims due to their simpler settings in the representation of the experimental conditions. This step is considered a validation of the modeled system for the later rotating directional solidification studies. The simulations are performed in the PACE3D framework as introduced in section 2.3.1. Likewise the accomplished procedure in the simulation studies of the NiAl-10Mo system, the Jackson-Hunt analysis is performed by the spacing variations and by measuring the resultant undercoolings. In this case, the considered  $\lambda$ -variation range is  $[0.7 \cdot \lambda_{JH}^{exp}, 1.5 \cdot \lambda_{JH}^{exp}]$ . The schematically illustrated setup in fig. 3.2(b), is utilized to perform these simulation series. In this configuration, the initial solid phases beneath the liquid phase are filled in  $\alpha\beta\alpha\delta$  arrangements based on the discussed experimental observations in section 4.2. The theoretical formulation of the boundary conditions is

shown in section 2.3.3, and their settlements in the domain are the same as fig. 3.2(b). The system temperature is varied with eq. (3.1), which affects the simulation domain linearly as illustrated schematically in fig. 3.2(a). In this formulation, the ultimate top segment of the domain modeled by the Dirichlet boundary condition, has the highest temperature, whereas the ultimate bottoms expressed with the Neumann  $BC$  has the lowest temperature. The elucidated moving window technique in section 2.3.4, makes the possibility of the growth consistency in the solidified phases resulting in the constant establishments of the solidification velocities and front temperatures.

Next, based on the achieved analytic validation, free microstructure evolutions in the larger simulation domains ( $\lambda \simeq 10 \cdot \lambda_{JH}^{exp}$ ) are performed. In order to give such a free evolution possibility to the system, Voronoi tessellations of the solid phases are set as the initial fillings and the nucleation mechanism (see section 2.3.5) is activated. The size of the initial solid-phase seeds is considerably small compared to the expected final lamellae. As a result, experimentally proclaimed phenomena like *phase invasion* or *phase exchange* (see section 4.2) are observed before the evolution of the final phase arrangements. The formed patterns are characterized by the variation of the system parameters, mainly the anisotropy strength in the interfacial energies.

In upcoming sections, the performed simulation procedure is discussed and the acquired results are reported.

### 6.2.1 Jackson-Hunt analysis in 2D

Considering the process conditions of the performed directional solidification experiments in the literature (see section 4.2), the growth velocity of  $v = 0.5 \mu\text{m s}^{-1}$  with the constant  $G^{DS} = 8 \text{ K mm}^{-1}$  can be a good choice for the process conditions in the simulation studies. This is due to the reported regularity and stability in the formed microstructures in this condition. The upcoming Jackson-Hunt studies use a base value of  $23.4 \mu\text{m}$  for the domain widths, which corresponds to the average value of the experimentally measured lamellar spacings  $\lambda_{JH}^{exp}$ . Hence, the domain size variation is set to be in the range of  $15 \mu\text{m}$  to  $35 \mu\text{m}$ . Additionally, two other amounts for the growth rates in the vicinity of  $v = 0.5 \mu\text{m s}^{-1}$  are considered to form the total velocity set of  $\{v_1 = 0.394 \mu\text{m s}^{-1}, v_2 = 0.5 \mu\text{m s}^{-1}, v_3 = 0.678 \mu\text{m s}^{-1}\}$  for the investigations. This set is selected due to the future need in the simulation studies of the  $RDS$  process in section 3.2, which lead to the appearance of these velocities in different rotating-disk segments. In the Jackson-Hunt studies, the lamellar spacings varied from  $20 \mu\text{m}$  to  $36 \mu\text{m}$  for  $v_1$  and from  $14 \mu\text{m}$  to  $30 \mu\text{m}$  for  $v_3$ , respectively. The material and process parameters are summarized in Table B.2 of Appendix B. Simulations in this section are performed assuming isotropic interfacial

energies, i.e.  $\zeta_{\hat{\alpha}\hat{\beta}} = 0$  in eq. (2.13). 35 million time steps, using 20 CPUs for each simulation, is the performance cost of the study with calculation times of up to 48 hours.

Figure 6.5, depicts the obtained results including the evolved microstructure as well as the Jackson-Hunt plots for the considered growth rates. In fig. 6.5(top), the achieved microstructure resulted from the stable growth of the solidified  $\alpha$ ,  $\beta$  and  $\delta$  phases into the liquid phase is illustrated. The microstructure belongs to the solidification velocity  $v_2$ . Furthermore, for the other simulated velocities, similar stable growths with  $\alpha\beta\alpha\delta$  stacking sequences are achieved. The domain size is  $75 \times 150$  cells (equal to  $23.4 \times 46.8 \mu\text{m}$ ) which is extended to  $23.4 \times 237.12 \mu\text{m}$ , by using the moving window technique. As it can be noticed, in the initial simulation steps, oscillations in the solid phase boundaries occur as the effect of the curved solid-liquid interface establishments. This effect is vanished in the further pattern evolution resulting in the final arrangements of the solid phases with almost flat solid-solid interfaces. The coloring indicates the concentrations of Bi in the phases for which good agreements with the CALPHAD data of fig. 5.6 are understood. In fig. 6.5(bottom), the Jackson-Hunt curves for the investigated growth velocities are depicted, based on the measured undercoolings at different spacings. The general shapes of the curves correlate well with the anticipated JH behavior which includes a global minimum,  $\lambda_{JH}^{sim}$ , in the undercooling-spacing plots. Such behavior has been observed either, in the simulation investigations of other material systems like Ni-Al-Cr in the literature [9]. The resultant values of  $\lambda_{JH}^{sim}$  for  $v_1$ ,  $v_2$  and  $v_3$  are equal to  $24.96 \mu\text{m}$ ,  $21.84 \mu\text{m}$  and  $19.34 \mu\text{m}$ , respectively.

Considering the reported mechanisms in the experimental works like the *lamellae branching* and the *phase exchange* (see section 4.2) which affect the final microstructure, the introduced nucleation mechanism in section 2.3.5 has to be activated to make the possibility of similar events. Hence, the conducted simulations with the solidification velocity of  $v_2 = 0.5 \mu\text{m s}^{-1}$  are redone with the active nucleation possibility. The achieved results are compared with the original configuration, consequently. It is observed that, in the cases of too small lamellar spacings ( $\lambda \ll \lambda_{JH}^{sim}$ ), which result in the eliminations of the  $\alpha$  and/or  $\delta$  solid phases, the expected  $\alpha\beta\alpha\delta$  arrangements are recovered by further nucleations of the ousted phases. In contrast, in the simulations with larger lamellar spacings, as the initial stable growths of the solid phases are not disturbed, no further nucleations take place. Figure 6.6 shows the mentioned results for the exemplary spacing values of  $15.5 \mu\text{m}$  and  $21.84 \mu\text{m}$ . Three highlighted areas are illustrated in order to show the pattern recovery in this example. Initially, one  $\alpha$  lamella is eliminated resulting in a small domain with the  $\alpha\beta\delta$  pattern. Later, the  $\delta$  phase is nucleated leading to a region with the  $\alpha\delta\beta$  pattern which is substituted by the final  $\alpha\beta\alpha\delta$  unit after a small pulling distance. This is achieved by further nucleation of an  $\alpha$  lamella. With the increase of the spacing to  $\lambda = 21.84 \mu\text{m} = \lambda_{JH}^{sim}$ , such instabilities are not observed anymore due to

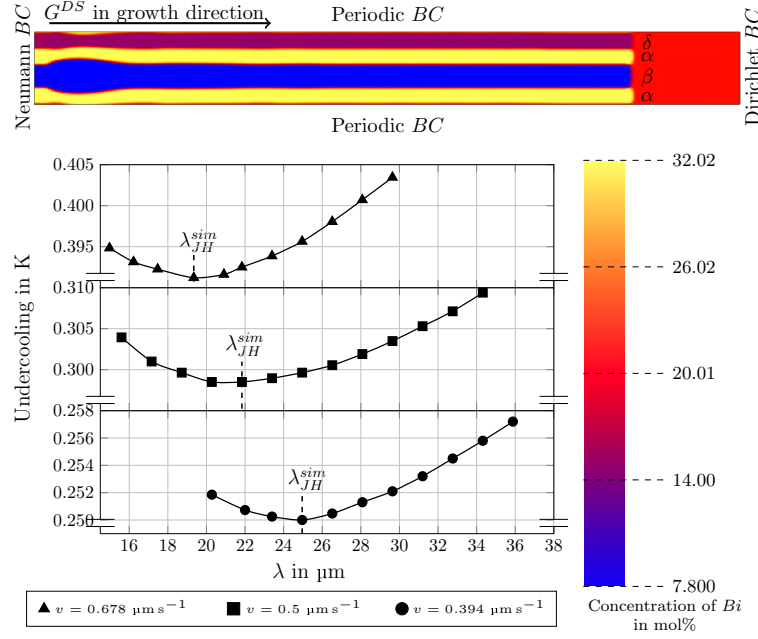


Figure 6.5: Top: the simulation result of the DS process in the Bi-In-Sn ternary eutectic system with  $v = 0.5 \mu\text{m s}^{-1}$  and  $G^{DS} = 8 \text{ K mm}^{-1}$ .  $\alpha$ : BiIn<sub>2</sub>,  $\beta$ :  $\beta$ -In and  $\delta$ :  $\gamma$ -Sn crystalline phases are illustrated with the yellow, blue and violet colors, respectively. Bottom: Jackson-Hunt plots showing the undercooling-spacing relations at the different growth rates. JH: Jackson-Hunt, sim: simulation based on [91].

the sufficient available spacing for the stable growths with the  $\alpha\beta\alpha\delta$  repeat units. The previously performed simulations for the Jackson-Hunt study are redone in a domain range of  $16 \leq \lambda \leq 34 \mu\text{m}$ , whose resultant undercoolings show a maximum deviation of 1%. The achieved negligible deviation concludes in the validation of the employed nucleation mechanism to be utilized in the forthcoming simulation studies.

## 6.2.2 Free growth of the solidified phases in 2D

The investigated two-dimensional simulations in larger spacings ( $\lambda \gg \lambda_{JH}^{exp}, \lambda_{JH}^{sim}$ ), serve as the basis of the phenomenological studies on ongoing mechanisms in free pattern evolutions. Ad hoc, in an analogous manner to the investigations of section 6.1.2, the initial solid phases are filled beneath the liquid phase in Voronoi tessellations. In contrast to the Ni-Al-Mo system in which two active solid phases are involved in the solidification reaction, in this case, the initial phase fillings are comprised of  $\alpha$ ,  $\beta$  and  $\delta$  crystalline phases. Therefore, the resultant phase arrangement is another factor that should be noted in this case. The considered nucleation mechanism in section 6.2.1 is active here either to facilitate the free evolution possibility. Due to the significant effects of interfacial energy anisotropies in the resultant microstructures (see section 4.2), various simulations with

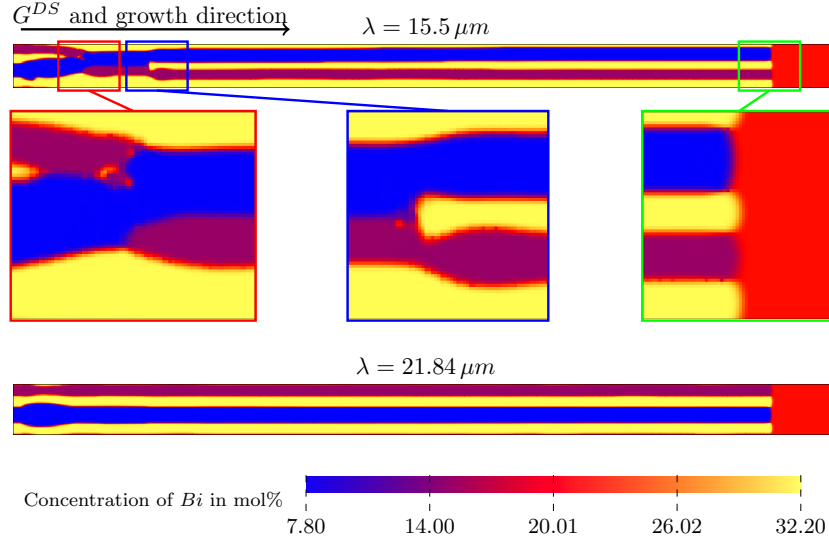


Figure 6.6: An exemplary illustration of the  $\alpha$  and  $\delta$  phase nucleations leading to the recovery of the  $\alpha\beta\alpha\delta$  pattern in the small spacings ( $\lambda \ll \lambda_{JH}^{sim}$ ). The solidification velocity is  $v_2 = 0.5 \mu\text{m s}^{-1}$ . At the higher spacing values (for example  $\lambda = 23.4 \mu\text{m}$ ) the similar results to fig. 6.5 are acquired without further instabilities.

differing anisotropy parameters are performed. The anisotropy strength which is defined by  $\zeta_{\hat{\alpha}\hat{\beta}}$  in eq. (2.13), is the main investigated parameter in upcoming studies. Based on Table B.2 of Appendix B in which the system and process parameters of the simulations are listed, the nondimensionalized values of the solid-solid interfacial energies are  $\gamma_{\alpha\beta} = \gamma_{\beta\delta} = 9.26 \cdot 10^{-4}$  [-] and  $\gamma_{\alpha\delta} = 2.78 \cdot 10^{-4}$  [-] for the upcoming simulations. Consequently, by applying different values for  $\zeta_{\alpha\beta}$  and  $\zeta_{\alpha\delta}$  which affects the interface profile (see eq. (2.12)), the interfacial energy plots can be drawn for different configurations. Figure 6.7 illustrates these plots which lead to the stable growth of the phases in the upcoming simulations.  $\zeta_{\alpha\beta}$  and  $\zeta_{\alpha\delta}$  are varied in ranges of 0.025 to 0.3 and 0.025 to 0.45, respectively. In the simulations for which  $\beta\delta$  interfaces are modeled anisotropically, the strengths are set equal to the  $\zeta_{\alpha\beta}$  values. Obviously, if  $\beta$  and  $\delta$  phases grow neighboring to each other, these amounts come in the calculations which can only happen in Voronoi tessellation fillings or neighboring nucleations of these phases. The simulations are performed in domains of  $750 \times 400$  cells which are extended to  $750 \times 2400$  cells by applying the moving window technique (see section 2.3.4). 192 CPUs are used in the HPC cluster of IAM-MMS institute taking an average computational time of 10 days to calculate 150 million time steps in each simulation. The solidification velocities are set to the value of  $0.5 \mu\text{m s}^{-1}$  and the other parameters are kept unchanged as same as the performed simulations in section 6.2.1. There is no dynamic parameter change in the performed simulations. I.e. the specified anisotropy parameters are set before the onset of the simulations and kept constant until the final evolution is completed.

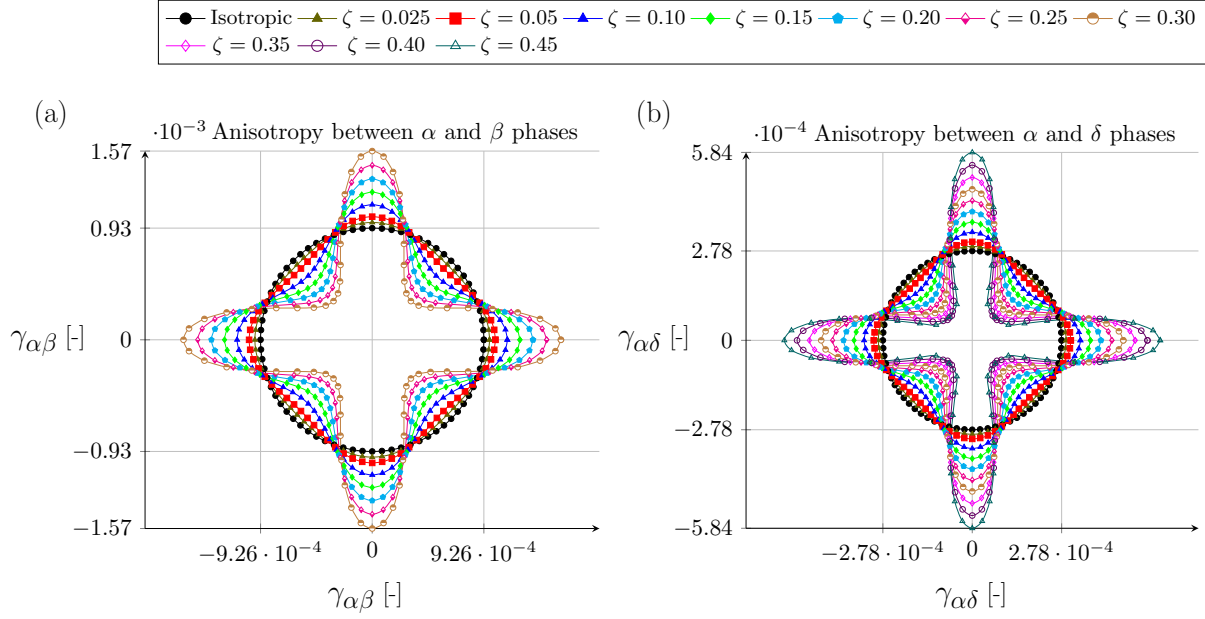


Figure 6.7: The interfacial energy plots of the anisotropic interfacial energies for (a):  $\alpha\beta$  and (b):  $\alpha\delta$  phase boundaries.  $\zeta$  stands for the anisotropy strength in eq. (2.13).

In the performed studies, initially, a simulation with the isotropically modeled interfaces is performed. Next, the anisotropy is activated and primitively is considered only in  $\alpha\beta$  interfaces. Its strength is increased in a stepwise manner and for each strength, a single simulation is performed. Afterward, a similar procedure is repeated for  $\alpha\delta$  interfaces to detect the resulting effects on the microstructures and to compare the evolved patterns with the  $\alpha\beta$  anisotropy. Finally, the anisotropy is activated in all phase boundaries and the evolved patterns for the highly anisotropic systems are studied.

As a start point, in fig. 6.8, the isotropic simulation result is compared with an anisotropic case with  $\zeta_{\alpha\beta} = 0.025$ . Other interfaces are modelled isotropically in this simulation. The investigated strength is the minimum value in the depicted plots of fig. 6.7. As it can be observed, both simulations result in the evolution of 7 stable lamellae with  $\alpha\beta\alpha\delta$  stacking sequences. The intermediate perturbations in the isotropic simulation before reaching the final arrangement are less than in the anisotropic case, indicating its more steadiness.  $a_1$  depicts a magnified area including nucleation of  $\alpha$  phase and its growth between  $\beta$  and  $\delta$  lamellae. This nucleation plays an essential role in the final formation of an  $\alpha\beta\alpha\delta$  unit.

Similarly, in  $a_2$ ,  $\alpha$  and  $\delta$  phases nucleate and grow stably till the end of the simulation. In the left bottom of  $a_2$ , there is the nucleation of  $\alpha$  on a thick bulk of the  $\beta$  phase which causes an instant elimination of  $\beta$  lamella, but it nucleates again and grows. All of these events do not lead to the deviation of the resultant microstructures from the

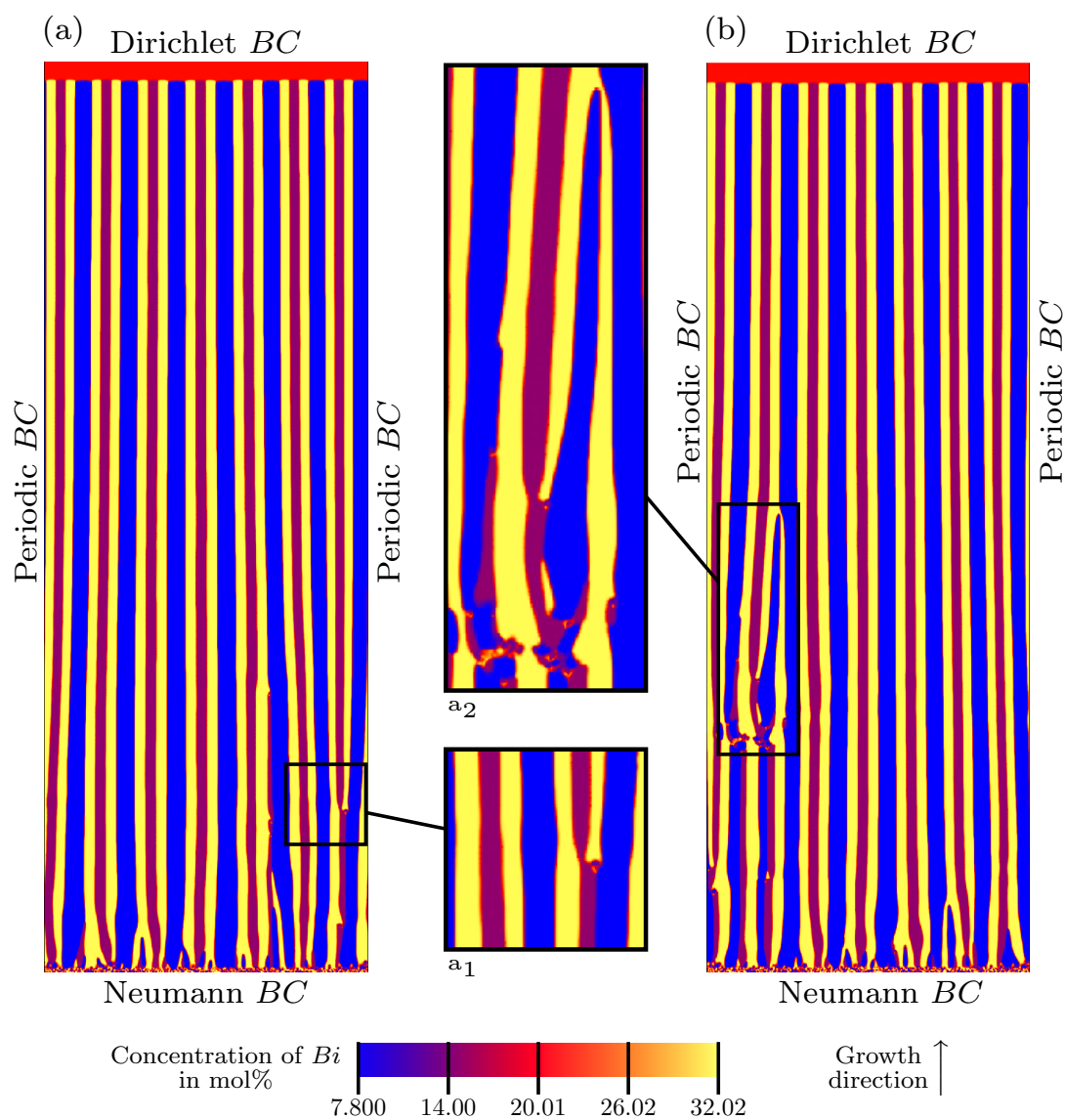


Figure 6.8: Simulation results of the DS process in the Bi-In-Sn ternary system with the Voronoi tessellation of the initial solid phases. (a): the isotropic interfacial energies ( $\zeta_{\alpha\beta}=\zeta_{\alpha\delta}=\zeta_{\beta\delta}=0$ ), (b): the anisotropy in the  $\alpha\beta$  interfaces ( $\zeta_{\alpha\beta}=0.025$ ,  $\zeta_{\alpha\delta}=\zeta_{\beta\delta}=0$ ). In both simulations, the magnified areas show the instabilities in the phase evolution processes.

expected pattern of the floating grains. Hence, it can be concluded that, for the investigated anisotropy strength, the system undergoes the transitional instabilities, but retains the isotropic behavior finally, apparently due to the weakness of the employed anisotropy. The other anisotropy strength values, shown in the interfacial energy plot of fig. 6.7(a), are also examined and the acquired microstructures are presented in figs. 6.9 and 6.10.  $\alpha\delta$  and  $\beta\delta$  interfaces are assumed to be isotropic in this configuration. In fig. 6.9,  $\zeta_{\alpha\beta}$  is varied in increments of 0.05, 0.10 and 0.15. Sub-figure (a) denotes the value of 0.05, in which three micrograph magnifications are displayed. In  $a_1$  and  $a_2$ ,  $\alpha$ -phase nucleation on the  $\beta$  phase occurs causing a sharp elimination of the  $\beta$ . Despite  $a_2$  in fig. 6.8, the  $\beta$  lamellae are overgrown here, due to the higher employed anisotropy strength. These eliminations lead to the formation of two  $[\alpha\beta]_1[\alpha\delta]_2$ -type patterns which are specified by the green rectangles on the right side of the figure. This pattern is one of the indicated superstructures in the experimental works, as discussed previously in section 4.2.  $a_3$  depicts  $\alpha$  nucleation in between  $\beta$  and  $\delta$  phases causing the formation of one  $\alpha\beta\alpha\delta$  unit. This behavior is similar to previously shown  $a_1$  in the isotropic simulation of fig. 6.8(a). The mechanism is observed again in the higher anisotropy strength of 0.10 as shown in  $b_1$  magnification in sub-figure 6.9(b), which leads to the construction of  $[\alpha\beta]_1[\alpha\delta]_2$  and  $[\alpha\beta]_2[\alpha\delta]_2$  motifs. In the formation of the later motif which is specified by the red rectangle, elimination of the  $\beta$  phase occurs caused by the nucleation of a  $\delta$  lamella on it. The occurred elimination-nucleation events which have essential roles in the formations of the final pattern can be regarded as a reproduction of the experimentally observed recovery mechanisms (see section 4.2) like the *phase invasion* or the *phase exchange*. It is worth emphasizing here that, although the physical natures of these mechanisms are three-dimensional in the experimental works (see fig. 8 of [86] for example), by activating the nucleation in the simulation studies the final products can be reproduced and studied in a much cheaper way. This cheapness is due to the possibility of a reduction in the simulation dimensions from 3D to 2D. As for other examples, the  $b_2$  magnification in fig. 6.9 shows the phase-exchange phenomenon. A similar phase exchange has happened in  $b_3$  either which has resulted in the formation of another  $[\alpha\beta]_1[\alpha\delta]_2$  sequence. In the magnified area  $c_1$  belonging to the higher anisotropy strength of 0.15, another  $\alpha$  nucleation between  $\beta$  and  $\delta$  lamellae has happened likewise to  $a_3$  and  $b_1$  magnifications. In  $c_2$ , one stable growth of  $\alpha\delta\alpha\delta$  unit from the initial steps of the simulation occurs as nice evidence of the inherent tendency of the anisotropic system to form this pattern. In  $c_3$ , by elimination of the  $\beta$  phase, the final formation of an  $\alpha\beta\alpha\delta$  pattern from  $[\alpha\beta]_2[\alpha\delta]_1$  has resulted which indicates disinclination of the system to form this superstructure. In addition, one  $\beta\alpha\delta$  arrangement has evolved in this anisotropy configuration either, which is specified by a pink rectangle.

In fig. 6.10,  $\zeta_{\alpha\beta}$  is increased to values of 0.20 and 0.25 and the evolved microstructures are shown in sub-figures 6.10(d) and 6.10(e). Further increase of  $\zeta_{\alpha\beta}$  leads to instabilities in the evolved phases and breakage of the simulations subsequently. Therefore,  $\zeta_{\alpha\beta} = 0.25$  is the maximum possible anisotropy strength in this configuration. As these figures show the results of the same study, the sub-labeling of the sub-figures with small letters a, b,... is continued from fig. 6.9 to fig. 6.10.

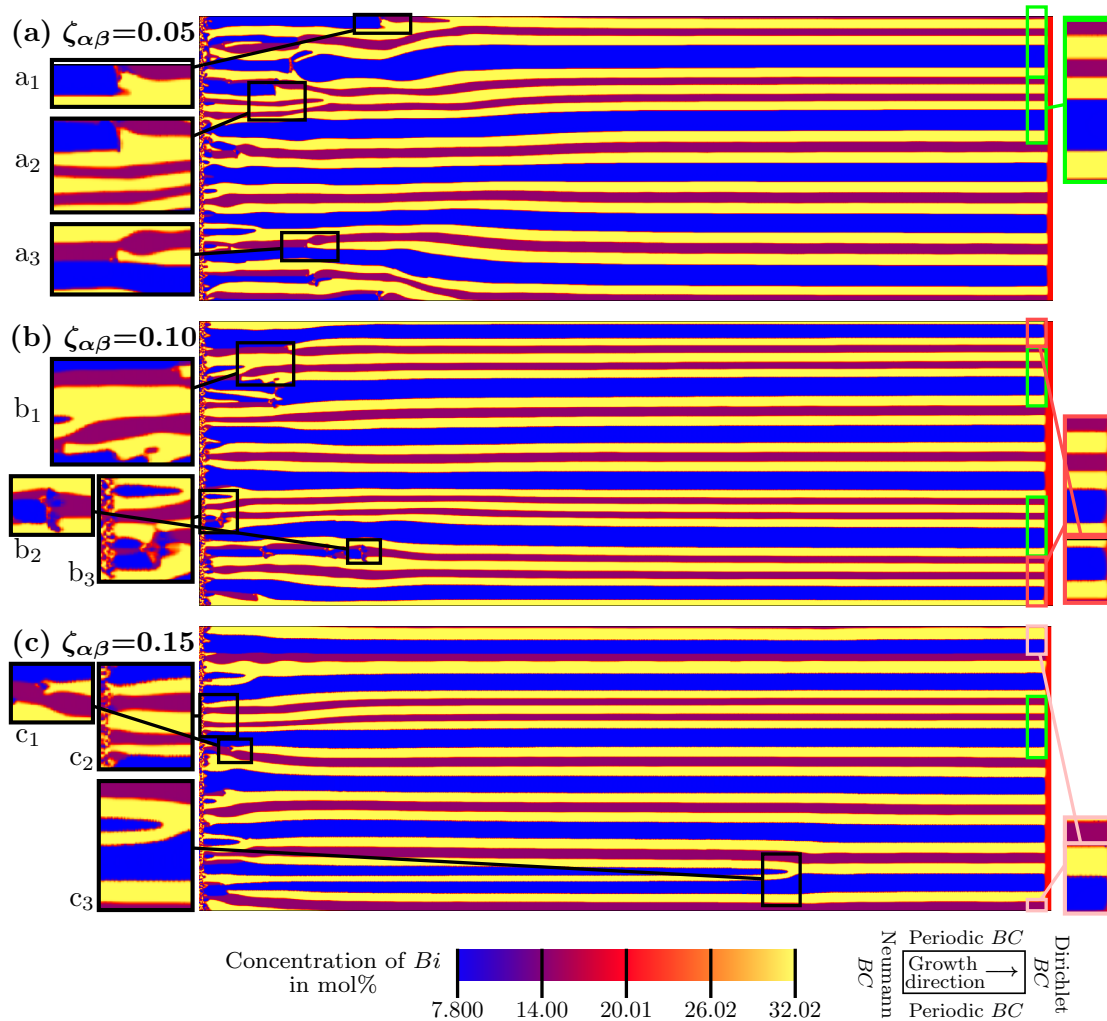


Figure 6.9: Effects of the anisotropic  $\alpha\beta$  interfaces on the pattern formation in the DS simulations of Bi-In-Sn system.  $\zeta_{\alpha\beta}$  is varied in a range of 0.05 to 0.15 based on the interfacial energy plot of fig. 6.7(a) and  $\zeta_{\alpha\delta} = \zeta_{\beta\delta} = 0$ . Magnified areas: the formed  $[\alpha\beta]_1[\alpha\delta]_2$ ,  $[\alpha\beta]_2[\alpha\delta]_2$  and  $\beta\alpha\delta$  patterns are specified with the green, red and pink rectangles, respectively.  $a_1$ ,  $a_2$ : the  $\beta$  elimination forming the  $[\alpha\beta]_1[\alpha\delta]_2$ .  $a_3$ ,  $b_1$  and  $c_1$ : the  $\alpha$  nucleation between the  $\beta$  and the  $\delta$ .  $b_2$ :  $\beta$ -to- $\delta$  phase exchange.  $b_3$ ,  $c_2$ : the stable growth of  $\alpha\delta\alpha\delta$ .  $c_3$ : the  $\beta$  elimination reducing the  $[\alpha\beta]_2[\alpha\delta]_1$  to the  $\alpha\beta\alpha\delta$ .

In fig. 6.10, the evolved  $[\alpha\beta]_1[\alpha\delta]_2$  motifs are specified by the same coloring as the previous figures. In segments  $d_2, e_1$  and  $e_2$ ,  $\alpha$  phase nucleations between the  $\beta$  and the  $\delta$  lamellae happen. The nucleated  $\alpha$  phases grow stably in all cases. In  $e_2$ , the  $\beta$  phase is eliminated in further simulation steps but in the other cases, it evolves steadily. In  $d_1$ ,  $\beta$ -to- $\delta$  phase exchange has happened with two evolving  $\delta$  phases showing more tendency of the system to form  $[\alpha\beta]_1[\alpha\delta]_2$  patterns compared to the previous cases.

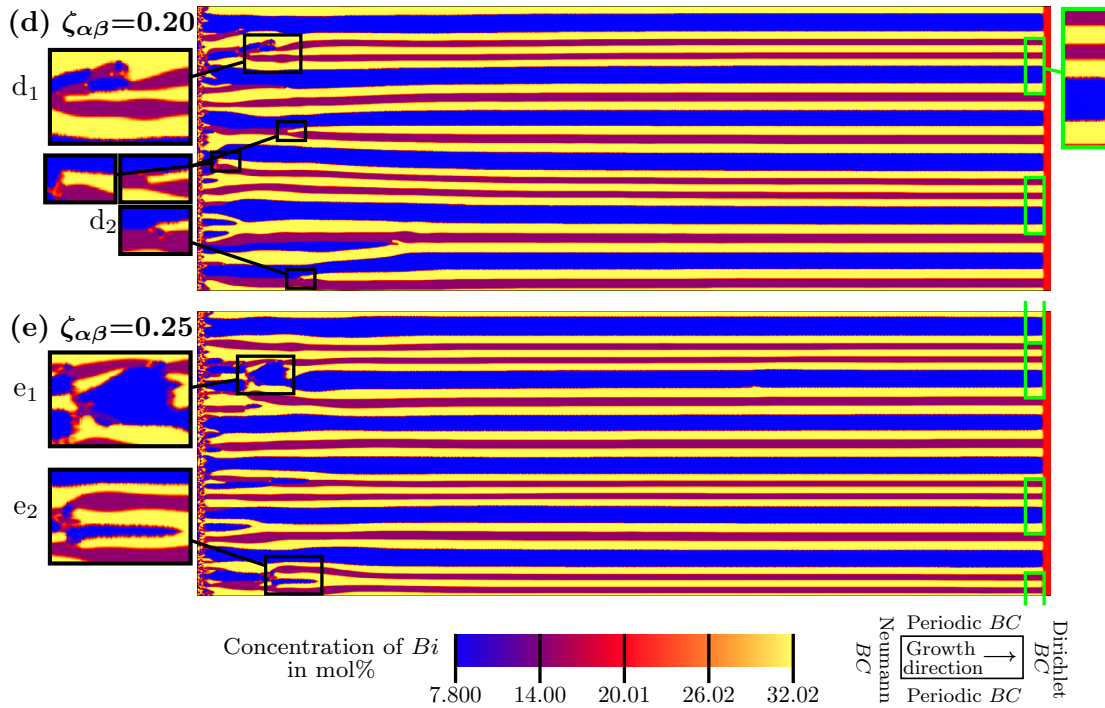


Figure 6.10: Effects of the anisotropic  $\alpha\beta$  interfaces on the pattern formation in the DS simulations of the Bi-In-Sn system.  $\zeta_{\alpha\beta}$  is varied in increments of 0.20 to 0.25 based on the interfacial energy plot of fig. 6.7(a) and  $\zeta_{\alpha\delta} = \zeta_{\beta\delta} = 0$ . Magnified areas: the formed  $[\alpha\beta]_1[\alpha\delta]_2$  patterns are specified with the green rectangles.  $d_1, e_2$ : the  $\beta$ -to- $\delta$  phase exchange.  $d_2, e_1$ : the  $\alpha$  growth between the  $\beta$  and the  $\delta$  phases.

In a comparable manner, the effects of anisotropic  $\alpha\delta$  interfaces on pattern formation are investigated in the following. In these cases, the values of  $\zeta_{\alpha\beta}$  and  $\zeta_{\beta\delta}$  are set to zero, and  $\zeta_{\alpha\delta}$  is varied based on the interfacial energy plot in fig. 6.7(b). The variation range is from 0.025 to 0.45, and the obtained micrographs are shown in figs. 6.11 and 6.12. Similar mechanisms to the anisotropic  $\alpha\beta$  cases are observed here as well. For example, in the magnified segments  $b_1, b_2, c_2, d_1, e_1, f_1$  and  $g_2$ , the  $\alpha$  phase is nucleated and has grown stably between the  $\beta$  and the  $\delta$  phases. Or in  $d_3, e_1, f_1$  and  $h_1$ , nucleation of the  $\alpha$  phases on the  $\beta$  lamellae has happened, leading to sharp eliminations of the  $\beta$  phases. In  $c_1, c_3$  and  $e_2$ ,  $\alpha$  eliminations in the initially formed  $[\alpha\beta]_2[\alpha\delta]_1$  patterns occur, reducing them to the regular  $\alpha\beta\alpha\delta$  patterns. In some other cases, as specified by the cyan rectangles,

stable growths of  $[\alpha\beta]_2[\alpha\delta]_1$  superstructures until the end of simulations are observed, for example, in sub-figures 6.11(c,d) and 6.12(f).  $\alpha\beta\delta$  is another pattern that is uniquely evolved in this configuration and is specified with the brown rectangles.

The resultant microstructure for  $\zeta_{\alpha\delta} = 0.025$  is represented in sub-figure 6.11(a), in which the nucleations of  $\alpha$  and  $\delta$  phases on the  $\beta$  phase have caused a 2D *lamella branching*. The resultant  $\alpha\delta\alpha\delta$  stacking has grown steadily till the end of the simulation forming an  $[\alpha\beta]_1[\alpha\delta]_2$  arrangement. In the magnified segment  $b_1$ , an unstable sawtooth microstructure is formed due to the repeated nucleation-eliminations of the  $\delta$  phase as a result of anisotropic  $\alpha\delta$  interfaces. This pattern is not repeated in further simulation steps of the evolved  $\delta$  lamella which is grown stably with almost flat phase boundaries. In  $d_1$  and  $d_2$ ,  $\alpha$ -to- $\delta$  and  $\beta$ -to- $\delta$  phase exchanges take place due to nucleations of  $\delta$  on the initially set  $\alpha$  and  $\beta$  phases. In area  $f_2$  of fig. 6.12, a stable  $[\alpha\beta]_2[\alpha\delta]_1$ -type pattern is formed from the initial steps of the simulation growing steadily till the end of the simulation. Another  $\beta$ -to- $\delta$  phase exchange happened in  $g_1$  in the drastically anisotropic strength of 0.35. In this configuration,  $[\alpha\beta]_2[\alpha\delta]_2$  is formed as the biggest observed superstructure in these simulations. In the next step, the  $\zeta_{\alpha\delta}$  is increased to 0.45 as the maximum investigated strength in this configuration. In further increased strength values, the simulations lose their stabilities and break consequently. As a primary conclusion, by comparing the possible variational ranges of  $\zeta_{\alpha\beta}$  and  $\zeta_{\alpha\delta}$ , it can be declared that the susceptibility of the system to  $\zeta_{\alpha\beta}$  changes is higher than  $\zeta_{\alpha\delta}$ . This observation is in good accordance with the discussed experimental evidence in section 4.2.

In the following, to get a deeper impression of the roles of anisotropy in the pattern construction, it is activated in all phase boundaries simultaneously. Based on previous observations,  $\zeta_{\alpha\beta}$  can have a maximum value of 0.25, whereas  $\zeta_{\alpha\delta}$  can still be increased up to 0.45. In order to have the maximum possible anisotropic behavior in the system,  $\zeta_{\beta\delta}$  is active either in the performed simulations. In figs. 6.13 and 6.14 all anisotropy strengths are varied in ranges of 0.025 to 0.20 by equal values in the individual simulations.  $a_1$  magnifies the elimination of one  $\beta$  lamella by nucleations of two  $\alpha$  and one  $\delta$  lamellae. The nucleated phases grow steadily till the end of the simulation.  $a_2$  magnifies the eliminations of  $\beta$  lamellae in different simulation segments reducing the initially constructed  $[\alpha\beta]_2[\alpha\delta]_1$  patterns to  $\alpha\beta\alpha\delta$ . In  $b_1$ , the  $\beta\delta$  pattern is exchanged to  $\delta\alpha\beta$ , due to the nucleations of the secondary phases on the initial phases. In  $b_2$ , the  $\alpha$  phase nucleates on the  $\beta$  but this nucleation does not lead to the complete elimination of the  $\beta$ , as  $\beta$  nucleates itself and grows steadily.  $b_3$  magnifies a  $\beta$ -to- $\delta$  phase exchange, together with another stable growth of the  $\delta$  phase from the onset of the simulation which leads to the formation of an  $\alpha\delta\alpha\delta$  unit. The  $\beta$ -to- $\delta$  phase exchanges are conventionally observed in the experimental work [86].

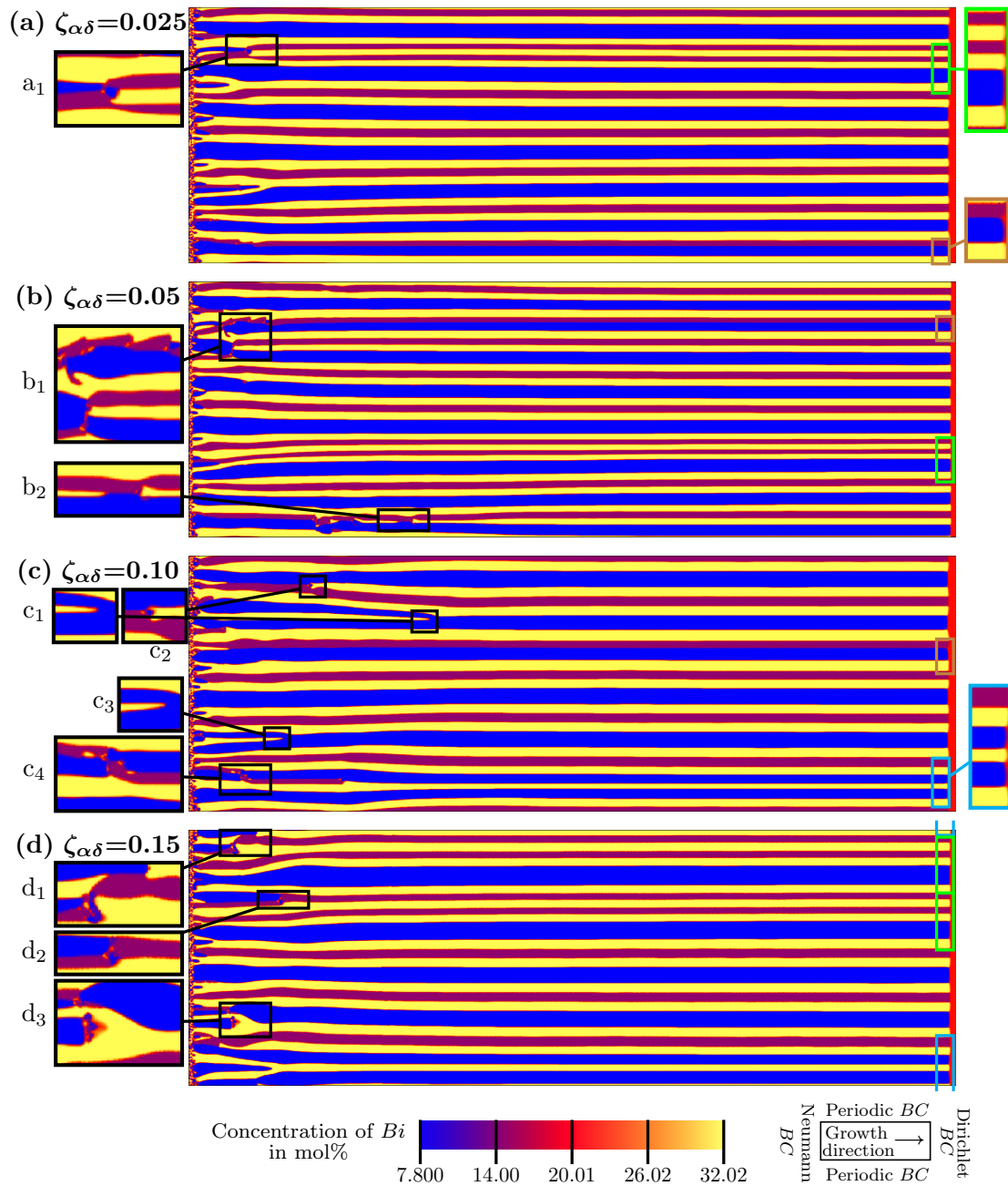


Figure 6.11: Effects of the anisotropic  $\alpha\delta$  interfaces on the pattern formation in the DS simulations of the Bi-In-Sn system.  $\zeta_{\alpha\delta}$  is varied in a range of 0.025 to 0.15 based on the interfacial energy plot of fig. 6.7(b) and  $\zeta_{\alpha\beta} = \zeta_{\beta\delta} = 0$ . Magnified areas: the formed  $[\alpha\beta]_1[\alpha\delta]_2$ ,  $[\alpha\beta]_2[\alpha\delta]_1$  and  $\alpha\beta\delta$  patterns are specified with the green, cyan and brown rectangles, respectively.  $a_1$ :  $\delta$ -lamella branching.  $b_1$ ,  $b_2$ ,  $c_2$ ,  $d_1$ : the  $\alpha$  nucleation between the  $\beta$  and the  $\delta$ .  $c_1$ ,  $c_3$ : the reduction of  $[\alpha\beta]_2[\alpha\delta]_1$  to  $\alpha\beta\alpha\delta$ .  $d_1$ ,  $d_2$ : the  $\alpha$ -to- $\delta$  and the  $\beta$ -to- $\delta$  phase exchanges.  $d_3$ : the sharp  $\beta$  elimination by the  $\alpha$  nucleation.

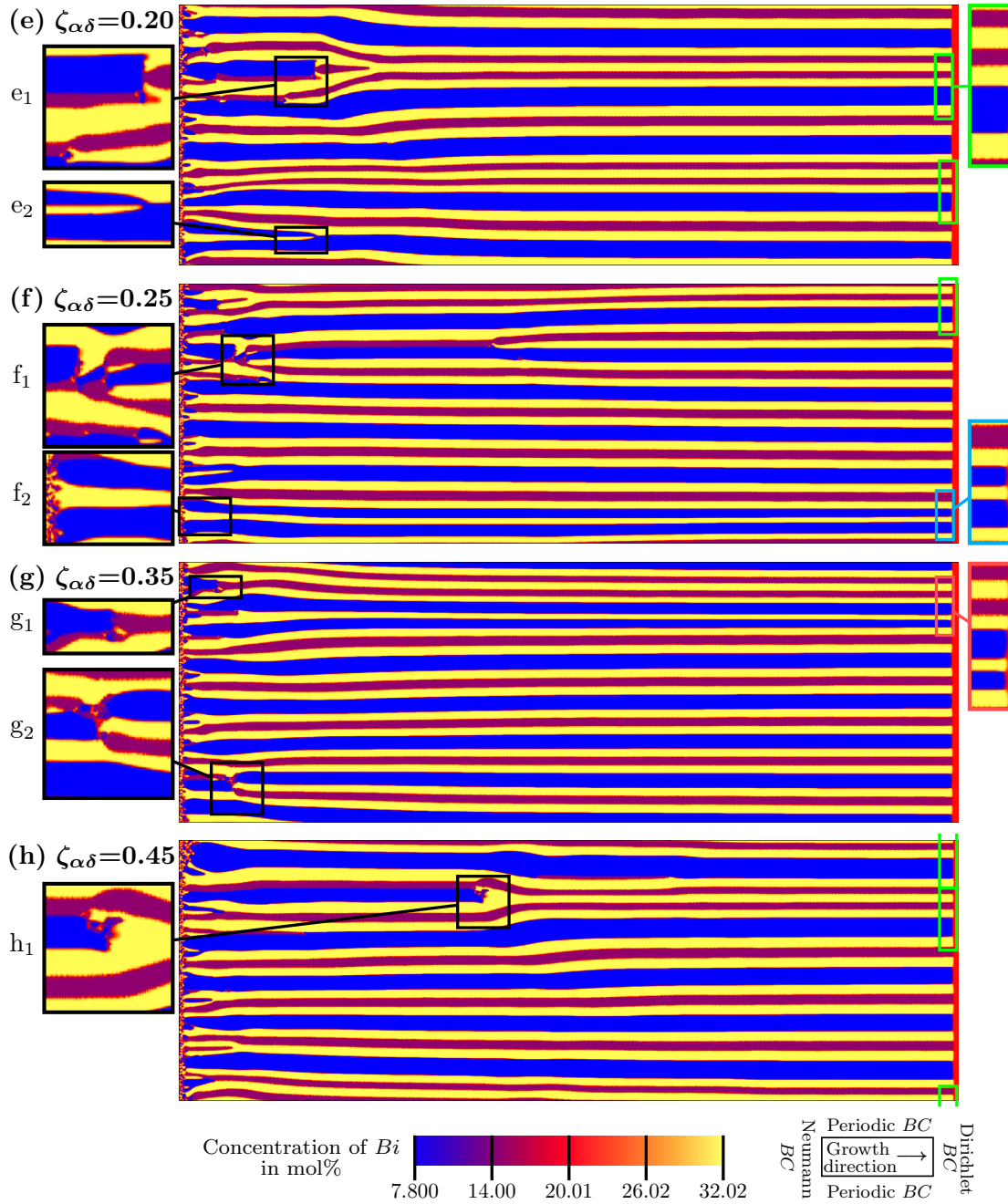


Figure 6.12: Effects of the anisotropic  $\alpha\delta$  interfaces on the pattern formation in the DS simulations of the Bi-In-Sn system.  $\zeta_{\alpha\delta}$  is varied in a range of 0.20 to 0.45 based on the interfacial energy plot of fig. 6.7(b) and  $\zeta_{\alpha\beta} = \zeta_{\beta\delta} = 0$ . Magnified areas: the formed  $[\alpha\beta]_1[\alpha\delta]_2$ ,  $[\alpha\beta]_2[\alpha\delta]_1$  and  $[\alpha\beta]_2[\alpha\delta]_2$  patterns are specified with the green, cyan and red rectangles, respectively.  $e_1$ ,  $f_1$ ,  $g_2$ : the  $\alpha$ -nucleation between the  $\beta$  and the  $\delta$  lamellae.  $e_2$ : reduction of the  $[\alpha\beta]_2[\alpha\delta]$  to the  $[\alpha\beta\alpha\delta]$ .  $f_2$ : the stable  $[\alpha\beta]_2[\alpha\delta]$  pattern from the initial simulation steps.  $g_1$ :  $\beta$ -to- $\delta$  phase exchange.  $e_1$ ,  $h_1$ : the  $\alpha$ -nucleation on the  $\beta$  and the sharp  $\beta$  elimination.

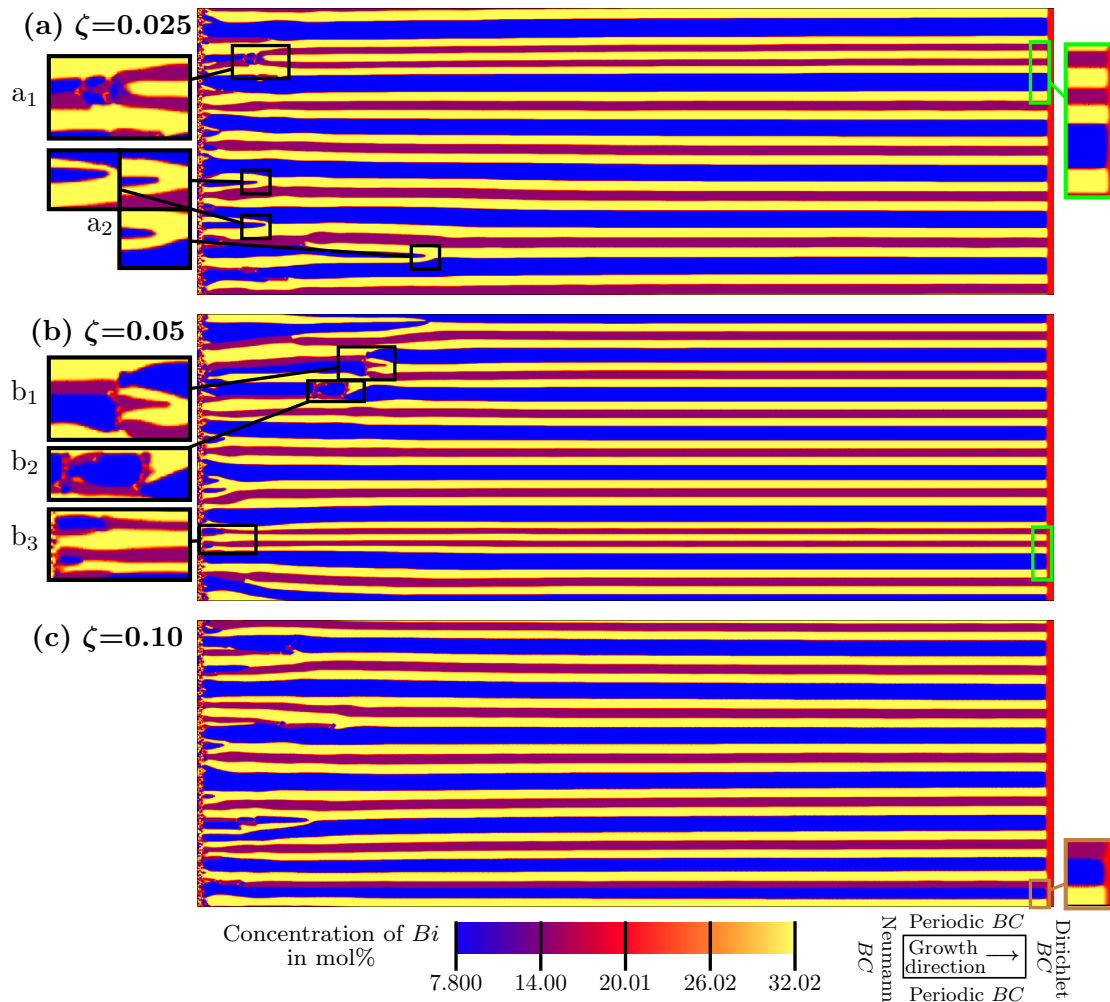


Figure 6.13: Effects of the anisotropic interfaces on the pattern formation in the DS simulations of the Bi-In-Sn system.  $\zeta = \zeta_{\alpha\beta} = \zeta_{\alpha\delta} = \zeta_{\beta\delta}$  is varied in a range of 0.025 to 0.10 based on the interfacial energy plots of fig. 6.7. Magnified areas: the formed  $[\alpha\beta]_1[\alpha\delta]_2$  and  $\alpha\beta\delta$  patterns are specified with the green and brown rectangles, respectively.  $a_1$ :  $\beta \rightarrow \alpha + \delta$ .  $a_2$ : reduction of the  $[\alpha\beta]_2[\alpha\delta]_1$  to the  $\alpha\beta\alpha\delta$ .  $b_1$ :  $\beta\delta \rightarrow \delta\alpha\beta$  phases exchange.  $b_2$ : nucleation of the  $\alpha$  on the  $\beta$  not leading to the complete  $\beta$  elimination.  $b_3$ : the  $\beta$ -to- $\delta$  phase exchange.

Figure 6.14 illustrates the evolved microstructures for the anisotropy strengths of 0.15 and 0.20. In  $d_1$ , the  $\alpha$  phase is nucleated between the  $\beta$  and the  $\delta$  lamellae in two different segments of the simulation domain like the previous observations of this phenomenon. In  $d_2$ , an initially formed  $[\alpha\beta]_2[\alpha\delta]_1$  is reduced to  $\alpha\beta\alpha\delta$  by elimination of the  $\beta$  lamella.  $e_1$  shows the formation of a stable  $\alpha\delta\alpha\delta$  pattern in which one  $\delta$  lamella has grown stably from the beginning of the simulation but the other one is the result of  $\beta$  phase elimination caused by a nucleation-elimination event.

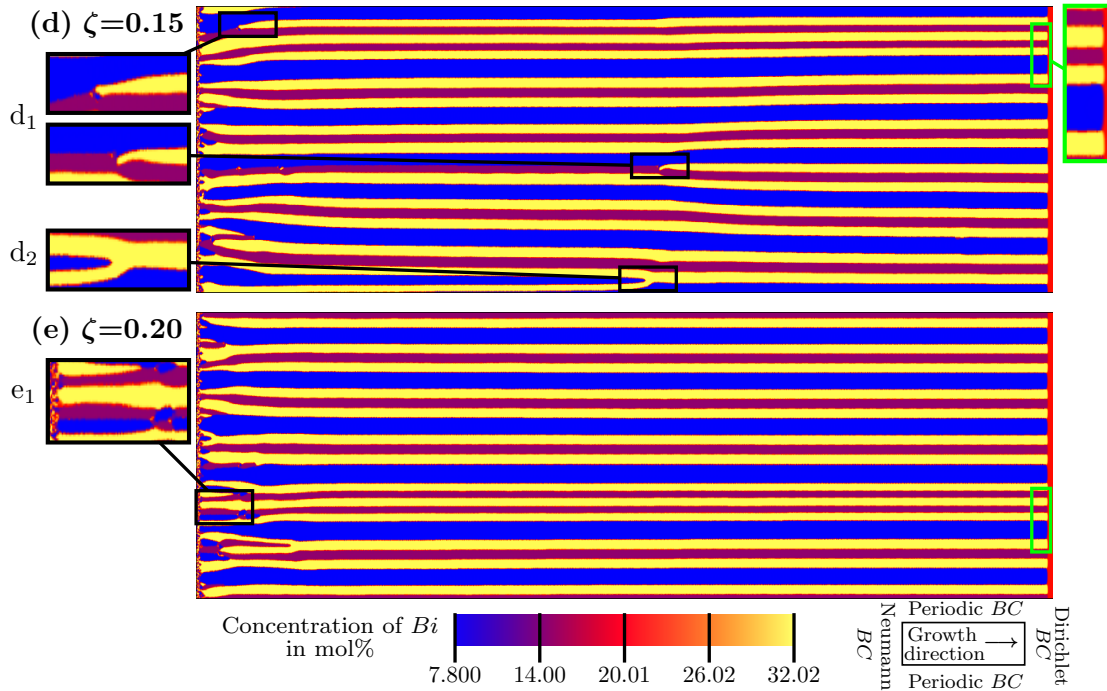


Figure 6.14: Effects of the anisotropic interfaces on the pattern formation in the DS simulations of the Bi-In-Sn system.  $\zeta = \zeta_{\alpha\beta} = \zeta_{\alpha\delta} = \zeta_{\beta\delta}$  is varied in values of 0.15 and 0.20 based on the interfacial energy plots of fig. 6.7. Magnified areas: the formed  $[\alpha\beta]_1[\alpha\delta]_2$  patterns are specified with the green rectangles.  $d_1$ : the  $\alpha$ -nucleation between the  $\beta$  and the  $\delta$  phases.  $d_2$ : the reduction of the  $[\alpha\beta]_2[\alpha\delta]_1$  to the  $\alpha\beta\alpha\delta$  pattern.  $e_1$ : the stable growth of the  $\alpha\delta\alpha\delta$  pattern from the initial simulation steps.

Figure 6.15, shows the evolved patterns in the maximum possible anisotropic configurations. In the simulation of fig. 6.15(a), the equal anisotropy strength value of 0.25 is set to all interfaces, whereas in fig. 6.15(b), the formed pattern in further increase of  $\zeta_{\alpha\delta}$  to 0.45, is depicted. As it can be observed, the final microstructures in both simulations have evolved into  $\alpha\beta\alpha\delta$ -type patterns akin to the behavior of the floating grains. These observations seem to be strange at first glimpse as there is no sign of the expected anisotropic behaviors in the grains. In order to reach an explanation, a summary of all observations is performed in the following. Figure 6.16 is such a succinct elucidation.

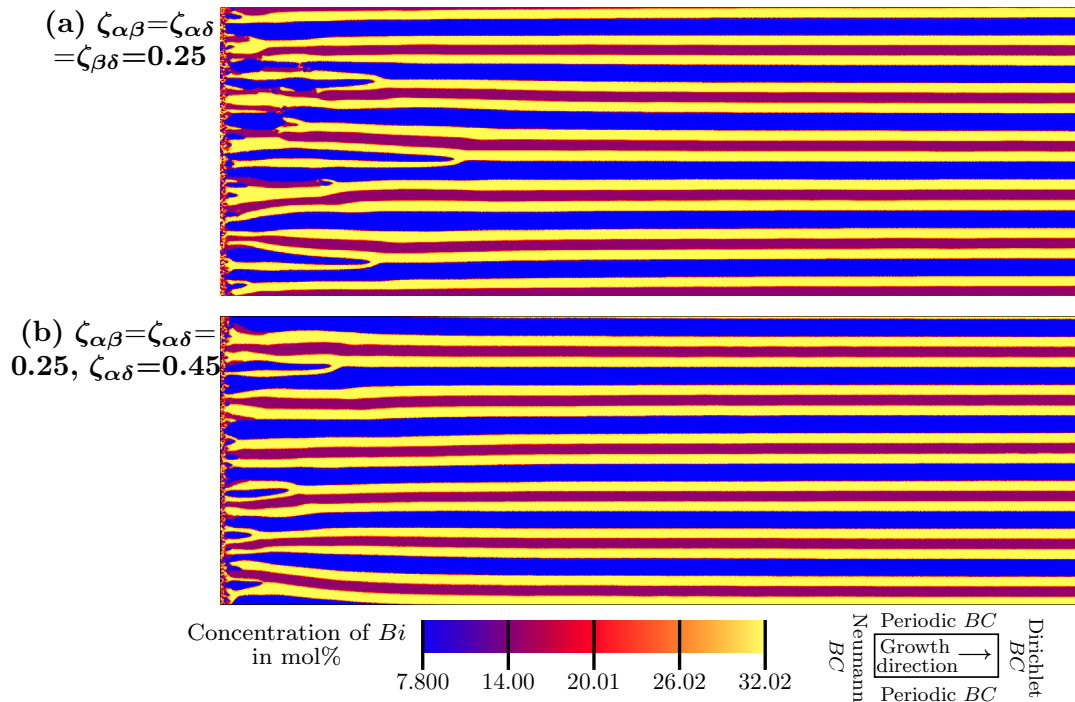


Figure 6.15: The evolved patterns in the DS simulations of the Bi-In-Sn system with the highest possible anisotropies in the interfaces.

Sub-figure 6.16(a) delineates the results of anisotropic  $\alpha\beta$  interfaces, whereas sub-figure 6.16(b) is dedicated to the anisotropic  $\alpha\delta$  interface results. 6.16(c) summarizes the results of figs. 6.13 to 6.15, which belong to the all-anisotropic-interface cases. In each configuration, the resultant  $\alpha\beta\alpha\delta$ ,  $\beta\alpha\delta$ ,  $[\alpha\beta]_2[\alpha\delta]_1$ ,  $[\alpha\beta]_1[\alpha\delta]_2$ ,  $[\alpha\beta]_2[\alpha\delta]_2$  and  $\alpha\beta\delta$  patterns are shown corresponding to the colored boxes of the previous pictures with white, pink, cyan, green, red and brown rectangles, respectively. As can be noticed,  $[\alpha\beta]_1[\alpha\delta]_2$  patterns have commonly evolved in all three configurations. The  $\beta\alpha\delta$  is observed just once when  $\alpha\beta$  interfaces are modeled anisotropically. In contrast,  $[\alpha\beta]_2[\alpha\delta]_1$  patterns are evolved only in anisotropic modeling of the  $\alpha\delta$  interfaces. The  $\alpha\beta\delta$  patterns are evolved when anisotropy is active in  $\alpha\delta$  or  $\alpha\delta$  together with all other interfaces.  $[\alpha\beta]_2[\alpha\delta]_2$  superstructures are acquired in both anisotropic  $\alpha\beta$  and  $\alpha\delta$  configurations, but in  $\alpha\beta$  at a lower anisotropy strength of 0.10.

The general behavior of the patterns in sub-figure 6.16(c), is more similar to sub-figure 6.16(a) which can be considered as a sign of the predominant role of the  $\alpha\beta$  anisotropy compared to the  $\alpha\delta$  in the microstructure evolution. In order to reach an explanation of the nature of the ongoing mechanisms, a schematic illustration is given in fig. 6.17. If we postulate the effect of the anisotropic  $mn$ -interface ( $m, n \in \{\alpha, \beta, \delta\}$ ) as the possible eliminations of  $m$  and/or  $n$  lamellae, the evolved patterns in different

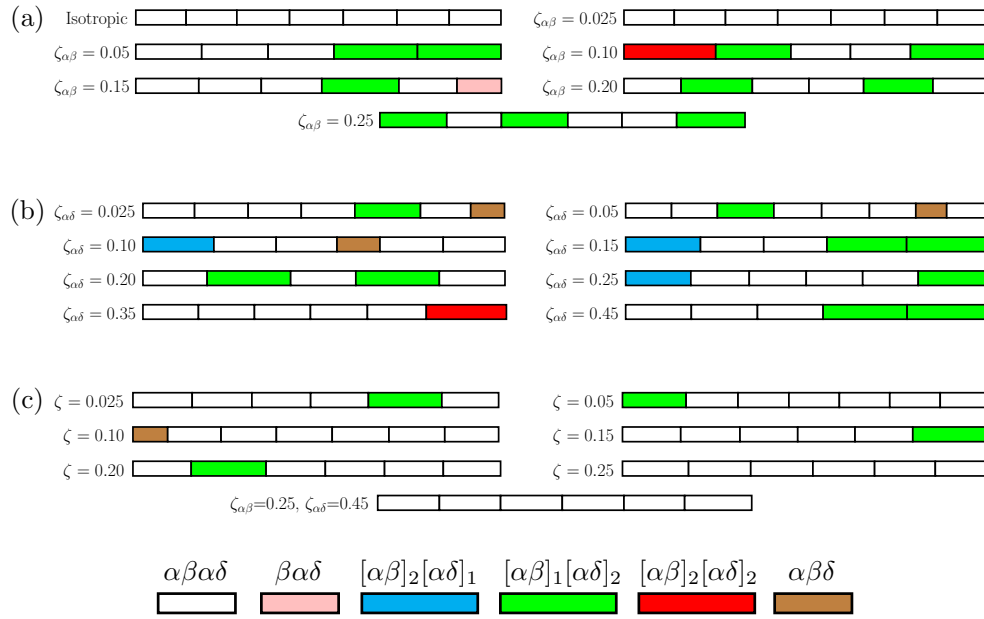


Figure 6.16: Summary of the formed patterns in different anisotropic configurations in the DS studies of the Bi-In-Sn eutectic system. (a): anisotropy only in  $\alpha\beta$  interfaces (based on figs. 6.8 to 6.10). (b): anisotropy only in  $\alpha\delta$  interfaces (based on figs. 6.11 and 6.12). (c): anisotropy in all  $\alpha\beta$ ,  $\alpha\delta$  and  $\beta\delta$  interfaces (based on figs. 6.13 to 6.15).

configurations can be in the forms of fig. 6.17. In sub-figure 6.17(a), three hypothetical neighboring  $\alpha\beta\alpha\delta$  stackings are shown. For the case of  $\alpha\beta$ -anisotropy, if the  $\beta$  lamella in the middle stacking is eliminated,  $[\alpha\beta]_1[\alpha\delta]_2$  pattern, and if the  $\alpha$  lamella in the middle stacking is eliminated, the  $\beta\alpha\delta$  pattern results. These patterns are illustrated with the same coloring style as fig. 6.16, and as it can be noted, there are good correlations with the evolved patterns in the simulation studies. For  $\alpha\delta$  anisotropy, the same procedure results in the formations of  $[\alpha\beta]_2[\alpha\delta]_1$  and  $\alpha\beta\delta$  patterns. These patterns are shown with cyan and brown rectangles in fig. 6.16(b). It should be mentioned here that, the made lamella-elimination hypotheses do not necessarily mean the formation of the regular  $\alpha\beta\alpha\delta$ -type patterns initially, and the declared eliminations in the later steps of the microstructure evolutions. Although this can happen either (like  $d_2$  in fig. 6.14), in many cases, the superstructures form from the initial simulation steps stably. I.e. the nature of the locked grains is to eliminate (or not form at all) some lamellae in the stacking sequences which would be formed in  $\alpha\beta\alpha\delta$  motifs if the interfacial energies were modeled isotropically.

Next point in comparison of fig. 6.17(a) with fig. 6.16 is the formation of  $[\alpha\beta]_1[\alpha\delta]_2$  as the most repeated pattern in all anisotropically simulated configurations. If we assume  $\alpha\beta$  interface anisotropy as the responsible factor to form this pattern, the dominance

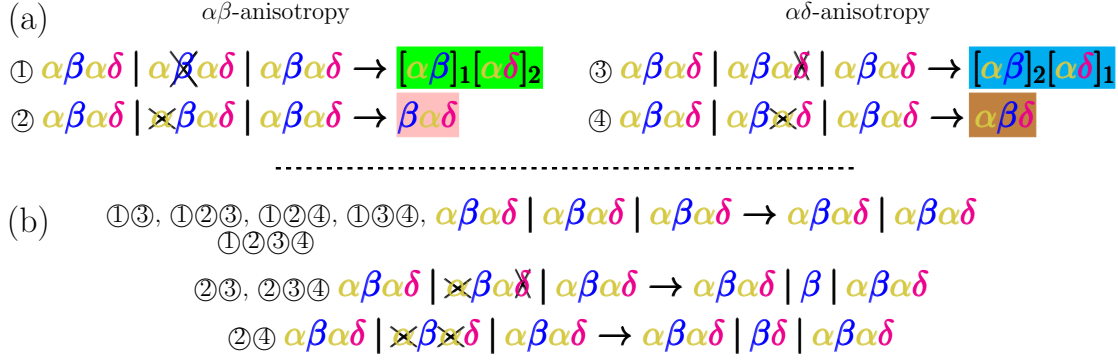


Figure 6.17: (a): schematic illustration of the phase eliminations and the formed patterns as the effects of the anisotropic interfaces. (b): possible resultant patterns in the different combinations of the cases in (a).

of this anisotropy type in the evolved microstructures is shown. Even when we have anisotropy in both  $\alpha\beta$  and  $\alpha\delta$  interfaces, the system behaves more likely towards to the  $\alpha\beta$ -anisotropic configuration. In addition, considering the presented ①, ②, ③ and ④ configurations in fig. 6.17(a), eleven different combinations of these configurations can be obtained for the cases in which the anisotropy is active in both  $\alpha\beta$  and  $\alpha\delta$  interfaces. Among these combinations, three new patterns can theoretically be achieved which are shown in fig. 6.17(b). In this notation,  $\textcircled{i}\textcircled{j} \dots$  stands for the combination of  $i, j \dots$  configurations in fig. 6.17(a). It can be said as the first conclusion that, when the system has anisotropic behavior in all of the solid-solid interfaces,  $\alpha\beta\alpha\delta$  stacking sequences can be formed similar to the behavior of the floating grains, but the lamellar spacings will consequently increase. The declared spacing increase is due to the reduction of the three stacking units to two in the assumed schematic illustration. This can be the probable reason for the evolved patterns in fig. 6.15 in which six  $\alpha\beta\alpha\delta$ -motifs are formed instead of the initially seen seven motifs in the isotropic system (fig. 6.8(a)).

Figure 6.17 concludes in the possible formations of single  $\beta$  lamellae or  $\beta\delta$  units either, but their formation probabilities are not high and they are not observed in the performed simulations. In general, the combination of  $\beta$  and  $\delta$  phases next to each other is rarely observed in the simulations and nor in the experiments. Therefore, it can be concluded that such combinations of the phases are not beneficial for the growth of the microstructures. In the next section, a summary of the achieved *DS* simulation results is presented discussing the necessity of further *RDS* studies.

### 6.2.3 Summary and conclusions

In this section, the directional solidification studies of the Bi-In-Sn ternary eutectic system are performed based on the obtained thermodynamic data from the CALPHAD database in section 5.3. In order to validate the achieved results, a Jackson-Hunt analysis is performed and comparisons with the available experimental data in the literature are done. The validated configuration serves as the basis of the simulations in larger domains with Voronoi tessellations of the initial solid phases. These simulations are benefited to study the effects of the anisotropic interfaces on the pattern formations. In the course of this endeavor, initially, one simulation is performed in which the interfaces are modeled isotropically. The evolved microstructure has the expected regular  $\alpha\beta\alpha\delta$ -type pattern. In the next step, anisotropy in the solid-solid interfacial energies is activated. This time, in the evolved patterns, the  $\alpha\beta\delta$ ,  $\beta\alpha\delta$  or the  $[\alpha\beta]_a[\alpha\delta]_b$  superstructures are formed. A summary of the evolved patterns in different anisotropic configurations is shown in fig. 6.16 and a schematic illustration for the ongoing mechanisms is shown in fig. 6.17. Although the mentioned illustration has good accordance with the observed patterns in *DS* simulations, further pieces of evidence for such a general conclusion seem to be vital. Hence, rotating directional solidification studies are performed in the next section and it is striven to gain new insights on the governing mechanisms of the microstructure evolutions in this system.

## 6.3 *RDS* simulation studies of Bi-In-Sn system

The introduced setup in section 3.2 serves as the basis of the *RDS* simulations in this section. As illustrated in fig. 3.4, the simulation domain is formed by a square which is confined to a circle by the barrier region. The square size is  $965 \times 965$  cells equal to  $301.8 \times 301.8 \mu\text{m}$ . An initial set of thirteen lamellae, each with the  $\alpha\beta\alpha\delta$  stacking sequences are filled in the bottom half of the simulation domain which are exposed to the low temperatures with the minimum value of  $T_{min}$  at  $y = 0$ . The simulated lamellae set in the considered domain size is small compared to the experimental works as a result of lack of the computational resources in the current study. The spacing of each stacking sequence is  $23.4 \mu\text{m}$  which is set based on the utilized  $\lambda$  values in the *DS* studies of section 6.2.1. Five of the set  $\alpha\beta\alpha\delta$  motifs build the solidification and five others build the melting fronts, respectively. This is due to the chosen value of 4.55 for the outer-to-inner radii proportion  $r_o/r_i$ , which has a similar amount as shown in Fig. 5 of [90]. The inner barrier which covers the rotation center  $\Omega$  is placed on the three remaining lamellar sets. As a consequence of zero growth velocity in the rotation center (see section 3.2), a single-phase formation in the center-vicinity areas is reported in the experimental works [90, 144, 145]. The barrier

in the center is modeled to prevent the formation of such a single-phase region which could affect the overall phase fractions and lead to growth-condition instabilities. This influence is more pronounced in the small domain size in the investigated simulations.

As mentioned in section 3.2, a one-cell thick layer of one of the solid phases has to be placed around the barrier sections in the simulation domain. Phase  $\beta$  is chosen as an exemplary phase for this purpose to establish a stable growth in the barrier boundaries. It is worth mentioning here that, this solid-phase placement can affect the evolved phase fractions and the achieved phase fractions in the solidified phases, consequently. As the purpose of the current work is a qualitative study of the experimentally observed patterns in the floating, as well as the locked grains instead of reproducing them quantitatively, this effect is neglected in the following. The evolved patterns in near-barrier lamellae are not taken into account in order to minimize the boundary impact on the made conclusions of the study.

The angular velocity of  $\omega = 0.309 \text{ }^\circ\text{s}^{-1}$ , results in adjustment of the investigated velocities  $v_1$  to  $v_3$  in the *DS* studies, in three different segments of the *RDS* disk. These segments are toward the centers of the three middle lamellae in the simulation domain in both solidification and melting fronts. Hence, in the upcoming sections, the *RDS* process is simulated with the mentioned constant value for the  $\omega$ . Due to the significant effect of the interfacial energy anisotropy on the pattern formation in the performed *DS* simulations, the *RDS* studies are conducted in two parts: Initially, a single simulation is performed with the isotropic interfacial energies in the solid-solid phase boundaries which is continued for two full rotations, i.e.  $4\pi$  rad rotation (section 6.3.1). The later  $2\pi$  rad rotation is completed to test the system capability in the development of the solidification and melting fronts and to test the proper formation of the expected circular trajectories. Then, the anisotropy in the interfacial energies is activated in the  $\alpha\beta$  and/or  $\alpha\delta$  and/or  $\beta\delta$  interfaces in section 6.3.2. The *RDS* simulations are conducted using 192 CPUs in the HPC cluster of the IAM-MMS. The performance of each  $2\pi$  rad rotation took an approximated computational time of four weeks. For the simulations with  $4\pi$  rad rotations, the evolved values of the lamellar spacings after each full rotation are measured and compared with each other for convergence checking. The additional simulation parameters in the *RDS* studies to the *DS* ones, have been summarized in Table B.2. As indicated previously in section 3.2, the temperature formulation has to satisfy the steady-state heat equation  $\nabla^2 T = 0$  at the different grid cells of the simulation domain. Based on the utilized values for the  $T_m$ ,  $A_0$  and  $G^{RDS}$ , it can easily be checked that the average deviation from the solution of the mentioned equation is equal to  $2.5 \cdot 10^{-25}$ . This deviation is neglected in the upcoming studies.

### 6.3.1 Isotropic interfacial energies

The obtained simulation result for the modeled system with the isotropic interfacial energies is shown in fig. 6.18 at different simulation times. At any time, the left sub-figure, illustrates the concentration of Bi in the involved phases, whereas the right sub-figure depicts the temperature field, respectively. The orange color represents the high-temperature area while the blue color represents the low temperatures in the temperature field. Based on this coloring, the expected near-uniform temperature distributions in the melt and solid-phase zones are resulted as discussed in the temperature formulation of eq. (3.4). These colors indicate a low-temperature gradient of  $0.786 \text{ K mm}^{-1}$  in the mentioned areas. The strong color transition from blue to orange in the middle of the simulation domain describes a multiple times higher gradient with a maximum value of  $240 \text{ K mm}^{-1}$  in the rotation center  $\Omega$ . In the concentration fields, the coloring style is same as the style set in section 5.3 for the Gibbs energies modeling and in sections 6.2.1 and 6.2.2 for the *DS* simulation results' visualization. Figure 6.18(a) shows the filling at *time* = 0, in which the straight lamellae of the initially filled solid phases lie beneath the liquid phase. Considering the forthcoming melting and growth phenomena, these solid phases will melt due to the temperature increase in the rotation direction of the temperature field. The solid-liquid interface is the only efficient part of the filling in the pattern formation. Hence, the straight trajectories are filled instead of the curved solid-solid interfaces for the sake of simplicity. As time pass, the other sub-figures illustrate the rotations of the temperature fields, as well as the evolved patterns respectively. The achieved good correlations between the temperature field and the solidification/melting fronts indicate the accuracy of the modeled temperature profile in the representation of the rotational effect. Furthermore, the resultant concentrations of Bi and In in the solidified phases are in good accordance with the CALPHAD database as plotted in fig. 5.6 of section 5.3. This accordance is retained throughout the whole simulation time.

After the approximate rotational angle of  $120^\circ$ , oscillations of the boundaries in the solidified phases come to exist as can be noticed in fig. 6.18(c). This effect has previously been observed in the *DS* studies of the system as illustrated in fig. 6.5, which indicates the transition state from unsteady to steady-state condition. However, in contrast to the *DS* case wherein the oscillations happen at the initial simulation time, in the *RDS* simulations they happen after passing a certain growth distance.

Figure 6.19(a), shows the summation of all-time results in one frame, depicting the full rotation with the circular trajectories of the solidified phases.  $\alpha\beta\alpha\delta$  stacking sequences of the three middle lamellae from the initially filled five lamellar sets has remained intact. The solidification velocities in the centers of these units are:  $v_1^{2\pi} = 0.394 \text{ } \mu\text{m s}^{-1}$ ,  $v_2^{2\pi} = 0.541 \text{ } \mu\text{m s}^{-1}$ ,  $v_3^{2\pi} = 0.678 \text{ } \mu\text{m s}^{-1}$ . The *DS* processes with these values, have previously

been studied in section 6.2.1 and the Jackson-Hunt plots have been shown in fig. 6.5. The lamellar spacing adjustments happen as a consequence of this radial velocity variation and the microstructure rearrangement takes place resulting in the 5phase eliminations. These effects are mainly observed in the near barrier area which is in similarity to the near boundary observations in the experiments [89, 90]. The phase eliminations, cause disruptions in the initially filled  $\alpha\beta\alpha\delta$  stacking sequences. At the approximate rotational angle of  $120^\circ$ , a  $\delta$  lamella is overgrown near the outer barrier, which leads to the formerly observed oscillations of the solidified phase boundaries in fig. 6.18(c). The thin  $\beta$  layer growths in the near barrier regions result in a stable solidification front, as well as a better establishment of the anticipated  $\alpha\beta\alpha\delta$  repeat units. This is due to the balance of the central lamellae adjustments caused by these thin layers.

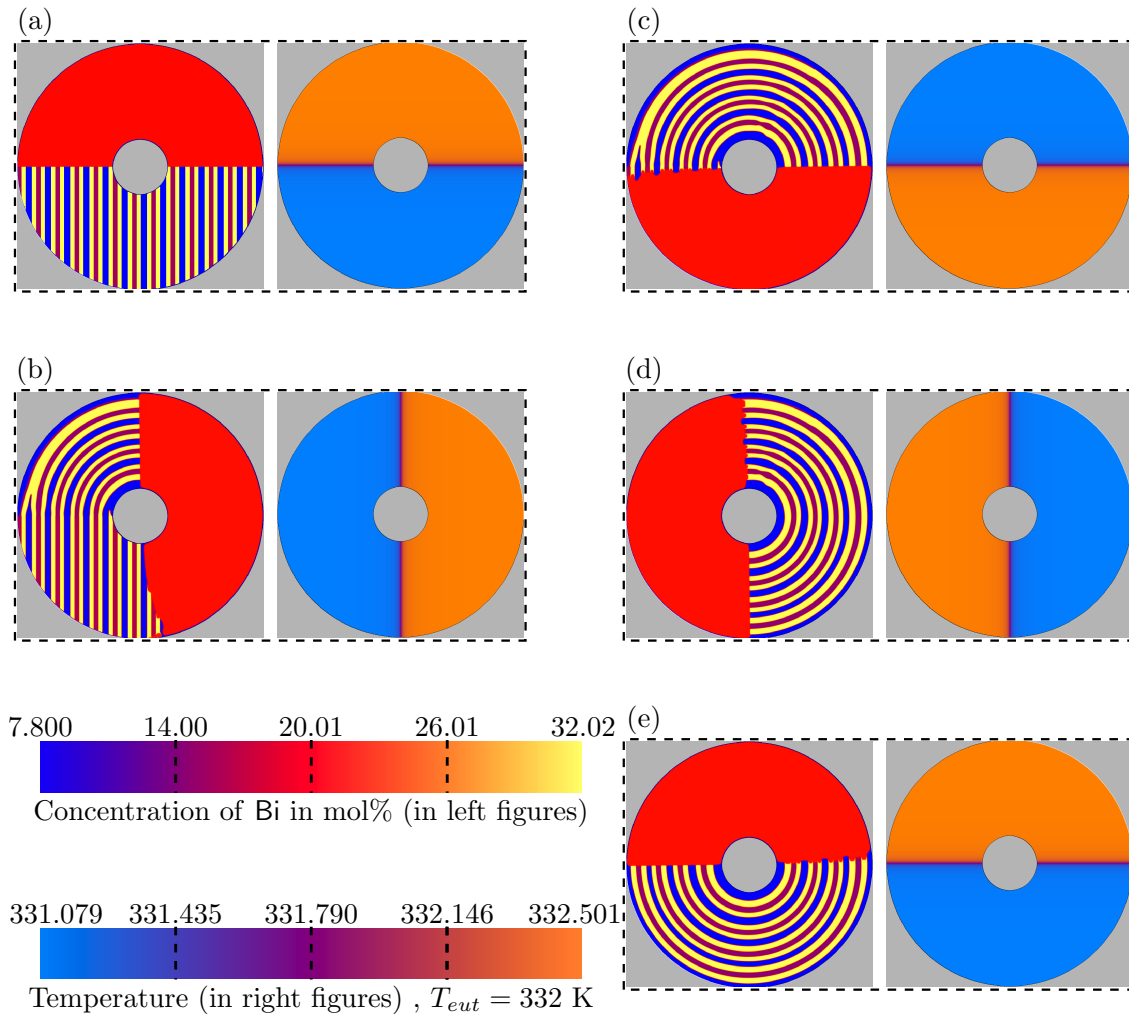


Figure 6.18: RDS simulation results for the isotropic system at (a):  $t = 0$ , (b):  $t = 24.2e6 \cdot dt$ , (c):  $t = 48.4e6 \cdot dt$ , (d):  $t = 72.6e6 \cdot dt$ , (e):  $t = 96.8e6 \cdot dt$ . At any time, the left figure illustrates the concentration field ( $c_{Bi}$ ), whereas the right figure is the temperature field. Domain size =  $301.8 \times 301.8 \mu\text{m}$ ,  $\omega = 0.309 \text{ }^\circ\text{s}^{-1}$ ,  $r_i = 33.15 \mu\text{m}$ ,  $r_o = 150.9 \mu\text{m}$  based on [91].

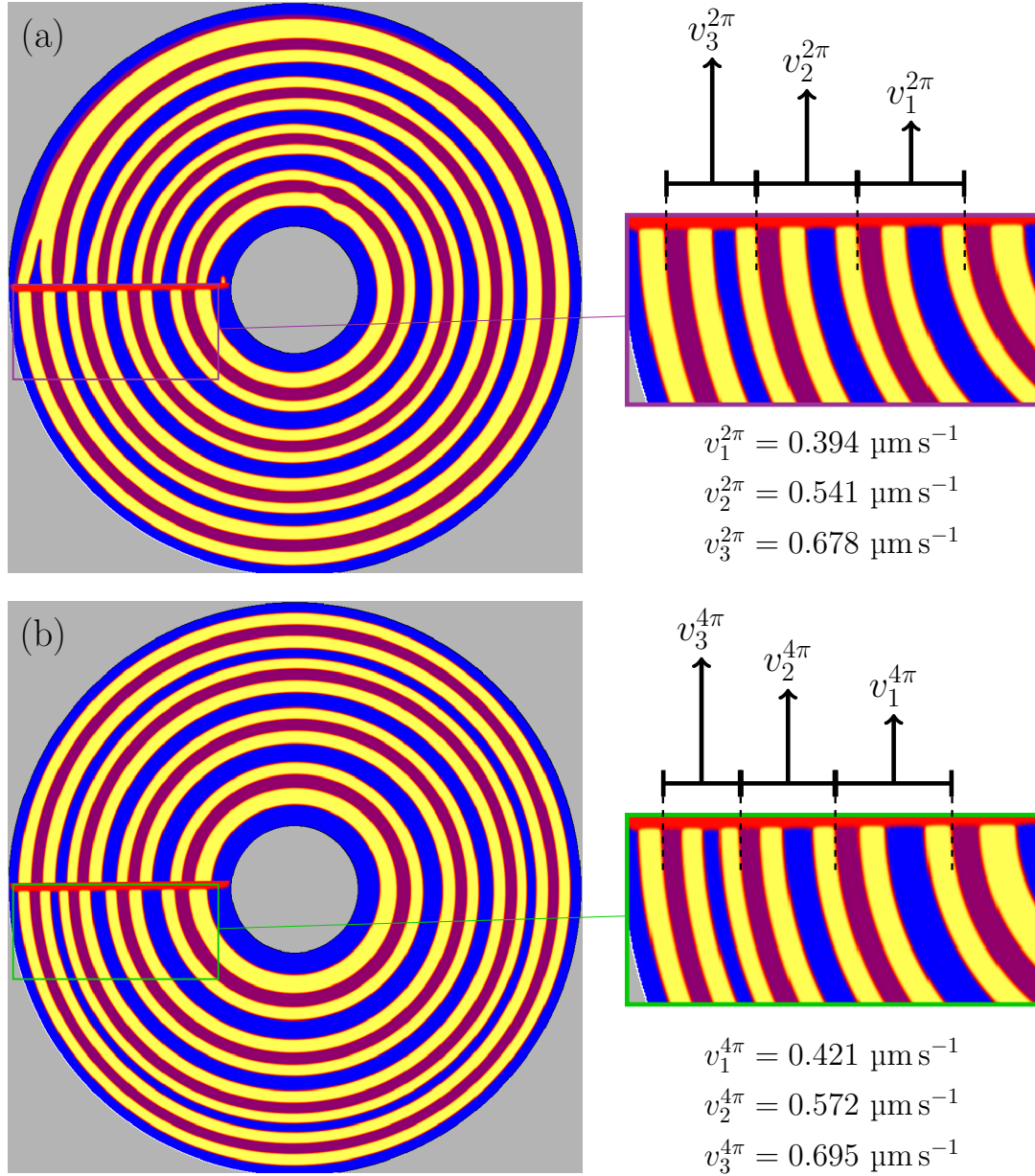


Figure 6.19: (a): all-time results of fig. 6.18 after the  $2\pi$  rad rotation in one frame, as well as the magnified areas of the middle lamellae showing the velocities  $v_{1,2,3}^{2\pi}$  in their centers. (b): the same configuration after a rotational angle of  $2\pi$  rad based on [91].

Figure 6.19(b), shows the simulation result at a rotational angle of  $4\pi$  radian. As it can be observed, the stable growth continues for this rotation and no further instabilities like the phase eliminations or the oscillations in the phase boundaries are noticed. Because of the set coincidence in the disk rotation center  $\Omega$  and the temperature field rotation center, the anticipated circular trajectories in the solidified phase boundaries are achieved in the simulations. This is in contrast with the resulted micrographs in the experimental work of the Mohagheghi et al. [90], as in their study misalignment between the two

centers comes to exist. Additionally, due to the assumption of the isotropic interfacial energies in this simulation, tilting of the solidified phase boundaries with respect to the imposed temperature gradient does not arise. Hence, a good agreement with the reported properties of the floating grains in [89, 90] can be concluded. In the magnified sections of fig. 6.19, the developed growth velocities in the evolved unit centers have been reported. The discrepancies of  $|\frac{v_1^{4\pi}}{v_1^{2\pi}}| = 6.5\%$ ,  $|\frac{v_2^{4\pi}}{v_2^{2\pi}}| = 5.7\%$ ,  $|\frac{v_3^{4\pi}}{v_3^{2\pi}}| = 2.5\%$  between the two rotations come to exist, respectively.

### 6.3.2 Anisotropic interfacial energies

Based on the achieved validation of the implemented *RDS* setup in section 6.3.1 for the isotropic system, the effects of the anisotropy of the interfacial energies on the evolved patterns are investigated in this section. As a start point, one simulation is performed with equal anisotropies in all solid phase boundaries with the strength of  $\zeta = 0.15$  (see the interfacial energy plots in fig. 6.7). The achieved microstructures after the rotational angles of  $2\pi$  rad and  $4\pi$  rad are shown in fig. 6.20. It can be noticed in the figure that, the  $\alpha\beta$  anisotropy (yellow to blue) has a more pronounced role in the tilting of the solidified phases, compared to the  $\alpha\delta$  (yellow to magenta) anisotropy. In fig. 6.20(b), the deviations in the phase borders, between the isotropic and anisotropic simulations are illustrated. The phase boundaries in the isotropic case are shown by the solid black lines, whereas the anisotropic result is illustrated colorfully. The shown segments belong to the middle lamella after  $\theta = \pi/2$  rad rotation in both simulations. In the rotational angle of  $\theta = \pi/4$  rad, the brown and cyan lines are depicted showing the transitions of  $\alpha\delta$  and  $\alpha\beta$  boundaries towards the rotational center, respectively. The value of 1.45 is resulted in the proportion of the cyan to brown line lengths indicating more sensitivity of the evolved pattern on the  $\alpha\beta$  anisotropy. This is in accordance with the experimental perceptions of Mohagheghi et al. [90] in the formation of the crystallographically-locked grains, as discussed in section 4.2. Likewise the isotropic simulation of fig. 6.19, the lamellae eliminations occur in the initial steps of the anisotropic simulation and the oscillations of the solid phase boundaries exist in the approximate rotational angle of  $120^\circ$ . Meanwhile, in the second rotation, the stable growth is continued and no further unexpected disturbances in the morphology arise. In order to compare the results of *DS* and *RDS* simulations with the experimentally reported values in [36], the velocity-spacing plot is illustrated in fig. 6.21. The dashed cyan line in fig. 6.21 connects the average values of the experimentally measured lamellar spacings in the solidification velocities  $0.251 \mu\text{m s}^{-1}$ ,  $0.5 \mu\text{m s}^{-1}$  and  $1.0 \mu\text{m s}^{-1}$ , respectively [36]. The highlighted area around this line is constructed based on the maximum and minimum values of the evolved spacings in the indicated velocities. The circles, squares and pentagons denote the results of *DS*, isotropic

*RDS* and anisotropic *RDS* simulations, respectively. The unfilled marks belong to the intermediate simulation results in half of the final times. For example, in case of *DS*, unfilled circles denote the achieved  $\lambda_{JH}^{sim}$  in the time of  $17.5e6 \times dt$ , and the filled circles denote  $t = 35e6 \times dt$ . The achieved good correlations is a sign to conclude the convergence of the *DS* simulations to the steady states. In the *RDS* sims, the unfilled marks stand for the  $2\pi$  rad rotations, whereas the filled marks stand for the  $4\pi$  rad rotations. The results of *DS* sims are generally located in the highlighted cyan area indicating the achieved good correlations between the simulations and the experiments. For the *RDS*<sup>iso</sup>, the anticipated Jackson-Hunt-type behavior between the growth velocities and the resultant lamellar spacings is realized which is more pronounced in the  $4\pi$  rad rotation. In contrast, for the *RDS*<sup>aniso</sup> simulation, this behavior is only observed after  $4\pi$  rad rotation indicating the necessity of more growth distance to reach the steady-state condition as a result of the anisotropically modeled interfacial energies. It can generally be concluded from fig. 6.21 that, in the *DS* simulations of the Bi-In-Sn ternary eutectic system, qualitative and quantitative agreements between the simulations and the experiments, as well as the theoretic Jackson-Hunt validation are achieved. In the *RDS* simulations, the Jackson-Hunt-type behavior is observed in the simulations and a qualitative agreement with the experimental *DS* results is attained.

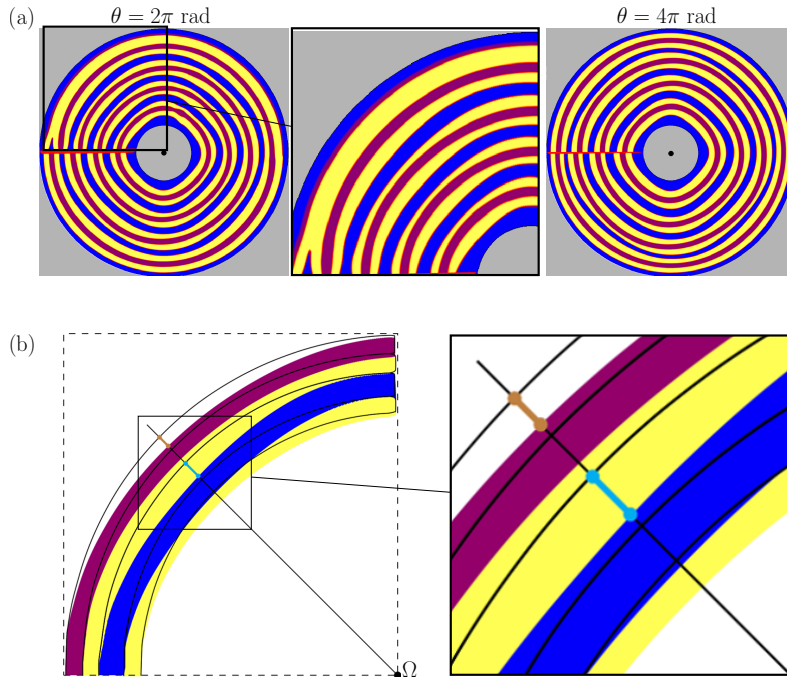


Figure 6.20: (a): tilted growth of the solidified phases as a result of the anisotropic interfacial energies ( $\zeta_{\alpha\beta} = \zeta_{\alpha\delta} = \zeta_{\beta\delta} = 0.15$ ) after  $2\pi$  rad and  $4\pi$  rad rotations. (b): the comparison between the isotropic simulation in fig. 6.19 (black lines) and the current anisotropic simulation (colored) after the  $\pi/4$  rad rotation. The red line length =  $3.83 \mu\text{m}$  and the green line length =  $5.56 \mu\text{m}$  indicating the dominance of the  $\zeta_{\alpha\beta}$  in the pattern formation [91].

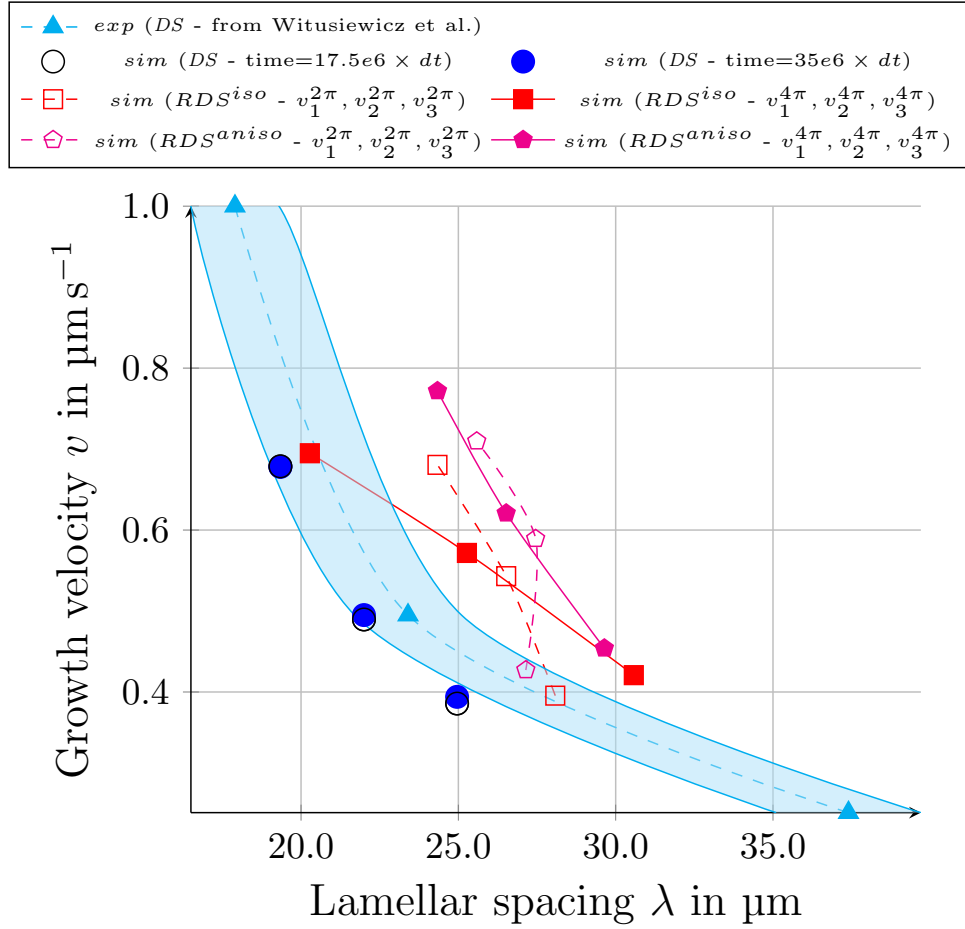


Figure 6.21: The comparison of the experimentally reported lamellar spacings in the work of Witusiewicz et al. [36] with the obtained  $\lambda_{JH}^{sim}$  in the different solidification velocities as reported in fig. 6.5 in section 6.2.1.  $v_i^{n\pi}$  indicates the velocity in the middle of  $i$ -th lamellae (see fig. 6.19) after the  $n\pi$  rad rotation. *iso*: isotropic simulation, *aniso*: anisotropic simulation [91].

As the next step in the current study, a systematic investigation of the anisotropy effects on the constructed patterns is intended. By considering sub-figure 6.20(b), studying the variations in the lamellae boundary radii can be a promising method for this purpose. In the course of the endeavor, which lamella to choose for this investigation will be the next question. Apparently, in the *RDS* simulation domain, the lamella with the approximate radius value equal to  $r = (r_i + r_o)/2$  has the least effects from the inner and the outer barrier phases, respectively. In the isotropic simulation, which is shown in fig. 6.22(a), an  $\alpha$  lamella is hatched which has the nearest radius amount to the indicated value. In addition, it has interfaces with both  $\beta$  and  $\delta$  phases, whose evolved profiles can be studied, subsequently.

In fig. 6.22(b), the variations of the  $\alpha\beta$  and  $\alpha\delta$  boundary radii with respect to the rotational angles  $\theta$ , are plotted. Based on these plots, there are almost linear dependencies between the evolved  $r$  and  $\theta$  values. In  $90^\circ \leq \theta \leq 135^\circ$ , the previously mentioned

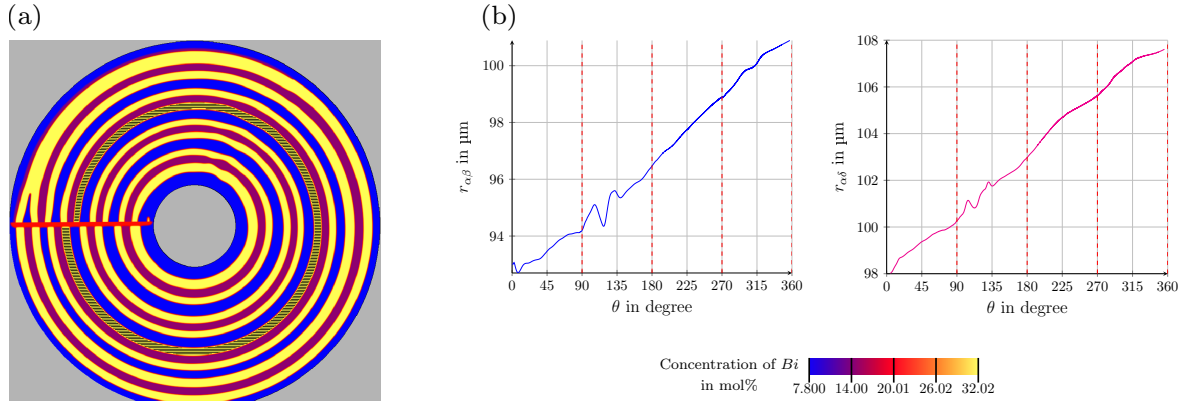


Figure 6.22: (a): the isotropic simulation result of fig. 6.19 at the rotational angle  $\theta = 2\pi$  rad. The hatched  $\alpha$  lamella has the radius of  $r \simeq (r_i + r_o)/2$  and is used to measure the interface radius values. (b): the radius variations of the  $\alpha\beta$  and  $\alpha\delta$  interfaces with respect to the rotational angle  $\theta$ .

oscillations in the solidified phase boundaries show up either in the depicted plots. The linear increases in the  $r_{\alpha\beta}$  and  $r_{\alpha\delta}$  values (*max* 10% in  $\theta = 360^\circ$ ), indicate the transition of the selected  $\alpha$  lamella shape from the circular form to the spiral form in this rotation. Such a transition in the simulation is much less than the experiments [90] due to the more precise alignments between the centers of the disks and the exposed temperature gradients, as discussed previously. The achieved uniformities in the  $r - \theta$  profiles indicate the straight growth of the solidified phases without the presence of any tilting in the phase boundaries. In order to study this effect, as well as the general effects of the anisotropy on the pattern formation, in procedures analogous to the *DS* studies, the interfacial anisotropies are varied systematically and the new simulations are conducted for each configuration. The variations are performed based on the plots of fig. 6.7 in section 6.2.2. As a start point, the simulation results for the exemplary anisotropy values of  $\zeta_{\alpha\beta} = 0.1$  and  $\zeta_{\alpha\delta} = 0.15$  are shown in fig. 6.23. In the sub-figure 6.23(a), the  $\alpha\delta$  and  $\beta\delta$  interfaces, and in sub-figure 6.23(b), the  $\alpha\beta$  and  $\beta\delta$  interfaces are modeled isotropically. The investigated  $\alpha$  lamellae whose  $\alpha\beta$  and  $\alpha\delta$  interface radii are measured are specified with the hatchings like the previous cases. In the attained plots, the radius profiles are waved in contrast to the previously observed monotonic behaviors in the isotropic system. The wavelength of  $90^\circ$  can be defined in these configurations for which the generally evolved shapes of the curves are iterating. In the iterating segments which are specified by the red dashed lines in the plots, the initial radii decreases are observed until reaching local minimums after the approximate rotational angles of  $\theta = 45^\circ$ . Then, the radii increase and reach a local maximum subsequently. The general shape of the periodic behavior does not change dramatically from the observed pattern in the first period ( $0^\circ \leq \theta \leq 90^\circ$ ). Although in  $90^\circ \leq \theta \leq 180^\circ$  oscillations in the solidified phase

boundaries exist, similar behaviors to the initial observations are formed afterwards. This gives a chance to decrease the needed computational time and power in the upcoming studies. As the aim is a qualitative study, the simulations can be interrupted at the quarters of full rotations, and the evolved patterns at those time-lapses can be analyzed. This reduces the necessary calculation time from approximately one month to about one week.

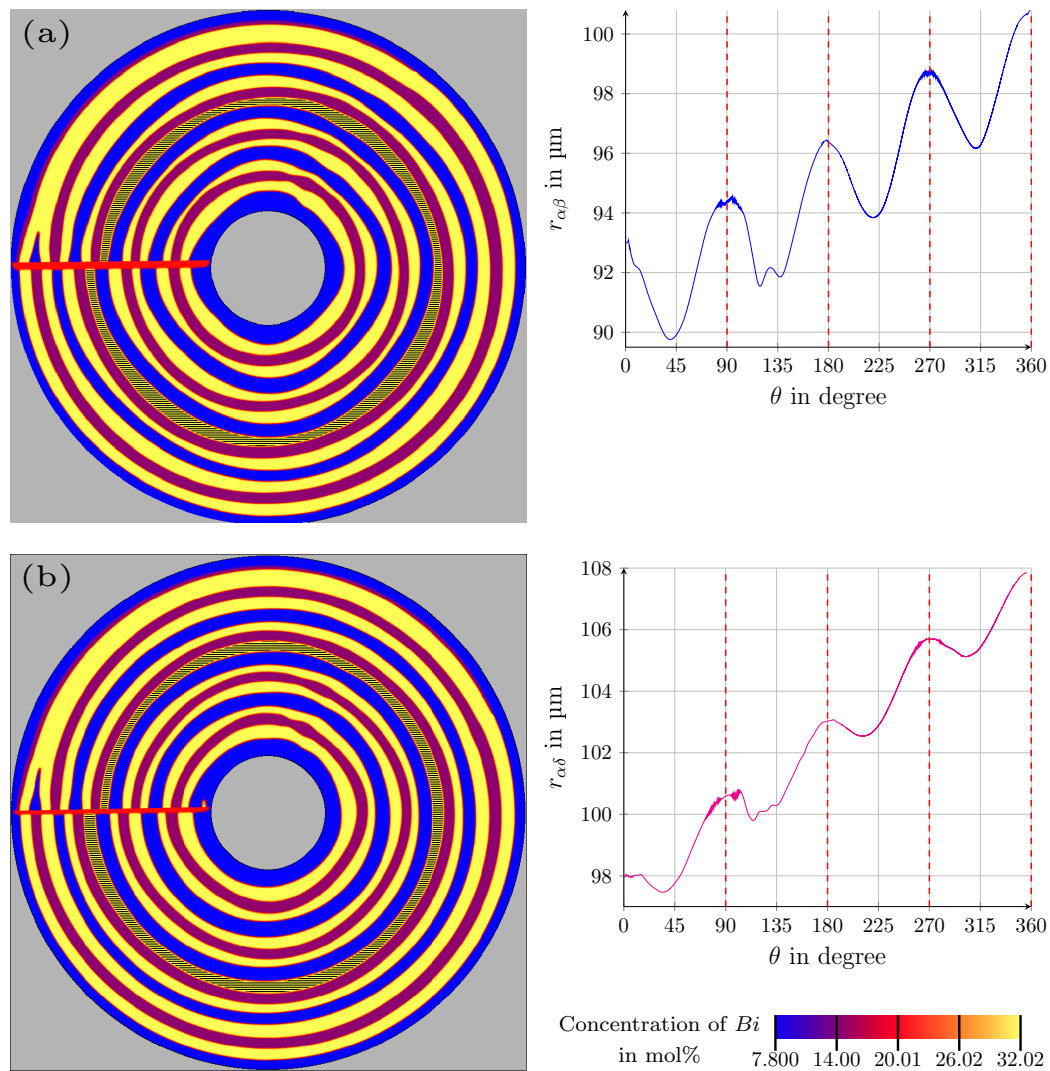


Figure 6.23: The radius variations with respect to the rotational angle in (a):  $\zeta_{\alpha\beta} = 0.1$  and (b):  $\zeta_{\alpha\delta} = 0.15$ . The middle hatched  $\alpha$  lamellae in both configurations are the base of the radius calculations.

In order to explain these observations, the generally observed variational behavior in the  $r - \theta$  plots is schematically illustrated in fig. 6.24(a). The radius values in each rotational angle  $\theta_i$  are noted with the  $r_{\theta_i}$  amounts, each having a special color. These values are plotted in fig. 6.24(b) with the same coloring style, forming a schematic depiction of

the phase boundary variations in  $360^\circ$  rotation of the temperature field. Apparently, the tilted growth of the solidified phase boundaries with respect to the temp. field is depicted with the curved black lines as the radius variations are not linear. Thus, studying the nature of the tilting phenomenon and its affecting parameters becomes the focus here; for which the additional *RDS* simulations are performed in the following.

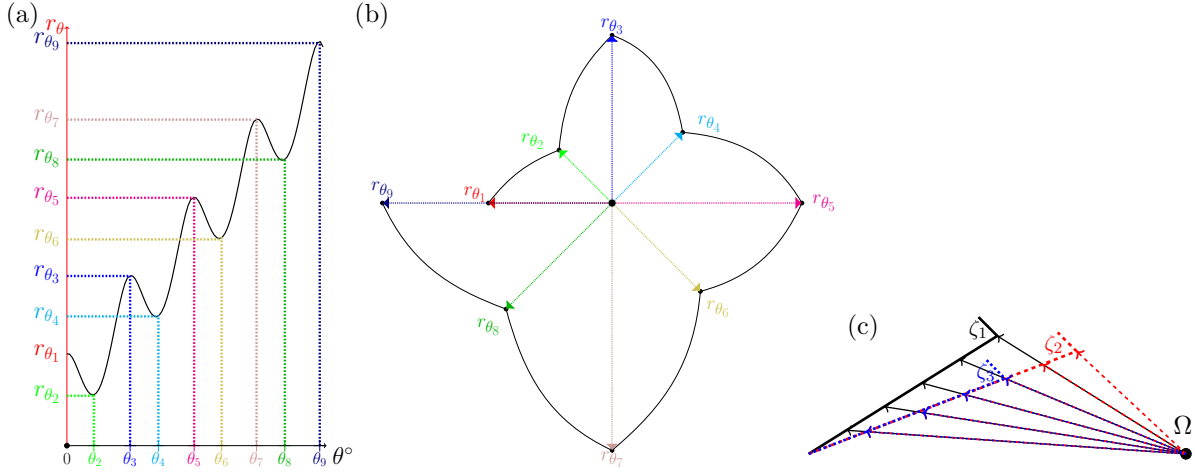


Figure 6.24: The schematic illustrations of (a): phase boundary radius  $r_\theta$  as a function of the rotational angle  $\theta$ . (b): The tilting of the solidified phase boundary (black lines) based on the depicted radii in (a). (c): The effects of the anisotropy strength increase on the tilt angle ( $\zeta_2, \zeta_3 > \zeta_1$ ).  $\Omega$ : the rotation center.

In fig. 6.25, the formed micrographs in  $\theta = 90^\circ$  are shown representing the evolved patterns for different  $\zeta_{\alpha\beta}$  values. The  $\alpha\delta$  and  $\beta\delta$  interfaces are modeled isotropically in these simulations. The strength in the anisotropically modeled  $\alpha\beta$  interfaces is increased up to the value of 0.25.

One of the interesting observations in this anisotropy configuration is the behavior of the  $\alpha$  lamellae in the simulated  $\alpha\beta\alpha\delta$ -type stacking sequences. In sub-figure 6.25(b) which denotes the  $\zeta_{\alpha\beta} = 0.10$ , the first  $\alpha$  lamellae in each repeat unit become thinner, whereas the second ones become thicker compared to the isotropic simulation. By increasing the  $\zeta_{\alpha\beta}$  to the value of 0.15 in fig. 6.25(c), two of the formed thin lamellae are eliminated in the approximate rotational angle of  $\theta = 30^\circ$ . In the next sub-figure denoting the  $\zeta_{\alpha\beta} = 0.20$ , the elimination angle decreases to the value of  $\theta \simeq 26^\circ$  and an additional  $\alpha$  lamella in the next stacking is eliminated. Although in fig. 6.25(e) the lamella eliminations occur at a slightly lower rotational angle, no further visual difference with the sub-figure(d) can be noticed. About the observed elimination behavior it can be questioned that, as all of the formed  $\alpha$  lamellae are surrounded by both  $\beta$  and  $\delta$  phases and any  $\alpha$  has one and only one interface with the neighboring  $\beta$ , why should the anisotropy affect only the first  $\alpha$ -s and not the seconds? The answer is in the natural tendency of the system to form  $\beta\alpha\delta$  patterns

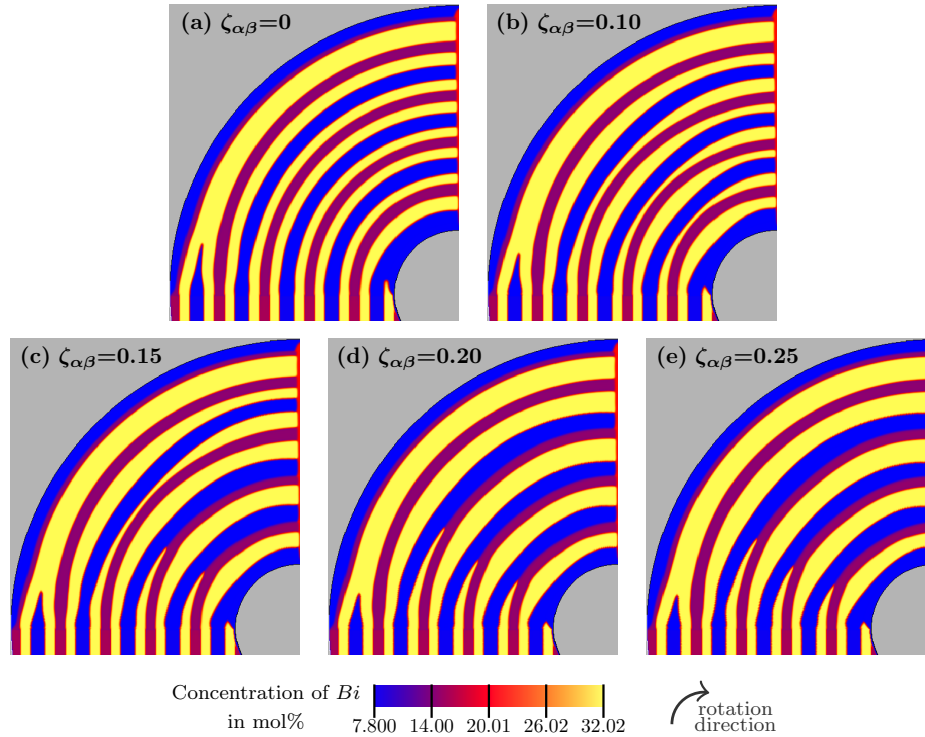


Figure 6.25: The evolved microstructures in the RDS studies of the Bi-In-Sn ternary eutectic system at the rotational angle of  $\theta = 90^\circ$ .  $\zeta_{\alpha\delta} = \zeta_{\beta\delta} = 0$  and  $\zeta_{\alpha\beta}$  is indicated in each sub-figure.

when the  $\alpha\beta$  interfaces are assumed to have anisotropic behavior. The formation of this pattern has previously been noticed in the DS simulations of section 6.2.2. As depicted in part ② of fig. 6.17(a), when we have anisotropy in the  $\alpha\beta$  interfaces, the formation of  $\beta\alpha\delta$  patterns demands elimination of the first  $\alpha$  lamellae in each stacking sequence. Such a phase arrangement can have a lower energy level in this anisotropy configuration compared to the  $\alpha\beta\delta$  arrangement which demands the second  $\alpha$  phase eliminations. For further studies, in fig. 6.26, the phase boundary radius variations in these simulations are plotted with respect to the rotational angle. The neighboring  $\beta$  and  $\delta$  lamellae to the  $\alpha$  which are located in the approximate middle segments of the simulation domains are considered for the radius measurements like the previous cases. In order to note the possible effects of the  $\alpha\beta$  interface anisotropy on the  $\alpha\delta$  interfaces, the measurements are performed in both interfaces. As a result, the tilting effects are observed in both which increase by the increase of the anisotropy strength. In  $r_{\alpha\delta}$ , for  $\zeta \geq 0.20$ , the initially formed pattern is changed due to the eliminations of the  $\alpha$  phases. However, the general descending-ascending behavior does not change indicating the continuous tilting of the solidified phases. The achieved global minimums in each curve are shown by the solid squares with the same coloring as the corresponding curves. It can be noticed that the squares are shifted to the higher  $\theta$  values by the increase of the  $\zeta$  from 0.10 to 0.20. In the

schematic illustration of fig. 6.24(c), such behavior is noted as  $\zeta_2$  which is depicted in red. This means longer distances of the solidified phases before their direction changes which take place after the minimums in the  $r - \theta$  curves. At  $0^\circ \leq \theta \leq 20^\circ$  and  $70^\circ \leq \theta \leq 90^\circ$ , the oscillations in the concentration fields are observed which are increased with the increase of the  $\zeta$ .

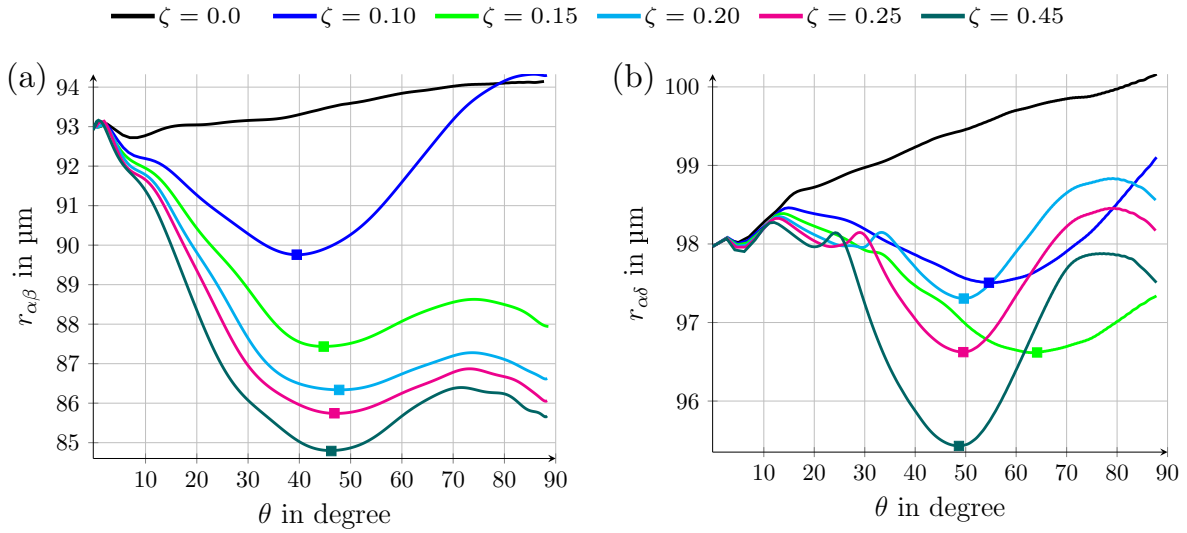


Figure 6.26: The radius variations in the simulations of fig. 6.25 with respect to the rotational angle, based on the formed middle  $\alpha$  lamella in (a):  $\alpha\beta$  and (b):  $\alpha\delta$  interfaces.  $\zeta$  denotes the  $\zeta_{\alpha\beta}$  and the other interfaces are modeled isotropically. The global minimums in the curves are specified with the solid squares.

In the following, a similar study is repeated investigating the anisotropy in the  $\alpha\delta$  interfaces.  $\zeta_{\alpha\beta}$  and  $\zeta_{\beta\delta}$  are assumed to be zero in this configuration. The obtained microstructures are shown in fig. 6.27 wherein the strength of anisotropy is varied in the range of  $[0.10, 0.40]$ . As it can be realized from the sub-figures(b-f), the expected tilted growths of the solidified phases occur but are less intense than the  $\alpha\beta$  anisotropy case. The second  $\alpha$  phases in the  $\alpha\beta\alpha\delta$ -type repeat units get thinner and the first elimination happens in  $\zeta_{\alpha\delta} = 0.35$ . The more pronounced influence of the  $\zeta_{\alpha\delta}$  on the second  $\alpha$  lamellae is in good accordance with the made predictions in part ④ of fig. 6.17(a) which is based on the  $DS$  results. This is another evidence to prove the shown anisotropic behavior in this schematic figure.

In fig. 6.28, the variations of  $\alpha\delta$  and  $\alpha\beta$  interface radii with respect to the rotational angles are plotted. The previously realized descending-ascending behavior is observed in this configuration as well. Based on the locations of the global minimums in the curves, it can be concluded that, by the increase of the anisotropy strength the length of the solidified lamellae increases, until a change in direction is reached. These changes take

place in the labeled angles as  $\theta_i$  in the schematic illustration of fig. 6.24(a). The observed trend is common in both of the studied anisotropic cases, i.e. the  $\alpha\delta$  and the  $\alpha\beta$  interface anisotropies. For  $\theta$  values between  $0^\circ$  and  $20^\circ$  and between  $70^\circ$  and  $90^\circ$ , the oscillations in  $r_{\alpha\delta}$  appear and increase by increase of the anisotropy strength. Thus, the largest oscillations are seen in  $\zeta_{\alpha\delta} = 0.40$ . The more dominant effects of the  $\alpha\beta$  anisotropy on the pattern formation can be concluded again here, by comparison of figs. 6.26 and 6.28.

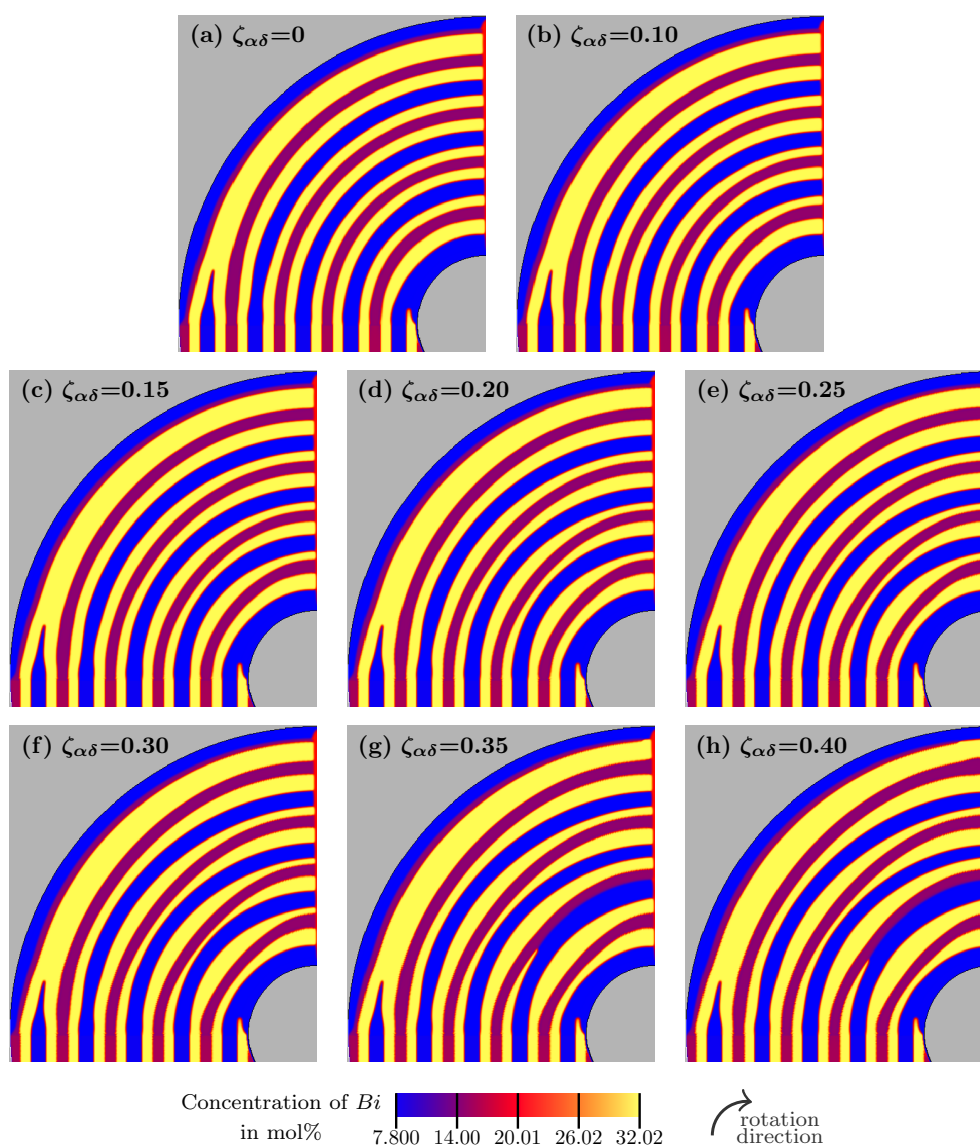


Figure 6.27: The evolved microstructures in the RDS studies of the Bi-In-Sn ternary eutectic system at the rotational angle of  $\theta = 90^\circ$ .  $\zeta_{\alpha\beta} = \zeta_{\beta\delta} = 0$  and  $\zeta_{\alpha\delta}$  is raised up to the value of 0.40.

Based on all of the observations in the dissociated roles of the  $\alpha\beta$  and  $\alpha\delta$  anisotropies, in the following the anisotropic behavior is activated in all interfaces simultaneously. The procedure is similar to the performed studies in the  $DS$  cases in section 6.2.2, however,

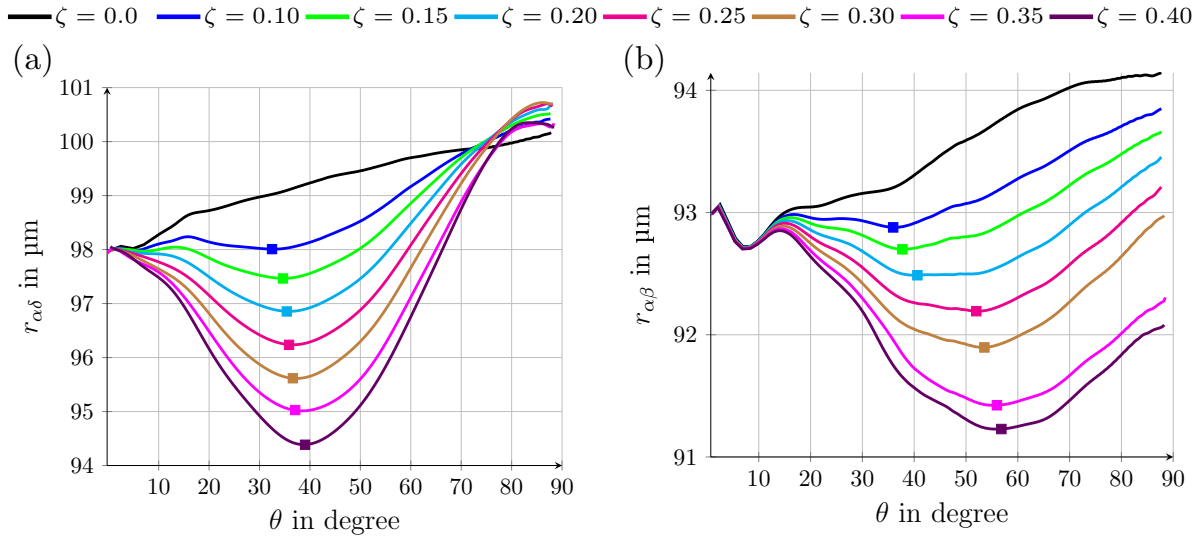


Figure 6.28: The radius variations in (a):  $\alpha\delta$  and (b):  $\alpha\beta$  phase boundaries, caused by the anisotropy of the interfacial energies in the  $\alpha\delta$  interfaces. The global minimums in the curves are specified with the solid squares.

the  $\zeta_{\alpha\delta}$  values are higher than those of  $\zeta_{\alpha\beta}$ . Due to the detected larger tilt angles in the  $\alpha\beta$  interfaces compared to the  $\alpha\delta$  in the same anisotropy strengths, this study is performed to check the possibility of the tilted growths in the *RDS* studies with almost parallel solid-phase boundaries. I.e. the experimentally observed patterns in fig. 3 of [90] for example. Ad hoc, the parameter  $r$  is defined as the proportion of  $\zeta_{\alpha\delta}$  to  $\zeta_{\alpha\beta}$ , which is varied in the range of [1.0, 3.0]. Obviously, the higher  $r$  values indicate the stronger anisotropies in the  $\alpha\delta$  interfaces. Figure 6.29 shows the simulation results for different configurations of the  $r$  quantity.  $\zeta_{\alpha\beta}$  and  $\zeta_{\beta\delta}$  are set to the values of 0.15 for which stable tilted growths in all of the solidified phases have been observed previously. The depicted micrograph in the sub-figure 6.29(a), belongs to a quarter of the first rotation in the previously shown simulation result in fig. 6.20. The higher value for  $\alpha\beta$  interface tilting compared to that of  $\alpha\delta$  is noticeable here as well. In the other sub-figures, implying a gradual increase in the  $\zeta_{\alpha\delta}/\zeta_{\alpha\beta}$  proportion, the more parallel evolutions in the solidified phase boundaries can be noticed visually. A radius-variation study is performed in fig. 6.30 analogous to the previous cases for a more precise investigation of this effect. Figure 6.30(a<sub>1</sub>) and (b<sub>1</sub>) depict these study results for the  $r_{\alpha\delta}$  and  $r_{\alpha\beta}$  quantities. The general shapes of the curves having global minimums are similar to the formerly depicted plots in figs. 6.26 and 6.28. The solid squares indicating the minimum points in the curves of fig. 6.30(a<sub>1</sub>) are shifted to the lower angles despite the observed behaviors in the previous  $r - \theta$  plots. This indicates the decrease in the length of the solidified lamellae with the increase of  $r$  before the direction change. In the previously shown fig. 6.24(c), such behavior is noted as  $\zeta_3$

and is illustrated in blue color. In order to analyze the parallelism between the solidified  $\alpha\beta$  and the  $\alpha\delta$  interfaces, the slopes of the tangent lines to their  $r - \theta$  curves in different rotational angles have to be compared. Hence, it is necessary to approximate the  $r - \theta$  profiles by some functions, whose derivatives can represent these slopes.

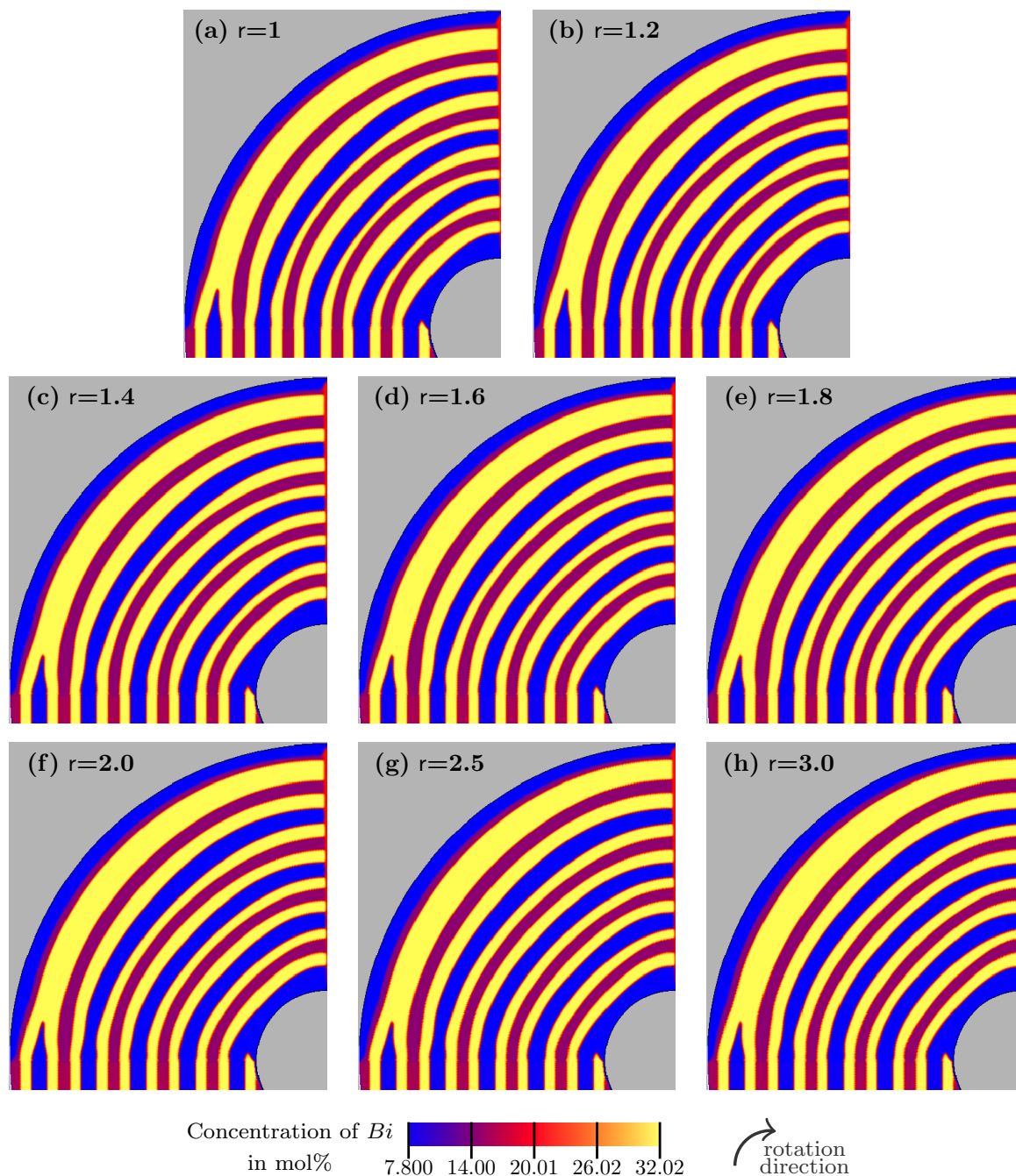


Figure 6.29: The evolved microstructures in the RDS studies of the Bi-In-Sn ternary eutectic system at the rotational angle of  $\theta = 90^\circ$ .  $\zeta_{\alpha\beta} = \zeta_{\beta\delta} = 0.15$  and  $r = \zeta_{\alpha\delta}/\zeta_{\alpha\beta}$  is risen up to 3.0.

From the observed general behavior in the curves, it is conjectured that the polynomial functions are able to approximate such behavior simply. Therefore, in fig. 6.30( $a_2$ ) and fig. 6.30( $b_2$ ) different polynomials are fitted to the  $\alpha\delta$  and  $\alpha\beta$  profiles, respectively. For the sake of simplicity, the results only for the  $r = 1$  and the  $r = 3$  values are illustrated for which the solid lines refer to the measured radius values in the simulated micrographs. The dashed and the dotted lines refer to the  $\alpha\delta$  and the  $\alpha\beta$  phase boundaries and the blue, green and red colors indicate the second, third and fourth-order polynomials, respectively. It can be noticed in the plots that, in the second and third-order polynomials there are higher deviations in the original and the approximated curves compared with the fourth-order functions. In Table 6.2, the maximum and the average deviations between the original phase boundary radii data and the fitted polynomials are summarized. As it is noticed, in both  $r = 1$  and  $r = 3$  values, the average deviations decrease by the approximate value of 14% for both  $\alpha\delta$  and  $\alpha\beta$  interface radii by increasing the polynomial order from two to the three. The order increase from three to four, makes more considerable reductions in the deviation values which lie in the range of [80%, 95%], respectively. These reductions are in good accordance with the visual observations of fig. 6.30( $a_2$ ) and ( $b_2$ ). With further increases in the polynomial order, the deviations decrease by the maximum of 3% which happens in the  $\alpha\beta$  phase boundaries. This amount is not much considerable compared to the previous jump in the deviations. It has to be mentioned that there is a slight increase in the average  $D_{\alpha\delta}$  from the value of 0.028 to 0.029 which is an undesired fact in this practice. It can be a sign of a probable divergence in the correct representation of the solid-solid boundary radius behavior in the further increases of the polynomial orders. Hence, in a conclusion, it can be declared that the fourth-order functions can represent the variational behaviors in the  $\alpha\beta$  and  $\alpha\delta$  interface radii, respectively.

In fig. 6.30(c), the  $dr/d\theta$  values are plotted as functions of the rotational angles in the different  $r$  values. The derivative values are calculated based on the fitted fourth-order polynomials to the  $r_{\alpha\beta}$  and  $r_{\alpha\delta}$  values. The curves representing the  $\alpha\delta$  and the  $\alpha\beta$  phase boundaries are drawn in the solid and the dashed lines, respectively. The black color which represents the  $r = 1$  value has the largest deviation between the solid and the dashed curves. By increase of the  $r$ , the two boundary curves come to have fewer deviations indicating the more parallel evolution in the solid-solid interfaces. The mentioned deviations have the least values for  $r = 2.5, 3$  as the largest investigated strengths in the  $\alpha\delta$  interface anisotropy.

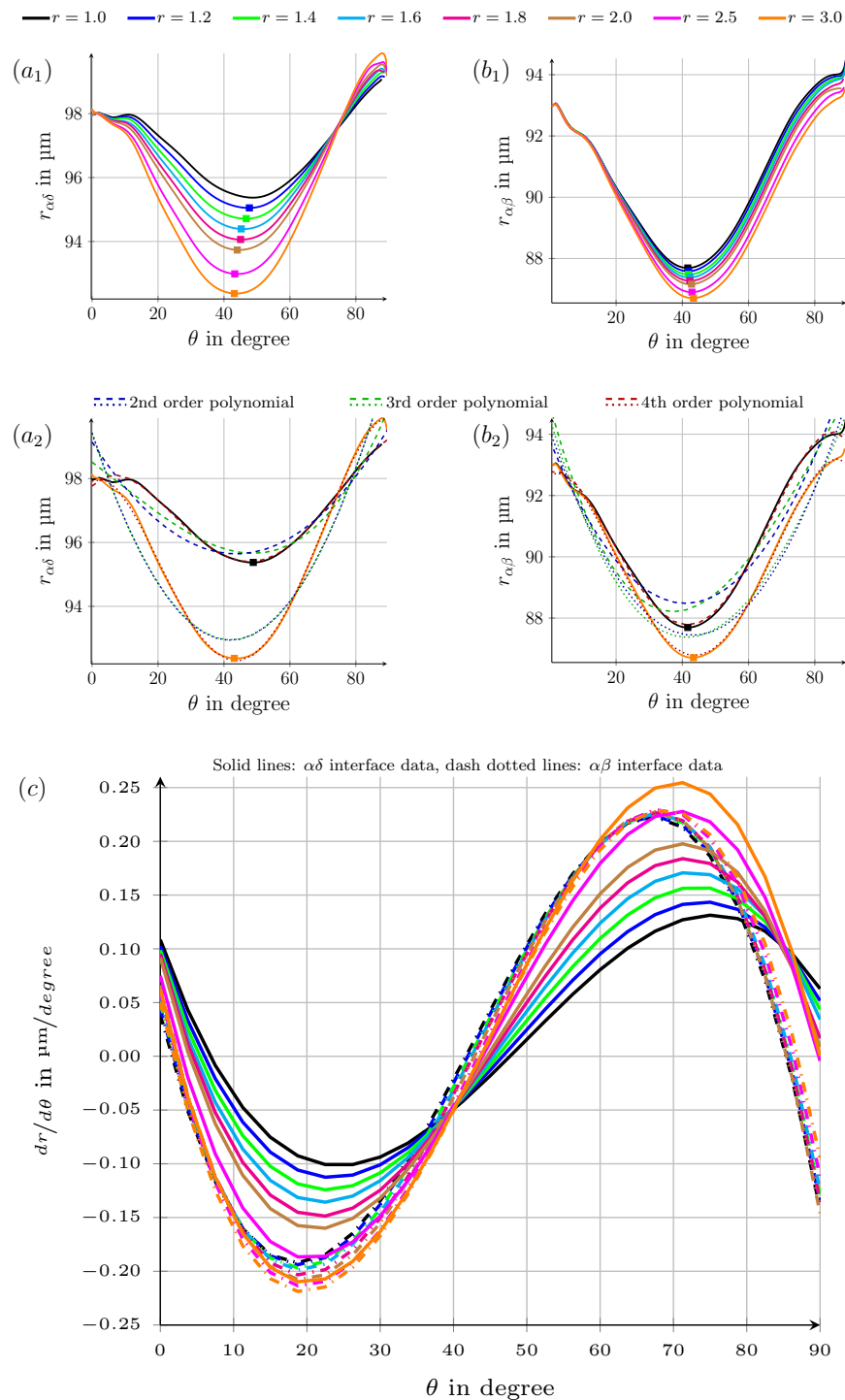


Figure 6.30: The radius variation analysis of the  $\alpha\delta$  and the  $\alpha\beta$  interfaces in the RDS studies of the Bi-In-Sn ternary eutectic system at the rotational angle of  $\theta = 90^\circ$ .  $\zeta_{\alpha\beta} = \zeta_{\beta\delta} = 0.15$  and  $r = \zeta_{\alpha\delta}/\zeta_{\alpha\beta}$  is risen up to 3.0. (a<sub>1</sub>):  $r_{\alpha\delta}$  and (b<sub>1</sub>):  $r_{\alpha\beta}$  variations with respect to the rotational angle variations in different  $\zeta_{\alpha\delta}/\zeta_{\alpha\beta}$  values. Fitting of the second-, third- and fourth-order polynomials to (a<sub>2</sub>):  $\alpha\delta$  and (b<sub>2</sub>):  $\alpha\beta$  interface radius amounts in the minimum and maximum  $r$  values. (c):  $dr/d\theta$  analysis in the  $\alpha\delta$  and  $\alpha\beta$  interfaces.

Table 6.2: The maximum, the minimum and the average deviations between the phase boundary radius data in the simulation results (solid lines in fig. 6.30( $a_2, b_2$ )) and the approximated polynomials (dashed and dotted lines in fig. 6.30( $a_2, b_2$ )).  $D$ : deviation in percent,  $min$ : minimum,  $max$ : maximum,  $ave$ : average.

polynomial order		$D_{\alpha\delta}$ in %		$D_{\alpha\beta}$ in %	
		$max$	$ave$	$max$	$ave$
2	$r = 1$	1.212	0.260	1.623	0.601
	$r = 3$	1.848	1.516	1.513	0.559
3	$r = 1$	0.613	0.224	1.814	0.521
	$r = 3$	1.886	1.516	1.379	0.543
4	$r = 1$	0.237	0.028	0.694	0.094
	$r = 3$	0.474	0.069	0.430	0.084
5	$r = 1$	0.194	0.029	0.614	0.091
	$r = 3$	0.426	0.069	0.428	0.084

### 6.3.3 Summary and conclusions

In this section, two-dimensional phase-field simulations of the  $RDS$  process are performed for the first time in the literature. The crucial roles of the material and process parameters on the pattern formation like the anisotropic solid-solid interfaces or the effects of the solidification velocities can be studied in precise manners by this technique. The modeled Bi-In-Sn ternary eutectic system is selected for this investigation whose directional solidification simulations are previously performed in this work. The anticipated circular trajectories with the  $\alpha\beta\alpha\delta$  stacking sequences are resulted in the simulations of the floating grains. Additionally, by employing the anisotropy in the modeled interfaces, the tilted growths in the evolutions of the solidified lamellae are observed. In the latter case, the dominance of the  $\alpha\beta$  interface anisotropy on the formation of the final patterns compared to the  $\alpha\delta$  anisotropy is realized. It is observed that in order to have almost parallel solid-phase boundaries, as observed in the experiments, higher anisotropy strengths have to be employed in the  $\alpha\delta$  interfaces. As a result, the  $\zeta_{\alpha\delta}/\zeta_{\alpha\beta}$  ratios higher than 2.5 lead to the almost equal slopes in the  $r_{\alpha\delta}$  and  $r_{\alpha\beta}$  curves at the same rotational angles, indicating the expected parallelism.

It is worth mentioning here that, the exact effects of the employed  $\beta$  layer in the near-barrier segments of the simulation domains can not be thoroughly verified in the current configurations. The observed adjustments in the solidified phases are influenced by several parameters like the properties of the neighboring phases, the solidification velocities and the boundary conditions. Therefore, separate studies on the influences of these parameters are required in future works which demand the implementation of

a new formulation for the barrier phases. In the new formulations, the need for the additional phases in the near-barrier regions has to be solved leading to enhancements in the calculation of the concentration and the phase fields. Nonetheless, the current configuration has given a good understanding of the effects of the anisotropy on the formed patterns and can still be used in further studies, for example, the role of the angular velocity on the evolved microstructures. Based on the primary unshown results,  $\omega$  increase leads to the formation of instabilities like the lamellae eliminations and the oscillations in the solidified phase boundaries in accordance with the reported experimental works [86].

The *RDS* studies generally assert the observed effects in the *DS* simulations and give further information on the pattern-formation-related facts. The mechanisms behind the developments of the  $\alpha\beta\delta$  and  $\beta\alpha\delta$  stacking sequences can be mentioned for the instance. In order to make complementary studies on the tilting event and its related parameters, in the next section, further simulations are conducted on the tilted growth in the directional solidification simulations.

## 6.4 Tilted growth in *DS* study of an idealized system

In the previous section, the tilted solid-phase growth with respect to the imposed temperature gradient has been studied in the *RDS* simulations. It is observed in the investigated simulations that, the solid-solid interface anisotropy can cause such growths. In addition, the deviations in the solid-solid interface directions with respect to the imprinted temperature gradients in the *DS* studies, have also been observed in the literature. As examples of these cases, the tilted growth in the *DS* experiments of the Bi-In-Sn ternary system can be mentioned which is discussed previously in section 4.2. Or the works of Woodruff et al. [146] and Karma [147] can be mentioned as the other examples in which the deviations in the solid-solid interface directions with respect to the imprinted temperature gradients have been studied. These deviations result in the undefined evolution directions for the solidified phases, which lead to the different macroscopic material properties [16]. Hence, the importance of a better understanding of the nature and governing mechanisms of the tilted growth in the *DS* studies is felt to be substantial, like the *RDS* cases. In the course of this endeavor, different experimental [29, 148] and theoretical [30] investigations in the binary material systems with two-dimensional geometries have been performed. It is reported in the works of [148–152] that, the tilt angle increase with the lamellar spacing increase. In the work of [149], a second-order polynomial is benefited to fit the tilt angle dependence on the investigated lamellar spacings. However, the mentioned increasing behavior is not observed in the phase-field and dynamic boundary integral studies by Ghosh et al. [153, 154], which are performed in the slow growth rates

and small *Péclet* numbers. Considering the multicomponent multiphase alloys, additional effects can lead to the tilted growth of the solidified phases, moreover to the anisotropic interfaces. As examples, in the works of Apel et al. [155] and Hötzer et al. [67] the tilting is proclaimed in the crystallographically isotropic systems. In [155], an asymmetric ternary phase diagram is considered to study the tilting effect in three-phase solidification with the  $\alpha$ ,  $\beta$  and  $\delta$  as the solidified phases. The absence of mirror symmetries in the diffusion field of the ternary system is reported to be the key parameter in the tilting, in contrast to the binary alloy's behavior. Hötzer et al. [67] have made a parameter study in a ternary system with isotropic interfaces in which the liquid phase is solidified into three solid phases. Based on their findings, the variation of the interfacial energies ratio between the solid phase boundaries and the solid-liquid phase boundaries can cause tilting in the solidification process. In the experimental and numerical work of Parisi et al. [151], the influence of the phase equilibria on the tilted growth has come into consideration, studying the ternary  $\text{CBr}_4\text{-C}_2\text{Cl}_6$  system. For this system, the solidification velocity as a process parameter is reported to have a substantial role in the inclined lamellar growth based on the work of Ginibre et al. [117].

Following the performed researches in the mentioned works, as well as the observed tilting-related phenomena in the previous section of the current work, the variation of the system and process parameters are investigated here for a systematic study of their effects on the tilting in the *DS* simulations. Ad hoc, the idealized ternary system introduced by Hötzer et al. [67] is used for which an automatized and unsupervised method is implemented to measure the resultant tilt angles in the two-dimensional simulations. The system has simplified material properties which leads to more symmetry in its structure. The commercial phase-field tool *WALBERLA* (see section 2.3.1) is benefited in the simulation studies in this section. Simulations are structured as following: Initially, the ternary material system is introduced and the studying parameters are declared in detail. Then the angle measurement technique is explained quantitatively and the simulations are performed in the discussed variational ranges of the investigated parameters. In the obtained results, the effects of the lamellar spacing  $\lambda$ , the interface energy ratio  $R$ , the diffusion coefficient  $D$ , the temperature gradients  $G^{DS}$  and the solidification velocity  $v$ , variation on the formed tilt angle are analyzed. Finally, a general fitting formulation is derived for the prediction of the tilt angle as the function of these studied parameters.

### 6.4.1 The system

Like all of the performed two-dimensional *DS* simulations in current work, the utilized setup in these simulations is based on the schematic illustration of fig. 3.2(b) in section 3.1. In this setup, fig. 6.31 depicts the solid phases arrangement as well as the tilt angle  $\varphi$  and

the interfacial energies. The initial lamellar arrangement of the solid phases with  $\alpha\beta\delta$  repeat unit is filled in the left segment of the figure. The solid-solid phase boundaries are initially located in the  $x$  direction and  $\lambda$  defines the value of the lamellar spacing. By tilted growth of the solidified phases, the difference between the direction of  $G^{DS}$  and the solid-solid interfaces is defined as the tilt angle  $\varphi$ . In order to measure the tilt angle, the original coordinate system  $x - y$  is rotated by the amount of the tilt angle to form the  $x^* - y^*$  coordinate system. Hence, the angle between  $x$  and  $x^*$  axis defines the  $\varphi$  value. The boundary conditions are exposed based on the formulations of section 2.3.3. The moving window technique is exploited (see section 2.3.4) for a reduction in the computational efforts.

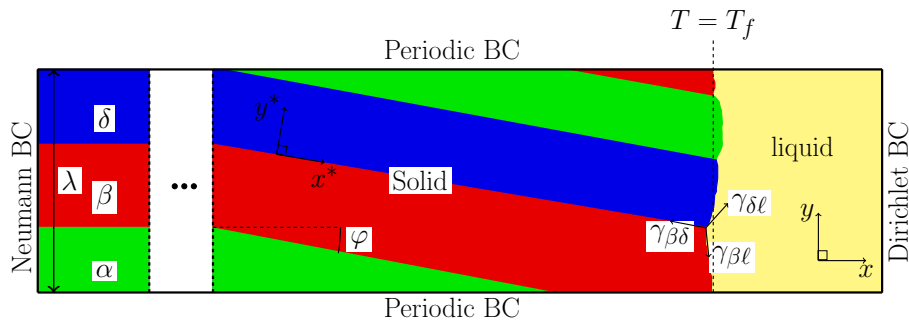


Figure 6.31: The schematic illustration of the tilting phenomenon in the DS simulations based on [156].  $x - y$ : the original coordinate system.  $x^* - y^*$ : the rotated coordinate system with the amount of the tilt angle  $\varphi$ .

The system parameters are summarized in Table B.3 in Appendix B.3, which includes the system idealization results based on [67]. This procedure is conducted to obtain a less complicated system in terms of material properties. The Gibbs energy parameters and the liquid concentration are specified with the  $\Xi$ ,  $\xi$ ,  $X$  and  $c_l$ , respectively. As it can be observed, the Gibbs energies of the solid phases are modeled by the simple congruent paraboloids, which are distributed in a symmetric manner around the center of the ternary diagram with A, B and C components. The mentioned central point contains the liquid phase defining paraboloid and therefore with equal element concentrations. The phase fractions of the involved solid phases are set to be equal, in order to prevent probable effects of parity-breakage in the unequal distribution of the solid phases. Due to the inherent complexities of the tilting phenomenon, this idealized system is selected in order not to deal with the additional complexities in physical systems. The diffusion coefficients in the solid phases are assumed to be zero, as their values in the liquid are higher in orders of magnitude [157]. Therefore, the solidified phases do not undergo further phase transformations with the simulation progresses. Three different levels of liquid diffusion are investigated instead. Considering the interface energies ratio as an efficient parameter

in the tilted growth [67],  $R = \gamma_{\alpha\beta}/\gamma_{\alpha l}$  is varied with values of 1.5, 2.5 and 3. The lamellar spacings are varied in the range of [60, 140] cells for which stable solid phase growths are obtained in the investigated parameters. In general, for  $\lambda$  values beyond this limit phase eliminations can happen. However, the accuracy of this statement may depend heavily on the other simulation parameters. In ensuing sections, the tilt angle variations depending on the defined combinations of the interfacial energy ratios, diffusion coefficients, lamellar spacings, solidification velocities and temperature gradients are investigated.

### 6.4.2 Tilt angle measurement technique

The implemented automatized angle measuring technique serves as the foundation for studying the dependency of the tilt angle on the considered physical and process parameters. The results from extensive phase-field simulations are analyzed by means of a computational algorithm as explained in the following. The solid-solid interfaces are detected by a marching cube algorithm [158], which works based on the detection of the equal order parameters. As shown in fig. 6.32, a continuous interface between the solid phases is structured considering the effect of the periodic boundary conditions on the total growth height. In order to achieve this continuous interface, natural multipliers of  $\lambda$  are employed to shift the solid-solid phase boundaries in the  $y$  direction. In the next step, the local maxima in the direction of  $x^*$  are determined in the constructed interface by employing a linear least-squares fitting. It is worth mentioning here that, even in the simulations which have the straight interfaces in the solidified phases boundaries visually, minor oscillations exist causing small maxima, which are used in the fitting approach. As the final step, the average tilt angle is measured as the angle between  $x^*$  in the shifted, and  $x$  in the original coordinate system. By this technique, high accuracy in the measurement of the tilt angles is ensured as a larger phase boundary is formed and the number of the local maxima is increased. A minimum amount of four maxima points are required in order to obtain the tilt angle.

Re-measurement of the manually retrieved tilt angles in the work of [67] by the implemented automatic measuring method in section 6.4.2, serves as the validation procedure of this implemented technique. In fig. 6.33, the resultant tilt angle values are compared for the interfacial energy ratio of  $R = 3$ , in which the red triangles denote the measured amounts and the black circles denote the reported values in [67]. The comparison is made in the increasing amounts of the lamellar spacings forming each curve of the plot. Rising behavior in the tilt angles is resulted until reaching a maximum  $\varphi_{max}$  at  $\lambda = \lambda_{peak}$ . Subsequently, the additional growth of  $\lambda$  from  $\lambda_{peak}$ , results in the reduction of the tilt angles. Considering the shape of the solid-solid interface boundaries, stationary lamellar growths are resulted for  $\lambda \leq \lambda_{peak}$ , whereas for  $\lambda > \lambda_{peak}$ , phase boundary oscillations

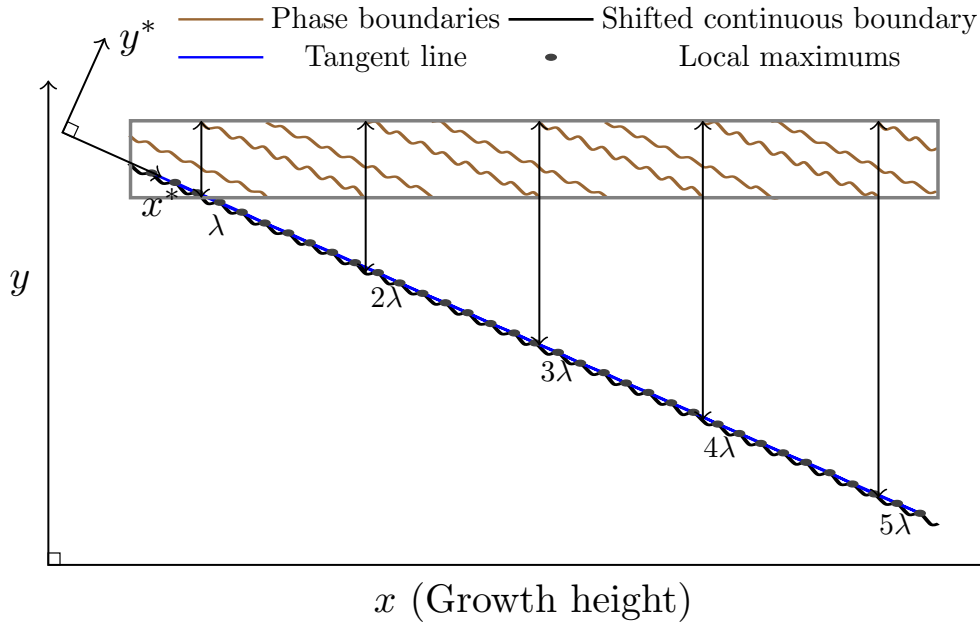


Figure 6.32: The schematic illustration of tilt angle measurement technique including the solid-solid phase boundary shifting based on [156].

come to exist. In general, the mentioned oscillations increase by the further lamellar spacing increase.

The qualitative agreement between the black and the red curves shows the applicability of the implemented angle measurement technique. Meanwhile, the occurred deviations can be summed up as the following:

- (i) The  $\lambda_{peak}$  is placed at  $\lambda \simeq 89$  cells in the hand measured values of [67], which results in  $\varphi = 7.14^\circ$ . For the automatized method,  $\lambda_{peak}$  is shifted to the smaller value of  $\lambda \simeq 86$  with a reduction in the tilt angle to  $\varphi = 7.065^\circ$ .
- (ii) For the smaller lamellar spacing values than  $\lambda_{peak}$ , the maximum deviation between the two curves is equal to  $0.05^\circ$  (1%). This deviation increases to  $0.63^\circ$  (10%) when  $\lambda > \lambda_{peak}$  at  $\lambda = 95$  cells.

The deviations can be explained due to the occurred errors in the hand-measured values which increase in the regions with the higher boundary oscillations in the solidified phases. Altogether, the achieved correlation in the illustrated curves indicates the capability of the automatized angle measurement technique for a quantitative parameter study in the upcoming simulations.

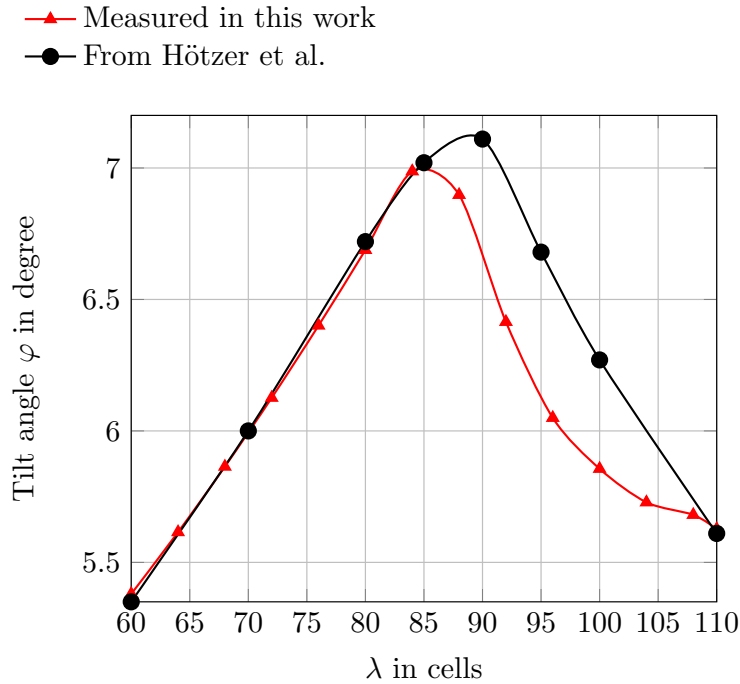


Figure 6.33: Validation of the implemented tilt angle measurement technique in current work, by comparison with the results of Hötzer et al. [67]. In the plotted curves:  $R = 3$ ,  $v = 2.8e - 3$ ,  $G = 1e - 4$  based on [156].

### 6.4.3 Effects of the process and system parameters on tilt angle

In this section, the analysis on the effects of the parameter variation on the tilt angle is performed. The investigated parameters are systematically varied according to Table B.3 and their effects on the resultant tilt angles are studied. In order to combine the results of the different parameter configurations, the dimensionless *Péclet* number is used in the following. As the final step, a fitting formulation is derived to approximate the tilt angles based on all the obtained results. The parameter study is conducted utilizing the validated tilt angle measurement technique in the previous section. The lamellar spacings are increased in the investigated cases until the overgrown of one of the solidified phases. The effects of the material-specific parameters, i.e. the interfacial energy ratios and the diffusion coefficients on the tilt angles are studied in the first simulation series. Then, the variations of the solidification velocities and the temperature gradients as the process parameters are conducted in the follow-up simulations. More than 950 simulations in total are performed in this study. The resultant tilt angles in the different investigated configurations are plotted in fig. 6.34 for  $R = 1.5$  and fig. 6.35 for  $R = 2.5$ . In these figures the following style is benefited for the sake of classification simplicity: The red

color denotes the diffusion coefficient  $D$  equal to 3, the blue color denotes  $D = 4$  and the green color represents the  $D = 5$ , respectively.

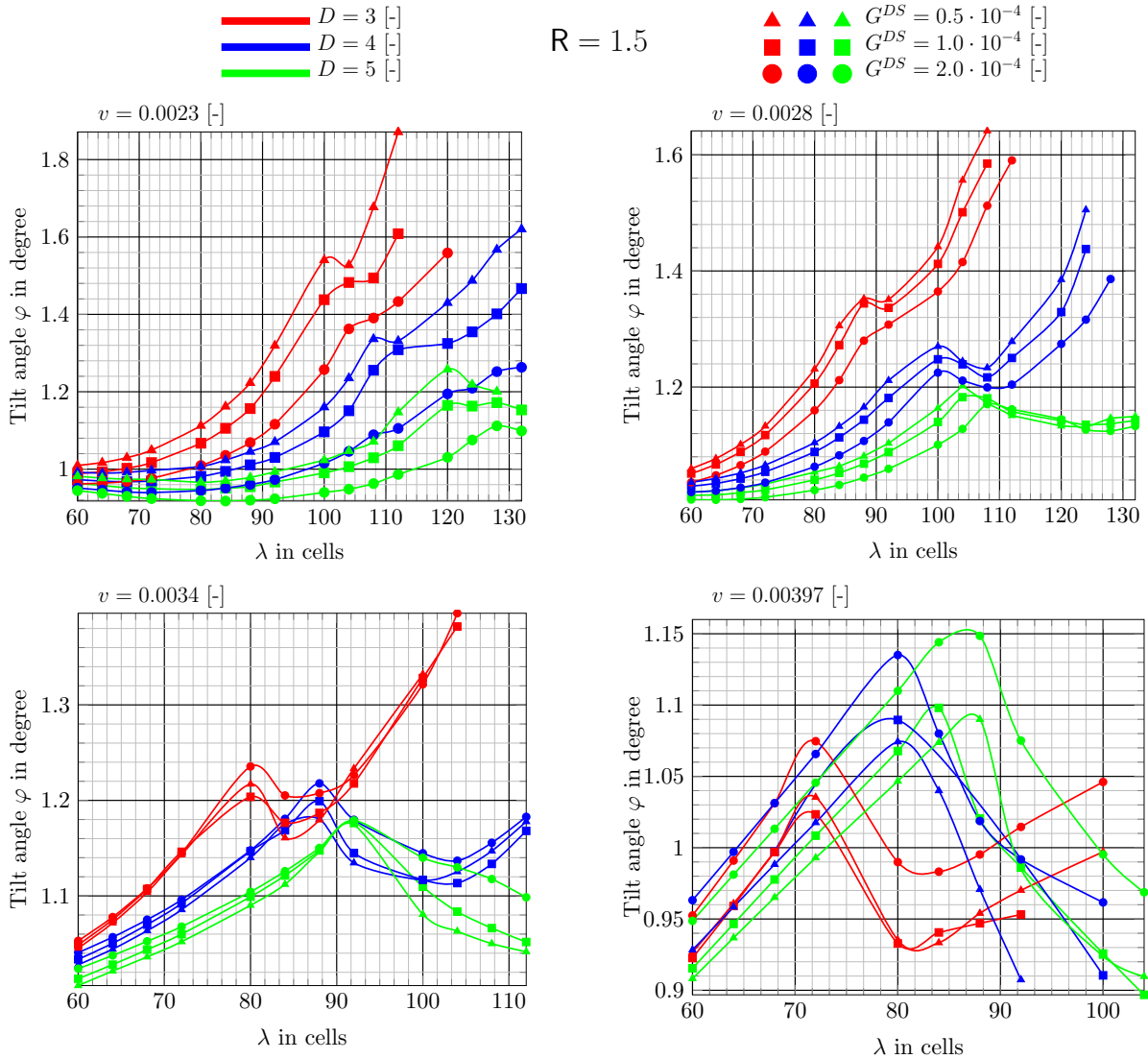


Figure 6.34: Variation of the resultant tilt angles  $\varphi$  with respect to the lamellar spacings  $\lambda$  in  $R = 1.5$ .  $G^{DS}$ : temperature gradient,  $D$ : diffusion coefficient,  $v$ : solidification velocity.

The used marks in the curves refer to the investigated temperature gradients, as the triangles to  $G^{DS} = 0.5 \cdot 10^{-4}$ , the squares to  $G^{DS} = 1.0 \cdot 10^{-4}$  and the circles to  $G^{DS} = 2.0 \cdot 10^{-4}$ . Each figure shows four plots, each corresponding to a single solidification velocity. As a general outcome from these plots it can be noticed that at each curve by the increase of the lamellar spacing, the tilt angles are increased. This increase for  $R = 1.5$  leads to a local maximum followed by a local minimum, consequently. By further increase of the  $\lambda$ , the higher values of  $\varphi$  evolve until the elimination of one of the solidified phases.

The lamellar spacing corresponding to these local maximums is defined as the  $\lambda_{peak}$  in the performed simulation series. Contrary to  $R = 1.5$ , for the higher value of  $R = 2.5$  the global maximums in the  $\varphi - \lambda$  plots are observed. Thus, the corresponding tilt angle value to  $\lambda_{peak}$ , results in the maximum possible amount for the tilt angle in this configuration.

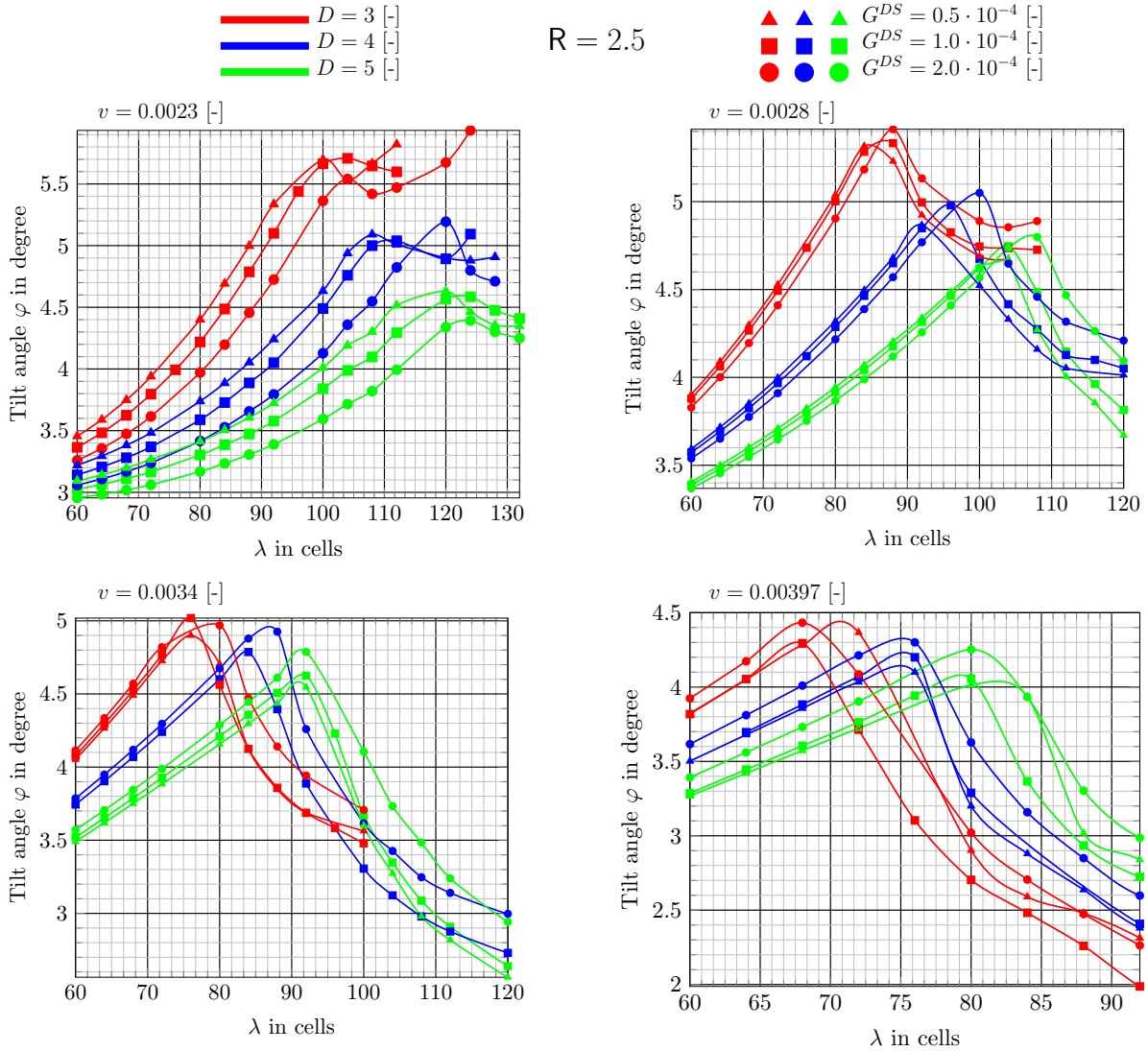


Figure 6.35: Variation of the resultant tilt angles  $\varphi$  with respect to the lamellar spacings  $\lambda$  in  $R = 2.5$ .  $G^{DS}$ : temperature gradient,  $D$ : diffusion coefficient,  $v$ : solidification velocity.

### 6.4.3.1 Interfacial energies ratio (R)

The curvature of the solidification front can be affected by the values of the interfacial energies and lead to the tilting as a response of the system to variation of the interfacial energies [67]. In the indicated reference, special ratios of the interfacial energies between

the solid-solid and the solid-liquid interfaces are resulted in the tilted growths of the solidified phases. Therefore, two main ratios of  $R = \gamma_{\alpha\beta}/\gamma_{\alpha l}$  as  $R = 0.24/0.16 = 1.5$  and  $R = 0.2875/0.1125 = 2.5$  are investigated. By making a comparison between fig. 6.34 and fig. 6.35, it can be noticed that an increase in the  $R$ , has a direct impact on the tilt angle increase which agrees well with the results of [67]. This increase can simply be checked in the resultant ranges of the tilt angle plots which are approximately 3 times higher in  $R = 2.5$  compared to the  $R = 1.5$ . Meanwhile, the values of  $\lambda_{peak}$  in equal amounts of the diffusion, temperature gradients and solidification velocities remain almost unchanged indicating its independence from the considered  $R$  amounts. It is worth mentioning that, for the larger values of  $R$  ( $R > 3$ ), instabilities in the triple points in the solidification fronts are observed based on Young's law. Therefore, the maximum of 2.5 is considered in the current study.

#### 6.4.3.2 Diffusion coefficients ( $D$ )

As shown by Apel et al. in [155], the concentration fluxes and rejection of the elements in the solidification fronts can result in tilting. By considering the *Péclet* number ( $Pe = \lambda v/D$ ) as a parameter to classify the speed of the solidification processes, in slow reactions the dependency of the evolving supersaturations on the diffusion coefficients is reported. Thus, the effect of these coefficients on the arising tilt angles is one of the studied parameters in the current work. Based on figs. 6.34 and 6.35, in general, the  $\lambda_{peak}$  is shifted to higher values by the increase of the diffusion in the liquid phase. The corresponding tilt angles are decreased, respectively.  $\lambda_{peak}$  shifting can be explained by the stability enhancement in the simulations in the higher diffusion values in which less distinct solid phase boundary oscillations are observed, either. The increase of diffusion results in the decrease of the concentration fluxes causing a less pronounced tilting mechanism in [155]. In figs. 6.34 and 6.35, at each color denoting a fixed diffusion amount, the deviations between the curves for  $\lambda > \lambda_{peak}$  increases in general. This is due to noticeable oscillations in the solidified phase boundaries in larger values of the lamellar spacings.

#### 6.4.3.3 Temperature gradient ( $G^{DS}$ )

Effects of non-dimensionalized temperature gradient with the values  $0.5 \cdot 10^{-4}$ ,  $1.0 \cdot 10^{-4}$  and  $2.0 \cdot 10^{-4}$  on the tilt angle can be observed in figs. 6.34 and 6.35. Despite the slight impact of the temperature gradient on the tilting, the overall tendency to this parameter is less noticeable compared to the other investigated parameters. This conclusion is in good agreement with the results of Akamatsu and Ihle [28] in their experimental and numerical studies for cellular growths.

#### 6.4.3.4 Solidification velocity ( $v$ )

In order to realize the effects of the solidification velocity on the tilting event, the unicolor-unimark curves should be compared in the different plots of figs. 6.34 and 6.35. Such a comparison makes the possibility to understand the velocity effects in the fixed diffusion and temperature gradient values. As it can be noticed, in general, by increase of the velocity both  $\lambda_{peak}$  and  $\varphi_{max}$  values are shifted to the smaller spacings and angles. This is due to the less pronounced effects of the diffusion in the higher solidification velocities. In addition, the slopes in the  $\varphi - \lambda$  plot curves remain almost unchanged for  $\lambda < \lambda_{peak}$ . In the case of  $R = 2.5$ , there are slight decreases in the mentioned slopes in the velocity increase from 0.0034 [-] to 0.00397 [-]. The generally observed behavior is due to two mechanisms that are driven by the velocity: the first mechanism is the concentration diffusion and the second is the driving force which is in the direction of the imprinted temperature gradient. For  $\lambda > \lambda_{peak}$ , in smaller values of the velocity, the tilt angle decrease is less pronounced. Furthermore, in the high velocities, the peaks of the curves become sharper resulting in the more restricted spacing ranges with the high tilt angle values.

#### 6.4.3.5 Overview of the affecting parameters

The analyzed influences of the material and process parameters on the tilt angles are summarized schematically in fig. 6.36. As the temperature gradient effect is less pronounced compared to the other parameters, it is not entered into this figure. The dimensionless *Péclet* number is benefited to characterize the parameter dependencies of the tilt angles in the works of Akamatsu et al. [28] and Ghosh et al. [153]. A similar study is done here and the resultant dependencies are illustrated in fig. 6.37. In this figure, the brown triangles indicate the interfacial energy ratio of 1.5 and the magenta pentagons indicate the  $R = 2.5$  values, respectively. The general shape of the data points in the  $\varphi - Pe$  diagram has the same characteristics as the previously investigated  $\varphi - \lambda$  diagrams. The quantity  $Pe_{peak}$  is defined corresponding to the  $\lambda_{peak}$  in the previous plots. The increase of the *Péclet* number can be interpreted as the deviation of the reaction from the diffusion-controlled solidification processes. Hence, larger scatterings in both  $R = 1.5$  and  $2.5$  values occur in this plot for  $Pe > Pe_{peak}$ . The increase of the additional oscillations in the solidified phase boundaries is due to this effect either.

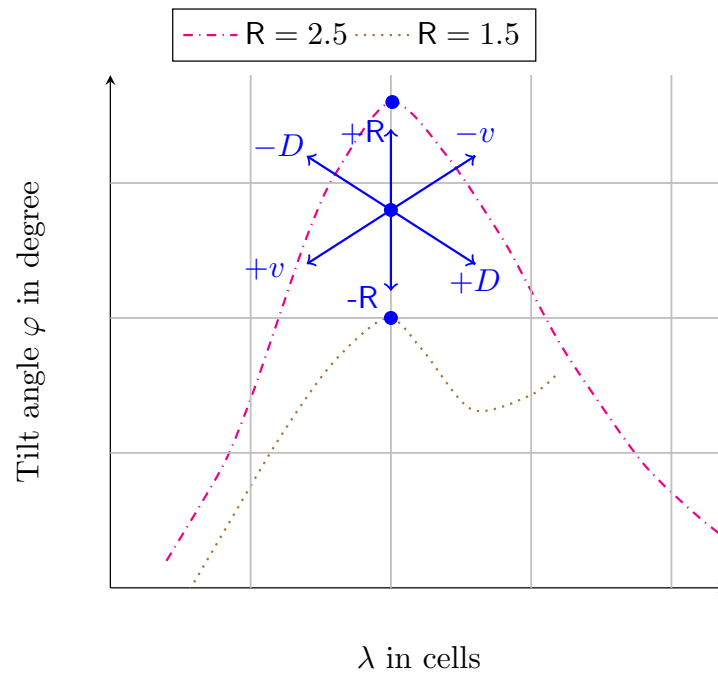


Figure 6.36: The schematic illustration of the location shifts in the peaks of the  $\varphi - \lambda$  plots, as the result of the variations in the investigated material and process parameters based on [156].  $D$ : diffusion coefficient,  $v$ : solidification velocity and  $R = \gamma_{\alpha\beta}/\gamma_{\alpha l}$ .

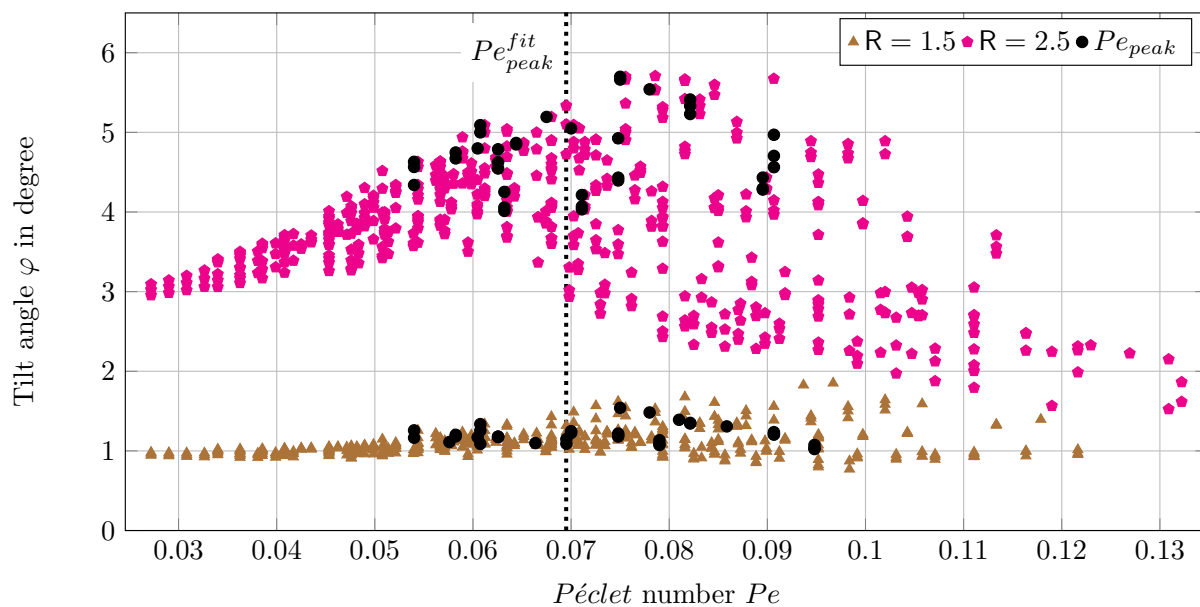


Figure 6.37: The variation of the measured tilt angles with respect to the Péclet number based on [156]. The dashed line refers to the value of  $Pe_{peak}^{fit} = 0.0695$ .

### 6.4.4 Approximation of the tilt angle

A fitting procedure is introduced here in order to predict the resultant tilt angles based on the investigated material and process parameters. This is performed due to the lack of a general analytic relation, characterizing the actual dependencies between the affecting parameters on the tilting phenomenon. In fig. 6.37, two different behaviors are observed in the resultant tilt angles with respect to the corresponding *Péclet* numbers: In  $Pe \leq Pe_{peak}$ , the stable lamellar patterns are observed, whereas in  $Pe > Pe_{peak}$  oscillations in the solidified phase boundaries occur. These oscillations are the result of the interplay between the diffusion and the solidification velocities. The following piecewise function is constructed of two different formulas in the *Péclet* domain, each representing the mentioned behaviors:

$$\varphi(D, v, \lambda, R) [^\circ] = \begin{cases} A_1 (\lambda Pe)^2 + B_1 (\lambda Pe) + C_1 & \text{if } Pe \leq Pe_{peak}^{fit} \\ A_2 (vD^{5/3} Pe^2)^2 + B_2 (vD^{5/3} Pe^2) + C_2 & \text{else.} \end{cases} \quad (6.3)$$

In order to derive eq. (6.3), the plotted values in fig. 6.37 are mapped into two different spaces to reduce their scatterings. I.e. the  $Pe$ , is mapped into  $\lambda Pe$  in  $Pe \leq Pe_{peak}$ , and it is mapped into  $vD^{(5/3)} Pe^2$  in  $Pe > Pe_{peak}$ , respectively. For  $R = 1.5$ , the average scattering value before the mapping is  $12.4^\circ$  with the variance of 0.09, whereas the scattering and variance values are  $47.03^\circ$  and 1.22 for  $R = 2.5$ , respectively. After the mapping, the scattering and the variance are reduced to  $8.53^\circ$  and 0.042 for  $R = 1.5$  and are reduced to  $29.56^\circ$  and 0.157 for  $R = 2.5$ . A second-order polynomial function is fitted after the mentioned mappings to attain eq. (6.3). The interfacial-energy-dependant coefficients  $A_i, B_i$  and  $C_i, i = 1, 2$  are calculated by a linear least square fit and the results are listed in Table 6.3.

Table 6.3: The interfacial-energy-ratio-dependent coefficients of eq. (6.3) based on [156].

$i$	$A_i$	$B_i$	$C_i$
1	$-0.05006R + 0.07668$	$0.6939R - 1.0133$	$0.95145R - 0.52444$
2	$15712117.267R - 22670209.5675$	$-15945.0451R + 22172.76245$	$5.36291R - 6.529$

A cross-validation technique is used for the investigated velocities and diffusivities which results in an average error of 7.28% in the fitted function. This convincing error value indicates the applicability of the calculated function in the investigated  $Pe$  domain. Based on the noticed less impact of the temperature gradient on the tilt angle in section 6.4.3.3, this parameter is neglected in the fitted function. By systematically

minimizing the occurred average error in eq. (6.3),  $P_{peak}^{fit}$  is calculated to be 0.0695 as shown by the black dotted line in fig. 6.37.

In fig. 6.38, a comparison is made between the measured and the predicted tilt angle values in order to validate the fitted function. In the plotted amounts, the average deviations between the two axis are  $0.07^\circ$  (6.1%) for  $R = 1.5$  and  $0.24^\circ$  (6.87%) for  $R = 2.5$ . The values  $1.031^\circ$  (32%) and  $0.55^\circ$  (37.1%) are the maximum errors in the mentioned interfacial energy ratios.

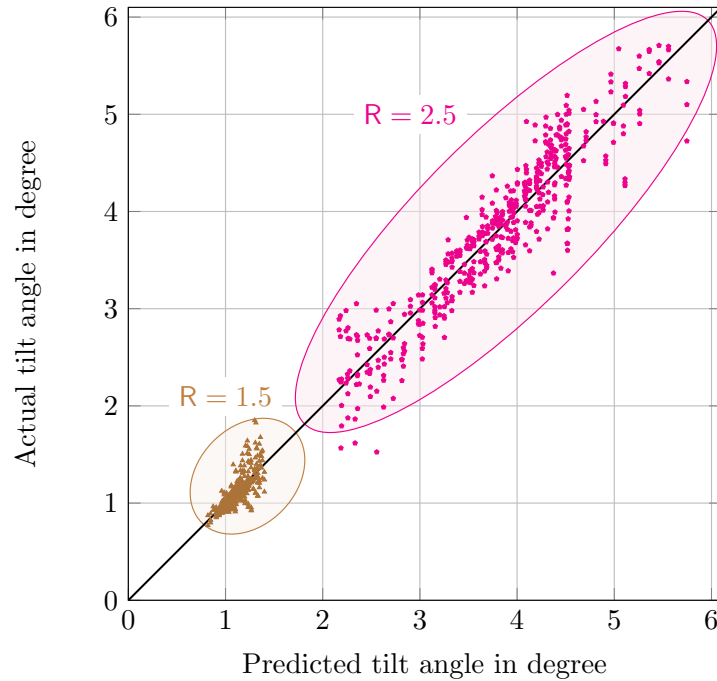


Figure 6.38: Comparison of the predicted and the measured tilt angles for the values of  $R = 1.5$  and  $R = 2.5$  based on [156].

A selective pairs of the measured and the predicted tilt angles are compared in fig. 6.39 for further visual comparisons between these amounts and to show the capability of the fitted function to predict the correct tilt angles. As it can be noticed, both solid and dashed curves show the same trends in each configuration.

### 6.4.5 Summary and conclusions

In this section,  $DS$  studies in an idealized ternary eutectic system are performed to find out the effects of the material and process parameters on the resultant tilt angles. The interfacial energies are assumed to be isotropic in this study. For different combinations of the interfacial energy ratios, solidification velocities, diffusion coefficients, temperature

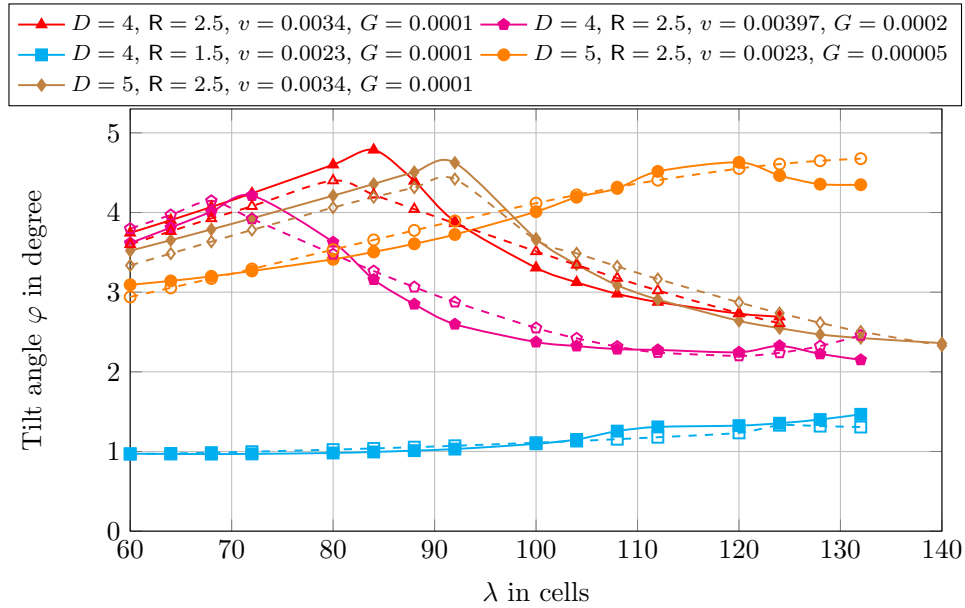


Figure 6.39: Comparison of the predicted (dashed curves with the unfilled marks) and the measured (solid curves with the filled marks) based on [156].

gradients and spacings, directional solidification simulations are conducted and the resultant tilt angles are measured. An unsupervised and automated technique is implemented to analyze the simulations and measure the evolved angles. The saved measurement results serve as the basis for fitting a function to predict the tilt angles as the final task in this section. The conclusions can be summarized as follows:

1. At a certain lamellar spacing, high tilt angles are achieved with high interfacial energy ratios, low velocities, and low diffusion coefficients.
2. The temperature gradient has the least influence on the formed tilt angles among the investigated parameters.
3. The observed tilting is the result of both interface energy-driven [67] and concentration-driven [159] mechanisms, with a complicated interplay between the driving forces caused by the undercoolings and the concentration fluxes. Thus, it is difficult to reach a general description to explain the influences of these parameters independently.
4. The approximated fitting function predicts the resultant tilt angles fairly accurately.
5. The observed trends and demonstrations in this study can be utilized in other similar idealized systems, as the investigated parameters are studied in a wide variational ranges.



# Chapter 7

## Summary and outlook

The utilized grand-potential-based phase-field model has shown convincing results in the simulation studies of the solidification processes in current study. The approximated Gibbs energy functions by means of the second-order polynomials are reliable in the representation of the thermodynamic properties. The method to approximate these functions works based on the calculation of the equilibrium conditions and the Gibbs energy values from the CALPHAD databases. The calculations are completed for all of the involved phases in the selected temperatures below the melting point. Consequently, the energy functions are constructed in the forms of the second-order polynomials as the functions of the element concentrations and the temperature, respectively. NiAl-10Mo and Bi-In-Sn ternaries are the material systems for which the Gibbs energy functions are approximated in order to simulate the eutectic solidification processes. To test the accuracy of the approximated functions, the equilibrium conditions between the involved phases of the reactions are recalculated and compared with the original CALPHAD data. Good compatibilities are observed indicating the appropriateness of these functions.

Directional and rotating directional solidification techniques are the two experimental methods which have been simulated in order to study the effects of the anisotropic interfacial energies on the evolved microstructures. In the performed three-dimensional *DS* studies in the NiAl-10Mo system, the experimentally reported fibrous microstructure with the hexagonal arrangement of the fibers in the matrix phase is resulted. The initially filled circular fibers are evolved into cubic shapes due to the effect of the anisotropic interfaces. The evolved fiber shapes are in good accordance with the experimental reports in the literature [35]. The *DS* and *RDS* studies are conducted to simulate the eutectic reaction in the Bi-In-Sn ternary system in two dimensions. In literature, the product which has three constituent solid phases is reported to have the  $\alpha\beta\alpha\delta$  phase arrangement when the interfaces are formed isotropically. In contrast, the formation of  $\alpha\beta\delta$  or  $[\alpha\beta]_a[\alpha\delta]_b$  units are reported either due to the anisotropic interfacial energies [22, 89, 90]. Hence,

the *DS* simulations in the current work are performed with both types of interfaces in order to study the anisotropy effects precisely. To enhance the possibility of free phase evolution in the simulations of the Bi-In-Sn system, two main opportunities are active in the simulations: First, the initial solid phases beneath the liquid phase are filled in Voronoi tessellations which gives more freedom to the system to choose its pattern, compared to the bulk fillings of the initial solid phases. Second is the nucleation mechanism which makes the possibility of new phases establishments in further steps of the simulation and the pattern changes, consequently. It is observed that, good accordances with the mentioned experimental results are achieved in formations of  $\alpha\beta\alpha\delta$ ,  $\alpha\beta\delta$ ,  $\beta\alpha\delta$  and  $[\alpha\beta]_a[\alpha\delta]_b$  units. Thus, the  $\alpha\beta$  and  $\alpha\delta$  interface anisotropies are activated (individually or simultaneously) and systematic studies on their effects on the formed microstructures are performed. In cases of anisotropic  $\alpha\beta$  interfaces,  $\beta\alpha\delta$  and  $[\alpha\beta]_1[\alpha\delta]_2$  patterns are formed. Furthermore, the anisotropic  $\alpha\delta$  interface modeling results in the formation of  $\alpha\beta\delta$ ,  $[\alpha\beta]_1[\alpha\delta]_2$  and  $[\alpha\beta]_2[\alpha\delta]_1$  units in the simulations. In order to explain this behavior, a schematic illustration in fig. 6.17 is presented in which the phase elimination is the responsible event in the formation of these patterns. If we consider the natural tendency of the floating grains to form the  $\alpha\beta\alpha\delta$  patterns, the later units in the locked grains can be formed by elimination of the different lamellae in the already formed  $\alpha\beta\alpha\delta$  sequences. Or the lamellae formation can be prevented from the initial steps of the simulations, instead. In addition, the more dominant role of the  $\alpha\beta$  interface anisotropy on the final microstructure compared to the  $\alpha\delta$  anisotropy is observed. This observation confirms well the experimental results [90].

In order to enhance the anisotropy-related understanding of the ongoing mechanisms in the solidification processes, the *RDS* simulations are completed as the next step in this work. To conduct these simulations, a rotating temperature profile is formulated to resemble the effects of the rotating disks and the influences of the hot and cold blocks in the experiments. In this configuration, as anticipated, the circular trajectories are evolved in the solidified phase boundaries when the grains are modeled isotropically. On the contrary, in the simulations of the locked grains, the inclined phases with respect to the imposed temperature gradients are evolved. It is observed that when the initial solid phases are filled in the  $\alpha\beta\alpha\delta$  patterns, the first  $\alpha$  lamellae are eliminated in the anisotropic  $\alpha\beta$  cases. This causes the formation of the  $\beta\alpha\delta$  sequences in the final microstructures. In contrast, the second  $\alpha$  lamellae are eliminated forming the  $\alpha\beta\delta$  patterns when the  $\alpha\delta$  interfaces are modeled anisotropically. The results in general affirm the previous conclusions made by the *DS* simulation results. It is also discovered that, in order to have the parallel  $\alpha\beta$  and  $\alpha\delta$  phase boundaries in the evolved locked grains, the anisotropy strength in the  $\alpha\delta$  interfaces has to be higher than  $\alpha\beta$  phase boundaries. This is new evidence for the more significant role of the  $\alpha\beta$  interface in the formation of final microstructures.

In order to investigate more precisely the tilting phenomenon and study its affecting parameters, further *DS* simulations are performed as the final research in this work. An idealized ternary system is selected for this purpose which is previously introduced by Hötzer et al. in [67]. In this system, the Gibbs energy paraboloid representing the liquid phase is postulated to be in the centroid of the ternary diagram. The three solid phases which represent the products of the process are located at equal distances from the liquid phase. The phases are modeled with the congruent paraboloids and have the initial  $\alpha\beta\delta$  arrangement filled with the equal phase fractions. This system is selected due to its symmetric structure which reduces the complexities caused by the material properties. The studied parameters are the ratio of the interfacial energies, the solidification velocity, the diffusion coefficients in the melt, the temperature gradient and the lamellar spacing, respectively. An automatized technique is implemented to measure the resultant tilt angles in each configuration in an accurate manner. It is observed that the variation in the temperature gradient has the least impact on the resultant tilt angles. In each configuration, the  $\varphi - \lambda$  plots are noticed to have an extremum point which is the local maximum if the interfacial energy ratio is 1.5 and is the global maximum if  $R = 2.5$ . The increase of  $R$ , the decrease of diffusion and the decrease of velocity lead to the increase of this extremum tilt angle. The influences of the two main mechanisms in the tilted growth which are the interfacial-energy driven [67] and concentration-driven [159] mechanisms are studied. It is noticed that, due to the complicated interplay between these mechanisms, it is difficult to reach a unique and general explanation on the cause of the solid phase tilting. Meanwhile, based on the obtained results, a fitting function is derived to approximate the tilt angles with respect to the system and process parameters. This function can be used in similar ternary systems either.

As the future directions, the large-scale 3D simulations with the Voronoi tessellations of the solid phases in the *DS* studies of **NiAl-10Mo** system can be performed. The affecting parameters on the arrangements and shapes of the evolved fibers can be studied, respectively. In addition to the performed qualitative study in *RDS* of the **Bi-In-Sn** system, quantitative simulations can be conducted in the future. This needs further optimizations of the current solver to make the possibility of the larger-scale 2D or quasi-2D simulations. The formulation of the barrier has to be optimized either, to solve the current need for a thin solid layer placement in the near-barrier segments of the simulation domain. The evolved phase fractions and the lamellar spacing values in the simulations can be affected, respectively. By investigating the quasi-2D simulations, the experimentally reported mechanisms in the formation of the physical effects like the phase exchange can be studied. It is intended that such investigations can reveal more facts about the principles of pattern formation.



# Acknowledgements

I would like to express my ultimate thanks towards my supervisor, professor Britta Nestler. Her continuous helps and supports made the possibility to accomplish the present thesis. I wish to acknowledge Prof. H. J. Seifert to be the referee of my dissertation. I am indebted to Dr. Michael Kellner who has helped a lot with sharing his valuable ideas in different scientific topics related to my research. I want to acknowledge Dr. Johannes Hötzer, Dr. Philipp Steinmetz, Mr. Marco Seiz, Mr. Henrik Hierl, Mr. Leon Geisen and Mr. Martin Bauer for the valuable consults and discussions which we have made in recent years. Many thanks to Prof. Mathis Plapp, Prof. Peter W. Voorhees and Prof. M. P. Gururajan for their very beneficial phase-field lectures from which I have learnt a lot. I am particularly thankful to the following agencies for providing the funding directly to this work or the related published articles: Helmholtz School "Integrated Materials Development for Novel High Temperature Alloys" with grant number VH-KO-610 at the Karlsruhe Institute of Technology (KIT), DFG project PAK 983/1 with the title "Phase-field simulation and experimental microstructure research" and the grant number MU 959/48, German Research Foundation for financial support within the project NE 822/14-2, the cooperative graduate school "Gefügeanalyse und Prozessbewertung" provided by the Ministry of Baden-Württemberg, the BMBF project SKAMPY provided by the German Ministry for Education and Research, the "Future Field" project "AcDC" of KIT and the Science Data Center "MoMaF" of the state Baden-Württemberg. I am also grateful for the prepared computational resources at the LRZ in Munich and bwUniCluster at KIT.

Finally, I thank my dear parents and my loving wife who have always supported me and have given me enthusiasm for hard work.



# Appendix A

## Appendices to chapter 5

### A.1 NiAl-10Mo system

Table A.1: Initial approximation results for the Gibbs energies of the NiAl-10Mo system based on [132]. Temperature 1871 K is used to calculate and compare the values of the Gibbs energies  $g$  and the chemical potentials  $\mu$  for different phases. *cal*: CALPHAD, *app*: approximated.

	matrix	fiber
$a_0(T)$	$-369.357T + 1165139.34$	$9734.081T - 15371378.8$
$a_1(T)$	$-7534.719T + 16621024.7$	$623.056T + 1570729.46$
$a_2(T)$	$769.721T - 1002807.01$	$8906.432T - 11229403.9$
$a_3(T)$	$391.801T - 1213214.43$	$-9715.107T + 12721894.7$
$a_4(T)$	$-373.727T + 534072.403$	$-1829.783T - 1984717.23$
$a_5(T)$	$-181.196T + 300714.575$	$1134.614T + 445115.066$
<i>ave dev</i> of $g_{app}$	0.00056%	0.0018%
<i>max dev</i> of $g_{app}$	0.003%	0.01%
$g_{app}^{eq} _{T=1871}$	-159765.182	-110198.043
$g_{cal}^{eq} _{T=1871}$	-159764.69	-110201.01
$\mu_0^{eq} = \frac{\partial g_{app}}{\partial c_0} _{T=1871}$	-10948.541913	-9321.194
$\mu_1^{eq} = \frac{\partial g_{app}}{\partial c_1} _{T=1871}$	55718.5782008	51125.910

liquid	
$a_0(T)$	$-57.489T + 281291.566$
$a_1(T)$	$-18.487T + 96784.103$
$a_2(T)$	$-24.348T + 179006.613$
$a_3(T)$	$64.605T - 297000.385$
$a_4(T)$	$11.553T - 42453.014$
$a_5(T)$	$-110.433T + 91835.592$
<i>ave dev</i> of $g_{app}$	0.000133%
<i>max dev</i> of $g_{app}$	0.0002%
$g_{app}^{eq} _{T=1871}$	-154505.98
$g_{cal}^{eq} _{T=1871}$	-154506.22
$\mu_0^{eq} = \frac{\partial g_{app}}{\partial c_0} _{T=1871}$	-11004.706
$\mu_1^{eq} = \frac{\partial g_{app}}{\partial c_1} _{T=1871}$	49482.931

Table A.2: Modified approximated Gibbs energy functions of the NiAl-10Mo system, used for the phase-field simulations in this work based on [132]. The exemplary temperature of 1871 K, below the melting point, is utilized to calculate and compare the values of the Gibbs energies  $g$  and the chemical potentials  $\mu$  for the different phases. *app*: approximated, *mod*: modified, *cal*: CALPHAD, *eq*: equilibrium.

	matrix	fiber
$a_0(T)$	$-1300.426T + 2902628.20$	$-3054.022T + 8548519.30$
$a_1(T)$	$-7970.744T + 17433820.7$	$-11806.786T + 24817509.4$
$a_2(T)$	$-102.330T + 622785.006$	$-15955.736T + 35269065.2$
$a_3(T)$	$1449.528T - 3185144.56$	$15252.910T - 33974178.4$
$a_4(T)$	$116.916T - 385991.425$	$23020.250T - 48460728.9$
$a_5(T)$	$-476.573T + 850980.846$	$-11292.974T + 23688082$
<i>ave dev</i> of $g_{app,mod}$	0.0083 %	0.003 %
<i>max dev</i> of $g_{app,mod}$	0.02 %	0.013 %
$g_{app,mod}^{eq} _{T=1871}$	-159764.392	-110201.12
$g_{cal}^{eq} _{T=1871}$	-159764.69	-110201.01
$\mu_{mod,0}^{eq} = \frac{\partial g_{app,mod}}{\partial c_0} _{T=1871}$	-8367.87	-8382.58
$\mu_{mod,1}^{eq} = \frac{\partial g_{app,mod}}{\partial c_1} _{T=1871}$	50667.43	50676.25

	liquid
$a_0(T)$	$-138.250T + 430879.432$
$a_1(T)$	$-945.677T + 1821352.34$
$a_2(T)$	$-274.839T + 642835.112$
$a_3(T)$	$294.671T - 723028.985$
$a_4(T)$	$357.285T - 684080.383$
$a_5(T)$	$-209.938T + 276459.004$
<i>ave dev of <math>g_{app}</math></i>	0.002 %
<i>max dev of <math>g_{app}</math></i>	0.007 %
$g_{app,mod}^{eq} _{T=1871}$	-154506.26
$g_{cal}^{eq} _{T=1871}$	-154506.22
$\mu_{mod,0}^{eq} = \frac{\partial g_{app,mod}}{\partial c_0} _{T=1871}$	-8366.74
$\mu_{mod,1}^{eq} = \frac{\partial g_{app,mod}}{\partial c_1} _{T=1871}$	50669.495

## A.2 Bi-In-Sn system

Table A.3: The parameters of the approximated Gibbs energy functions in the simulation studies of the Bi-In-Sn ternary eutectic based on [91]. The approximated function values  $g$  with the original CALPHAD data are compared at the exemplary temperature of 331 K. The resultant chemical potentials  $\mu$  for the involved phases are compared either. *eq*: equilibrium, *app*: approximated, *cal*: CALPHAD.

	$\alpha$	$\beta$		
$a_0(T)$	$3014.607T - 896340.473$	$-143.363T + 55902.219$		
$a_1(T)$	$7087.078T - 2189377.1803$	$138.230T - 37075.096$		
$a_2(T)$	$3296.242T - 929782.259$	$355.122T - 115506.027$		
$a_3(T)$	$-4116.795T + 1186641.527$	$-255.378T + 78337.588$		
$a_4(T)$	$-10523.232T + 3220675.0386$	$-198.487T + 51646.124$		
$a_5(T)$	$4106.939T - 1263269.831$	$3.884T - 15477.151$		
	$\delta$	liquid		
$a_0(T)$	$-871.762T + 301469.411$	$-13.421T + 13192.535$		
$a_1(T)$	$122.777T - 26128.366$	$12.381T + 4229.506$		
$a_2(T)$	$348.878T - 139478.362$	$23.675T - 5488.634$		
$a_3(T)$	$22.402T - 5281.841$	$-20.932T - 1575.961$		
$a_4(T)$	$-154.236T + 40925.907$	$-14.338T - 8078.906$		
$a_5(T)$	$-30.836T - 6902.264$	$-70.776T + 8898.941$		
	$\alpha$	$\beta$	$\delta$	liquid
$g_{\text{app}}^{\text{eq}} _{331\text{K}}$	-20879.5	-20042.9	-19632.7	-20315.536
$g_{\text{cal}}^{\text{eq}} _{331\text{K}}$	-20885.512	-20047.493	-19650.776	-20315.829
$\mu_{\text{app},1}^{\text{eq}} = \frac{\partial g_{\text{app}}}{\partial c_{\text{In}}} _{331\text{K}}$	-2294.85	-2266.95	-2315.73	-2294.48
$\mu_{\text{app},0}^{\text{eq}} = \frac{\partial g_{\text{app}}}{\partial c_{\text{Bi}}} _{331\text{K}}$	-3522.53	-3470.85	-3449.36	-3521.90

# Appendix B

## Appendices to chapter 6

### B.1 NiAl-10Mo system

Table B.1: The used dimensionless simulation and numerical parameters in the DS studies of the NiAl-10Mo system and their values in physical units based on [132]. *F*: fiber, *M*: matrix, *L*: liquid, *eut*: eutectic.

Parameter	Simulation value	Physical value
$G^{DS}$	$1.31 \cdot 10^{-7}$	$33.4 \text{ K mm}^{-1}$ [35]
$T_{eut}$	1.0	1875.47 K
$\gamma_{ML}$	$8.84 \cdot 10^{-3}$	$0.65 \text{ J m}^{-2}$
$\gamma_{FL}$	$8.84 \cdot 10^{-3}$	$0.65 \text{ J m}^{-2}$
$\gamma_{MF}$	$8.84 \cdot 10^{-3}$	$0.65 \text{ J m}^{-2}$
$\gamma_{MFL}$	$15 \cdot \gamma_{\hat{\alpha}\hat{\beta}}$	
$\mathbf{D}$	3.68	$10^{-3} \text{ mm}^2 \text{ s}^{-1}$ [160]
$\tau_{MF}, \tau_{FM}$	8.5	calculated
$\tau_{ML}, \tau_{LM}$	0.00168	from
$\tau_{FL}, \tau_{LF}$	0.094	[39]
$dx$	1.0, 2.0	$0.00737, 0.00368 \text{ }\mu\text{m}$
$dt$	0.02, 0.06	$4, 12 \cdot 10^{-9} \text{ s}$
$\epsilon$	4	29.48 nm
$\zeta_{\hat{\alpha}\hat{\beta}}$	0.07	in range of used amounts in [161]

## B.2 Bi-In-Sn system

Table B.2: The utilized simulation parameters and their physical values in the DS and RDS studies of the Bi-In-Sn ternary eutectic system based on [91].  $\alpha$  : BiIn<sub>2</sub>,  $\beta$  :  $\beta$  - In,  $\delta$  :  $\gamma$  - Sn,  $L$  : liquid iso: isotropic simulation, anis: anisotropic simulation,  $m$  : melting point, eut: eutectic.

Parameter	Simulation value	Physical value
$A_0$	0.001374	0.456 K
$T_m$	0.99937	331.79 K
$T_{eut}$	1	332 K [114]
$\gamma_{\alpha\beta}, \gamma_{\beta\delta}, \gamma_{\beta L}$	$9.26 \cdot 10^{-4}$	$0.2888 \text{ J m}^{-2}$
$\gamma_{\alpha\delta}, \gamma_{\alpha L}$	$2.78 \cdot 10^{-4}$	$0.0866 \text{ J m}^{-2}$
$\gamma_{\delta L}, \gamma_{L\delta}$	$4.63 \cdot 10^{-4}$	$0.1444 \text{ J m}^{-2}$ [162]
$\gamma_{\hat{\alpha}\hat{\beta}\hat{\delta}}$	$15 \cdot \gamma$	-
$G^{DS}$	$7.52 \cdot 10^{-6}$	$8 \text{ K mm}^{-1}$
$G^{RDS}$	$7.4 \cdot 10^{-6} - 2.255 \cdot 10^{-4}$	$0.786 - 240 \text{ K mm}^{-1}$
$D_{\hat{\alpha}L}$	0.62	$10^{-9} \text{ m}^2 \text{ s}^{-1}$ [163]
$\omega$	$3.24 \cdot 10^{-7}$	$0.309 \text{ }^\circ \text{ s}^{-1}$
$\tau_{\alpha\beta}, \tau_{\beta\delta}$	13.64	} calculated from [39]
$\tau_{\alpha\delta}, \tau_{\delta\alpha}$	21.68	
$\tau_{\alpha L}, \tau_{L\alpha}$	1.45	
$\tau_{\beta L}, \tau_{L\beta}$	2.73	
$\tau_{\delta L}, \tau_{L\delta}$	1.31	
$\zeta_{\hat{\alpha}\hat{\beta}}^{iso}$	0	-
$\zeta_{\hat{\alpha}\hat{\beta}}^{aniso}$	in range of 0.025 and 0.45	-
$dx$	1.0	$0.312 \text{ } \mu\text{m}$
$dt$	0.2	$1.2 \cdot 10^{-5} \text{ s}$
$A$	5.0	-
$i$	400	-
$c_{limit}$	5%	-

### B.3 Idealized system

Table B.3: Parameters of the idealized system with the symmetric phase diagram and the equal phase fractions based on [67]. The liquid phase is placed in the center of the ternary diagram and the solid phases  $\alpha, \beta, \delta$  are placed around the center symmetrically.  $\Xi, \xi, X$  are the Gibbs energy parameters of the phases.  $w$ : phase fraction.

Parameter	Simulation value				Physical value			
	phase	$\alpha$	$\beta$	$\delta$	$l$			
$\gamma$	$\alpha$	$\begin{bmatrix} - & \gamma_{\alpha\beta} & 0.2 & \gamma_{\alpha l} \\ \gamma_{\alpha\beta} & - & 0.2 & 0.2 \\ 0.2 & 0.2 & - & 0.2 \\ \gamma_{\alpha l} & 0.2 & 0.2 & - \end{bmatrix}$				0.1 J m <sup>-2</sup>		
	$\beta$							
	$\delta$							
	$l$							
	$R_1)$	$R_2)$	$R_3)$		$R_1)$	$R_2)$	$R_3)$	
$\gamma_{\alpha\beta}$	0.24	0.2875	0.3		0.12	0.1436	0.15	J m <sup>-2</sup>
$\gamma_{\alpha l}$	0.16	0.1125	0.1		0.08	0.0563	0.05	
$R$	1.5	2.5	3.0		1.5	2.5	3.0	
$D$	$d_1)$	$d_2)$	$d_3)$		$d_1)$	$d_2)$	$d_3)$	$\cdot 10^{-9}$ m <sup>2</sup> s <sup>-1</sup>
	3	4	5		4.59	6.08	7.6	
$\gamma_{\hat{\alpha}\hat{\beta}\hat{\delta}}$	2.6				1.3	J m <sup>-2</sup>		
$\mathbf{c}_l = [c_A^l, c_B^l, c_C^l]$	0. $\bar{3}$ , 0. $\bar{3}$ , 0. $\bar{3}$				0. $\bar{3}$ , 0. $\bar{3}$ , 0. $\bar{3}$	mol-fraction		
$w_\alpha, w_\beta, w_\delta$	0. $\bar{3}$ , 0. $\bar{3}$ , 0. $\bar{3}$				0. $\bar{3}$ , 0. $\bar{3}$ , 0. $\bar{3}$			
$T_{eut}$	1.0				773.6	K		
$G^{DS}$	$G_1)$	$G_2)$	$G_3)$	$\cdot 10^{-4}$	$G_1)$	$G_2)$	$G_3)$	K mm <sup>-1</sup>
	0.5	1	2		100	200	400	
$v$	$v_1)$	$v_2)$			$v_1)$	$v_2)$		$\cdot 10^{-3}$ mm s <sup>-1</sup>
	2.3	2.8			0.89	1.09		
	$v_3)$	$v_4)$			$v_3)$	$v_4)$		
	3.4	3.97			1.32	1.54		
$\lambda$	60 until 140				2.334 $\cdot 10^{-5}$ until 5.446 $\cdot 10^{-5}$	m		
$\Xi_\alpha, \xi_\alpha, X_\alpha$	$\begin{bmatrix} 2 & 1 \\ 1 & 2 \end{bmatrix},$	$\begin{bmatrix} -2.8 \\ -2.0 \end{bmatrix},$	1.04					

---

$$\begin{array}{l} \Xi_{\beta}, \xi_{\beta}, X_{\beta} \\ \Xi_{\delta}, \xi_{\delta}, X_{\delta} \\ \Xi_l, \xi_l, X_l \end{array} \begin{array}{l} \begin{bmatrix} 2 & 1 \\ 1 & 2 \end{bmatrix} \\ \begin{bmatrix} 2 & 1 \\ 1 & 2 \end{bmatrix} \\ \begin{bmatrix} 2 & 1 \\ 1 & 2 \end{bmatrix} \end{array}, \begin{array}{l} \begin{bmatrix} -2.0 \\ -2.8 \end{bmatrix} \\ \begin{bmatrix} -1.2 \\ -1.2 \end{bmatrix} \\ \begin{bmatrix} -2.0 \\ -2.0 \end{bmatrix} \end{array}, \begin{array}{l} 1.04 \\ 0.24 \\ 3.\bar{3} - 2.\bar{6}T \end{array}$$

---

# List of Symbols

Symbol	Description	Page No. (first used)
$N$	Total number of phase fields	6
$K$	Total number of components	6
$\mathbf{x}$	Space	6
$t$	Time	6
$\alpha\beta\delta, \dots, \eta$	Phase names	6
$\phi$	Phase field	6
$\Omega$	Simulation domain	6
$\boldsymbol{\phi}$	Phase-field vector	6
$c$	Concentration	6
$\mathbf{c}$	Concentration-field vector	6
$S$	Bulk entropy	6
$s$	Bulk entropy density	6
$e$	Internal energy of system	6
$\varepsilon$	Interface length	6
$a$	Gradient energy density	6
$w$	Potential energy density	6
$f_\alpha$	Free energy density of phase $\alpha$	6
$T$	Temperature	6
$\mu$	Chemical potential	7
$\boldsymbol{\mu}$	Chemical-potential vector	7
$\Psi$	Grand-potential functional	7
$\psi$	Driving force	7
$h$	Interpolation function	7
$\mathbf{q}$	Generalized gradient vector	8
$\gamma$	Interfacial energy	8
$\tau$	Kinetic coefficient of phase evolution	8
$\Lambda$	Lagrange multiplier	8
$M$	Mobility function	8

Symbol	Description	Page No. (first used)
$J_{at}$	Anti-trapping current	8
$D$	Diffusion coefficient matrix	9
$g$	Gibbs free energy	9
$g^0$	Gibbs energies due to the mechanical mixing	9
$^{id}g_{mix}$	Gibbs energies due to the ideal mixing	9
$^{xs}g_{mix}$	Excess energies of mixing	9
$a_c$	Anisotropy term	10
$\zeta$	Anisotropy strength	10
$dt$	Time step	11
$U$	Phase/chemical-potential field	12
$\xi_\delta$	Nucleation noise term	13
$A$	Nucleation noise Amplitude	13
$n_{dist}$	Nucleation noise distribution function	13
$i$	Nucleation test number	13
$c_{limit}$	Nucleation limit	13
$T_0$	Base temperature	15
$G^{DS}$	Temperature gradient in $DS$	15
$v$	Solidification velocity	15
$T_f$	Front temperature	15
$T_M$	Melting temperature	15
$\lambda$	Lamellar/Fiber spacing	16
$\Omega$	Rotating disk center	17
$T_{max}$	Maximum temperature	17
$T_{min}$	Minimum temperature	17
$T_m$	Rotating disk center temperature	17
$\omega$	Angular velocity	17
$G^{RDS}$	Temperature gradient in $RDS$	17
$\theta$	Rotational angle	18
$A_0$	Constant coefficient in $RDS$ formulation	18
$r$	Radius	19
$r_o$	Outer radius	19
$r_i$	Inner radius	19
$v_f$	Volume fraction	23
$R$	Gas constant	34
$a_0 - a_5$	Gibbs energies approximation coefficients	34
$K_1, K_2$	Constants of Jackson-Hunt relation	46
$\lambda_{JH}$	Jackson-Hunt spacing	46
$\lambda_{JH}^{sim}$	Jackson-Hunt spacing in simulation	47

Symbol	Description	Page No. (first used)
$\lambda_{min}^{exp}$	Experimentally measured minimum spacing	47
$\lambda_{max}^{exp}$	Experimentally measured maximum spacing	47
$\lambda_{ave}^{exp}$	Experimentally measured average spacing	47
$x_{growth}$	Growth distance	49
$\mathbf{r}$	$\zeta_{\alpha\delta}/\zeta_{\alpha\beta}$	84
$x^* - y^*$	Rotated $x - y$ coordination system	91
$\varphi$	Tilt angle	91
$\Xi, \xi, X$	Gibbs energy parameters	91
A, B, C	Concentration vector components	91
R	$\gamma_{\alpha\beta}/\gamma_{\alpha l}$	92
$A_i, B_i, C_i$	Interfacial-energy-dependant coefficients	100



# List of Abbreviations

Abbreviation	Description	Page No. (first used)
CALPHAD	CALculation of PhAse Diagrams	i
<i>DS</i>	Directional Solidification	i
<i>RDS</i>	Rotating Directional Solidification	i
eq.	Equation	8
<i>id</i>	Ideal	9
<i>xs</i>	Excess	9
PACE3D	Parallel Algorithms for Crystal Evolution in 3D	10
HPC	High-Performance Computing	10
WALBERLA	Widely Applicable Lattice-Boltzmann from ERLAngen	10
<i>BC</i>	Boundary Condition	12
<i>dist</i>	Distribute	13
<i>pos</i>	Position	15
<i>const</i>	Constant	17
<i>max</i>	Maximum	17
<i>min</i>	Minimum	17
<i>eq</i>	Equilibrium	32
<i>modi</i>	Modification	33
<i>app</i>	Approximated	37
<i>mod</i>	Modified	39
<i>sim</i>	Simulation	47
<i>dev</i>	Deviation	48
CPU	Central Processing Unit	49
<i>iso</i>	Isotropic	76
<i>aniso</i>	Anisotropic	76

---

<b>Abbreviation</b>	<b>Description</b>	<b>Page No. (first used)</b>
<i>exp</i>	Experimental	77
<i>ave</i>	Average	88
<i>Pe</i>	<i>Péclet</i>	98
<i>cal</i>	CALPHAD	110

# List of Figures

2.1	Schematic illustrations of (a): the spatial positions to calculate parameters of eq. (2.6) [50] and (b): the algorithm to calculate temporal evolutions of eqs. (2.6) and (2.7) with the time step of $dt$ [64]. . . . .	11
3.1	Schematic illustrations of the experimental setups in directional solidification for (a): bulk samples [72] and (b): thin samples [86]. . . . .	15
3.2	Schematic illustrations of (a): the temperature formulation in eq. (3.1), (b) and (c): the utilized setups in the <i>DS</i> studies of two- and three-dimensional simulations. . . . .	16
3.3	Schematic illustrations of (a): <i>RDS</i> setup based on the experimental work of Mohagheghi et al. [90]. (b): The temperature profile in <i>RDS</i> simulations (eq. (3.4)) at time = 0. $T_{max}$ and $T_{min}$ represent the temperatures of the hot and cold blocks or the considered maximum and minimum temperatures in the simulations, respectively. The solidification/melting fronts are located in the "high-temperature gradient area" [91]. . . . .	17
3.4	Schematic illustration of the <i>RDS</i> setup based on [91]. The simultaneous effects of the temperature and concentration fields on the whole domain are shown by the semicircle depictions for the sake of simplicity. . . . .	19
4.1	Bottom left: The ternary diagram of the Ni-Al-Mo system including the liquidus projections. Dashed line: The isopleth matrix-fiber connecting cut of NiAl-10Mo ternary eutectic. Top left: The eutectic concentrations of the elements in the constituent phases at $T = 1875.47$ K. Right: Two-dimensional phase diagram in the isopleth cut of the ternary diagram. All data are based on the CALPHAD database of [113]. . . . .	24
4.2	Ternary diagram of the Bi-In-Sn system [114] including the liquidus projections and the concentrations of the elements in the eutectic reaction. . . . .	28

5.1	Flowchart of the Gibbs energies approximation algorithm, used in the current work based on [132]. . . . .	33
5.2	The liquidus projections of the ternary system Ni-Al-Mo based on [113]. In the magnified regions, the calculation points with a spacing of $\Delta x = 0.1 \text{ mol} - \% \text{Mo}$ , $\Delta y = 0.1 \text{ mol} - \% \text{Al}$ around the equilibrium (bold point) for each phase are shown in the temperature $T = 1871 \text{ K}$ . The dashed line indicates the later used isopleth section for the NiAl-10Mo ternary eutectic.	37
5.3	Comparisons between the generated Gibbs energy curves (solid lines) with the CALPHAD database in the NiAl-10Mo system [113] for matrix, fiber and liquid phases. The temperature is 1871 K and the concentrations of Mo are shown next to each curve. (a): The initial approximation results before modification (Table A.1), (b): The modified Gibbs energy functions (Table A.2) based on [132]. . . . .	38
5.4	Rebuilding of the CALPHAD phase diagram in the NiAl-10Mo system (the blue lines) as illustrated in fig. 4.1 (the black lines). This is performed by the initially approximated Gibbs energy formulations in Table A.1. T is the temperature in Kelvin and C is the concentration of Mo in mol-%. The segments I, II and III are the areas in the vicinity of the fiber, liquid and matrix phases, respectively. . . . .	39
5.5	Rebuilding of the CALPHAD phase diagram in the NiAl-10Mo system (the blue lines) as illustrated in fig. 4.1 (the black lines). This is performed by the modified Gibbs energy formulations in Table A.2 (blue lines). T is the temperature in Kelvin and C is the concentration of Mo in mol-%. The segments I, II and III are the the areas in vicinity of the fiber, liquid and matrix phases, respectively. . . . .	40
5.6	The comparisons between the equilibrium concentrations in the involved phases of the eutectic reaction in the Bi-In-Sn system, based on the CALPHAD data (solid points) [114] and the approximated functions in this work (solid lines) [91]. . . . .	42
6.1	2D simulation result of the eutectic solidification in the NiAl-10Mo ternary system with the growth velocity $v = 30 \mu\text{m s}^{-1}$ . Top: the illustration of the Mo-rich fiber embedded in the NiAl-rich matrix, below the liquid phase in a single lamella based on [132]. Bottom: the plots of the concentration fields in the middle of the individual phases. . . . .	46

- 6.2 The Jackson-Hunt analysis results of the simulation studies in the NiAl-10Mo system based on [132]. (a): comparison of the obtained minimums in the simulations with the minimum, the maximum and the average experimental values of [35]. (b): comparison of the simulation results with the analytic solution proposed in [115] and the average values of the fiber spacings in [35]. exp: experimental, sim: simulation, max: maximum, min: minimum, ave: average. . . . . 48
- 6.3 2D simulation of the fibrous microstructure in eutectic solidification of the NiAl-10Mo system with Voronoi tessellation of the initial nuclei. The solidification velocity is  $30 \mu\text{m s}^{-1}$ . The solid-liquid interface profiles as well as the evolving microstructures in different growth distances are illustrated on the left. The concentration of Mo in the involved phases is depicted in this figure. . . . . 50
- 6.4 Evolution of the fibers in the eutectic solidification of the NiAl-10Mo system from the initial circular filling to the final square shape. The shape change is due to the anisotropy of the interfacial energies. . . . . 51
- 6.5 Top: the simulation result of the  $DS$  process in the Bi-In-Sn ternary eutectic system with  $v = 0.5 \mu\text{m s}^{-1}$  and  $G^{DS} = 8 \text{ K mm}^{-1}$ .  $\alpha$ :  $BiIn_2$ ,  $\beta$ :  $\beta - In$  and  $\delta$ :  $\gamma - Sn$  crystalline phases are illustrated with the yellow, blue and violet colors, respectively. Bottom: Jackson-Hunt plots showing the undercooling-spacing relations at the different growth rates.  $JH$ : Jackson-Hunt,  $sim$ : simulation based on [91]. . . . . 55
- 6.6 An exemplary illustration of the  $\alpha$  and  $\delta$  phase nucleations leading to the recovery of the  $\alpha\beta\alpha\delta$  pattern in the small spacings ( $\lambda \ll \lambda_{JH}^{sim}$ ). The solidification velocity is  $v_2 = 0.5 \mu\text{m s}^{-1}$ . At the higher spacing values (for example  $\lambda = 23.4 \mu\text{m}$ ) the similar results to fig. 6.5 are acquired without further instabilities. . . . . 56
- 6.7 The interfacial energy plots of the anisotropic interfacial energies for (a):  $\alpha\beta$  and (b):  $\alpha\delta$  phase boundaries.  $\zeta$  stands for the anisotropy strength in eq. (2.13). . . . . 57
- 6.8 Simulation results of the  $DS$  process in the Bi-In-Sn ternary system with the Voronoi tessellation of the initial solid phases. (a): the isotropic interfacial energies ( $\zeta_{\alpha\beta}=\zeta_{\alpha\delta}=\zeta_{\beta\delta}=0$ ), (b): the anisotropy in the  $\alpha\beta$  interfaces ( $\zeta_{\alpha\beta}=0.025$ ,  $\zeta_{\alpha\delta}=\zeta_{\beta\delta}=0$ ). In both simulations, the magnified areas show the instabilities in the phase evolution processes. . . . . 58

- 6.9 Effects of the anisotropic  $\alpha\beta$  interfaces on the pattern formation in the *DS* simulations of Bi-In-Sn system.  $\zeta_{\alpha\beta}$  is varied in a range of 0.05 to 0.15 based on the interfacial energy plot of fig. 6.7(a) and  $\zeta_{\alpha\delta} = \zeta_{\beta\delta} = 0$ . Magnified areas: the formed  $[\alpha\beta]_1[\alpha\delta]_2$ ,  $[\alpha\beta]_2[\alpha\delta]_2$  and  $\beta\alpha\delta$  patterns are specified with the green, red and pink rectangles, respectively.  $a_1$ ,  $a_2$ : the  $\beta$  elimination forming the  $[\alpha\beta]_1[\alpha\delta]_2$ .  $a_3$ ,  $b_1$  and  $c_1$ : the  $\alpha$  nucleation between the  $\beta$  and the  $\delta$ .  $b_2$ :  $\beta$ -to- $\delta$  phase exchange.  $b_3$ ,  $c_2$ : the stable growth of  $\alpha\delta\alpha\delta$ .  $c_3$ : the  $\beta$  elimination reducing the  $[\alpha\beta]_2[\alpha\delta]_1$  to the  $\alpha\beta\alpha\delta$ . 60
- 6.10 Effects of the anisotropic  $\alpha\beta$  interfaces on the pattern formation in the *DS* simulations of the Bi-In-Sn system.  $\zeta_{\alpha\beta}$  is varied in increments of 0.20 to 0.25 based on the interfacial energy plot of fig. 6.7(a) and  $\zeta_{\alpha\delta} = \zeta_{\beta\delta} = 0$ . Magnified areas: the formed  $[\alpha\beta]_1[\alpha\delta]_2$  patterns are specified with the green rectangles.  $d_1$ ,  $e_2$ : the  $\beta$ -to- $\delta$  phase exchange.  $d_2$ ,  $e_1$ : the  $\alpha$  growth between the  $\beta$  and the  $\delta$  phases. . . . . 61
- 6.11 Effects of the anisotropic  $\alpha\delta$  interfaces on the pattern formation in the *DS* simulations of the Bi-In-Sn system.  $\zeta_{\alpha\delta}$  is varied in a range of 0.025 to 0.15 based on the interfacial energy plot of fig. 6.7(b) and  $\zeta_{\alpha\beta} = \zeta_{\beta\delta} = 0$ . Magnified areas: the formed  $[\alpha\beta]_1[\alpha\delta]_2$ ,  $[\alpha\beta]_2[\alpha\delta]_1$  and  $\alpha\beta\delta$  patterns are specified with the green, cyan and brown rectangles, respectively.  $a_1$ :  $\delta$ -lamella branching.  $b_1$ ,  $b_2$ ,  $c_2$ ,  $d_1$ : the  $\alpha$  nucleation between the  $\beta$  and the  $\delta$ .  $c_1$ ,  $c_3$ : the reduction of  $[\alpha\beta]_2[\alpha\delta]_1$  to  $\alpha\beta\alpha\delta$ .  $d_1$ ,  $d_2$ : the  $\alpha$ -to- $\delta$  and the  $\beta$ -to- $\delta$  phase exchanges.  $d_3$ : the sharp  $\beta$  elimination by the  $\alpha$  nucleation. 63
- 6.12 Effects of the anisotropic  $\alpha\delta$  interfaces on the pattern formation in the *DS* simulations of the Bi-In-Sn system.  $\zeta_{\alpha\delta}$  is varied in a range of 0.20 to 0.45 based on the interfacial energy plot of fig. 6.7(b) and  $\zeta_{\alpha\beta} = \zeta_{\beta\delta} = 0$ . Magnified areas: the formed  $[\alpha\beta]_1[\alpha\delta]_2$ ,  $[\alpha\beta]_2[\alpha\delta]_1$  and  $[\alpha\beta]_2[\alpha\delta]_2$  patterns are specified with the green, cyan and red rectangles, respectively.  $e_1$ ,  $f_1$ ,  $g_2$ : the  $\alpha$ -nucleation between the  $\beta$  and the  $\delta$  lamellae.  $e_2$ : reduction of the  $[\alpha\beta]_2[\alpha\delta]$  to the  $[\alpha\beta\alpha\delta]$ .  $f_2$ : the stable  $[\alpha\beta]_2[\alpha\delta]$  pattern from the initial simulation steps.  $g_1$ :  $\beta$ -to- $\delta$  phase exchange.  $e_1$ ,  $h_1$ : the  $\alpha$ -nucleation on the  $\beta$  and the sharp  $\beta$  elimination. . . . . 64

- 6.13 Effects of the anisotropic interfaces on the pattern formation in the *DS* simulations of the **Bi-In-Sn** system.  $\zeta = \zeta_{\alpha\beta} = \zeta_{\alpha\delta} = \zeta_{\beta\delta}$  is varied in a range of 0.025 to 0.10 based on the interfacial energy plots of fig. 6.7. Magnified areas: the formed  $[\alpha\beta]_1[\alpha\delta]_2$  and  $\alpha\beta\delta$  patterns are specified with the green and brown rectangles, respectively. a<sub>1</sub>:  $\beta \rightarrow \alpha + \delta$ . a<sub>2</sub>: reduction of the  $[\alpha\beta]_2[\alpha\delta]_1$  to the  $\alpha\beta\alpha\delta$ . b<sub>1</sub>:  $\beta\delta \rightarrow \delta\alpha\beta$  phases exchange. b<sub>2</sub>: nucleation of the  $\alpha$  on the  $\beta$  not leading to the complete  $\beta$  elimination. b<sub>3</sub>: the  $\beta$ -to- $\delta$  phase exchange. . . . . 65
- 6.14 Effects of the anisotropic interfaces on the pattern formation in the *DS* simulations of the **Bi-In-Sn** system.  $\zeta = \zeta_{\alpha\beta} = \zeta_{\alpha\delta} = \zeta_{\beta\delta}$  is varied in values of 0.15 and 0.20 based on the interfacial energy plots of fig. 6.7. Magnified areas: the formed  $[\alpha\beta]_1[\alpha\delta]_2$  patterns are specified with the green rectangles. d<sub>1</sub>: the  $\alpha$ -nucleation between the  $\beta$  and the  $\delta$  phases. d<sub>2</sub>: the reduction of the  $[\alpha\beta]_2[\alpha\delta]_1$  to the  $\alpha\beta\alpha\delta$  pattern. e<sub>1</sub>: the stable growth of the  $\alpha\delta\alpha\delta$  pattern from the initial simulation steps. . . . . 66
- 6.15 The evolved patterns in the *DS* simulations of the **Bi-In-Sn** system with the highest possible anisotropies in the interfaces. . . . . 67
- 6.16 Summary of the formed patterns in different anisotropic configurations in the *DS* studies of the **Bi-In-Sn** eutectic system. (a): anisotropy only in  $\alpha\beta$  interfaces (based on figs. 6.8 to 6.10). (b): anisotropy only in  $\alpha\delta$  interfaces (based on figs. 6.11 and 6.12). (c): anisotropy in all  $\alpha\beta$ ,  $\alpha\delta$  and  $\beta\delta$  interfaces (based on figs. 6.13 to 6.15). . . . . 68
- 6.17 (a): schematic illustration of the phase eliminations and the formed patterns as the effects of the anisotropic interfaces. (b): possible resultant patterns in the different combinations of the cases in (a). . . . . 69
- 6.18 *RDS* simulation results for the isotropic system at (a):  $t = 0$ , (b):  $t = 24.2e6 \cdot dt$ , (c):  $t = 48.4e6 \cdot dt$ , (d):  $t = 72.6e6 \cdot dt$ , (e):  $t = 96.8e6 \cdot dt$ . At any time, the left figure illustrates the concentration field ( $c_{Bi}$ ), whereas the right figure is the temperature field. Domain size =  $301.8 \times 301.8 \mu\text{m}$ ,  $\omega = 0.309 \text{ }^\circ\text{s}^{-1}$ ,  $r_i = 33.15 \mu\text{m}$ ,  $r_o = 150.9 \mu\text{m}$  based on [91]. . . . . 73
- 6.19 (a): all-time results of fig. 6.18 after the  $2\pi$  rad rotation in one frame, as well as the magnified areas of the middle lamellae showing the velocities  $v_{1,2,3}^{2\pi}$  in their centers. (b): the same configuration after a rotational angle of  $2\pi$  rad based on [91]. . . . . 74

- 6.20 (a): tilted growth of the solidified phases as a result of the anisotropic interfacial energies ( $\zeta_{\alpha\beta} = \zeta_{\alpha\delta} = \zeta_{\beta\delta} = 0.15$ ) after  $2\pi$  rad and  $4\pi$  rad rotations. (b): the comparison between the isotropic simulation in fig. 6.19 (black lines) and the current anisotropic simulation (colored) after the  $\pi/4$  rad rotation. The red line length =  $3.83 \mu m$  and the green line length =  $5.56 \mu m$  indicating the dominance of the  $\zeta_{\alpha\beta}$  in the pattern formation [91]. . . . . 76
- 6.21 The comparison of the experimentally reported lamellar spacings in the work of Witusiewicz et al. [36] with the obtained  $\lambda_{JH}^{sim}$  in the different solidification velocities as reported in fig. 6.5 in section 6.2.1.  $v_i^{n\pi}$  indicates the velocity in the middle of  $i$ -th lamellae (see fig. 6.19) after the  $n\pi$  rad rotation. iso: isotropic simulation, aniso: anisotropic simulation [91]. . . 77
- 6.22 (a): the isotropic simulation result of fig. 6.19 at the rotational angle  $\theta = 2\pi$  rad. The hatched  $\alpha$  lamella has the radius of  $r \simeq (r_i + r_o)/2$  and is used to measure the interface radius values. (b): the radius variations of the  $\alpha\beta$  and  $\alpha\delta$  interfaces with respect to the rotational angle  $\theta$ . . . . . 78
- 6.23 The radius variations with respect to the rotational angle in (a):  $\zeta_{\alpha\beta} = 0.1$  and (b):  $\zeta_{\alpha\delta} = 0.15$ . The middle hatched  $\alpha$  lamellae in both configurations are the base of the radius calculations. . . . . 79
- 6.24 The schematic illustrations of (a): phase boundary radius  $r_\theta$  as a function of the rotational angle  $\theta$ . (b): The tilting of the solidified phase boundary (black lines) based on the depicted radii in (a). (c): The effects of the anisotropy strength increase on the tilt angle ( $\zeta_2, \zeta_3 > \zeta_1$ ).  $\Omega$ : the rotation center. . . . . 80
- 6.25 The evolved microstructures in the *RDS* studies of the Bi-In-Sn ternary eutectic system at the rotational angle of  $\theta = 90^\circ$ .  $\zeta_{\alpha\delta} = \zeta_{\beta\delta} = 0$  and  $\zeta_{\alpha\beta}$  is indicated in each sub-figure. . . . . 81
- 6.26 The radius variations in the simulations of fig. 6.25 with respect to the rotational angle, based on the formed middle  $\alpha$  lamella in (a):  $\alpha\beta$  and (b):  $\alpha\delta$  interfaces.  $\zeta$  denotes the  $\zeta_{\alpha\beta}$  and the other interfaces are modeled isotropically. The global minimums in the curves are specified with the solid squares. . . . . 82
- 6.27 The evolved microstructures in the *RDS* studies of the Bi-In-Sn ternary eutectic system at the rotational angle of  $\theta = 90^\circ$ .  $\zeta_{\alpha\beta} = \zeta_{\beta\delta} = 0$  and  $\zeta_{\alpha\delta}$  is raised up to the value of 0.40. . . . . 83

6.28	The radius variations in (a): $\alpha\delta$ and (b): $\alpha\beta$ phase boundaries, caused by the anisotropy of the interfacial energies in the $\alpha\delta$ interfaces. The global minimums in the curves are specified with the solid squares. . . . .	84
6.29	The evolved microstructures in the <i>RDS</i> studies of the <b>Bi-In-Sn</b> ternary eutectic system at the rotational angle of $\theta = 90^\circ$ . $\zeta_{\alpha\beta} = \zeta_{\beta\delta} = 0.15$ and $r = \zeta_{\alpha\delta}/\zeta_{\alpha\beta}$ is risen up to 3.0. . . . .	85
6.30	The radius variation analysis of the $\alpha\delta$ and the $\alpha\beta$ interfaces in the <i>RDS</i> studies of the <b>Bi-In-Sn</b> ternary eutectic system at the rotational angle of $\theta = 90^\circ$ . $\zeta_{\alpha\beta} = \zeta_{\beta\delta} = 0.15$ and $r = \zeta_{\alpha\delta}/\zeta_{\alpha\beta}$ is risen up to 3.0. ( $a_1$ ): $r_{\alpha\delta}$ and ( $b_1$ ): $r_{\alpha\beta}$ variations with respect to the rotational angle variations in different $\zeta_{\alpha\delta}/\zeta_{\alpha\beta}$ values. Fitting of the second-, third- and fourth-order polynomials to ( $a_2$ ): $\alpha\delta$ and ( $b_2$ ): $\alpha\beta$ interface radius amounts in the minimum and maximum $r$ values. (c): $dr/d\theta$ analysis in the $\alpha\delta$ and $\alpha\beta$ interfaces. . . . .	87
6.31	The schematic illustration of the tilting phenomenon in the <i>DS</i> simulations based on [156]. $x - y$ : the original coordinate system. $x^* - y^*$ : the rotated coordinate system with the amount of the tilt angle $\varphi$ . . . . .	91
6.32	The schematic illustration of tilt angle measurement technique including the solid-solid phase boundary shifting based on [156]. . . . .	93
6.33	Validation of the implemented tilt angle measurement technique in current work, by comparison with the results of Hötzer et al. [67]. In the plotted curves: $R = 3$ , $v = 2.8e - 3$ , $G = 1e - 4$ based on [156]. . . . .	94
6.34	Variation of the resultant tilt angles $\varphi$ with respect to the lamellar spacings $\lambda$ in $R = 1.5$ . $G^{DS}$ : temperature gradient, $D$ : diffusion coefficient, $v$ : solidification velocity. . . . .	95
6.35	Variation of the resultant tilt angles $\varphi$ with respect to the lamellar spacings $\lambda$ in $R = 2.5$ . $G^{DS}$ : temperature gradient, $D$ : diffusion coefficient, $v$ : solidification velocity. . . . .	96
6.36	The schematic illustration of the location shifts in the peaks of the $\varphi - \lambda$ plots, as the result of the variations in the investigated material and process parameters based on [156]. $D$ : diffusion coefficient, $v$ : solidification velocity and $R = \gamma_{\alpha\beta}/\gamma_{\alpha\delta}$ . . . . .	99
6.37	The variation of the measured tilt angles with respect to the <i>Péclet</i> number based on [156]. The dashed line refers to the value of $Pe_{peak}^{fit} = 0.0695$ . . . . .	99

---

6.38	Comparison of the predicted and the measured tilt angles for the values of $R = 1.5$ and $R = 2.5$ based on [156]. . . . .	101
6.39	Comparison of the predicted (dashed curves with the unfilled marks) and the measured (solid curves with the filled marks) based on [156]. . . . .	102

# List of Tables

2.1	The utilized boundary conditions B.S. in the simulation studies and their definitions. . . . .	12
5.1	The utilized approaches to obtain the approximated Gibbs energy functions in STEP 3 of the toolchain based on [132]. . . . .	34
5.2	The equilibrium concentrations of the involved solid phases in the eutectic reaction of NiAl-10Mo system at the exemplary temperature of 1871 K [113]. The concentrations of the non-variant reaction at the eutectic temperature are reported as the liquid concentrations. . . . .	36
5.3	The equilibrium concentrations of the involved phases in the eutectic reaction at the exemplary temperature of 331 K based on [114]. The concentrations of the non-variant reaction at the eutectic temperature are reported as the liquid concentrations. . . . .	41
6.1	Comparison of the evolved phase fractions in the simulation studies with the experimental results of [35] based on [132]. . . . .	48
6.2	The maximum, the minimum and the average deviations between the phase boundary radius data in the simulation results (solid lines in fig. 6.30( $a_2$ , $b_2$ )) and the approximated polynomials (dashed and dotted lines in fig. 6.30( $a_2$ , $b_2$ )). D: deviation in percent, min: minimum, max: maximum, ave: average. . . . .	88
6.3	The interfacial-energy-ratio-dependent coefficients of eq. (6.3) based on [156]. . . . .	100
A.1	Initial approximation results for the Gibbs energies of the NiAl-10Mo system based on [132]. Temperature 1871 K is used to calculate and compare the values of the Gibbs energies $g$ and the chemical potentials $\mu$ for different phases. cal: CALPHAD, app: approximated. . . . .	110

A.2	Modified approximated Gibbs energy functions of the <b>NiAl-10Mo</b> system, used for the phase-field simulations in this work based on [132]. The exemplary temperature of 1871 K, below the melting point, is utilized to calculate and compare the values of the Gibbs energies $g$ and the chemical potentials $\mu$ for the different phases. <i>app</i> : approximated, <i>mod</i> : modified, <i>cal</i> : CALPHAD, <i>eq</i> : equilibrium. . . . .	111
A.3	The parameters of the approximated Gibbs energy functions in the simulation studies of the <b>Bi-In-Sn</b> ternary eutectic based on [91]. The approximated function values $g$ with the original CALPHAD data are compared at the exemplary temperature of 331 K. The resultant chemical potentials $\mu$ for the involved phases are compared either. <i>eq</i> : equilibrium, <i>app</i> : approximated, <i>cal</i> : CALPHAD. . . . .	113
B.1	The used dimensionless simulation and numerical parameters in the <i>DS</i> studies of the <b>NiAl-10Mo</b> system and their values in physical units based on [132]. <i>F</i> : fiber, <i>M</i> : matrix, <i>L</i> : liquid, <i>eut</i> : eutectic. . . . .	114
B.2	The utilized simulation parameters and their physical values in the <i>DS</i> and <i>RDS</i> studies of the <b>Bi-In-Sn</b> ternary eutectic system based on [91]. $\alpha$ : <i>BiIn<sub>2</sub></i> , $\beta$ : $\beta - In$ , $\delta$ : $\gamma - Sn$ , <i>L</i> : <i>liquid</i> iso: isotropic simulation, anis: anisotropic simulation, <i>m</i> : melting point, <i>eut</i> : eutectic. . . . .	115
B.3	Parameters of the idealized system with the symmetric phase diagram and the equal phase fractions based on [67]. The liquid phase is placed in the center of the ternary diagram and the solid phases $\alpha$ , $\beta$ , $\delta$ are placed around the center symmetrically. $\Xi$ , $\xi$ , $X$ are the Gibbs energy parameters of the phases. <i>w</i> : phase fraction. . . . .	116

# Bibliography

- [1] J. Hötzer\*, M. Kellner\*, P. Steinmetz\*, and B. N. (\*equal authors). Applications of the phase-field method for the solidification of microstructures in multi-component systems. *Journal of the Indian Institute of Science*, 2016.
- [2] L. Q. Chen. Phase-field models for microstructure evolution. *Annual review of materials research*, 32(1):113–140, 2002.
- [3] I. Steinbach. Phase-field models in materials science. *Modelling and simulation in materials science and engineering*, 17(7):073001, 2009.
- [4] E. Wesner, A. Choudhury, A. August, M. Berghoff, and B. Nestler. A phase-field study of large-scale dendrite fragmentation in Al–Cu. *Journal of Crystal Growth*, 359:107–121, 2012.
- [5] Y. Zhao, B. Zhang, H. Hou, W. Chen, and M. Wang. Phase-field simulation for the evolution of solid/liquid interface front in directional solidification process. *Journal of Materials Science & Technology*, 35(6):1044–1052, 2019.
- [6] P. Galenko, S. Reutzler, D. Herlach, S. Fries, I. Steinbach, and M. Apel. Dendritic solidification in undercooled Ni-Zr-Al melts: Experiments and modeling. *Acta Materialia*, 57(20):6166 – 6175, 2009.
- [7] A. Choudhury, M. Kellner, and B. Nestler. A method for coupling the phase-field model based on a grand-potential formalism to thermodynamic databases. *Current Opinion in Solid State and Materials Science*, 2015.
- [8] S. N. Enugala, M. Kellner, R. Kobold, J. Hötzer, M. Kolbe, B. Nestler, and D. Herlach. Theoretical and numerical investigations of rod growth of an Ni-Zr eutectic alloy. *Journal of Materials Science*, 54(19):12605–12622, 2019.
- [9] M. Kellner, I. Sprenger, P. Steinmetz, J. Hötzer, B. Nestler, and M. Heilmaier. Phase-field simulation of the microstructure evolution in the eutectic NiAl-34Cr system. *Computational Materials Science*, 128:379–387, 2017.

- [10] J. Hötzer, M. Jainta, P. Steinmetz, B. Nestler, A. Dennstedt, A. Genau, M. Bauer, H. Köstler, and U. Rüde. Large scale phase-field simulations of directional ternary eutectic solidification. *Acta Materialia*, 93(0):194 – 204, 2015.
- [11] F. Hinrichs, M. Kellner, J. Hötzer, and B. Nestler. Calibration of a concentration-driven nucleation mechanism for phase-field simulations of eutectic and off-eutectic compositions in AlCu-5Ag. *Scripta Materialia*, 186:89–94, 2020.
- [12] T. S. Lo, A. Karma, and M. Plapp. Phase-field modeling of microstructural pattern formation during directional solidification of peritectic alloys without morphological instability. *Physical Review E*, 63(3):031504, 2001.
- [13] D. Phelan, M. Reid, and R. Dippenaar. Kinetics of the peritectic phase transformation: In-situ measurements and phase field modeling. *Metallurgical and Materials Transactions A*, 37(3):985–994, 2006.
- [14] H. Ramanarayan and T. Abinandanan. Phase field study of grain boundary effects on spinodal decomposition. *Acta materialia*, 51(16):4761–4772, 2003.
- [15] D. Seol, S. Hu, Y. Li, J. Shen, K. Oh, and L. Chen. Three-dimensional phase-field modeling of spinodal decomposition in constrained films. *Metals and Materials International*, 9(1):61–66, 2003.
- [16] W. Kurz and D. Fisher. Fundamentals of solidification. *Trans Tech Publications Ltd, Trans Tech House, 4711, Aedermannsdorf, Switzerland, 1986. 244*, 1986.
- [17] J. F. O’Hara, E. Smirnova, A. K. Azad, H.-T. Chen, and A. J. Taylor. Effects of microstructure variations on macroscopic terahertz metafilm properties. *Active and Passive Electronic Components*, 2007.
- [18] W. F. Murphy. *Effects of microstructure and pore fluids on the acoustic properties of granular sedimentary materials*. Stanford University, 1982.
- [19] A. Patel, O. Kravchenko, and I. Manas-Zloczower. Effect of curing rate on the microstructure and macroscopic properties of epoxy fiberglass composites. *Polymers*, 10(2):125, 2018.
- [20] F. Greco, L. Leonetti, R. Luciano, and P. N. Blasi. Effects of microfracture and contact induced instabilities on the macroscopic response of finitely deformed elastic composites. *Composites Part B: Engineering*, 107:233–253, 2016.
- [21] O. Lopez-Pamies and P. P. Castañeda. Microstructure evolution in hyperelastic laminates and implications for overall behavior and macroscopic stability. *Mechanics of materials*, 41(4):364–374, 2009.

- [22] S. Bottin-Rousseau, M. Şerefoğlu, S. Yüçetürk, G. Faivre, and S. Akamatsu. Stability of three-phase ternary-eutectic growth patterns in thin sample. *Acta Materialia*, 109:259–266, 2016.
- [23] S. Akamatsu, S. Bottin-Rousseau, and G. Faivre. Experimental evidence for a zigzag bifurcation in bulk lamellar eutectic growth. *Physical review letters*, 93(17):175701, 2004.
- [24] L. Rátkai, G. I. Tóth, L. Környei, T. Pusztai, and L. Gránásy. Phase-field modeling of eutectic structures on the nanoscale: the effect of anisotropy. *Journal of Materials Science*, 52:5544–5558, 2017.
- [25] M. Plapp and A. Karma. Eutectic colony formation: A phase-field study. *Physical Review E*, 66(6):061608, 2002.
- [26] A. Lahiri, C. Tiwary, K. Chattopadhyay, and A. Choudhury. Eutectic colony formation in systems with interfacial energy anisotropy: A phase field study. *Computational Materials Science*, 130:109–120, 2017.
- [27] A. Karma and A. Sarkissian. Morphological instabilities of lamellar eutectics. *Metallurgical and Materials Transactions A*, 27(3):635–656, 1996.
- [28] S. Akamatsu and T. Ihle. Similarity law for the tilt angle of dendrites in directional solidification of non-axially-oriented crystals. *Physical Review E*, 56(4):4479, 1997.
- [29] S. Akamatsu and M. Plapp. Eutectic and peritectic solidification patterns. *Current Opinion in Solid State and Materials Science*, 20(1):46–54, 2016.
- [30] K. Kassner, A. Valance, C. Misbah, and D. Temkin. New broken-parity state and a transition to anomalous lamellae in eutectic growth. *Physical Review E*, 48(2):1091, 1993.
- [31] R. Hoyle, G. McFadden, and S. Davis. Pattern selection with anisotropy during directional solidification. *Philosophical Transactions of the Royal Society of London. Series A: Mathematical, Physical and Engineering Sciences*, 354(1721):2915–2949, 1996.
- [32] C. Ming-Wen, L. Man, Y. Lin, W. Yu-Yan, W. Zi-Dong, and X. Jian-Jun. The effect of anisotropic surface tension on the morphological stability of planar interface during directional solidification. *Chinese Physics B*, 18(4):1691, 2009.
- [33] S. A. Norris, S. H. Davis, S. J. Watson, and P. W. Voorhees. Faceted interfaces in directional solidification. *Journal of crystal growth*, 310(2):414–427, 2008.

- [34] L. L. Wang, Z. J. Wang, X. Lin, M. Wang, and W. D. Huang. The effect of interfacial energy anisotropy on planar interface instability in a succinonitrile alloy under a small temperature gradient. *Chinese Physics B*, 21(6):066801, 2012.
- [35] J. f. Zhang, S. Jun, Z. Shang, W. Lei, and H. z. Fu. Directional solidification and characterization of NiAl-9Mo eutectic alloy. *Transactions of Nonferrous Metals Society of China*, 23(12):3499–3507, 2013.
- [36] V. Witusiewicz, U. Hecht, S. Rex, and M. Apel. In situ observation of microstructure evolution in low-melting Bi-In-Sn alloys by light microscopy. *Acta materialia*, 53(13):3663–3669, 2005.
- [37] M. Ruggiero and J. Rutter. Origin of microstructure in the 332 K eutectic of the Bi-In-Sn system. *Materials science and technology*, 13(1):5–11, 1997.
- [38] S. Rex, B. Böttger, V. Witusiewicz, and U. Hecht. Transient eutectic solidification in In-Bi-Sn: two-dimensional experiments and numerical simulation. *Materials Science and Engineering: A*, 413:249–254, 2005.
- [39] A. Choudhury and B. Nestler. Grand-potential formulation for multicomponent phase transformations combined with thin-interface asymptotics of the double-obstacle potential. *Physical Review E*, 85(2):021602, 2012.
- [40] M. Plapp. Unified derivation of phase-field models for alloy solidification from a grand-potential functional. *Physical Review E*, 84(3):031601, 2011.
- [41] B. Sundman, H. Lukas, and S. Fries. *Computational thermodynamics: the CALPHAD method*. Cambridge university press Cambridge, 2007.
- [42] B. Nestler, H. Garcke, and B. Stinner. Multicomponent alloy solidification: phase-field modeling and simulations. *Physical Review E*, 71(4):041609, 2005.
- [43] A. A. Wheeler, W. J. Boettinger, and G. B. McFadden. Phase-field model for isothermal phase transitions in binary alloys. *Physical Review A*, 45(10):7424, 1992.
- [44] G. Caginalp and W. Xie. Phase-field and sharp-interface alloy models. *Physical Review E*, 48(3):1897, 1993.
- [45] J. A. Warren and W. J. Boettinger. Prediction of dendritic growth and microsegregation patterns in a binary alloy using the phase-field method. *Acta Metallurgica et Materialia*, 43(2):689–703, 1995.
- [46] J. Tiaden, B. Nestler, H. J. Diepers, and I. Steinbach. The multiphase-field model with an integrated concept for modelling solute diffusion. *Physica D: Nonlinear Phenomena*, 115(1-2):73–86, 1998.

- [47] C. Beckermann, H. J. Diepers, I. Steinbach, A. Karma, and X. Tong. Modeling melt convection in phase-field simulations of solidification. *Journal of Computational Physics*, 154(2):468–496, 1999.
- [48] A. Karma. Phase-field formulation for quantitative modeling of alloy solidification. *Physical Review Letters*, 87(11):115701, 2001.
- [49] B. Echebarria, R. Folch, A. Karma, and M. Plapp. Quantitative phase-field model of alloy solidification. *Physical Review E*, 70(6):061604, 2004.
- [50] J. Hötzer, A. Reiter, H. Hierl, P. Steinmetz, M. Selzer, and B. Nestler. The parallel multi-physics phase-field framework Pace3D. *Journal of computational science*, 26:1–12, 2018.
- [51] Software package Parallel Algorithms for Crystal Evolution in 3D – Pace3D. <https://www.h-ka.de/en/idm/profile/pace3d-software>, [Accessed: April 2023].
- [52] C. Feichtinger, S. Donath, H. Köstler, J. Götz, and U. Rüde. Walberla: HPC software design for computational engineering simulations. *Journal of Computational Science*, 2(2):105–112, 2011.
- [53] M. Bauer, S. Eibl, C. Godenschwager, N. Kohl, M. Kuron, C. Rettinger, F. Schornbaum, C. Schwarzmeier, D. Thönnies, H. Köstler, et al. walberla: A block-structured high-performance framework for multiphysics simulations. *Computers & Mathematics with Applications*, 81:478–501, 2021.
- [54] M. Seiz, P. Offenhäuser, S. Andersson, J. Hötzer, H. Hierl, B. Nestler, and M. Resch. Lustre I/O performance investigations on Hazel Hen: experiments and heuristics. *The Journal of Supercomputing*, 77(11):12508–12536, 2021.
- [55] R. Barthel and S. Raffener. ForHLR: a new tier-2 high-performance computing system for research. In *Proceedings of the 3rd bwHPC-Symposium, Universitätsbibliothek Heidelberg, Heidelberg*, pages 73–75, 2017.
- [56] M. Seiz and B. Nestler. Modelling and simulation of the freeze casting process with the phase-field method. *Computational Materials Science*, 193:110410, 2021.
- [57] N. Prajapati, M. Spath, L. Knecht, M. Selzer, and B. Nestler. Quantitative phase-field modeling of faceted crystal dissolution processes. *Crystal Growth & Design*, 21(6):3266–3279, 2021.
- [58] A. August, F. Jamshidi, A. Kneer, R. H. Wolf, M. Wirtz, and B. Nestler. Development of synthetic open porous structures for improved heat transfer. *International Journal of Heat and Mass Transfer*, 159:120071, 2020.

- [59] C. Godenschwager, F. Schornbaum, M. Bauer, H. Köstler, and U. Rüde. A framework for hybrid parallel flow simulations with a trillion cells in complex geometries. In *Proceedings of the International Conference on High Performance Computing, Networking, Storage and Analysis*, pages 1–12, 2013.
- [60] C. Feichtinger, J. Habich, H. Köstler, U. Rüde, and T. Aoki. Performance modeling and analysis of heterogeneous lattice boltzmann simulations on CPU-GPU clusters. *Parallel Computing*, 46:1–13, 2015.
- [61] P. Steinmetz, J. Hötzer, M. Kellner, A. Dennstedt, and B. Nestler. Large-scale phase-field simulations of ternary eutectic microstructure evolution. *Computational Materials Science*, 117:205–214, 2016.
- [62] S. Donath, C. Feichtinger, T. Pohl, J. Götz, and U. Rüde. Localized parallel algorithm for bubble coalescence in free surface lattice-Boltzmann method. In *European Conference on Parallel Processing*, pages 735–746. Springer, 2009.
- [63] J. Götz, K. Iglberger, C. Feichtinger, S. Donath, and U. Rüde. Coupling multi-body dynamics and computational fluid dynamics on 8192 processor cores. *Parallel Computing*, 36(2-3):142–151, 2010.
- [64] M. Bauer, J. Hötzer, M. Jainta, P. Steinmetz, M. Berghoff, F. Schornbaum, C. Godenschwager, H. Köstler, B. Nestler, and U. Rüde. Massively parallel phase-field simulations for ternary eutectic directional solidification. In *Proceedings of the international conference for high performance computing, networking, storage and analysis*, pages 1–12, 2015.
- [65] J. Hötzer, O. Tschukin, M. Ben Said, M. Berghoff, M. Jainta, G. Barthelemy, N. Smorchkov, D. Schneider, M. Selzer, and B. Nestler. Calibration of a multi-phase field model with quantitative angle measurement. *Journal of Materials Science*, 51(4):1788–1797, 2015.
- [66] P. Steinmetz, Y. Yabansu, J. Hötzer, M. Jainta, B. Nestler, and S. Kalidindi. Analytics for microstructure datasets produced by phase-field simulations. *Acta Materialia*, 103:192–203, 2016.
- [67] J. Hötzer, P. Steinmetz, M. Jainta, S. Schulz, M. Kellner, B. Nestler, A. Genau, A. Dennstedt, M. Bauer, H. Köstler, et al. Phase-field simulations of spiral growth during directional ternary eutectic solidification. *Acta Materialia*, 106:249–259, 2016.

- [68] A. Vondrous, M. Selzer, J. Hötzer, and B. Nestler. Parallel computing for phase-field models. *The International Journal of High Performance Computing Applications*, 28(1):61–72, 2014.
- [69] E. Schoof, D. Schneider, N. Streichhan, T. Mittnacht, M. Selzer, and B. Nestler. Multiphase-field modeling of martensitic phase transformation in a dual-phase microstructure. *International Journal of Solids and Structures*, 134:181–194, 2018.
- [70] M. Kellner, J. Hötzer, E. Schoof, and B. Nestler. Phase-field study of eutectic colony formation in NiAl-34Cr. *Acta Materialia*, 182:267–277, 2020.
- [71] P. W. Bridgman. Certain physical properties of single crystals of tungsten, antimony, bismuth, tellurium, cadmium, zinc, and tin. In *Collected Experimental Papers, Volume III*, pages 1851–1932. Harvard University Press, 2013.
- [72] R. P. Mooney, S. McFadden, Z. Gabalcová, and J. Lapin. An experimental–numerical method for estimating heat transfer in a bridgman furnace. *Applied Thermal Engineering*, 67(1-2):61–71, 2014.
- [73] W. Higgins, J. Glodo, E. Van Loef, M. Klugerman, T. Gupta, L. Cirignano, P. Wong, and K. Shah. Bridgman growth of LaBr<sub>3</sub>:Ce and LaCl<sub>3</sub>:Ce crystals for high-resolution gamma-ray spectrometers. *Journal of crystal growth*, 287(2):239–242, 2006.
- [74] R. Mooney, S. McFadden, M. Rebow, and D. Browne. A front tracking model for transient solidification of Al–7wt%Si in a bridgman furnace. *Transactions of the Indian Institute of Metals*, 65(6):527–530, 2012.
- [75] F. Shi-Ji, S. Guan-Shun, W. Wen, L. Jin-Long, and L. Xiu-hang. Bridgman growth of Li<sub>2</sub>B<sub>4</sub>O<sub>7</sub> crystals. *Journal of crystal growth*, 99(1-4):811–814, 1990.
- [76] P. Chevuart, U. El-Hanani, D. Schneider, and R. Triboulet. CdTe and CdZnTe crystal growth by horizontal bridgman technique. *Journal of crystal growth*, 101(1-4):270–274, 1990.
- [77] M. Gündüz and E. Çadırılı. Directional solidification of aluminium–copper alloys. *Materials Science and Engineering: A*, 327(2):167–185, 2002.
- [78] H. Yu, J. Li, X. Lin, L. Wang, and W. Huang. Anomalous overgrowth of converging dendrites during directional solidification. *Journal of crystal growth*, 402:210–214, 2014.
- [79] E. Cadirli, A. Ülgen, and M. Gündüz. Directional solidification of the aluminium–copper eutectic alloy. *Materials Transactions, JIM*, 40(9):989–996, 1999.

- [80] R. J. Schaefer and D. J. Lewis. Directional solidification in a AgCuSn eutectic alloy. *Metallurgical and Materials Transactions A*, 36(10):2775–2783, 2005.
- [81] A. Karma, W. J. Rappel, B. Fuh, and R. Trivedi. Model of banding in diffusive and convective regimes during directional solidification of peritectic systems. *Metallurgical and Materials Transactions A*, 29:1457–1470, 1998.
- [82] H. Zhong, S. Li, H. Lü, L. Liu, G. Zou, and H. Fu. Microstructure evolution of peritectic Nd<sub>14</sub>Fe<sub>79</sub>B<sub>7</sub> alloy during directional solidification. *Journal of Crystal Growth*, 310(14):3366–3371, 2008.
- [83] T. A. Lograsso, B. Fuh, and R. Trivedi. Phase selection during directional solidification of peritectic alloys. *Metallurgical and Materials Transactions A*, 36(5):1287–1300, 2005.
- [84] J. Zhang and R. Singer. Hot tearing of nickel-based superalloys during directional solidification. *Acta Materialia*, 50(7):1869–1879, 2002.
- [85] Y. Zhang and J. Li. Characterization of the microstructure evolution and microsegregation in a Ni-based superalloy under super-high thermal gradient directional solidification. *Materials Transactions*, 53(11):1910–1914, 2012.
- [86] S. Mohagheghi and M. Şerefoğlu. Dynamics of spacing adjustment and recovery mechanisms of ABAC-type growth pattern in ternary eutectic systems. *Journal of Crystal Growth*, 470:66–74, 2017.
- [87] M. Kellner, W. Kunz, P. Steinmetz, J. Hötzer, and B. Nestler. Phase-field study of dynamic velocity variations during directional solidification of eutectic NiAl-34Cr. *Computational Materials Science*, 145:291–305, 2018.
- [88] P. Oswald, M. Moulin, P. Metz, J.-C. Géminard, P. Sotta, and L. Sallen. An improved directional growth apparatus for liquid crystals: applications to thermotropic and lyotropic systems. *Journal de Physique III*, 3(9):1891–1907, 1993.
- [89] S. Akamatsu, S. Bottin-Rousseau, M. Şerefoğlu, and G. Faivre. Lamellar eutectic growth with anisotropic interphase boundaries: Experimental study using the rotating directional solidification method. *Acta Materialia*, 60(6-7):3206–3214, 2012.
- [90] S. Mohagheghi and M. Şerefoğlu. Quasi-isotropic and locked grain growth dynamics in a three-phase eutectic system. *Acta Materialia*, 151:432–442, 2018.
- [91] K. Dargahi Noubary, M. Kellner, and B. Nestler. Rotating directional solidification of ternary eutectic microstructures in Bi-In-Sn: A phase-field study. *Materials*, 15(3):1160, 2022.

- [92] M. Ben Said, M. Selzer, B. Nestler, D. Braun, C. Greiner, and H. Garcke. A phase-field approach for wetting phenomena of multiphase droplets on solid surfaces. *Langmuir*, 30(14):4033–4039, 2014.
- [93] N. Prajapati, M. Selzer, B. Nestler, B. Busch, and C. Hilgers. Modeling fracture cementation processes in calcite limestone: a phase-field study. *Geothermal Energy*, 6(1):1–15, 2018.
- [94] F. Wang and B. Nestler. Wetting transition and phase separation on flat substrates and in porous structures. *The Journal of Chemical Physics*, 154(9):094704, 2021.
- [95] R. Darolia. NiAl alloys for high-temperature structural applications. *JoM*, 43(3):44–49, 1991.
- [96] R. Darolia, D. Lahrman, and R. Field. The effect of iron, gallium and molybdenum on the room temperature tensile ductility of NiAl. *Scripta metallurgica et materialia*, 26(7):1007–1012, 1992.
- [97] K. Bochenek and M. Basista. Advances in processing of NiAl intermetallic alloys and composites for high temperature aerospace applications. *Progress in Aerospace Sciences*, 79:136–146, 2015.
- [98] R. Darolia. Ductility and fracture toughness issues related to implementation of NiAl for gas turbine applications. *Intermetallics*, 8(9-11):1321–1327, 2000.
- [99] S. Milenkovic, A. Coelho, and R. Caram. Directional solidification processing of eutectic alloys in the Ni-Al-V system. *Journal of crystal growth*, 211(1-4):485–490, 2000.
- [100] T. Venkatesh and D. Dunand. Reactive infiltration processing and secondary compressive creep of NiAl and NiAl-W composites. *Metallurgical and Materials Transactions A*, 31(3):781–792, 2000.
- [101] D. Johnson, X. Chen, B. Oliver, R. D. Noebe, and J. Whittenberger. Processing and mechanical properties of in-situ composites from the NiAlCr and the NiAl(Cr,Mo) eutectic systems. *Intermetallics*, 3(2):99–113, 1995.
- [102] J. D. Whittenberger, R. D. Noebe, S. M. Joslin, and B. Oliver. Elevated temperature compressive slow strain rate properties of several directionally solidified NiAl-(Nb,Mo) alloys. *Intermetallics*, 7(6):627–633, 1999.
- [103] A. Misra, R. Gibala, and R. Noebe. Optimization of toughness and strength in multiphase intermetallics. *Intermetallics*, 9(10-11):971–978, 2001.

- [104] M. C. Galetz, B. Rammer, and M. Schütze. The protection of aluminides by alloying with molybdenum in high chlorine containing atmospheres at 1,000 °C. *Oxidation of metals*, 81(1-2):151–165, 2014.
- [105] H. Latreche, G. Tegeder, G. Wolf, P. J. Masset, T. Weber, and M. Schütze. New approaches to improve high temperature corrosion resistance in chlorine-based atmospheres. In *Materials Science Forum*, volume 595, pages 307–321. Trans Tech Publ, 2008.
- [106] H. Li, L. Zheng, H. Zhang, S. Li, H. Zhang, and S. Gong. Effects of solidification parameters on microstructures of Ni<sub>3</sub>Al based single crystal. *Procedia Engineering*, 27:1187–1192, 2012.
- [107] L. Sheng, J. Guo, and H. Ye. Microstructure and mechanical properties of NiAl-Cr(Mo)/Nb eutectic alloy prepared by injection-casting. *Materials & Design*, 30(4):964–969, 2009.
- [108] L. Sheng, W. Zhang, J. Guo, and H. Ye. Microstructure and mechanical properties of Hf and Ho doped NiAl-Cr(Mo) near eutectic alloy prepared by suction casting. *Materials characterization*, 60(11):1311–1316, 2009.
- [109] A. Misra, Z. Wu, M. Kush, and R. Gibala. Microstructures and mechanical properties of directionally solidified NiAl-Mo and NiAl-Mo(Re) eutectic alloys. *Materials Science and Engineering: A*, 239:75–87, 1997.
- [110] H. Bei and E. George. Microstructures and mechanical properties of a directionally solidified NiAl-Mo eutectic alloy. *Acta Materialia*, 53(1):69–77, 2005.
- [111] J. F. Zhang, J. Shen, Z. Shang, Z. R. Feng, L. S. Wang, and H. Z. Fu. Microstructure and room temperature fracture toughness of directionally solidified NiAl-Mo eutectic in situ composites. *Intermetallics*, 21(1):18–25, 2012.
- [112] J. Hunt and K. Jackson. Lamellar and rod eutectic growth. *Trans. Metall. Soc. AIME*, 236:1129–1142, 1966.
- [113] J. Peng, P. Franke, and H. J. Seifert. Experimental investigation and CALPHAD assessment of the eutectic trough in the system NiAl-Cr-Mo. *Phase Equilibria and Diffusion*, 37(5):592–600, 2016.
- [114] V. Witusiewicz, U. Hecht, B. Böttger, and S. Rex. Thermodynamic re-optimisation of the Bi-In-Sn system based on new experimental data. *Journal of Alloys and Compounds*, 428(1–2):115 – 124, 2007.

- [115] A. Choudhury, M. Plapp, and B. Nestler. Theoretical and numerical study of lamellar eutectic three-phase growth in ternary alloys. *Physical Review E*, 83(5):051608, 2011.
- [116] S. Akamatsu, S. Bottin-Rousseau, M. Perrut, G. Faivre, V. Witusiewicz, and L. Sturz. Real-time study of thin and bulk eutectic growth in succinonitrile-(d) camphor alloys. *Journal of crystal growth*, 299(2):418–428, 2007.
- [117] M. Ginibre, S. Akamatsu, and G. Faivre. Experimental determination of the stability diagram of a lamellar eutectic growth front. *Physical Review E*, 56(1):780, 1997.
- [118] G. Faivre. Morphological instabilities of lamellar eutectic growth fronts: a survey of recent experimental and numerical results. *Journal of Crystal growth*, 166(1-4):29–39, 1996.
- [119] S. Akamatsu, S. Bottin-Rousseau, M. Şerefoğlu, and G. Faivre. A theory of thin lamellar eutectic growth with anisotropic interphase boundaries. *Acta Materialia*, 60(6-7):3199–3205, 2012.
- [120] J. O. Andersson, T. Helander, L. Höglund, P. Shi, and B. Sundman. Thermo-Calc & DICTRA, computational tools for materials science. *Calphad*, 26(2):273–312, 2002.
- [121] T. Kitashima. Coupling of the phase-field and CALPHAD methods for predicting multicomponent, solid-state phase transformations. *Philosophical magazine*, 88(11):1615–1637, 2008.
- [122] M. Welland, M. Piro, S. Hibbins, and N. Wang. A method of integrating CALPHAD data into phase-field models using an approximated minimiser applied to intermetallic layer growth in the Al-Mg system. *Calphad*, 59:76–83, 2017.
- [123] S. Zhang, R. Zhang, X. Qu, W. Fang, and M. Liu. Phase field simulation for non-isothermal solidification of multicomponent alloys coupled with thermodynamics database. *Transactions of Nonferrous Metals Society of China*, 23(8):2361 – 2367, 2013.
- [124] J. L. Fattebert, M. Wickett, and P. Turchi. Phase-field modeling of coring during solidification of Au-Ni alloy using quaternions and CALPHAD input. *Acta Materialia*, 62:89–104, 2014.
- [125] J. Wang, M. Osawa, T. Yokokawa, H. Harada, and M. Enomoto. Modeling the microstructural evolution of Ni-base superalloys by phase field method combined with CALPHAD and CVM. *Computational materials science*, 39(4):871–879, 2007.

- [126] I. Steinbach, B. Böttger, J. Eiken, N. Warnken, and S. Fries. CALPHAD and phase-field modeling: A successful liaison. *Journal of phase equilibria and diffusion*, 28(1):101–106, 2007.
- [127] R. Qin and E. Wallach. A phase-field model coupled with a thermodynamic database. *Acta materialia*, 51(20):6199–6210, 2003.
- [128] B. Böttger, J. Eiken, and M. Apel. Multi-ternary extrapolation scheme for efficient coupling of thermodynamic data to a multi-phase-field model. *Computational Materials Science*, 108:283–292, 2015.
- [129] J. Zhu, Z. Liu, V. Vaithyanathan, and L. Chen. Linking phase-field model to CALPHAD: application to precipitate shape evolution in Ni-base alloys. *Scripta Materialia*, 46(5):401–406, 2002.
- [130] H. Kobayashi, M. Ode, S. G. Kim, W. T. Kim, and T. Suzuki. Phase-field model for solidification of ternary alloys coupled with thermodynamic database. *Scripta Materialia*, 48(6):689 – 694, 2003.
- [131] R. Davies, A. Dinsdale, J. Gisby, J. Robinson, and A. M. Martin. MTDATA-thermodynamic and phase equilibrium software from the national physical laboratory. *Calphad*, 26(2):229–271, 2002.
- [132] K. D. Noubary, M. Kellner, J. Hötzer, M. Seiz, H. J. Seifert, and B. Nestler. Data workflow to incorporate thermodynamic energies from CALPHAD databases into grand-potential-based phase-field models. *Journal of Materials Science*, 56(20):11932–11952, 2021.
- [133] F. Wang, P. Altschuh, A. M. Matz, J. Heimann, B. S. Matz, B. Nestler, and N. Jost. Phase-field study on the growth of magnesium silicide occasioned by reactive diffusion on the surface of Si-foams. *Acta Materialia*, 2019.
- [134] F. Wang, A. M. Matz, O. Tschukin, J. Heimann, B. S. Mocker, B. Nestler, and N. Jost. Numerical and experimental investigations on the growth of the intermetallic  $Mg_2Si$  phase in Mg infiltrated Si-foams. *Advanced Engineering Materials*, 19(10):1700063, 2017.
- [135] P. Steinmetz, M. Kellner, J. Hötzer, A. Dennstedt, and B. Nestler. Phase-field study of the pattern formation in Al-Ag-Cu under the influence of the melt concentration. *Computational Materials Science*, 121:6–13, 2016.
- [136] R. Mukherjee, A. Choudhury, and B. Nestler. Composition pathway in Fe-Cu-Ni alloy during coarsening. *Modelling and Simulation in Materials Science and Engineering*, 21(7):075012, oct 2013.

- [137] B. Sundman, U. R. Kattner, M. Palumbo, and S. G. Fries. OpenCalphad—a free thermodynamic software. *Integrating Materials and Manufacturing Innovation*, 4(1):1, 2015.
- [138] W. Cao, S. L. Chen, F. Zhang, K. Wu, Y. Yang, Y. Chang, R. Schmid-Fetzer, and W. Oates. PANDAT software with PanEngine, PanOptimizer and PanPrecipitation for multi-component phase diagram calculation and materials property simulation. *Calphad*, 33(2):328–342, 2009.
- [139] R. Otis and Z. K. Liu. pycalphad: CALPHAD-based computational thermodynamics in python. *Journal of Open Research Software*, 5(1), 2017.
- [140] C. Bale, E. Bélisle, P. Chartrand, S. Deckerov, G. Eriksson, K. Hack, I.-H. Jung, Y.-B. Kang, J. Melançon, A. Pelton, C. Robelin, and S. Petersen. FactSage thermochemical software and databases—recent developments. *Calphad*, 33(2):295–311, 2009.
- [141] S. Akamatsu, S. Bottin-Rousseau, and G. Faivre. Determination of the Jackson-Hunt constants of the In-In<sub>2</sub>Bi eutectic alloy based on in situ observation of its solidification dynamics. *Acta materialia*, 59(20):7586–7591, 2011.
- [142] D. McCartney, J. Hunt, and R. Jordan. The structures expected in a simple ternary eutectic system: Part 1. theory. *Metallurgical Transactions A*, 11(8):1243–1249, 1980.
- [143] T. Himemiya and T. Umeda. Three-phase planar eutectic growth models for a ternary eutectic system. *Materials Transactions, JIM*, 40(7):665–674, 1999.
- [144] M. Şerefoğlu and R. Napolitano. On the role of initial conditions in the selection of eutectic onset mechanisms in directional growth. *Acta materialia*, 59(3):1048–1057, 2011.
- [145] R. Napolitano and M. Şerefoğlu. Control and interpretation of finite-size effects and initial morphology in directional solidification of a rod-type eutectic transparent metal-analog. *JOM*, 64(1):68–75, 2012.
- [146] D. P. Woodruff and I. Ward. *The solid-liquid interface*, volume 1. Cambridge University Press, 1973.
- [147] A. Karma. Beyond steady-state lamellar eutectic growth. *Physical review letters*, 59(1):71, 1987.
- [148] S. Akamatsu and G. Faivre. Anisotropy-driven dynamics of cellular fronts in directional solidification in thin samples. *Physical Review E*, 58(3):3302, 1998.

- [149] S. Akamatsu and G. Faivre. Traveling waves, two-phase fingers, and eutectic colonies in thin-sample directional solidification of a ternary eutectic alloy. *Physical Review E*, 61(4):3757, 2000.
- [150] S. G. Kim, W. T. Kim, T. Suzuki, and M. Ode. Phase-field modeling of eutectic solidification. *Journal of crystal growth*, 261(1):135–158, 2004.
- [151] A. Parisi and M. Plapp. Stability of lamellar eutectic growth. *Acta Materialia*, 56(6):1348–1357, 2008.
- [152] M. Plapp. Three-dimensional phase-field simulations of directional solidification. *Journal of crystal growth*, 303(1):49–57, 2007.
- [153] S. Ghosh, A. Choudhury, M. Plapp, S. Bottin-Rousseau, G. Faivre, and S. Akamatsu. Interphase anisotropy effects on lamellar eutectics: A numerical study. *Physical Review E*, 91(2):022407, 2015.
- [154] S. Ghosh and M. Plapp. Influence of interphase anisotropy on lamellar eutectic growth patterns. *Transactions of the Indian Institute of Metals*, 68(6):1235–1238, 2015.
- [155] M. Apel, B. Böttger, V. Witusiewicz, U. Hecht, and I. Steinbach. Lamellar pattern formation during 2D-directional solidification of ternary eutectic alloys. *Solidification and Crystallization*, pages 271–279, 2004.
- [156] K. D. Noubary, M. Kellner, P. Steinmetz, J. Hötzer, and B. Nestler. Phase-field study on the effects of process and material parameters on the tilt angle during directional solidification of ternary eutectics. *Computational Materials Science*, 138:403–411, 2017.
- [157] E. L. Cussler. *Diffusion: mass transfer in fluid systems*. Cambridge university press, 2009.
- [158] W. E. Lorensen and H. E. Cline. Marching cubes: A high resolution 3D surface construction algorithm. In *ACM siggraph computer graphics*, volume 21 4, pages 163–169. ACM, 1987.
- [159] M. Apel, B. Boettger, H. Diepers, and I. Steinbach. 2D and 3D phase-field simulations of lamella and fibrous eutectic growth. *Journal of crystal growth*, 237:154–158, 2002.

- 
- [160] L. Hu, W. Hu, G. Gottstein, S. Bogner, S. Hollad, and A. Bührig-Polaczek. Investigation into microstructure and mechanical properties of NiAl-Mo composites produced by directional solidification. *Materials Science and Engineering: A*, 539:211–222, 2012.
- [161] J. J. Eggleston, G. B. McFadden, and P. W. Voorhees. A phase-field model for highly anisotropic interfacial energy. *Physica D: Nonlinear Phenomena*, 150(1-2):91–103, 2001.
- [162] S. Akbulut, Y. Ocak, N. Maraşlı, K. Keşlioğlu, H. Kaya, and E. Çadırlı. Determination of interfacial energies of solid Sn solution in the In-Bi-Sn ternary alloy. *Materials characterization*, 60(3):183–192, 2009.
- [163] W. Yao, X. Han, and B. Wei. Microstructural evolution during containerless rapid solidification of Ni-Mo eutectic alloys. *Journal of alloys and compounds*, 348(1-2):88–99, 2003.